MICROELECTROMECHANICAL SYSTEMS (MEMS) INTERRUPTER FOR SAFE AND ARM DEVICES

THESIS

Steven S. Mink, Captain, USAF

AFIT/GE/ENG/06-43

DEPARTMENT OF THE AIR FORCE
AIR UNIVERSITY

AIR FORCE INSTITUTE OF TECHNOLOGY

Wright-Patterson Air Force Base, Ohio

AFIT/GE/ENG/06-43

MICROELECTROMECHANICAL SYSTEMS (MEMS)

INTERRUPTER FOR SAFE AND ARM DEVICES

THESIS

Presented to the Faculty

Department of Electrical and Computer Engineering

Graduate School of Engineering and Management

Air Force Institute of Technology

Air University

Air Education and Training Command

In Partial Fulfillment of the Requirements for the

Degree of Master of Science in Electrical Engineering

Steven S. Mink, BSEE

Captain, USAF

March 2006

AFIT/GE/ENG/06-43

MICROELECTROMECHANICAL SYSTEMS (MEMS)

INTERRUPTER FOR SAFE AND ARM DEVICES

Steven S. Mink, BSEE
Captain, USAF

Approved:

_____/signed_____   _____
LaVern A. Starman (Chairman)   date

_____/signed/_____   _____
James A. Fellows (Member)   date

_____/signed/_____   _____
Guna S. Seetharaman (Member)   date

AFIT/GE/ENG/06-43

Abstract

This thesis addresses the development of a new micro-scale interrupter mechanism for a safe and arm device used in modern weapon systems. The interrupter mechanism often consists of a physical barrier that prevents an initial source of energy, in an explosive train, from being transferred to subsequent charges. In general, when the physical barrier is removed, the weapon is considered armed, and the charge is allowed to propagate. Several issues facing current safe and arm devices systems are the shrinking industrial base for manufacturing these devices and the desire for modern safe and arm devices to be compatible with next generation weapon systems that are generally decreasing in size and increasing in complexity. The solution proposed here is to design, fabricate, and test a conceptual interrupter mechanism using Microelectromechanical Systems (MEMS) components. These components have inherent benefits over current devices, such as smaller feature sizes and lower part counts, which have the capability to improve performance and reliability. After an extensive review of existing micro-scale safe and arm devices currently being developed, a preliminary design was fabricated in a polysilicon surface micromachining process. The operating principle of this conceptual interrupter mechanism is to have MEMS actuators slide four overlapping plates away from each other to create an aperture, thus providing an unimpeded path for an initiating energy source to propagate. Operation of the fabricated MEMS interrupter mechanism was successfully demonstrated with an approximate aperture area of 1024 μm^2 being created.

iv

AFIT/GE/ENG/06-43

To Nicholas and Jeffrey

Acknowledgments

       This thesis would have been impossible without the daily motivation and encouragement provided by my family. Without their support and patience during the countless long days and nights, this endeavor could never have been completed. I would like to express my gratitude to Major LaVern Starman, my faculty advisor, for his encouraging guidance and patience throughout my endless hours in the lab and at the computer. Furthermore, I am indebted to my other committee members, Lt Col James Fellows and Dr. Guna Seetharaman, for the guidance and assistance they provided, which are reflected in the final product. I would also like to thank Capt Ken Bradley and Mr. Ed Wild, from AFRL/MN, who provided essential details about the slapper design and offered encouraging comments about the final fabricated device. Thanks also goes to Capt Paul Kladitis, whose excitement about MEMS first inspired me in choosing this topic for my research. In addition, Gabriel Safford must be recognized for providing the initial research on micro-scale safe and arm devices while working at AFIT during the summer of 2004.

       My fellow classmates, especially Frank Parada and Jeff Clark, deserve a hearty thank you for battling alongside me through the trenches that are AFIT. Without their assistance, the rigors of this experience would have been much more difficult to endure. A special thanks goes to my fellow MEMS warrior, Dan Denninghoff. The results of this work would not have been the same without Dan asking the important question, "What is

it again that this device is supposed to do?" His commitment to the truth and willingness to assist in analyzing the theory behind my research contributed significantly to the thoroughness of this thesis.

I am also grateful to the following list of AFIT professionals: Bill Trop and Rick Patton, whose unwavering laboratory support enabled me to produce most of the data presented in this thesis; the AFIT library personnel, whose amazing document retrieval skills enabled me to acquire critical bits of information that are included throughout this document; and Tetsuo Kaieda for providing me with invaluable laboratory equipment training and offering the type of guidance that could only come from a graduating student. In addition, thanks also goes to the following people outside of AFIT: Antonio Crespo, from AFRL/SNDI, for his assistance in fixing one of my design errors with a focused ion beam; and Steve Topper for making himself available to give my "final" thesis a thorough scrubbing so that the work contained within this document is a much more professional product. Finally, a special thanks goes out to all Ammo troops—past, present, and future—whose never-ending effort goes largely unnoticed.

Steven S. Mink

Table of Contents

List of Figures

Figure   Page

List of Tables

MICROELECTROMECHANICAL SYSTEMS (MEMS)

INTERRUPTER FOR SAFE AND ARM DEVICES

1. Introduction

For the people that work around explosive weapons, safety is a vital concern that affects all facets of a weapon's life – from transportation, to storage, to maintenance, to buildup, to upload, to flight, and to release. The potential for a major mishap, to include both equipment and personnel, exists if a weapon is inadvertently armed during one of these operations. To ensure that the weapon is in an "armed" condition only when desired and in a "safe" condition at all other times is the function of the safe and arm device [1], which is an integral part of the weapon's fuze.

1.1   Safe and Arm Device Functional Description

The safe and arm (S&A) device is an element of the fuze, which is a critical component of all munition items. The fuze is responsible for initiating the sequence of steps that ultimately leads to weapon detonation. The method of initiation for a particular fuze depends on the intended launch environment, or the desired effect upon detonation. For example, fuzes can be designed to initiate the explosive train on impact, by sensing a relative proximity to a target, or by sensing depth of penetration through a target. This latter example applies to bunker busting-type weapons where it is desirable to penetrate through various levels of dirt and/or concrete barriers before detonation. A critical

requirement for fuzes is their high reliability standards that must be maintained throughout years of storage, maintenance, and use in a variety of surroundings. For instance, fuzes and their internal components need to endure extreme environmental conditions that range anywhere from large temperature fluctuations during many years of dormant storage to the high acceleration forces experienced both prior to and in the launch environment [2], [3]. Figure 1-1 shows several pictures of fuzes currently used for both air-to-air and air-to-ground munition systems. The S&A device is a component within each of these fuzes.

The S&A device has the essential function of preventing a premature detonation by eliminating the potential for energy to reach the main charge. This is accomplished by
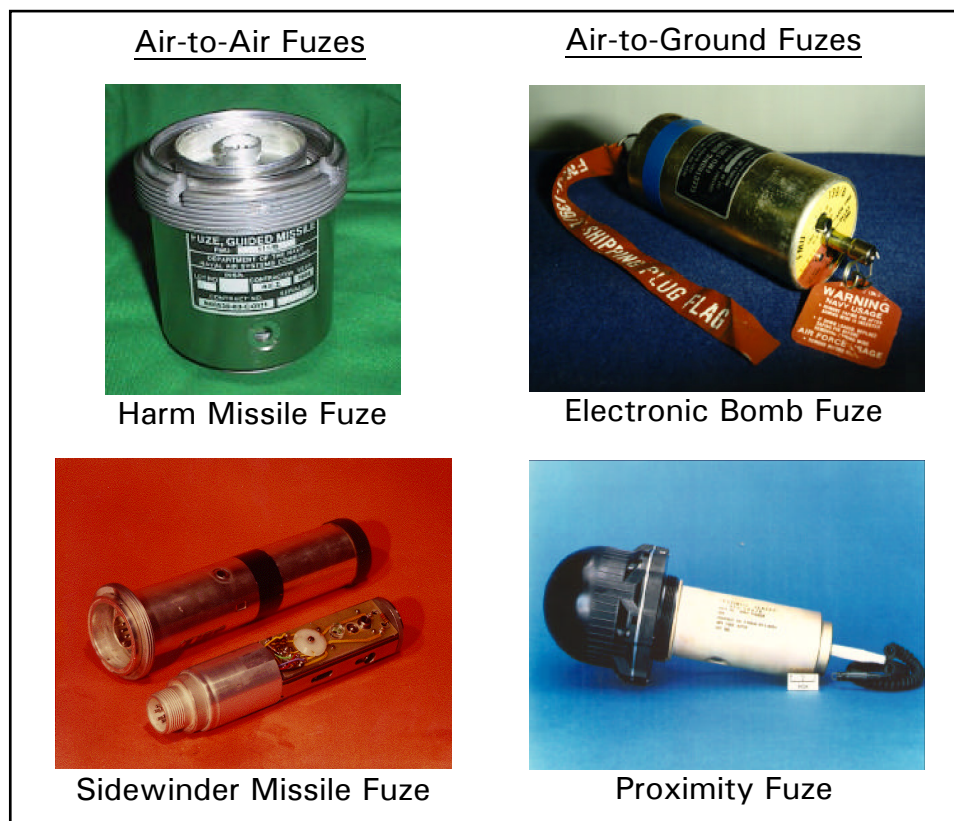
Figure 1-1. Fuzes currently being used in military weapons [4]. Safe and arm devices are a critical component within each of these fuzes.

eliminating a continuous path for the energy to propagate through the explosive train. Toward this objective, S&A devices often "interrupt" the explosive train by making use of in-line mechanisms as a way to prevent inadvertent arming. Figure 1-2 shows a schematic diagram of a generic explosive train that depicts the spatial relationship between explosive charges and the S&A device. Another function of the S&A device, equally important as preventing a continuous path, is allowing a continuous path. When a predetermined set of conditions are satisfied, the physical mechanisms (within the S&A device) that interrupt the explosive components are removed, thereby enabling the explosive energy to propagate toward the main charge, ultimately resulting in weapon detonation. In this case, an input energy source is detected by a detonator, which is a very sensitive explosive element designed to amplify a weak initial signal. The next explosive element is the lead charge, which represents the next stage of amplification. The booster charge depicts the final stage of amplification that provides the necessary explosive force to detonate the main charge [1]. To be effective, the device must remain
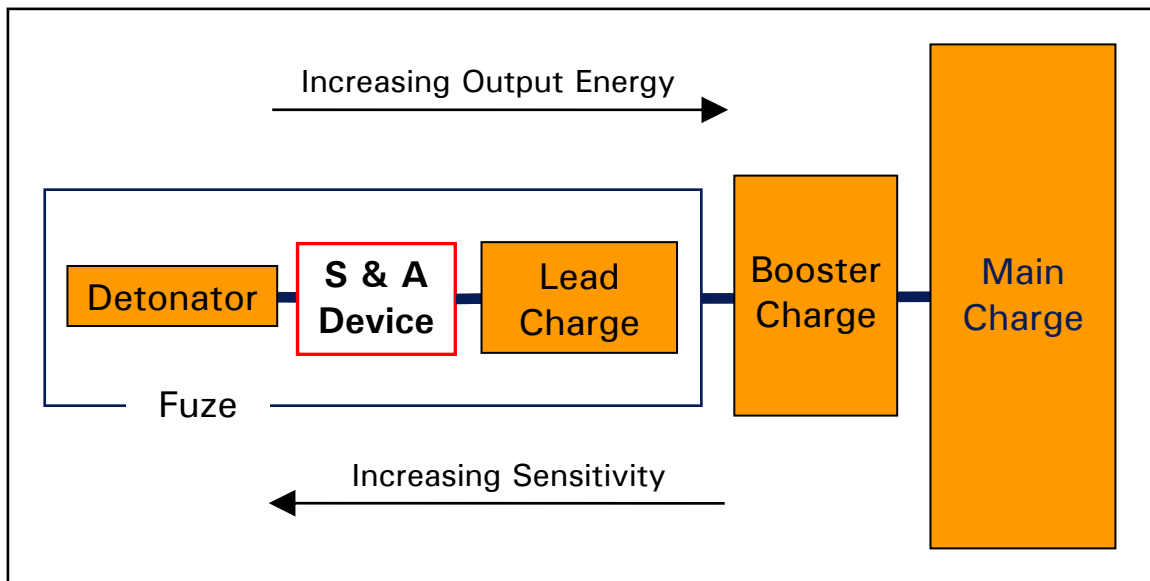
Figure 1-2. Schematic diagram of a generic explosive train. The spatial relationship between fuze, S&A device, and other charges is shown.

in a safe configuration during most of its lifetime, thus preventing an armed condition until the last possible instant. Additionally, the S&A device must be able to move very rapidly, and accurately, into the armed condition since most munitions travel at high velocities once launch has been initiated [5].

The "interruption" method used by manufacturers of S&A devices vary, but most call the mechanism that performs this function the interrupter. Interruption can be performed by misaligning the explosive components or by providing a physical barrier so that the explosive components cannot propagate through the explosive train in the case of an inadvertent initiation. Various levels of complexity can be designed into this interrupter mechanism to ensure it remains safe; however, device complexity usually has a direct impact on device reliability. More complex interrupter schemes have a greater potential to introduce single-point failure modes into the explosive train, which can result in a launched weapon that fails to detonate [6].

In order for the interrupter to move into the armed position, a specific sequence of events (for which the S&A device is designed) must be detected to ensure a valid launch command has occurred. This is typically achieved by ensuring at least two distinct environmental conditions are satisfied, which indicate an intentional detonation sequence has been initiated [7]. Care must be taken that the selected environmental stimuli will not be experienced in the munition lifecycle except when the munition is in the proper launch cycle. The launch cycle is defined as the period between when "the munition is irreversibly committed to launch" and some relatively short time after it leaves the weapon launch platform [7]. The launch platform could be an aircraft, ship, artillery tube, or rifle.

1.2   Problem Statement

One of the issues facing the munitions community in recent years is the age of fuzes and their components in existing weapons systems. The reliability of these older fuzes tend to decrease over time, and existing systems will require components to be replenished in the coming years, either through product improvement or new development programs [8], [9]. In addition to finding replacement components for older weapons systems, new S&A devices need to be developed for munitions currently being acquired. Many designs that exist today use mechanisms that were designed over two decades ago and some designs are too complex and costly with respect to other improvements being made to modern weapon systems [10]. Modern munition items tend to be designed for more reliability and accuracy, and as such require a S&A device that achieves an equal, if not better, level of performance to ensure both infallible safety and lethal functionality.

Another problem, which compounds the issue of an aging stockpile, is that old S&A designs are difficult to reproduce since the industrial base that manufactures these devices is shrinking. From 1987 to 2001, the firms that produce electronic and electromechanical fuzes shrunk by over 80 percent (from 31 to 6) [2]. Additionally, the suppliers of Army fuzes have reduced in numbers from 20 to 5 since 1999 [11]. The military downsizing that occurred in the 1990's reduced the dollars available for munitions expenditures, and as a result many manufacturers stopped producing fuzes because it became less profitable [9], [11].

1.3   Proposed Solution

A common approach in designing modern weapon systems is to miniaturize munitions, which places a 'smaller is better' requirement on all components that make up a munition item, including the S&A device. Advances in solid-state fabrication techniques have made it possible to create micrometer-scale mechanical systems, which enable alternative design possibilities for fuze designers. Consequently, S&A devices designed using micro-electro-mechanical systems (MEMS) concepts become an obvious area to explore for potential exploitation. MEMS technology is based on the thoroughly refined fabrication methods used in the integrated circuit community. The processes used in fabricating integrated circuit devices using solid-state materials have been well proven over the last 50 years. Starting with the first transistor developed in 1947 by engineers at Bell Laboratories and the first integrated circuit demonstrated in 1958 by Texas Instruments [12], tremendous advances have been made in the material research and processing technologies that enable the complex electronic devices produced today.

The attractiveness of MEMS S&A devices for modern weapons systems is their inherent benefits over current macro-scale devices. One example is that their smaller feature size offers the advantage of decreased mass, which directly benefits enhanced range and maneuverability requirements. This can be shown by considering the scale factor, S, of an object. Mass is known to scale in relation to the volume of an object, therefore, the scale factor for mass is S^3 [13]. For instance, consider a cube where the length of each edge is one meter. If each edge length is reduced to one micrometer (10^{-6} meter), the mass of the cube will decrease by $1/10^{18}$ ($S = 1/10^6$), or by a factor of 10^{18}. On a more practical scale, consider the length of each edge scaling from one millimeter

(10^{-3} meter) to one micrometer (10^{-6} meter). Applying the mass scale factor of S^3 to this example, results in the mass decreasing by a factor of 10^9.

Another example of the inherent benefits of MEMS devices is the higher fabrication volumes, which typically contributes to lower costs over time. The decrease in cost is a result of the capability to produce these devices in large volumes. This has been irrefutably witnessed in the processes used to fabricate integrated circuits, which are very similar to the processes used in MEMS fabrication. As a final example of inherent MEMS benefits, the lower part counts, that are generally characteristic of these devices, have a tendency to increase reliability over systems with a larger part count.

Clearly, if an S&A device, designed with components manufactured with MEMS techniques, could be successfully demonstrated, it would allow more design flexibility for the replenishment of fuze elements in current munitions, and enable additional approaches in the design of modern weapon systems. Additionally, MEMS-based S&A devices could be used for advanced munitions concepts, such as miniature weapons on unmanned aerial vehicles (UAV) and 'smart' bullets.

1.4   Conclusion

This research effort will focus on an interrupter design concept created completely in a MEMS fabrication process.   The Multi-User MEMS Processes (MUMPs®) fabrication process was used for all four design iterations submitted as part of this thesis. Each device uses polysilicon as the structural layers and hence the specific process provided by MUMPs® is called PolyMUMPs™. The PolyMUMPs process is a three-layer, general-purpose surface micromachining process that offers two releasable polysilicon layers and one metal layer [14].

Chapter 2 of this thesis will discuss some basic concepts that must be considered when designing a munition fuze, along with the forces typically encountered in military weapons. In addition, several micro-scale S&A devices currently being investigated will be presented. Chapter 3 will discuss some common devices used to initiate explosive trains, along with a look at a specific detonator device that has been fabricated using microelectronic fabrication techniques. Chapter 3 will conclude with some ideas on how to integrate the MEMS interrupter concept proposed in this research with a microdetonator device. Chapter 4 will discuss the theory involved in designing a MEMS interrupter mechanism, and the motivation for selecting the individual components that are incorporated into the final fabricated device. Chapter 5 will discuss the test results used to characterize the performance of the individual actuation mechanisms, along with the experimental results of the fabricated S&A interrupter device. Lastly, Chapter 6 will discuss the conclusions reached based on these experimental results and present some recommendations for future work in this area.

Bibliography

[1] MIL-HDBK-757(AR). "*Fuzes*." Military Handbook. 15 April 1994.

[2] Skibbie, Lawrence F. "Fuze Industrial Base Problems Should No Longer Be Ignored," *National Defense Magazine*, (June 2001). March 2005. <http://www.nationaldefensemagazine.org/issues/2001/Jun/Fuze_Industrial.htm>.

[3] MIL-STD-331B. "*Environmental and Performance Tests for Fuze and Fuze Components*." Military Standard. 1 December 1989.

[4] Cope, Randall D. "Fuzing Overview." Report to 44th Annual Fuze Conference (April 2000). Naval Air Warfare Center, Weapons Division. March 2005. <http://www.dtic.mil/ndia/44fuze/cope.pdf>.

[5] Giladett, Leo V. "Safing and Arming Mechanism." US Patent 4619199. 28 October 1986.

[6] Hardt, Lee R. and James E. Means. "Thermomagnetic Safe Arm Device." US Patent 5083041. 21 January 1992.

[7] MIL-STD-1316E. "*Safety Criteria For Fuze Design*." Department of Defense Design Criteria Standard. 10 July 1998.

[8] Tobik, Timothy. "Air Force Fuze Technology Overview." Report to 49th Annual Fuze Conference (April 2005). Air Force Research Laboratory, Munitions Directorate. June 2005. <http://proceedings.ndia.org/5560/Wednesday/Session_II/ Tobik.pdf>.

[9] Erwin, Sandra I. "Munitions Sector 'In Trouble,' Despite New Funds," *National Defense Magazine*, (December 2001). June 2005. <http://www.nationaldefense magazine.org/issues/2001/Dec/Munitions_Sector.htm >.

[10] Jensen, Norman E. and Bennett W. Kelley. "Safe/Arm Explosive Transfer Mechanism." US Patent 4667600. 26 May 1987.

[11] Erwin, Sandra I. "Army Not Producing Enough Ammunition," *National Defense Magazine*, (May 2003). June 2005. <http://www.nationaldefensemagazine.org/ issues/2001/Dec/Munitions_Sector.htm>.

[12] Neamen, Donald A. *Semiconductor Physics and Devices* (3rd Edition)*.* New York: McGraw-Hill, 2003.

[13] Trimmer, William and Robert H. Stroud. "Scaling of Micromechanical Devices," in *The MEMS Handbook*. Ed. Mohamed Gad-el-Hak. Boca Raton: CRC Press LLC, 2002.

[14] Koester, David and others. *PolyMUMPs Design Handbook (Revision 11.0)*. MEMSCAP, 2005. August 2005. < http://www.memsrus.com/documents/ PolyMUMPs.DR.v11.pdf>.

2. Background

Since S&A devices are in most cases subcomponents of fuzes, the fundamentals of fuze operation and general design considerations are briefly discussed below. Additionally, the types of environmental forces typically encountered in munitions items and their relative magnitudes will be presented. Finally, several MEMS-based S&A devices currently being investigated will be summarized.

2.1   Fuze Fundamentals

The fuze's role is to make decisions for the munition that provide for: 1) *safety*, by separating the detonator from other elements in the explosive train until after separation activities, 2) *arming*, which includes sensing the environment(s) associated with intentional separation, aligning explosive trains (or removing a barrier), and preparing the munition for functioning (i.e., closing switches or logic links), and 3) *initiation* at the desired point in space or time [1]. This thesis will only focus on the first two functions – safety and arming. Also, note that "separation", as used in this document, can mean both launch from an airframe, or firing from a rifle or tube. In most cases, launch will be used instead of separation, but ultimately the type of munition being described will determine the correct terminology.

Fuze functioning can also be described in terms of its explosive train, which begins with an initiating stimulus and proceeds through the explosive amplification stages to the detonation of the main charge of the munition. Amplification is required to convert a small, insensitive initial energy impulse into sufficient energy to detonate the

main charge in a reliable and controllable manner that also satisfies safety requirements [1]. As shown in Figure 1-2, the explosive train is a sequence of explosive elements arranged in an order of increasing output energy and decreasing sensitivity.

Some important considerations that must go into a fuze design are safety, reliability, producibility, lifecycle costs, and standardization. Standardization has the overall effect of reducing development time, lowering costs, and decreasing manpower requirements [1]. Managing these considerations is a challenge for the fuze designer when selecting a design approach to satisfy mission requirements due to the large variety of munition types that exist in most stockpiles. Different munitions usually have unique fuzing requirements based upon their intended use environment and physical size. A list of munition types could include mines, grenades, projectiles, pyrotechnics, rockets, missile warheads, and artillery/tank/mortar ammunition [1]. This is only a partial list; however, it is obvious that a large assortment of fuzes is needed to accommodate these varying munitions. Clearly, the range of munition requirements and associated performance parameters complicates fuze standardization.

2.2   Environmental Factors in Fuze Design

To ensure safety and reliably control arming, it is critical to fully understand the environments and associated stresses that a fuze will encounter during its entire lifetime, or its "factory-to-function sequence" [1]. S&A devices have to be designed to function flawlessly under these varying conditions. These environments can be characterized as either natural or induced, depending on the source of generation. Environments independent of human interaction are considered natural environments, and include temperature, pressure, humidity, rain, hail, dust, and salinity. Environments that are

generated from human-made equipment or munitions are considered induced environments, and include acceleration, spin, dynamic air pressure (ram air), thermodynamic heating, vibration, drag, creep, and target impact [1].

All of the munition types mentioned in the previous section will be subjected to most of these environments, either during its storage lifetime or its flight/launch lifetime. Consequently, the fuzes and S&A devices that are designed for these munitions will also be exposed to these environments. Furthermore, while each munition type will generally be exposed to similar environments during storage, handling, and maintenance, the environments during launch will be dramatically different depending on the physical dimensions of the munition and its method of separation, i.e., rocket-propelled launch, cartridge fired, or separation due to gravity. In other words, a large missile fired from an aircraft will experience forces much different than a small rotating projectile fired from an automatic cannon, or a bomb dropped from an aircraft. As a result of the conflicting environments exposed to different munition types, a large and diverse group of fuzes and S&A devices must be designed to take advantage of the "most predictable and consistent" environmental forces available for a particular type of munition and its application [1].

Clearly, environments such as temperature, vibration, shock, and humidity must be tolerated by all fuzes so that safety is maintained and future functioning is not degraded [1]. In addition, at least two independent environmental conditions must be sensed in order to ensure an intentional launch has occurred and prevent unintentional arming [2]. Some common environments used to operate S&A mechanisms and arm munitions are acceleration (to include both setback and angular), deceleration (creep or

drag), rotational velocity (centrifugal force), ram air pressure, hydrostatic pressure, aerodynamic heating, and gravity [1]. The range and magnitudes of forces for the typical munition categories are listed in Table 2-1.

As can be seen from the table, projectiles experience forces greater than any other type of munition. Both acceleration and spin are the environments most commonly used to induce arming in projectile fuzes because they are reasonably predictable. Likewise, launched grenades generate acceleration and spin forces of sufficient magnitude to perform the arming function (the values listed in Table 2-1 are for the 40-mm grenade) [1]. However, the spin rate for missiles and rockets is not usually large enough to trigger the arming mechanisms. Therefore, missile fuzes typically use acceleration for at least

Table 2-1. Typical Forces During Launch and Free Flight [1].

*	PROJECTILE		ROCKET	MISSILE	LAUNCHED GRENADE	MORTAR
	Small Caliber	Large Caliber				
Acceleration (Setback), [g]	$71 - 125$ $\times 10^3$	$2.5 - 60$ $\times 10^3$	$40 - 6500$	$12 - 40$	$18 - 65$ $\times 10^3$	$0.3 - 10$ $\times 10^3$
Spin, [rps]	$1917 - 2030$	$45 - 500$	$0 - 50$	$3 - 12$	$63 - 200$	$10 - 50$
Spin, [rpm]	$115 - 122$ $\times 10^3$	$2.7 - 30$ $\times 10^3$	$0 - 3$ $\times 10^3$	$180 - 720$	$3.78 - 12$ $\times 10^3$	$0.6 - 3$ $\times 10^3$
Velocity, [m/s]	$825 - 1080$	$610 - 1173$	$514 - 1116$	$96 -$ supersonic	$76 - 366$	$242 - 320$
Velocity, [Mach]	$2.42 - 3.17$	$1.79 - 3.45$	$1.51 - 3.28$	$.028 +$	$0.22 - 1.08$	$0.71 - 0.94$
Deceleration (Creep), [g]	> 10	$3 - 32$	3	n/a	n/a	< 1
Aerodynamic Heating, [K]	753	673	698	negligible +	negligible	negligible

* g – acceleration due to gravity (1 g = 9.8 m/s at sea level); rps – revolutions per second; rpm – revolutions per minute

one environmental energy source with the other independent source usually coming from onboard batteries used to power secondary locks for out-of-line mechanisms. Rocket fuzes encounter similar environments as missile fuzes, except that their launch acceleration is usually higher. Also, newer versions of rocket fuzes have made use of ram air as an energy source to supply electrical power for arming devices [1].

For other munitions, like mortars, the use of spin as an arming environment largely depends on the launch method. For example, 60-mm and 81-mm caliber mortars are launched from smooth-bored tubes, which do not induce spin on the projectile. The predominant environmental forces for these mortars are acceleration and ram air. On the other hand, the larger 4.2-in. (~ 107 mm) caliber mortar is launched from a rifled barrel, which does induce spin on the round, and the resulting centrifugal force, along with the induced acceleration force, provides enough energy to arm the fuze [1].

Other munition types not listed in Table 2-1 are scatterable mines and submunitions. These munitions are capable of being fired from a 155-mm howitzer projectile or dropped from an aircraft. Environments used for arming these types of fuzes are acceleration, spin, and ram air. For comparison purposes, the Ground Emplaced Mine Scattering System used by the Army and the CBU-24/B Cluster Bomb (BLU-26/B submunition) used by the Air Force have spin rates of approximately 53 revolutions per second (rps) and 45 rps, respectively [1].

2.3   Current Research Efforts on MEMS-Based Safe and Arm Devices

Various government agencies have been actively studying S&A devices that have been designed and fabricated using MEMS techniques in order to capitalize on the reliability, repeatability, and economic benefits that come from microelectronic

fabrication. Moreover, MEMS S&A devices have the potential to revolutionize the design of munition systems that are currently limited due to physical constraints imposed on them by individual component dimensions. In the following paragraphs, the research that these agencies have been performing on micro-scale S&A devices is examined. To begin with, the work being done by two of the U. S. Navy's warfare centers is discussed. Next, a device being developed by Sandia National Laboratories, followed by the micro-scale S&A efforts of the U. S. Army is presented. Lastly, the U.S. Air Force's approach to miniaturizing munition components will be reviewed.

2.3.1 Naval Surface Warfare Center – Indian Head Division

The Naval Surface Warfare Center (NSWC) is part of the Naval Sea Systems Command, which is the primary activity for designing, engineering, integrating, building, and procuring U.S. Navy ships and their associated combat systems [3]. Their Indian Head Division, which develops explosives and propellants for use in state-of-the-art weapons systems [4], has been investigating MEMS-based S&A devices for over a decade. One of their objectives is to provide a "smarter" device that increases reliability and safety, while simultaneously improving accuracy [5], [6]. A majority of their efforts have concentrated on the development of an S&A for the Canistered Countermeasure Anti-Torpedo (CCAT) program [6]–[8].

The size advantage to using MEMS technology is readily apparent when one considers that firing devices for Navy torpedoes have decreased in volume by 87% (from 118 in.^{3} to 15 in.^{3}) since the 1970's [7]. Figure 2-1 shows the relative size of the S&A die in comparison to other CCAT warhead components. The outer diameter of the CCAT is 6.75 in. and the package that contains the actual S&A die is less than 1 in.^{3}. Although

not depicted in the figure, the firing device contains three additional MEMS components. One is an acceleration sensor that senses the g-forces due to an actual launch, and the other two are an internal measurement unit and a flow sensor used to ensure safe separation from the launching platform [8].

Functional Description

The fundamental concept for their S&A device is the interruption of optical energy required to charge a photocell that ultimately produces the high voltage output
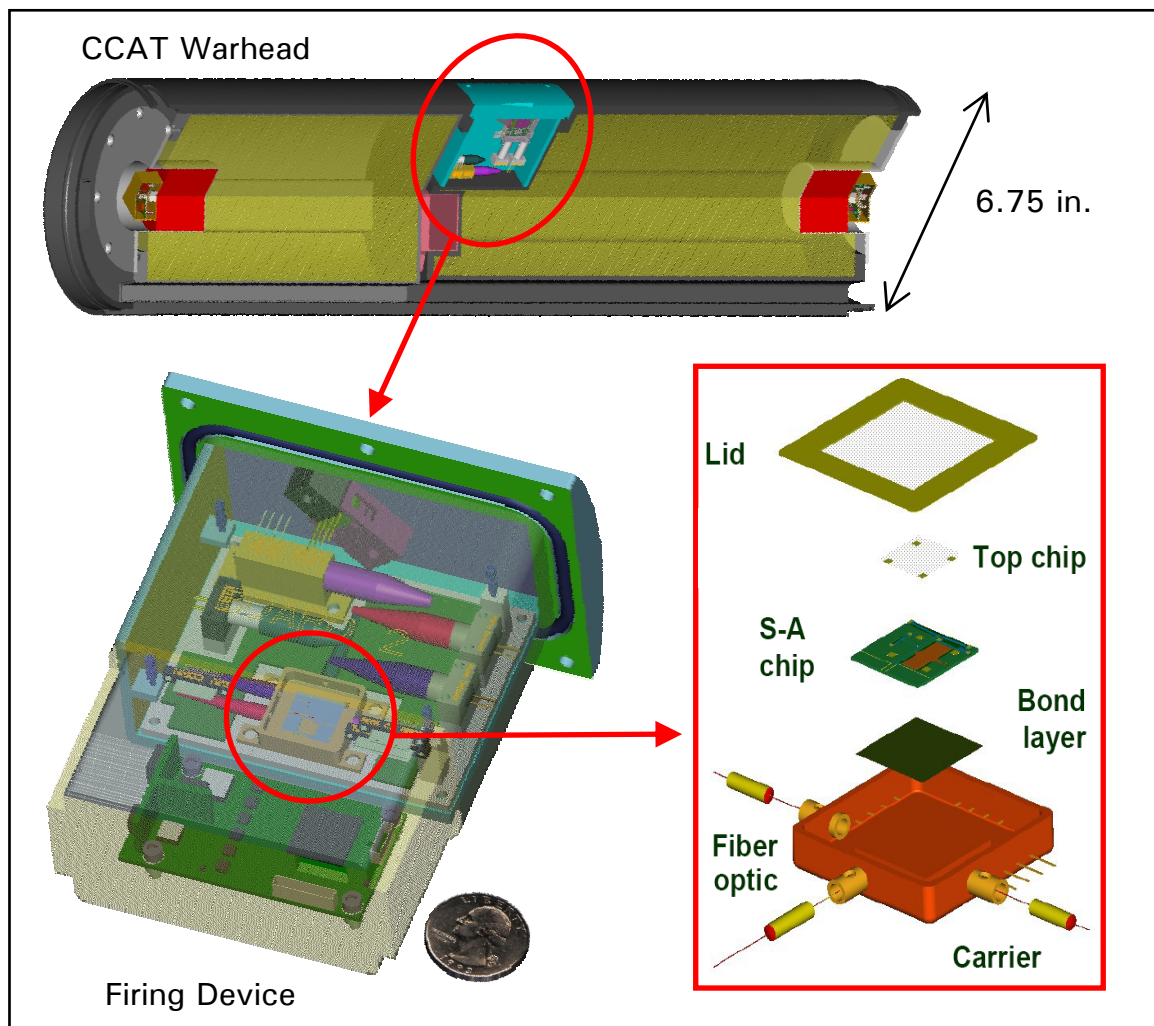
Figure 2-1. Relative size comparison between CCAT warhead, firing device, and MEMS-based S&A device [7], [8]. Warhead outer diameter is 6.75 in. and the entire S&A package is approximately 1 in.^{3}.

that is used to initiate the detonators [9]. Two fiber optic cables (a source fiber and a receiver fiber) are used to propagate the optical energy. The MEMS-based interrupter ensures safety by decoupling the energy from the source fiber to the receiver fiber.

Three different MEMS-based approaches to designing an interrupting/coupling actuator for the optical energy were considered. These preliminary designs were fabricated using a LIGA process where nickel was used as the reflecting material. (LIGA is a German acronym for lithographie, galvanoformung, and abformung, which means lithography, electroplating, and molding. This process is capable of producing high-aspect ratio metallic structures with very smooth sidewalls [10]). The chosen design concept consists of a 45º edge reflector fabricated on a MEMS-based actuator that reflects the optical energy in the source fiber into the receiver fiber. This approach offers a relatively simple actuator design with a measured optical efficiency of almost 80% [9].

Figure 2-2 shows a schematic diagram of the edge reflector concept. When the edge reflector is misaligned in relation with the source fiber, the optical energy is effectively interrupted from continuing along its intended path. Conversely, when the arming command is initiated, a comb drive actuator is used to align the edge reflector with the source fiber and thus allow the transmission of energy to the receiver fiber.

More recently, the NSWC moved to a Deep Reactive Ion Etching (DRIE) process that has seen improvements in performance and a lower cost per unit [7]. DRIE uses a high-density plasma source to repeatedly etch silicon resulting in very high-aspect ratio structures [10]. One of the drawbacks with this process is the sidewall roughness that occurs on the edge reflector as a result of the scalloping effects produced during the DRIE process. This surface roughness produces a less than ideal reflectivity, resulting in
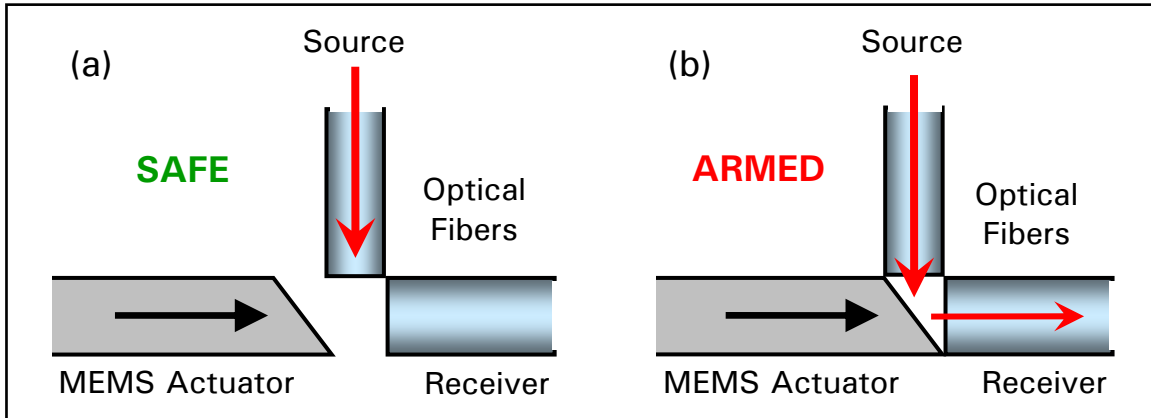
Figure 2-2. Design concept of the 45º edge reflector as an optical switch in both the (a) safe and (b) armed position [11].

an average measured optical efficiency of about 53.7%, which is approximately 10% less than the average calculated efficiency. Nevertheless, the excess energy absorbed by the reflector did not result in device failure due to structural melting. A laser diode with an emission wavelength of 810 nm and an output power of 1000 mW was used for these measurements [11].

Figure 2-3(a) depicts the comb drive actuator used to move the edge reflector surface in-line with the source fiber, along with the approximate device dimensions in millimeters. Figure 2-3(b) is a scanning electron microscope (SEM) image that shows the fabricated comb drive actuator. Figure 2-4 shows an SEM image of the edge reflector in relation to the source and receiver fibers used in this device. Note the thickness of the reflector is approximately 100 μm. The comb drive actuator was shown to be capable of moving the reflector 200 μm with a drive signal of 50 VDC [11].

NSWC Conclusion

The successful results of the NSWC efforts have facilitated progress for the CCAT acquisition program, which is scheduled to enter Low Rate Initial Production in
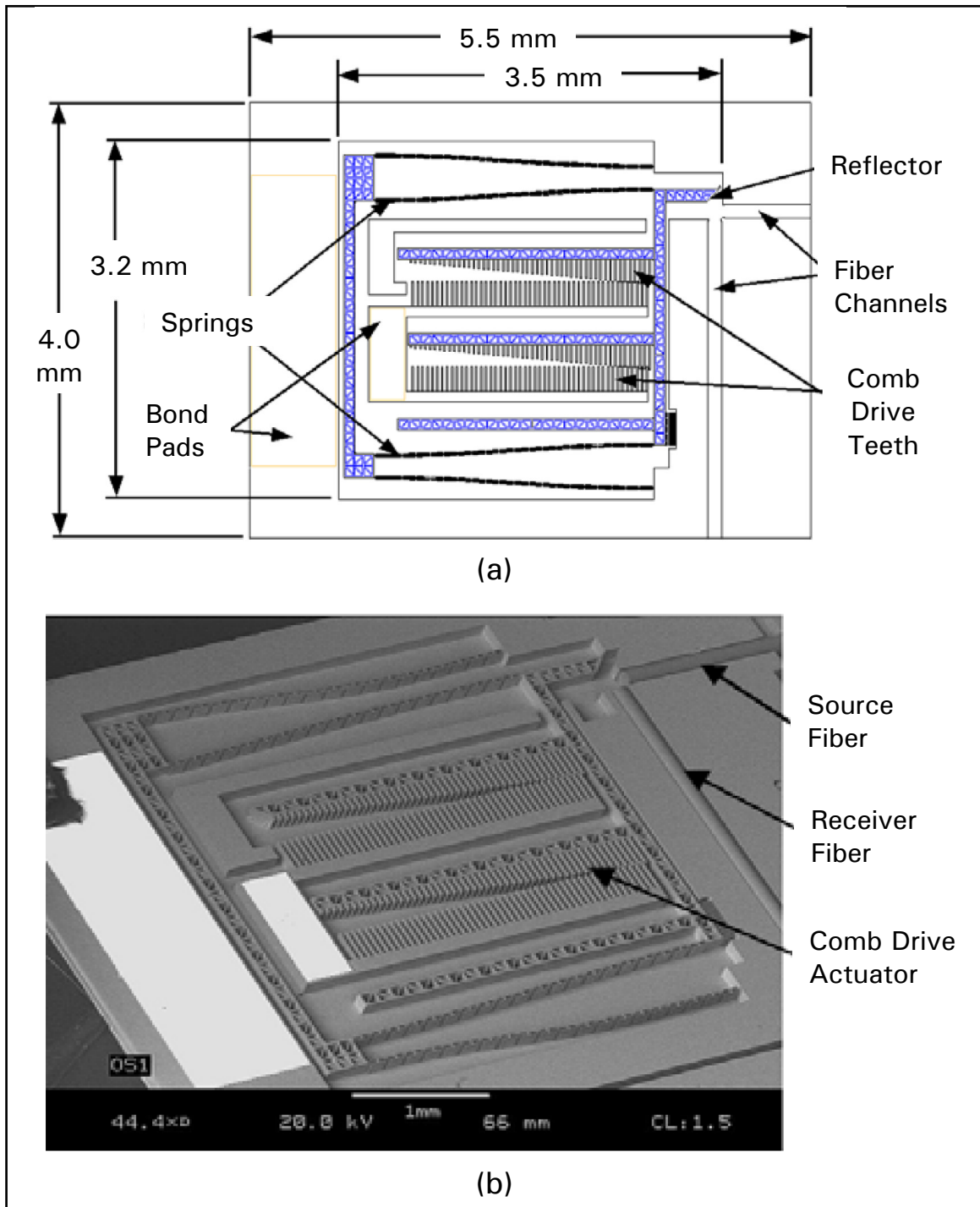
Figure 2-3. (a) Schematic of comb drive actuator used to align the edge reflector with the source fiber. (b) SEM image of fabricated comb drive actuator along with both the source and receiver optical fibers [11].
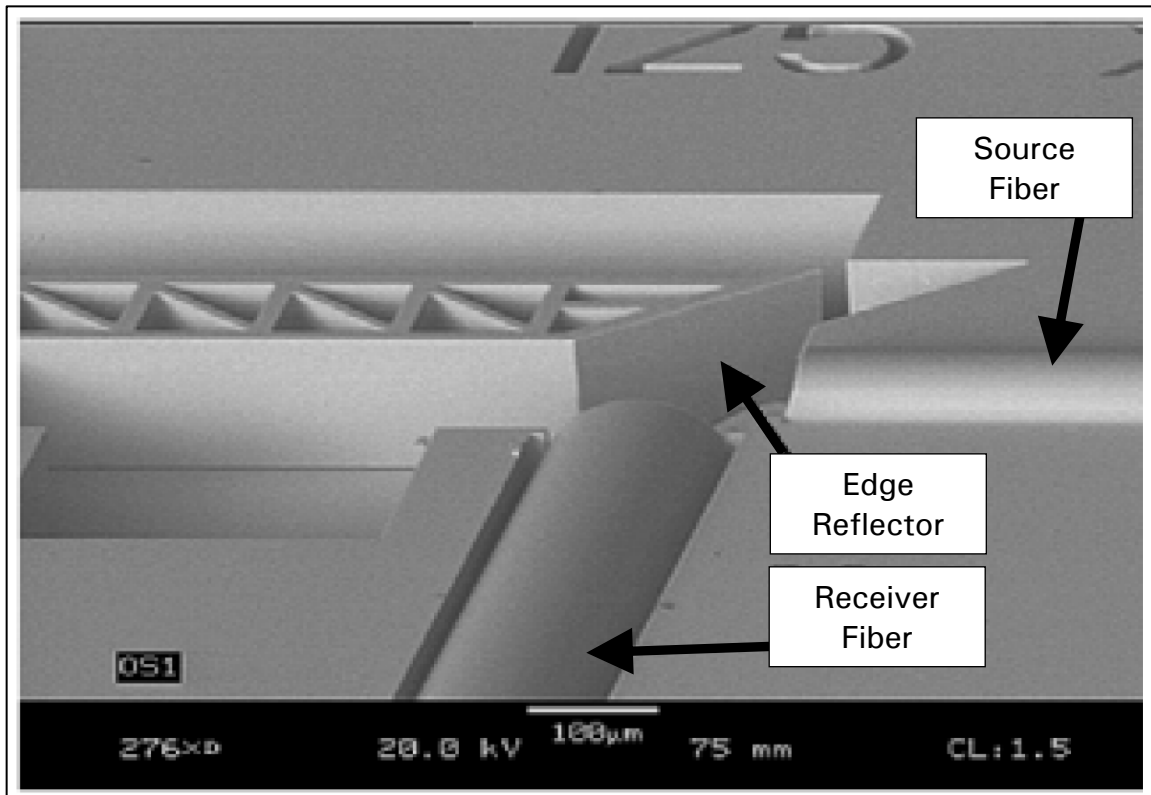
Figure 2-4. SEM image of the source and receiver fiber alignment with the gold-coated silicon reflector. The thickness of the reflector is approximately 100 μm [11].

fiscal year (FY) 2008 [12]. Their research has also enabled the development of a MEMS S&A for a shipboard submunition that senses arming environments and will eventually be capable of integration with novel energetic materials at low cost. This submunition S&A is designed to use an out-of-line microdetonator (< 300-µm thick) that requires less explosive material than conventional detonators, by about two orders of magnitude [8]. Finally, the work of the NSWC has enabled the possibility for a new generation of Navy underwater weapon systems that maintain safety and ensure arming through the use of MEMS-based S&A devices [6].

2.3.2 Naval Air Warfare Center – Weapons Division

The Naval Air Warfare Center (NAWC) is part of the Naval Air Systems Command, which is the primary activity for developing, testing, and managing "technologically superior" airborne weapon systems [13]. Their Weapons Division has been investigating a distributed S&A system that uses an arming control unit to generate unique arming commands to selected microdetonators in the system. The arming control unit interprets the environmental conditions received from the MEMS sensors prior to generating the arming commands. Each "smart" detonator in their distributed system incorporates an electromagnetically actuated MEMS slider mechanism, microelectronics, and miniaturized explosive components [8], [14]. Figure 2-5 shows the exploded view of the distributed S&A system for a conceptual warhead.
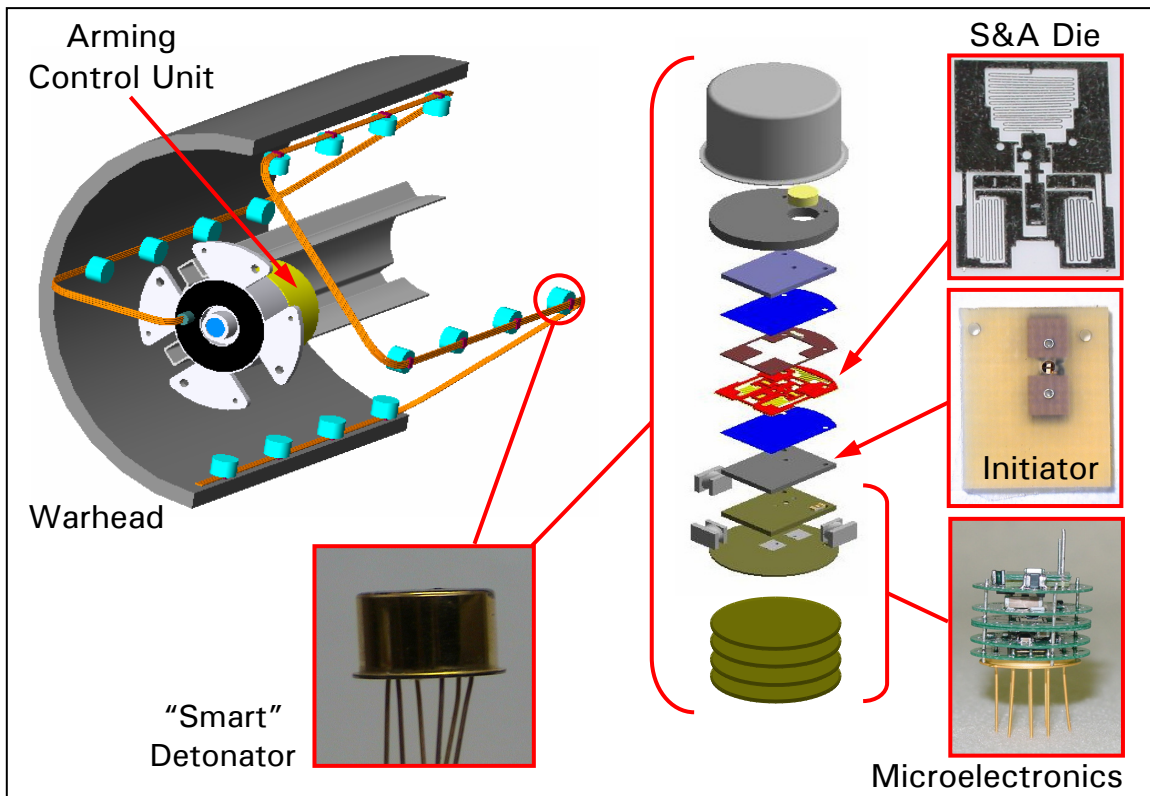
Figure 2-5. Exploded view of the distributed S&A system in a conceptual warhead application. Diameter of "smart" detonator package is 13 mm [15].

Functional Description

The S&A function is performed by a spring-loaded slider mechanism with an attached explosive primer. In the safe position, this primer is physically separated from the follow-on explosive components to ensure an interrupted explosive train. The slider is locked in the safe position by two spring-loaded latch mechanisms that are disengaged by miniature electromagnets when the proper signal is received from the arming control unit. In this unlatched (armed) condition, the slider is free to move the primer in-line with both the detonator and the follow-on explosive charges to allow a continuous explosive train. The slider mechanism moves because of a pre-loaded spring flexure that pushes the slider when the latches are disengaged [14]. An operational schematic of the MEMS slider along with an image of the actual device is shown in Figure 2-6.
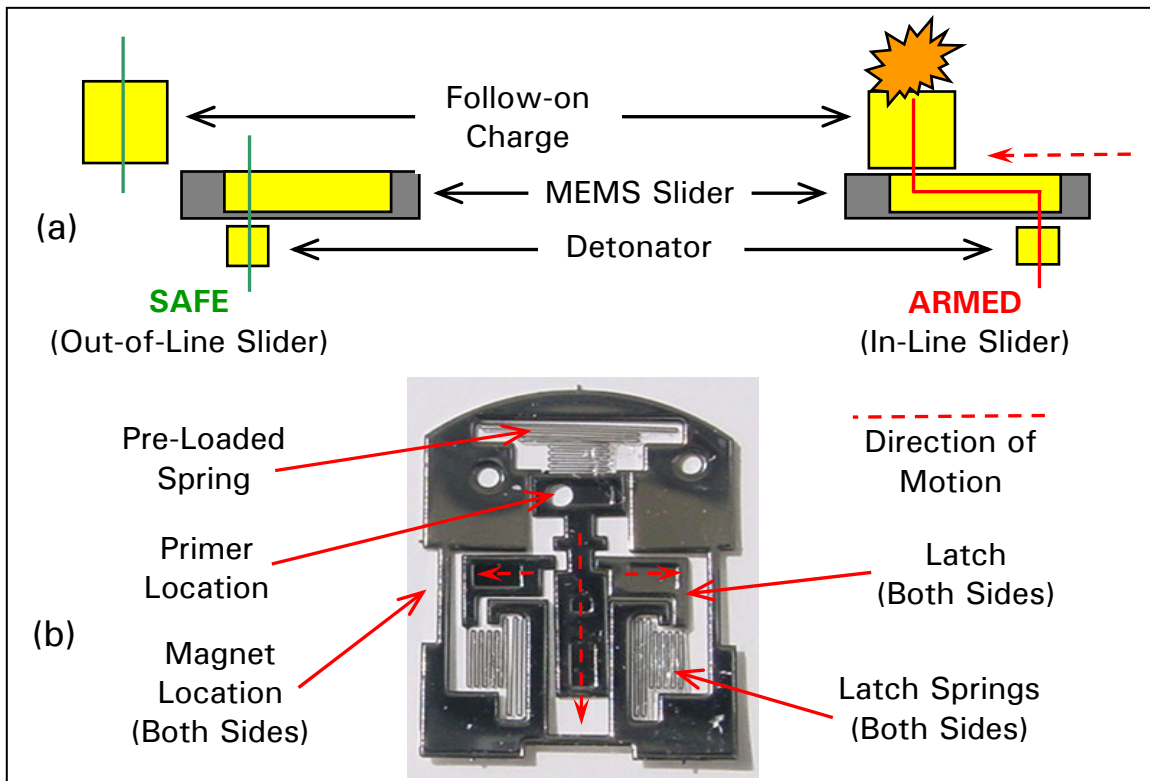
Figure 2-6. (a) Schematic diagram of slider mechanism. (b) MEMS slider mechanism shown with significant components labeled [14].

2-13

One of the benefits of this design is that it gives the warhead some performance capability by allowing the arming control unit to determine the most advantageous way to initiate the distributed system of detonators. For example, a line of detonators or a staged sequence of detonators could be initiated in order to direct the detonation energy of the warhead in a specific direction. This allows for increased flexibility and opens up additional design possibilities for future generation weapons [14]. A diagram of different initiation schemes is shown in Figure 2-7.

NAWC Conclusion

Major accomplishments of the NAWC "smart" detonator program include a successful demonstration of the safety provided by the out-of-line primer and energy transfer of small in-line charges using the MEMS-based slider mechanism. Additionally, the sequential firing of multiple detonators has been shown. This program has smoothed the progress for other integrated MEMS and microelectronic S&A devices that are significantly smaller than what can be provided by current technologies [8]. Clearly, the capability to produce miniaturized "smart" detonators by integrating MEMS actuators, microelectronics, and micro-explosive components will assist other designers of micro-scale S&A devices to facilitate future weapon concepts and applications.

Single Point Initiation   Staged Initiation
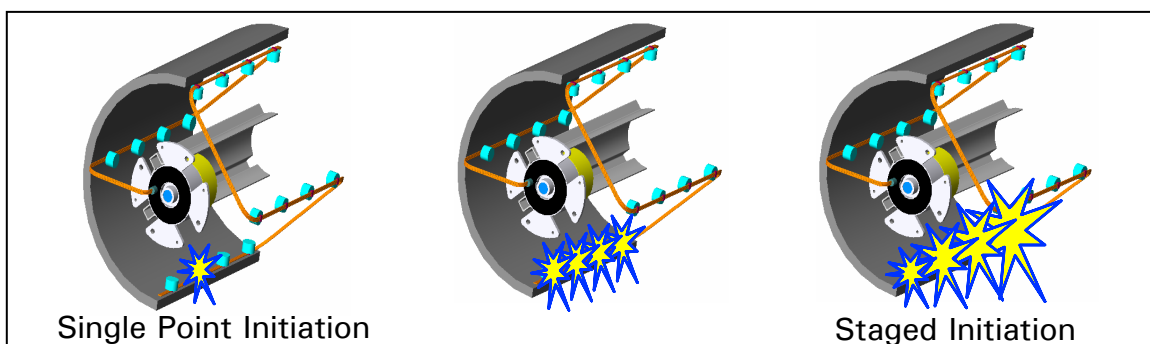
Figure 2-7. Different detonator initiation schemes provides for a potential aiming capability by directing the blast of the warhead [14].

2.3.3 Armament Research, Development and Engineering Center

The Armament Research, Development and Engineering Center (ARDEC) is the U. S. Army's principal activity responsible for the development and sustainment of current and future armament technologies [16]. Recently, their Fuze Division, which is part of the Fuze and Precision Armaments Technology Directorate, has been extensively characterizing a MEMS-based S&A device for incorporation into high-explosive air-burst munitions [17]. The robustness of their device has been proven from the demonstrations that have been performed to date. Currently, they are leveraging off the success of this device to facilitate improved producibility of MEMS-based S&A devices for advanced munitions. The success of these efforts will allow this technology to become more affordable and enable a high-volume manufacturing capability advantage for commercial companies [18].

Functional Description

ARDEC's S&A device uses several slider mechanisms that operate as environmental sensors for the acceleration and spin forces generated after separation from the gun barrel. For safety, the device maintains a transfer charge out-of-line from in-between the detonator and lead charges of the fuze. The arming slider's out-of-line and in-line (armed) positions are controlled by mechanical locks, which are disengaged by two independent environmental forces. See Figure 2-8 and Figure 2-9 for a schematic of the S&A device in both the safe and armed positions, respectively. Initially, the linear acceleration due to launch is encountered, which causes a setback slider to move against a spring-tensioned load. If the proper amount of acceleration is sensed (indicating a valid launch), a safety lock lever on the arming slider is disengaged. Next, the centrifugal

force, resulting from the spin of the projectile, forces the arming slider to move against its pre-loaded spring. This action places the transfer charge in-line with the other explosive components; thereby completing the explosive train. An additional safety feature on this S&A die is a command slider that prevents the arming slider from moving into a fully armed position unless independently enabled by high-pressure propellant gases when the weapon is committed to launch. This method to actuate the command slider is notional and it may eventually be actuated by other means. Two main advantages for this S&A device is its simplicity and the fact that it does not rely on any external environmental sensors [19].
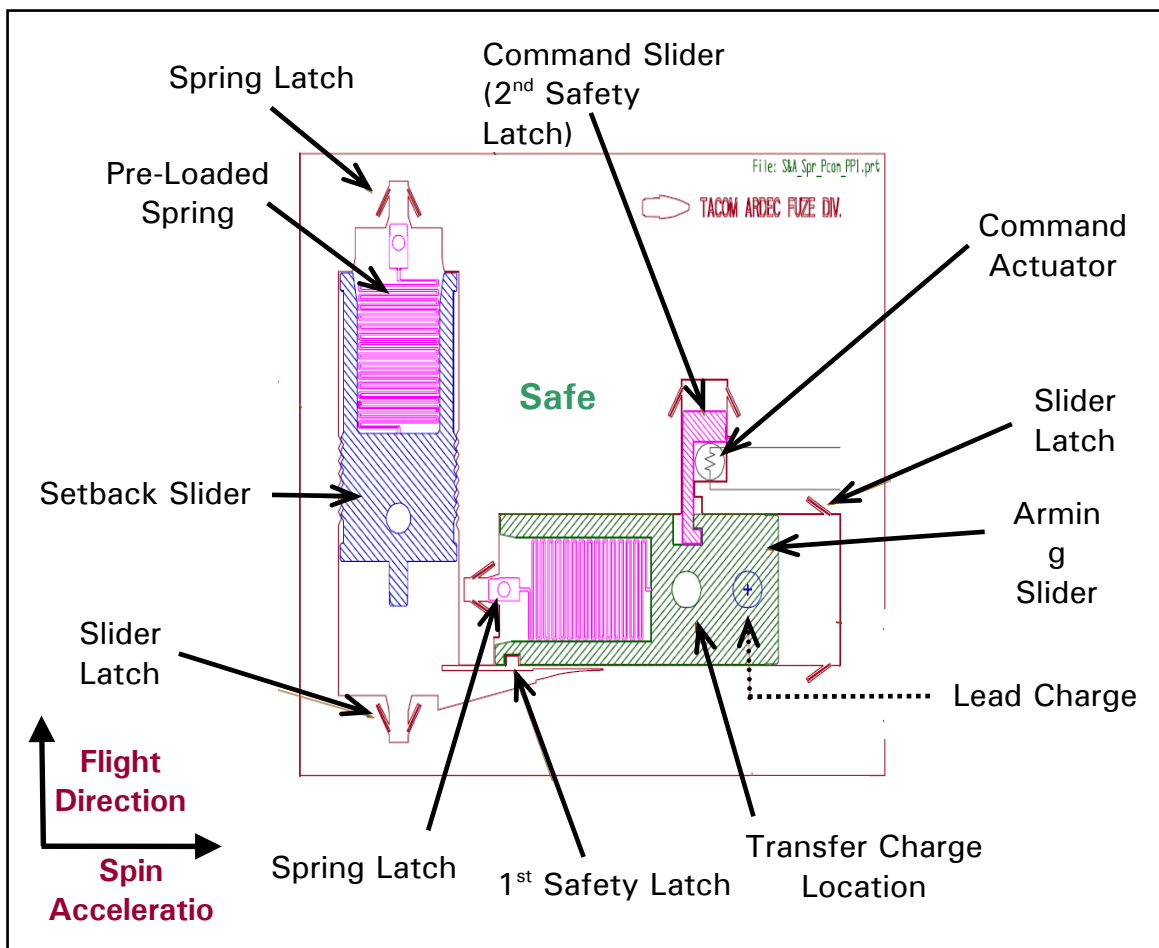
Figure 2-8. Operational schematic of the ARDEC S&A device in the safe position [19].
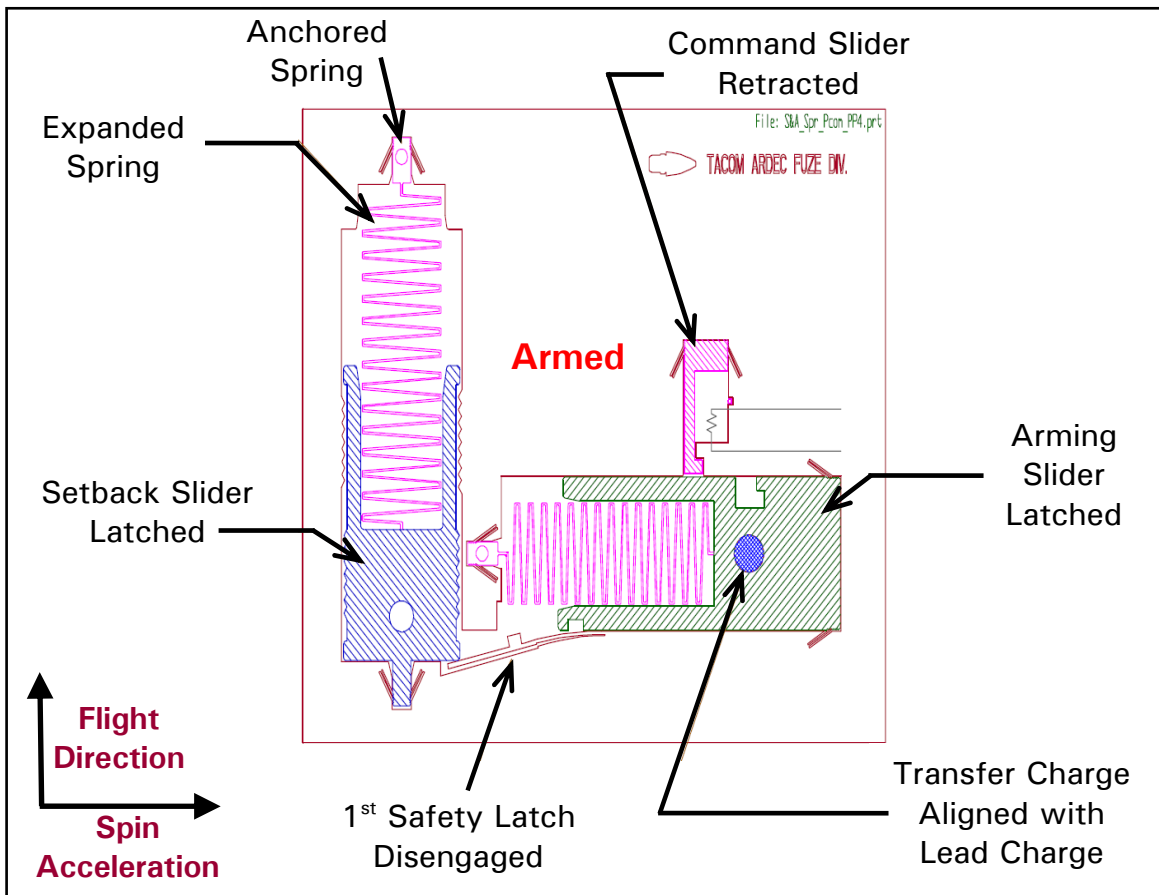
Figure 2-9. Operational schematic of the ARDEC S&A device in the armed position [19].

ARDEC Conclusion

Follow-on steps for ARDEC's MEMS-based S&A device include continued research into end-to-end manufacturing objectives and successful integration into current weapon systems. In FY 2008, this device is scheduled to be incorporated into two existing acquisition programs that will be entering Low Rate Initial Production [17]. Noticeable benefits of this device are increased safety for the warfighter, while simultaneously improving lethality by enabling an increased warhead size due to smaller mechanical and electrical components. Additionally, smaller components contribute to the overall reduction of logistic burdens, as well as a decrease in the carrying load for individual soldiers [18]. Finally, the reduction in cost, resulting from the volume

production offered by MEMS technology, ultimately facilitates commercial interest in manufacturing these devices and serves to advance the development of state-of-the-art MEMS S&A devices.

2.3.4 Air Force Research Laboratory – Munitions Directorate

The Air Force Research Laboratory – Munitions Directorate (AFRL/MN), is the U. S. Air Force organization responsible for developing conventional munitions technologies [20]. The Fuze Branch of its Ordnance Division is using MEMS technology in the development of an accelerometer suitable for use in the harsh environments typically encountered by penetrator-type weapons just prior to fuze initiation. In an effort to understand the material properties required to operate in these high-stress, high-shock, and high-temperature environments, AFRL/MN has been investigating the stress development and fundamental failure mechanisms of thin-film silicon carbide (SiC) structures [21]. Data collected from these tests will enable better characterizations of device failure modes and be used to improve future devices.

SiC was selected as the sensing material due to its superior mechanical properties over other microprocessing-friendly materials. For example, the bulk modulus for SiC is more than double the value for silicon, and the thermal conductivity is more than 3.5 times that of silicon. In addition, the energy bandgap for SiC is twice the bandgap for silicon at 300 K [21], [22]. Three types of SiC MEMS devices were designed and fabricated using Plasma Enhanced Chemical Vapor Deposition (PECVD) to deposit a thin epilayer of SiC over a bulk micromachined SiC substrate to form a suspended membrane. Piezoresistive elements were fabricated on top of the SiC membrane to measure stresses in the membrane when subjected to extreme shock conditions. Figure

2-10a depicts a cross-section of the fabricated test structure and Figure 2-10b shows the stress contour plot of the membrane under an applied shock load. Notice the location and relative magnitudes of resulting compressive and tensile stress [21].

AFRL Conclusion

This type of material research will foster improvements in the performance of next generation fuzing for munitions such as the High Speed Penetrator (HSP). A key requirement for a penetrating warhead, like the HSP, is the ability for the fuze to survive a high-speed impact into reinforced barriers and still operate properly [23]. Currently, the baseline design fuze for the HSP is a modified Multiple-Event Hard-Target Fuze (MEHTF) [24]. This fuze has shown the capability to survive loads that are comparable to those expected by impact and penetration [23]. Clearly, the investigation of exotic materials, combined with the benefits offered by MEMS technology, will enable the development of micro-scale fuzing technology that is capable of performing safety, arming and initiation functions for demanding weapons concepts like the HSP [24].
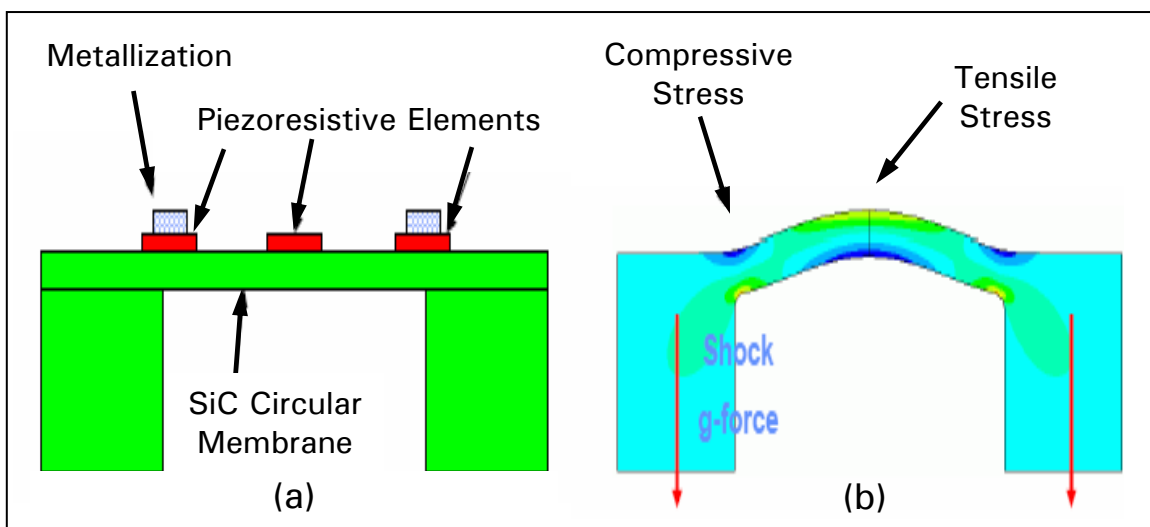
Figure 2-10. (a) Depiction of circular SiC membrane formed over a bulk etched SiC substrate. (b) Stress counter plot of a similar structure under an applied shock load [21].

2.4   Introduction of Design Concept for MEMS S&A Device

The devices discussed above introduced novel MEMS-based S&A device concepts being considered for implementation. In all these devices, the key method of ensuring safety was interruption of the explosive train in some manner. For instance, this could be accomplished by providing a physical barrier that prevents the detonator energy from reaching the lead charge or by removing an explosive component away from the detonator charge to prevent propagation of the explosive energy in the case of inadvertent initiation. Alternatively, arming was accomplished by moving a MEMS actuator in such a way as to align the necessary components to enable propagation of the detonator energy when the proper initiation signal is transmitted by the fuze. The obvious commonality between all these devices is that they are designed and fabricated using MEMS technology.

The design concept that will be discussed in the remainder of this thesis leverages on proven MEMS fabrication techniques that provide the inherent advantages of miniaturization, large volume production, reduced costs per unit, and lower parts counts. The focus of this research will be to design, fabricate, and demonstrate an interrupter mechanism consisting of an aperture that is normally closed while in the safe mode and opened when in the armed mode. It is envisioned that this interrupter would be used in concert with a microdetonator and other MEMS-based sensors to ensure the required independent environmental conditions are present prior to arming. Details of this design will be discussed in the chapters that follow.

Bibliography

[1]   MIL-HDBK-757(AR). *"Fuzes."* Military Handbook. 15 April 1994.

[2]   MIL-STD-1316E. *"Safety Criteria For Fuze Design."* Department of Defense Design Criteria Standard. 10 July 1998.

[3]   Naval Surface Warfare Center. January 2006. <http://www.nswcdc.navy.mil/>.

[4]   Naval Sea Systems Command. *Naval Surface Warfare Center – Indian Head Division Fact Sheet* (August 2004). January 2006. <http://www.ih.navy.mil/ NSWC_IndianHead.pdf>.

[5]   Last, Howard R., Bruce W. Dudley, and Robert L. Wood. "MEMS Reliability, Process Monitoring and Quality Assurance," *Proceedings of the SPIE Conference on MEMS Reliability for Critical and Space Applications.* 140-147. SPIE Vol. 3880. 21 September 1999.

[6]   Babcock, Wade G. and Lawrence C. Fan. *Applied MEMS Technology for Navy Fuzing/Safety and Arming (F/S&A) Systems*. Naval Surface Warfare Center, Indian Head Division, July 2001 (ADB297087).

[7]   Hendershot, John. "Weapon Fuzing/Safety & Arming Technology Programs Overview." Report to 48th Annual Fuze Conference (April 2004). Naval Surface Warfare Center, Indian Head Division. March 2005. <http://www.dtic.mil/ndia/ 2004fuze/hendershot.pdf>.

[8]   Robbins, John. "United States Navy Overview." Report to 49th Annual Fuze Conference (April 2005). Navy Energetics Enterprise. October 2005. <http://proceedings.ndia.org/5560/Wednesday/Session_II/Robbins.pdf>.

[9]   Beamesderfer, Michael and others. "Analysis of an Optical Energy Interrupter for MEMS Based Safety and Arming Systems," *Proceedings of the SPIE Conference on MEMS Reliability for Critical and Space Applications.* 101-111. SPIE Vol. 3880. 21 September 1999.

[10] Kovacs, Gregory T. A. *Micromachined Transducers Sourcebook.* Boston: The McGraw Hill Company, 1998.

[11] Cochran, Kevin R., Lawrence Fan, and Don L. DeVoe. "Moving Reflector Type Micro Optical Switch for High-Power Transfer in a MEMS-Based Safety and Arming System," *Journal of Micromechanics and Microengineering*, 14: 138-146 (January 2004).

[12] Deputy Under Secretary of Defense (Advanced Systems & Concepts), Office of Technology Transition. *Low Cost, Reliable Packaging & Integration of Miniaturized Explosive Components*. Navy Manufacturing Technology Program Revision A (July 2005). Arlington: ODUSD(AS&C)OTT. January 2006. <https://www.dodmantech.com/successes/Navy/subs/subs_PackagingMECs_12150 5.pdf>.

[13] Naval Air Systems Command. *Naval Air Systems Command Fact Sheet* (no date). January 2006. <http://pao.navair.navy.mil/factsheets/NAVAIRteam.pdf>.

[14] Cope, Randall D. "MEMS S-A Technology." Naval Air Warfare Center, Weapons Division, China Lake, July 1999.

[15] Cope, Randall D. "NAVAIR Fuze Overview." Report to 48th Annual Fuze Conference, (April 2004). Naval Air Warfare Center, Weapons Division, China Lake. March 2005. <http://www.dtic.mil/ndia/2004fuze/cope.pdf>.

[16] Armament Research, Development and Engineering Center. *The Army's Center of Lethality (2004)*. January 2006. <http://www.pica.army.mil/PicatinnyPublic/ organizations/ardec/index.asp>.

[17] Sanchez, Camilo A. and Charlie Robinson. "MEMS Based S&A Development for 25 mm HEAB Munitions." Report to NDIA 50th Annual Joint Services Small Arms Symposium. U. S. Army Armament Research, Development and Engineering Center. 12 May 2004.

[18] Merkwan, John. "ARDEC Overview." Report to 49th Annual Fuze Conference, (April 2005). Armament Research, Development and Engineering Center. January 2006. <http://proceedings.ndia.org/5560/Wednesday/Session_II/Merkwan2.pdf>.

[19] Robinson, C. H., R. H. Wood, and T. Q. Hoang. "Development of Inexpensive, Ultra-Miniature MEMS-Based Safety and Arming (S&A) Device for Small-Caliber Munition Fuzes." Report to 23rd Army Science Conference. Armament Research, Development and Engineering Center Fuze Division. 3 December 2002.

[20] Air Force Research Laboratory, Munitions Directorate (Oct 2005). January 2006. <http://www.mn.afrl.af.mil/>.

[21] Bradley, Ken. "Testing and Analysis of Piezoresistive Signals from SiC MEMS Accelerometers with Application to Penetration Fuzing." Report to 48th Annual Fuze Conference, (April 2004). Air Force Research Laboratory Munitions Directorate, Fuzes Branch. March 2005. <http://www.dtic.mil/ndia/2004fuze/ bradley.pdf>.

[22] Ioffe Physico-Technical Institute. "New Semiconductor Materials - Characteristics and Properties," (2003). January 2006. <http://www.ioffe.rssi.ru/SVA/NSM/>.

[23] Plenge, Mary. "Developing a Penetrator to Survive High-Speed Impact," *Air Force Research Laboratory Technology Horizons*, Document #MN-03-14 (October 2004). January 2006. <http://www.afrlhorizons.com/Briefs/Oct04/MN0314.html>.

[24] Tobik, Timothy. "Air Force Fuze Technology Overview." Report to 49th Annual Fuze Conference (April 2005). Air Force Research Laboratory, Munitions Directorate. June 2005. <http://proceedings.ndia.org/5560/Wednesday/Session_II/ Tobik.pdf>.

3. Explosive Initiation Devices and Concepts

A variety of initiator devices have been used in the past to provide the initial energy needed to begin the detonation process in an explosive train. In this chapter, some common initiating devices that have been used extensively in the past will be presented. This will be followed by a discussion of a particular initiator that has been shown to be reproducible using microelectronic fabrication techniques, and thus would be compatible with the MEMS S&A interrupter that is the focus of this thesis. In addition, a few solid-state versions of this device will be briefly presented to illustrate the various methods used to fabricate these detonators. Finally, this chapter will conclude with the description of some conceptual interruption methods and present a possible method to integrate a MEMS interrupter into a solid-state detonator in order to create a compact initiating device with a built-in S&A mechanism.

3.1 Explosive Initiation Devices

The requirement for an initiator device comes from the fact that a small impulse of energy is needed to begin the energy propagation process in an explosive train. The number of different initiators and the means in which they perform their function are large. They are often classified according to both their input energy and output characteristics. For instance, input energy usually comes from three sources: stab, percussion, or electric. Mechanical energy is used as the input energy in both stab and percussion initiators, while electric initiators use such methods as hot wire bridges or exploding bridgewires (EBW) to detonate their charge. On the other hand, output

characteristics are related to the process used to initiate follow-on explosive charges. For example, primers and squibs convert mechanical or electrical energy into explosive energy through the use of a small flame. These two devices are not generally used to initiate follow-on high explosives directly because their output energy is relatively small. However, detonators are often used to initiate follow-on high explosive (HE) charges since their output energy usually consists of an intense shock wave [1].

One common initiator device used extensively in the past is the hot wire bridge. This type of device places a high resistance wire in direct contact with a priming charge whose output energy is sufficient to initiate follow-on HE charges. When voltage is applied to the initiator, the wire bridge becomes hot enough to initiate the priming charge. Even though these devices have proven themselves reliable, they are susceptible to spurious currents that have the potential to stimulate the wire bridge. Therefore, their use is precluded in applications where safety is critical [1], [2].

Another common initiator device is the exploding bridgewire (EBW) detonator, which consists of a small bridgewire that is electrically exploded to initiate the follow-on HE charge. When a very high and very short current pulse is forced through the bridgewire, it explodes before it has a chance to melt and disrupt the circuit. This output energy has a magnitude of approximately one joule, and has been used to initiate such high explosives as pentaerythritol tetranitrate (PETN), and cyclotrimethylenetrinitramine (RDX) [1], [3]. Yet, one of the disadvantages for PETN and RDX is that they are not approved for fuze designs that use an uninterrupted explosive train. On the other hand, hexanitrostilbene (HNS) is approved for use with uninterrupted fuze designs since it is relatively insensitive to electrostatic discharge, drops, or friction, and has a large

operating temperature range (-196 ºC to 200 ºC) [4]. However, because of this insensitivity, HNS requires more energy to induce initiation, thus one of the main drawbacks of an EBW detonator is that it does not initiate HNS readily. The next section will discuss a newer detonator concept that is capable of detonating HE charges approved for use in uninterrupted fuze designs (e.g., HNS), and is a natural extension of the EBW detonator [1].

3.2   Exploding Foil Initiator

The exploding foil initiator (EFI) was first introduced in a 1976 report issued by Lawrence Livermore National Laboratory. In this report, the author John Stroud described "a new kind of detonator" that he informally called "the slapper" [5]. This type of detonator has several advantages over the EBW detonator. One advantage is that the exploding metal material and the follow-on explosive charge are physically separated by a thin insulating material and air gap. This contributes to safety as spurious current is eliminated as a potential for inducing detonation. Other benefits of the EFI are a reduction in input energy required for initiation and the fact that the output energy can readily detonate HNS [1].

The major components of an EFI detonator are shown in Figure 3-1. Starting from the bottom, the first component is an insulating "flyer" material that has metal foil etched on the underside. The reduced area (increased resistance) in the center of the metal foil causes vaporization of the flyer material when a high voltage is applied. The magnitude of this voltage has been reported to be in the thousands of volts for various EFI designs [5]–[7]. The middle component consists of an insulating disk that has a hole, or barrel, patterned in the center, directly above the reduced area in the metal foil. The

High Explosive Pellet
(Typically HNS)

Insulating Disk

Barrel

Insulated

Etched Metal Foil
(Underside)
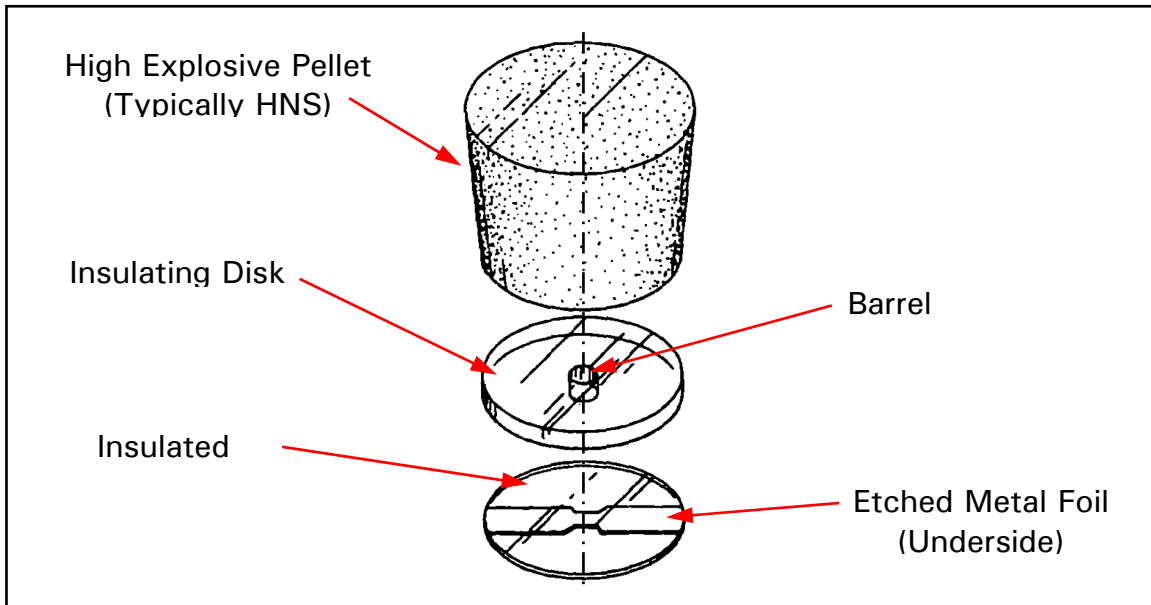
Figure 3-1. Major components used in an Exploding Foil Initiator [1].

barrel serves to shear a portion of the flyer material and acts as a channel for the detached

flyer material on its way to the HE pellet. The top component in Figure 3-1 is the high

density HE pellet whose output is used to begin the propagation of explosive energy to

the main charge [1]. As discussed above, the explosive pellet is typically HNS, but

PETN and RDX have also been used [4], [6].

The sequence of events that occur during the functioning of an EFI device is

illustrated in Figure 3-2. Step 1 shows the initiator in the static condition. Step 2 shows

the initiator after a high-current pulse has been applied, which vaporizes the metal foil

due to the reduced area in the center. This subsequently causes the sheared flyer material

to accelerate through the barrel of the insulating disk toward the HE pellet. As the flyer

impacts the HE pellet, a shock wave is transmitted into the explosive material which

causes detonation. From this description, it is clear why the EFI is more commonly

referred to as a slapper detonator. This more familiar nomenclature will be continued

throughout the remainder of this thesis.
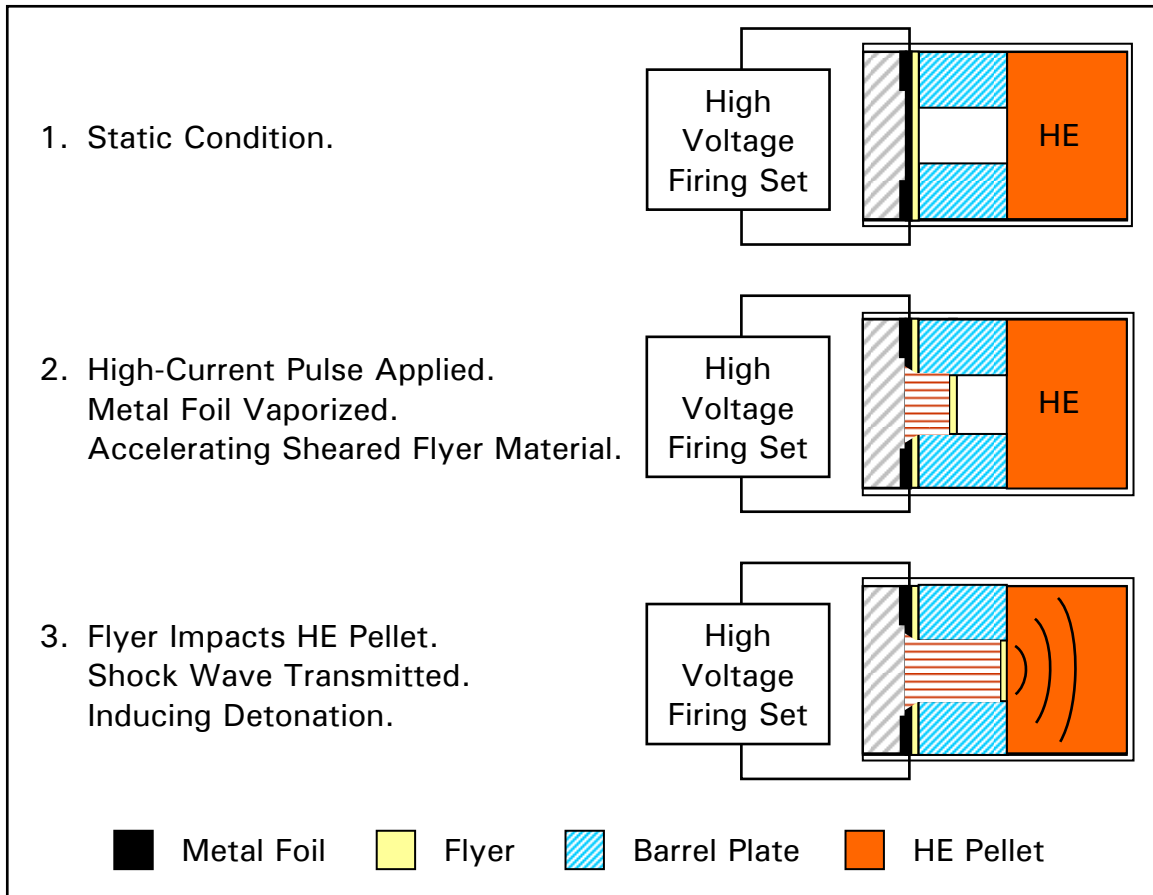
Figure 3-2. Schematic cross-section of Exploding Foil Initiator showing the sequence of steps during functioning [1].

The magnitude of the energy required to induce detonation of the HE pellet can be described in terms of the minimum kinetic energy required to induce initiation. This threshold energy is dependent on a variety of factors to include the properties of the explosive and flyer material, the volume of the flyer and the velocity of the flyer as it travels through the barrel [4], [6]. Due to the large number of factors that can contribute to the threshold energy, it is difficult to reference a single value to describe this performance parameter. However, values of 12.15 J/cm^2 and 7.0 J/cm^2 (with Mylar flyer thicknesses of 76.2 μm and 20.0 μm, respectively) have been reported as minimum energy densities for a particular manufactured lot of HNS [8]. For PETN, a kinetic

energy of 19.17 mJ and 10.31 mJ can be calculated using Equation (3.1) and the reported velocities for a Kapton flyer of 3 mm/μs and 2.2 mm/μs, respectively [6], [9]. By making the assumption that the impact area is also the surface area of the flyer material, the threshold energy density can be estimated to be 15.98 J/cm^2 and 8.59 J/cm^2, which is comparable to the values reported for HNS. An exact comparison is difficult because of the diverse explosive properties (i.e., density and material surface area), the infinite possibilities for flyer material characteristics (i.e., area and density), and the chosen input current density which directly relates flyer velocity.

$$KE = \frac{1}{2}mv^2 \quad \text{(J)} \tag{3.1}$$

where

$$m = mass\ of\ the\ flyer \quad \text{(kg)}$$
$$v = velocity\ of\ the\ flyer \quad \text{(m/s)}$$

3.3   Solid-State Slapper Detonators

Since the 1980's, other EFI designs have emerged that are based on the slapper concept proposed by John Stroud in 1976. These designs are slightly modified in terms of appearance and packaging, but the functioning method remains consistent with the above description.   For example, modifications have included variations in physical dimensions and material characteristics for the metal foil, flyer material, and barrel size in order to maximize the flyer output energy while minimizing the energy required to vaporize the foil. In addition, device packaging and the integration of components have been varied to increase reliability and structural integrity over long periods of time. These types of modifications include improving the quality of the foil contacts with external circuitry and barrel alignment between the flyer and HE pellet [10]–[12]. Long-

term reliability is an especially important criteria for slappers used in applications that have long shelf lives, (e.g., munition fuzes). Clearly, the specific application for the slapper detonator will drive modifications in one way or another. For instance, the desired output energy of the detonator may impact the requirement for flyer velocity, which depends on the input electrical energy applied to the foil [13]. Furthermore, the applications for slapper detonators extend beyond their use for military weapons, namely, large-scale drilling and mining operations.

As recently as 1989, slapper detonators have been fabricated using microelectronic fabrication techniques [14]. These solid-state detonators bring with them the inherent benefits of large volume/low-cost production and high-reproducibility. Using this method also eliminates the precise machining, aligning, and bonding that must occur when conventional slappers are manufactured [7]. Another obvious advantage to fabricating slapper detonators using microfabrication techniques is the ease at which additional circuitry can be fabricated directly on the die. For example, the circuitry necessary to fire the slapper could be added, along with other switches or sensors required for device operation. Finally, these advantages are compatible with typical munition development objectives (i.e., reduced volume and decreased mass) [15]. In the next section, three solid-state slapper designs will be briefly discussed to show that microfabrication can provide a method for improving these already successful devices.

3.3.1   Design for Silicon-Based Slapper Detonator

In a patent issued in 1989, Nerheim et al. described a method in which slapper detonators could be fabricated using standard microelectronic fabrication techniques almost exclusively. Illustrations of the proposed silicon slapper detonator are shown in

Figure 3-3 and Figure 3-4. The process begins with an epitaxial layer of silicon grown on a typical silicon wafer. This layer eventually becomes the flyer material and is described as being grown to approximately 25-µm thick, but other thicknesses may be more appropriate depending on the application. Next, a 0.3 – 0.7 µm layer of silicon dioxide is grown on the epitaxial silicon to serve as an insulating layer. This step is followed by the deposition and patterning of the two metal contacts and a reduced center area for the vaporizing metal (foil). Alternatively, a higher density metal could be deposited in the center area in order to provide more vaporizing mass, which would increase the velocity of the flyer. This would subsequently provide an exponential increase in the kinetic energy impacting the HE pellet, as shown in Equation (3.1). Finally, the backside of the wafer is masked, and an isotropic wet etchant is used to etch completely through the silicon wafer stopping at the epitaxial grown silicon layer. This process defines the barrel and exposes the flyer for the slapper detonator [14].
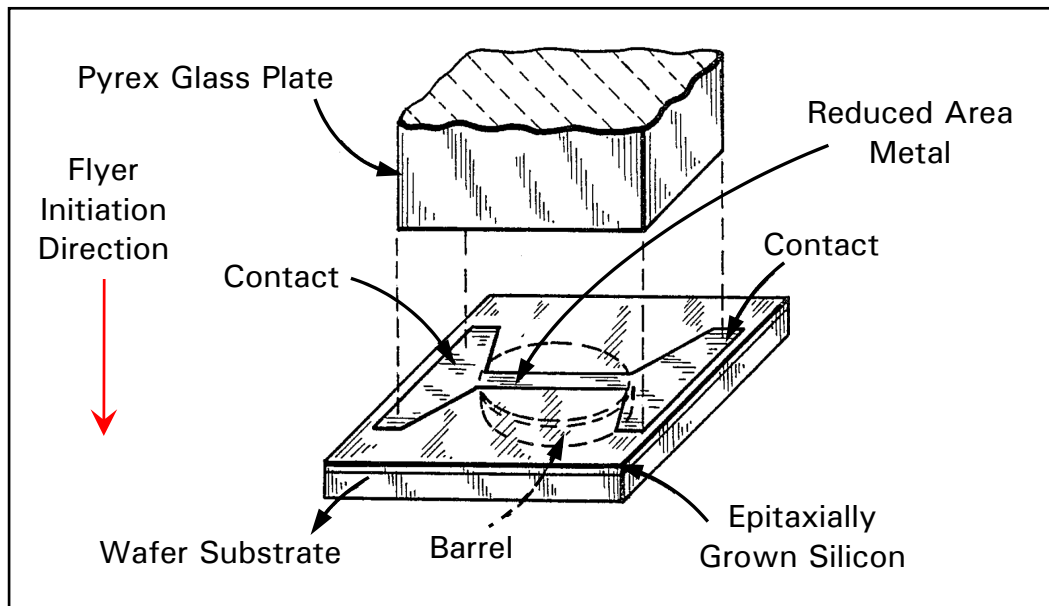
Figure 3-3. Illustration of a proposed silicon slapper detonator design [14]. All layers are deposited using microfabrication techniques, except for the Pyrex glass plate, which is epoxy, bonded during post-processing steps.
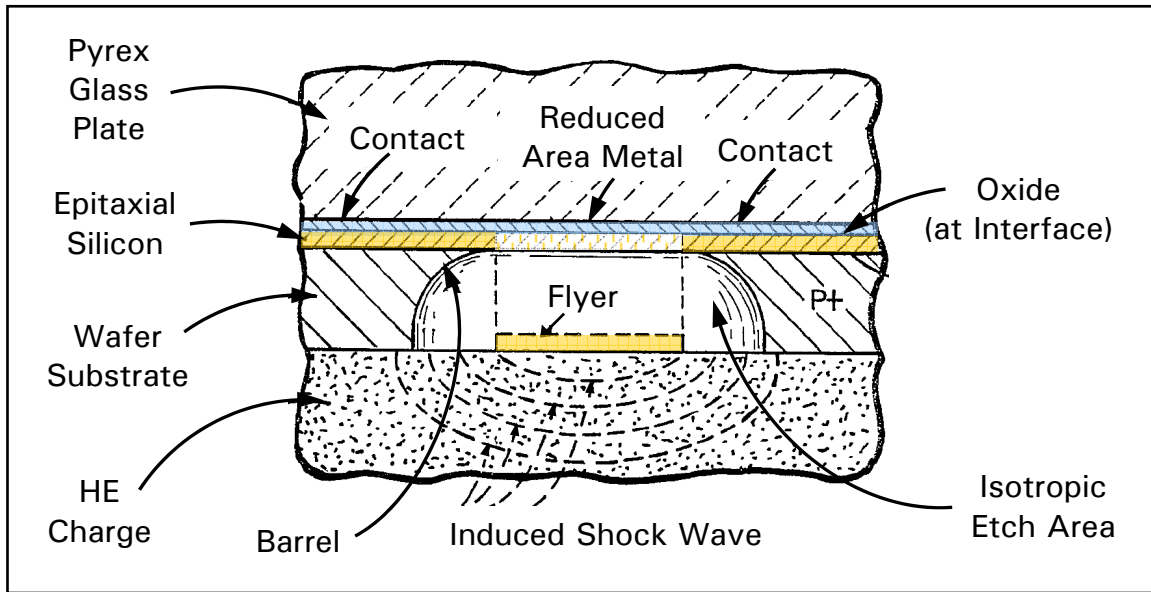
Figure 3-4. Cross-sectional illustration of proposed silicon slapper detonator [14]. Note the flyer and resulting shock wave depict the slapper after firing has occurred.

Obviously, this single device could be repeated multiple times on a silicon wafer to provide many slapper detonators in a single fabrication run. After the steps described in the last paragraph, the wafer would be diced into individual die and post-processing steps would take place. Typical post-processing steps envisioned for this device are the epoxy bonding of a Pyrex glass plate over the center metal area, packaging the device with an appropriate explosive charge, and connecting the contacts to a suitable circuit for firing. The purpose of the Pyrex glass plate is to act as a counter mass for directing the energy from the exploding metal into the direction of the flyer [14].

3.3.2   Microfabricated Slapper Device

In 1993, Henderson, et al. actually fabricated a conceptual slapper device using microelectronic fabrication techniques. In this device, a 635 μm × 635 μm cavity was first formed by etching the surface of the silicon substrate using potassium hydroxide (KOH) [7]. KOH is an anisotropic etchant that etches the silicon much slower in the

(111) crystal plane of the silicon crystal, as opposed to the (100) crystal plane [16]. The overall effect is the formation of a cavity in the silicon substrate as shown in Figure 3-5. This cavity serves as the barrel in their slapper design. The next step involved growing a layer of silicon dioxide over the entire wafer to provide an insulating layer between the substrate and metal, which is the next deposition.

The metal was deposited using two different methods. In one method, the metal was deposited using a lift-off process, which was patterned to provide a reduced metal area in the center of the etched cavity as well as the metal contacts that are located outside the cavity region. This reduced area provides increased resistance that causes vaporization of the metal in this region when a high voltage is applied. Figure 3-6 shows an illustration of the conceptual slapper device fabricated using deposited metal. In the other method, impurity atoms are diffused into the substrate cavity through a silicon dioxide pattern. The diffusion creates a conductive path for current to flow in this region. Electrical contacts, in this second method, are prepared by depositing metal in the region
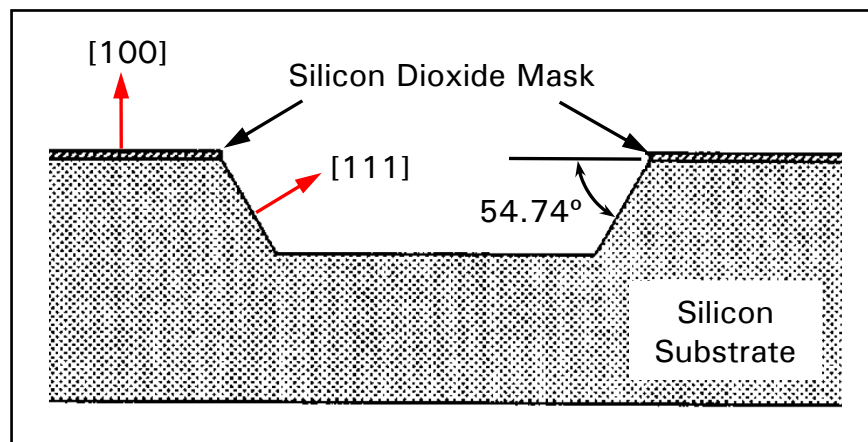
Figure 3-5. An illustration of the preferential etching of silicon by an anisotropic etchant [7]. To protect the areas where etching is not desirable, a layer of silicon dioxide is deposited to prevent the etchant from making contact with the silicon. The bracketed numbers represent specific crystal directions.

outside the cavity by a similar process performed in the first method. Figure 3-7 shows

the conceptual slapper device fabricated using diffused impurity atoms. Finally, to

complete the fabrication of this slapper device, a drop of polyimide is deposited into the

cavity to act as the flyer material [7].

Deposited Metal

127 μm

635 μm

Anisotropically
Etched Cavity

(a)

Polyimide Flyer

635 μm

Deposited Metal

127 μm

127 μm

381 μm

(b)
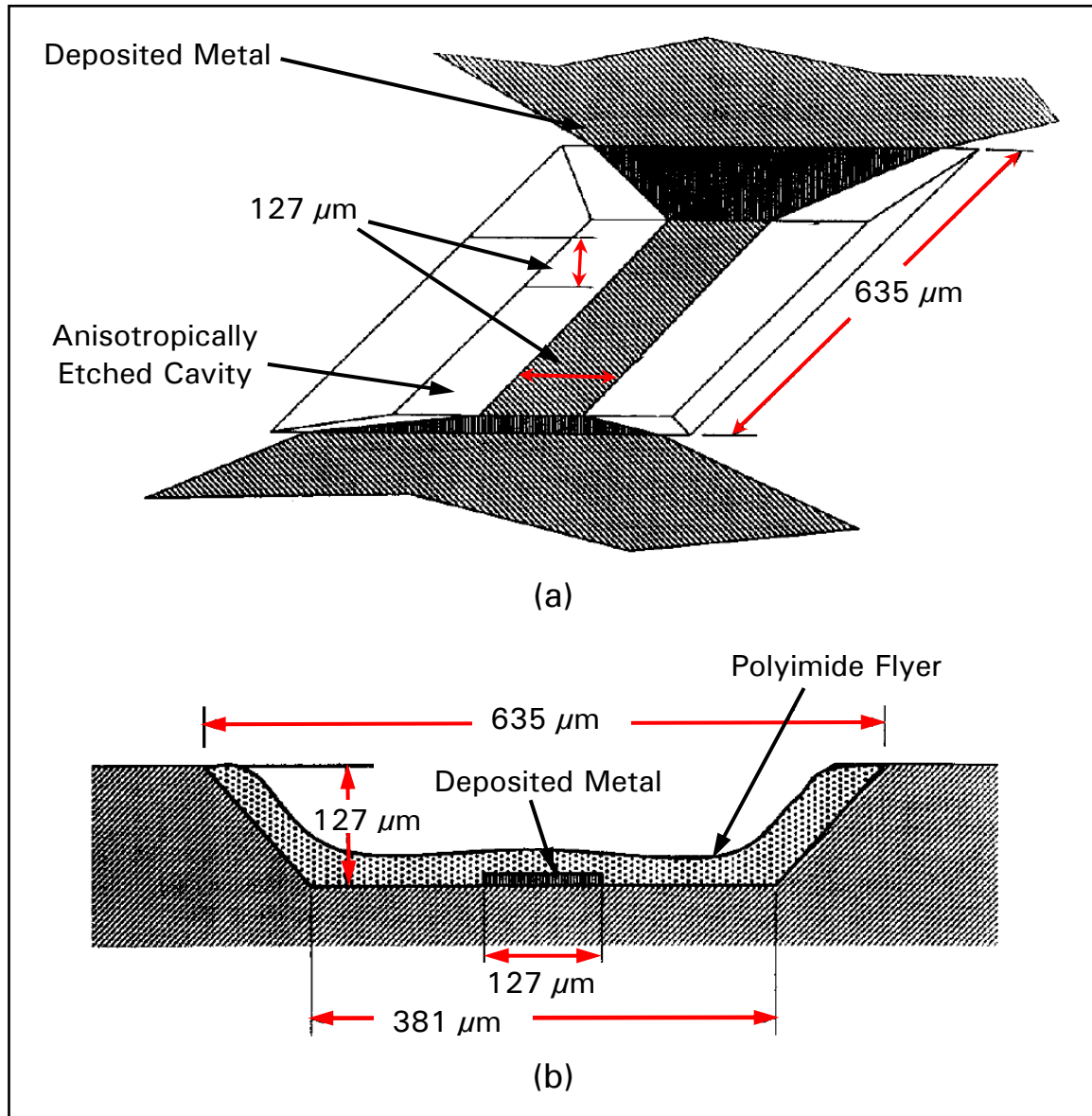
Figure 3-6. (a) Illustration of conceptual slapper device fabricated in a silicon substrate
with deposited metal conductor. (b) Cross-sectional view of cavity showing deposited
metal conductor [7].
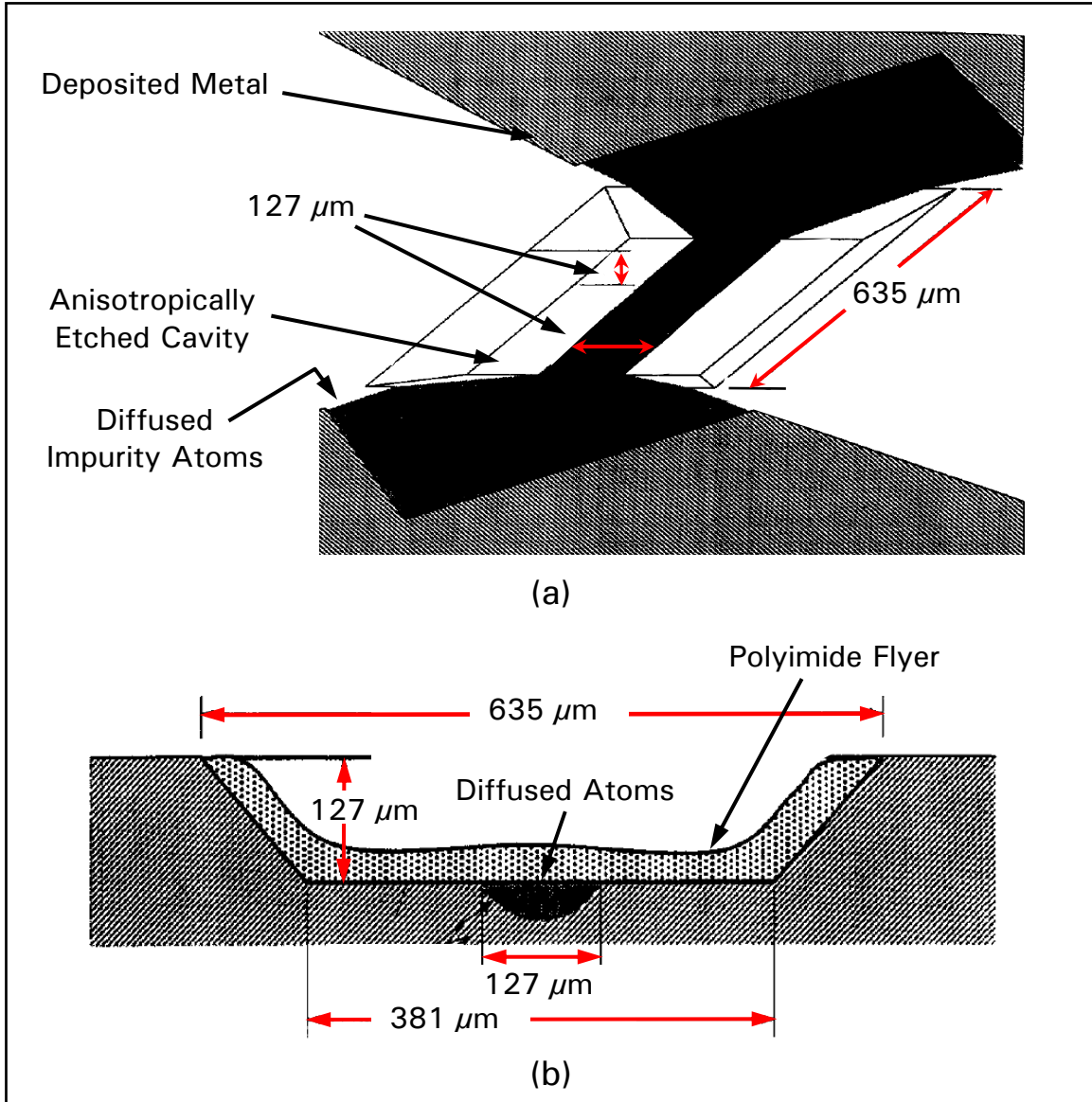
Figure 3-7. (a) Illustration of conceptual slapper device fabricated in a silicon substrate with diffused impurity atoms. (b) Cross-sectional view of cavity showing diffused impurity atoms [7].

Both device types were tested using a high voltage switch that consisted of a bank of capacitors designed to operate at 1 kV and provide 1 J of energy to the bow-tie region. The measured resistance of the metal bow-tie conductor and the diffused bow-tie conductor was 100 mΩ and 95-100 Ω, respectively. When the slapper device was fired, the flyer material was successfully ejected from the cavity in both designs [7]. The

kinetic energy produced by the ejected flyer was not measured, and there was no HE pellet incorporated into this slapper design. Therefore, it is difficult to determine whether or not the ejected flyer could have initiated detonation of the follow-on charge. Nevertheless, the fabrication of a conceptual slapper device using microelectronic fabrication techniques was effectively realized.

To show an alternative method for fabricating a slapper device, Henderson et al. also illustrated a conceptual design that consisted of fabricating two separate wafers that can be subsequently bonded together to make up the slapper device. The first wafer functions as the vaporizing metal layer with polyimide deposited on top to act as the flyer. This wafer is fabricated using a diffusion process like the one previously described. Next, three holes are etched completely through the second wafer to provide for a barrel opening and two pass-through areas for the electrical contacts. After processing these two wafers separately, they would be bonded together to make up the slapper detonator [7]. This conceptual device is shown in Figure 3-8.
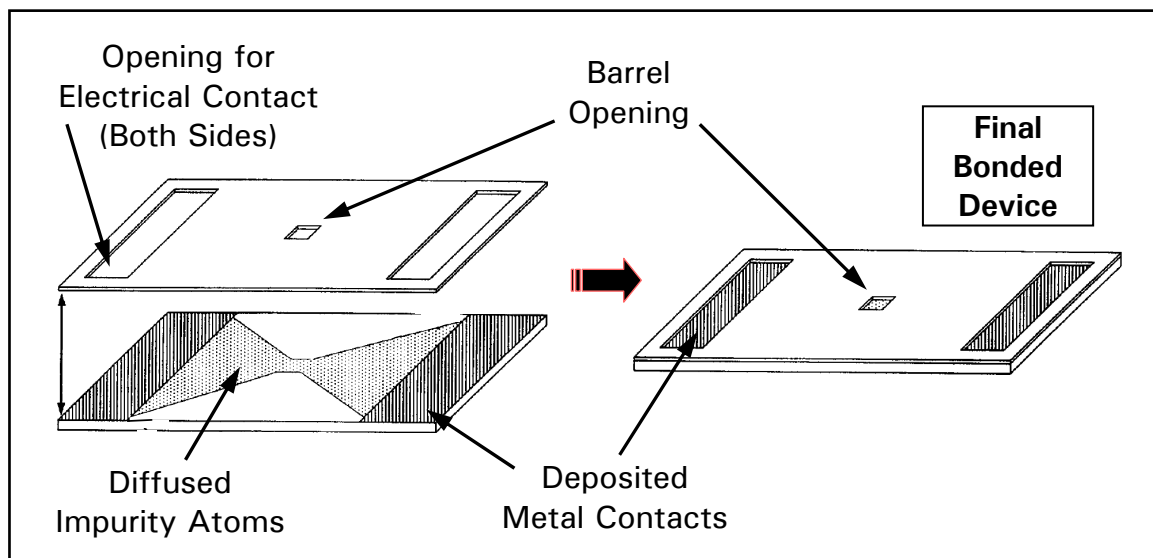
Figure 3-8. Conceptual slapper device produced by bonding two separately fabricated semiconductor wafers [7].

3.3.3 Solid-State Slapper Detonator System

In 1998, O'Brien et al. illustrated the fabrication of a slapper detonator system that includes all the electrical circuitry required to fire the solid-state device. This device includes the capacitor for storing the electrical energy needed to vaporize the metal foil, the switch and trigger circuitry to actually fire the device, the metal foil, and the flyer material. The first series of steps in fabricating this device is the formation of the capacitor. Metal is deposited on the substrate, followed by the deposition of a dielectric layer. Next, another layer of metal and another layer of dielectric are deposited. The two metal layers are placed askew to each other so that electrical connections can be made in later processing steps. The two dielectric layers are placed directly over each other in order to maximize the capacitive area. At this point, the solid-state capacitor is complete; however, additional layer depositions could be used to increase the capacitance value of the device [15]. Figure 3-9 shows both a top and side view of the processing steps completed thus far.
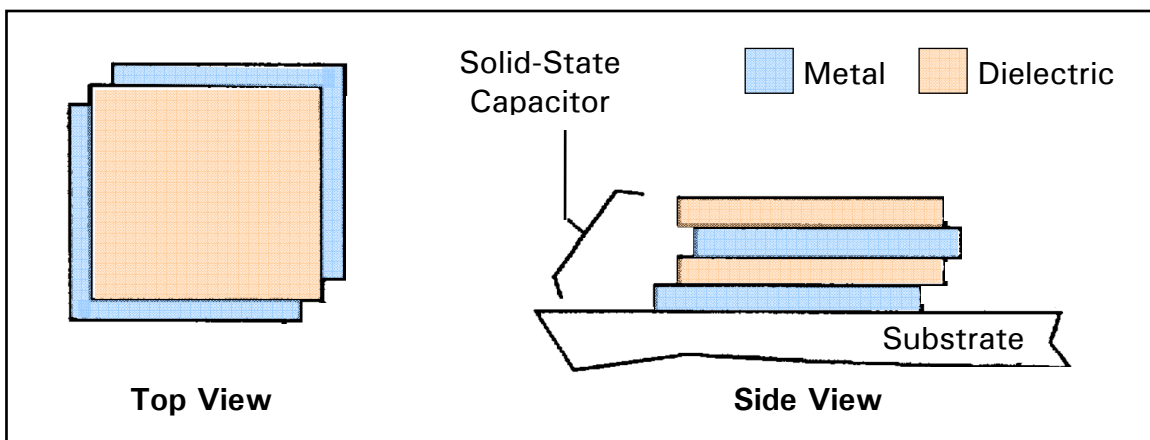
Figure 3-9. Illustration of both the top and side view of the solid-state capacitor fabricated for the slapper detonator system [15].

The second series of steps in fabricating this device is the creation of the switch used to fire the slapper. First, another dielectric layer is deposited on top of the last capacitor dielectric layer. Next, a thin metal layer is deposited askew to the previous layers, so that a small area is exposed. This metal layer will serve as the trigger electrode for the final device. Then, another dielectric layer is deposited followed by a metal layer that becomes the top of the switch. Figure 3-10 illustrates the top and side view of both the solid-state capacitor and switch fabricated for the slapper detonator system. This switch operates by pulsing the trigger electrode to overstress the three dielectric layers in between the two metal layers. When this occurs, a large burst of current is allowed to flow before the switch catastrophically fails [15].

The final series of steps in fabricating this device is the deposition of layers that make up the actual slapper detonator. First, a dielectric layer is deposited to insulate the slapper from the rest of the device. Next, the metal foil layer is deposited to have a reduced area on top and long legs that extend down both sides of the entire device. Connections are made between this top metal layer, the top metal layer of the switch and
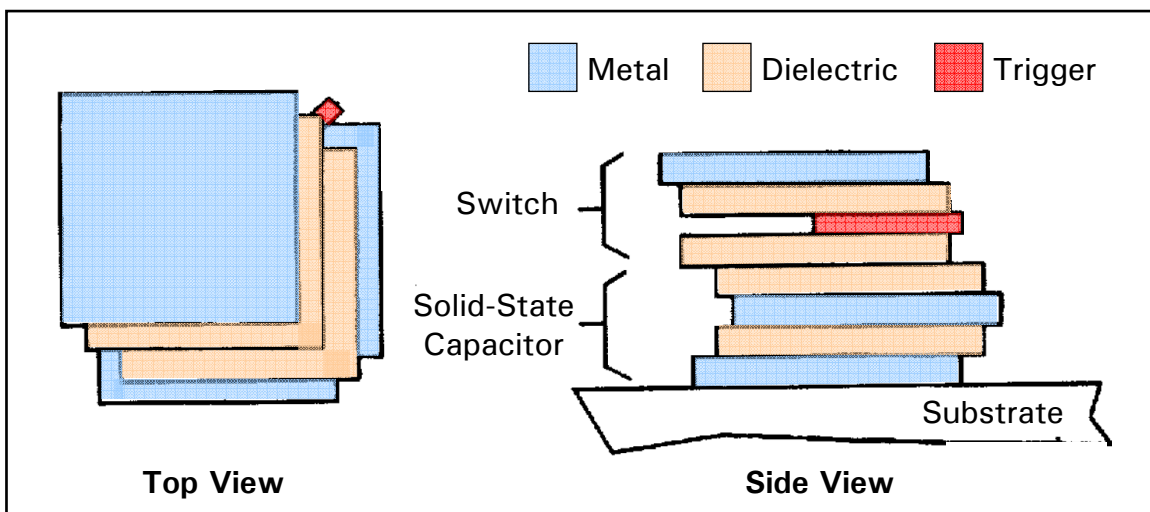
Figure 3-10. Illustration of the top and side view of both the solid-state capacitor and switch fabricated for the slapper detonator system [15].

the bottom metal layer of the capacitor. Finally, the last layer is deposited, which is a polymer that acts as the flyer material. This polymer layer is patterned and etched to expose the reduced area of the metal foil and to function as a barrel (e.g., to shear and direct the flyer material upon activation). Figure 3-11 shows the complete solid-state slapper detonator system including some additional components such as a resistor used to bleed down stray charges in the capacitor, and a circuit used for driving the trigger switch [15]. As with the last slapper device, the kinetic energy produced by this type of detonator is not known. However, the method described here takes the fabrication of a slapper detonator using microelectronic technology one step further by presenting a process in which a complete system could be produced. Clearly, using these fabrication techniques, which have been proven successfully for integrated circuits, would be advantageous for designing next generation fuzes for advanced munition systems.

3.4   Solid-State Slapper Interrupter Concept

Based on the work discussed in the previous section, it is easy to see how modern slapper detonators could be produced in a more efficient and cost effective manner than conventional slapper detonators. Another improvement to the basic slapper design would be to provide some sort of interruption mechanism in-line with the accelerating flyer material in order to provide an additional level of safety for munitions. This interrupter mechanism would have to be capable of preventing the flyer from impacting the HE pellet while in the safe mode, and also have the ability to move out-of-line so that the flyer could impact the HE pellet and initiate detonation. In the safe mode, the interrupter material would have to be able to withstand the energy imparted by the flyer and prevent that energy from passing through to the HE pellet. On the other hand, a requirement for
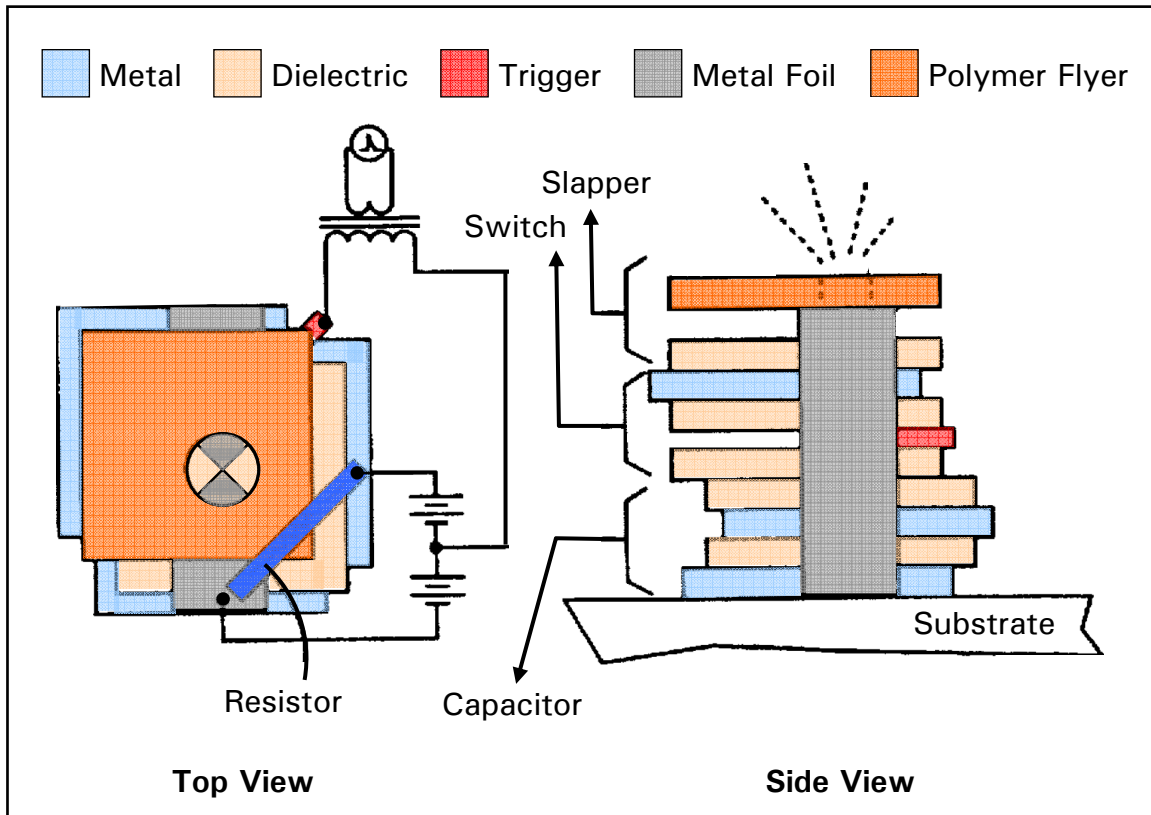
Figure 3-11. Illustration of the top and side view of the complete solid-state slapper detonator system, including a resistor to bleed stray charges in the capacitor, and an external circuit used for driving the trigger switch [15].

the arming mode would be the ability to rapidly move to the out-of-line position quickly enough in response to an activation signal.

Additionally, it would be advantageous for the interrupter mechanism to be capable of sensing at least one of the two independent environmental conditions that prevents unintentional arming and confirms an intentional launch as required by MIL-STD-1316E [17]. Ideally, the energy from this sensed environmental condition could be used either directly or indirectly for actuation of the S&A interrupter device. However, an alternative approach could be to have the environmental sensing function come from an external sensor, which (upon receipt of a valid launch signal) would apply the input

necessary to actuate the interrupter. Upon actuation, the interrupter mechanism would move to an out-of-line position and allow a free path for the flyer to impact the HE pellet.

There are several ways that this interruption could be designed. One example does not involve providing an additional interruption component, but entails fixing the HE pellet to an actuator that would move the explosive charge from the safe out-of-line position to the armed in-line position (in relation to the slapper detonator's flyer). This approach was depicted by O'Brien et al. in which it was described that a safely stowed HE pellet could be positioned into an in-line (armed) position through the use of a motor (e.g., an induction motor, a stepper motor, or a piezoelectric motor). Figure 3-12 illustrates this method of explosive train interruption [15].

Another example for an interruption method that does not involve additional components is to move the barrel out-of-line (safe) and in-line (armed), while keeping
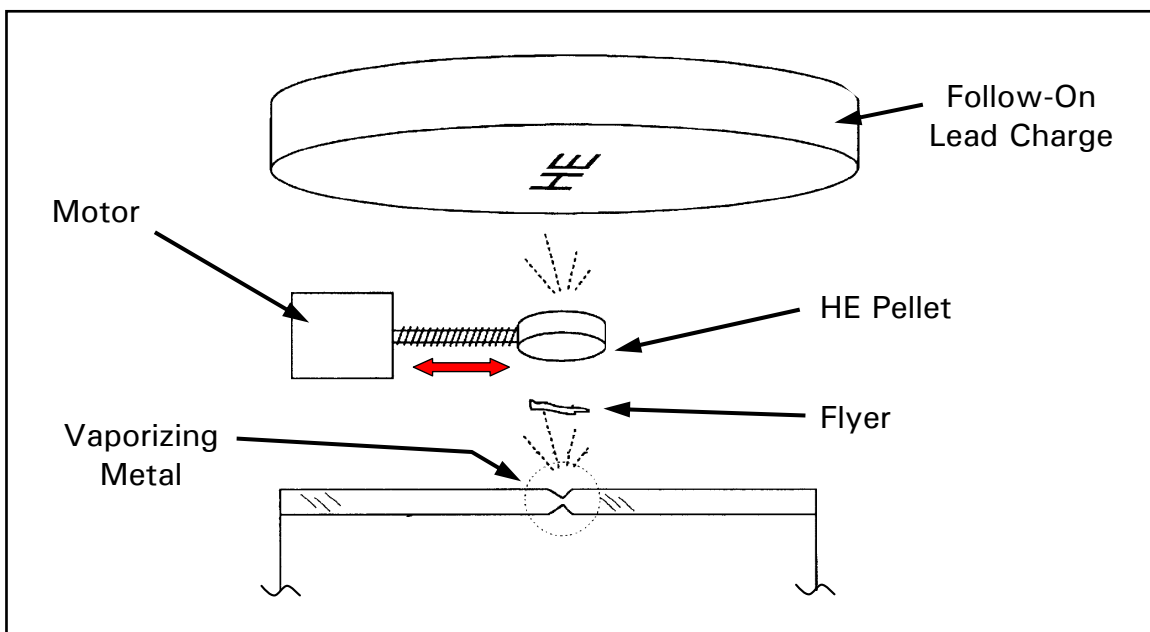
Figure 3-12. Depiction of explosive train interruption by moving the HE pellet out-of-line with the initiating flyer material [15]. The in-line (armed) position in shown.

other elements such as the flyer and HE pellet in a fixed, in-line position. A plate containing the barrel (actually a hole in the barrel plate) could be attached to an actuator capable of moving the barrel in the correct position to shear the flyer and provide a channel to the HE pellet when the slapper is fired. In the case of an inadvertent firing, the barrel plate would be in an out-of-line position with the flyer and explosive detonation would be prevented because impact of the flyer with the HE pellet would be interrupted by the barrel plate. This type of interruption mechanism is described by Garvick et al., in which they suggest the use of MEMS electrothermal actuators as the method to move the barrel plate [2]. A conceptual illustration of their slidable barrel plate is shown in Figure 3-13.

In contrast, an integrated slapper-interrupter mechanism could be designed in which an additional component would be inserted between the flyer and HE pellet.
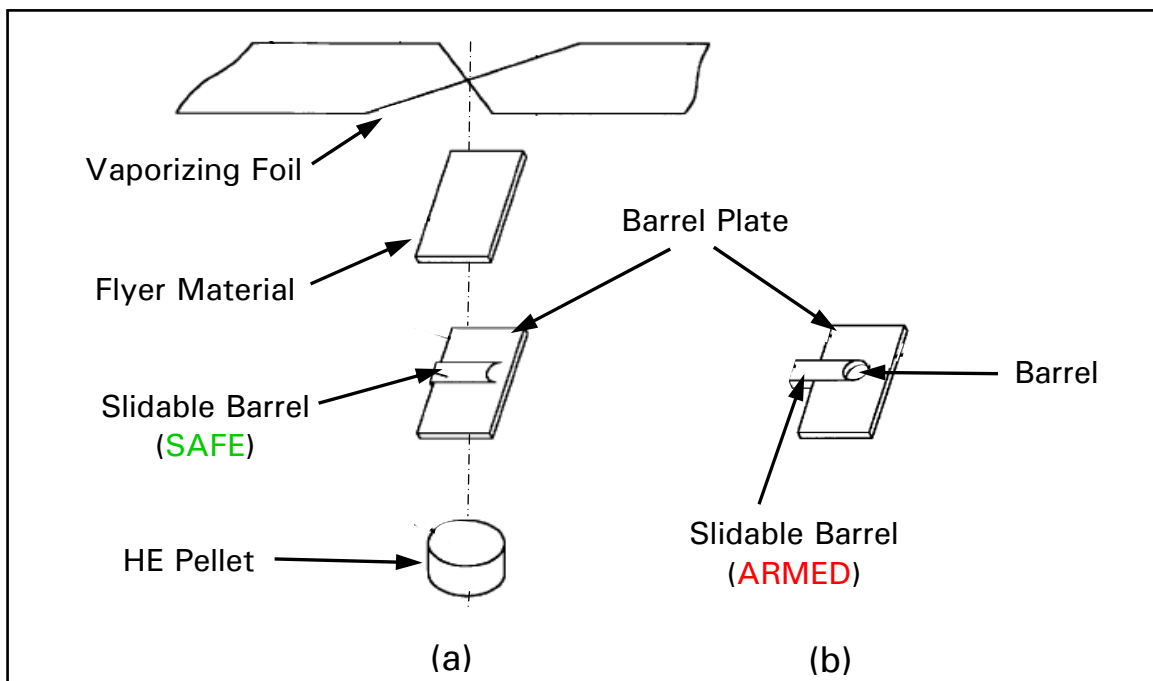
Figure 3-13. Conceptual illustration of an explosive train interruption method using a slidable barrel. (a) Depicts the barrel in the safe position. (b) Depicts the barrel in the armed position [2].

Considering the arrangement of a slapper detonator, the most likely location for an interrupter mechanism to be placed would be after the barrel and before the HE pellet. This location would allow for the flyer and barrel to remain in direct contact with each other, so that the flyer would still be sheared as it accelerated down the barrel. This type of interruption method would also require some sort of actuation device (similar to what was described in the above examples) to move the interrupter from a safe to armed position.

3.5   Introduction of MEMS S&A Interrupter Concept

This leads to the focus of this research, which is to design, fabricate and demonstrate an S&A interrupter mechanism consisting of an opening and closing aperture controlled through the use of MEMS electrothermal actuators. This device consists of four moveable interrupter plates that are normally closed, indicating the safe mode, and opened when in the armed mode. It is envisioned that this interrupter would be used in concert with a solid-state slapper detonator similar to the ones discussed in section 3.3. It is also conceivable that the integration of this interrupter component could be accomplished by bonding the semiconductor wafer containing the fabricated MEMS interrupter to the semiconductor wafer (or layer) functioning as the barrel. This would be similar to the concept shown in Figure 3-8, but with a slight modification. The variation would involve bonding a third semiconductor wafer to the top of the barrel layer shown in Figure 3-8, thus enabling a complete slapper detonator with an integrated S&A interrupter mechanism to be produced. This is illustrated in Figure 3-14 by adding a third layer to the figure presented by Henderson et al. Wafer bonding is a relatively simple process that has proven itself successful in many different areas to include,
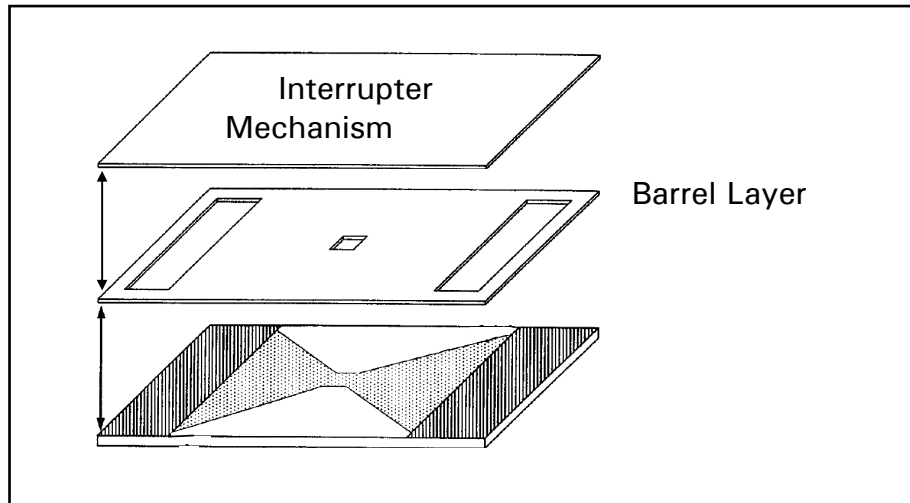
Figure 3-14. Conceptual design for the integration of a MEMS interrupter mechanism with a solid-state slapper detonator. This is a modification of the concept proposed by Henderson et al. [7] and shown in Figure 3-8.

microelectronics, optoelectronics, and MEMS. This process facilitates the fabrication of a variety of devices made up of different material combinations that would be impossible to produce otherwise [18]. The details of designing and fabricating a MEMS interrupter mechanism using a typical surface-micromachining fabrication process will be presented in the next chapter.

Bibliography

[1]   MIL-HDBK-757(AR). *"Fuzes."* Military Handbook. 15 April 1994.

[2]   Garvick, Donald R., Lawrence C. Fan, Bruce R. Kuester, and Gregory R. Birk. "MEMS Energetic Actuator with Integrated Safety and Arming System for a Slapper/EFI Detonator." US Patent 6173650. 16 January 2001.

[3]   Krause, Horst H. "New Energetic Materials," in *Energetic Materials*. Ed. Ulrich Teipel. Weiheim: Wiley-VCH, 2005.

[4]   Neyer, Barry T., Lloyd Cox, Terry Stoutenborough, and Robert Tomasoski. "HNS-IV Explosive Properties and Characterization Tests," *Proceedings of the 39th AIAA/ASME/SAE/ASEE Joint Propulsion Conference and Exhibit.* AIAA Paper 2003-5138. July 2003.

[5]   Stroud, John. *A New Kind of Detonator – The Slapper*. UCRL-77636. Livermore CA: Lawrence Livermore Laboratory. 27 February 1976.

[6]   Mendes, R., J. Campos, I. Plaksin, and J. Ribeiro. "Shock Initiation of Explosives by Micro Slapper," *Technical Papers of the 12th International Detonation Symposium* (August 2002). University of Coimbra. January 2006. <http://www.intdetsymp.org/detsymp2002/PaperSubmit/FinalManuscript/pdf/Mendes-091.pdf>.

[7]   Henderson, John H. and Thomas A. Baginski. "Two Novel Monolithic Silicon Substrate Slapper Detonators." *Proceedings of the 1993 Industry Applications Society Annual Meeting*. Volume 3, 2479 – 2482. IEEE Press, 1993.

[8]   Hasman, E., M. Gvishi, and A. Solomonovici. "The Initiation Threshold Sensitivity of HNS Explosive as a Function of its Grain Size," *Propellants, Explosives, Pyrotechnics*. Volume 12, Issue 4: 130 – 132 (August 1987).

[9]   *Kapton Polyimide Film - Summary of Properties*. E.I. du Pont Canada Company, 2005. January 2006. <http://www.dupont.com/kapton/general/H-38492-2.pdf>.

[10] MacDonald, Herbert J. and Robert E. Zoret. "Exploding Foil Detonator." US Patent 4602565. 29 July 1986.

[11] Huber, Klaus B., Nolan C. Lerche, Arnold G. Edwards, Kenneth E. Rozek, and Edward G. Smith Jr. "Method and Apparatus for Safe Transport Handling Arming and Firing of Perforating Guns Using a Bubble Activated Detonator." US Patent 5088413. 18 February 1992.

[12] Williams, Matthew R. and Steven V. Werling. "Slapper Detonator." US Patent 5370053. 6 December 1994.

[13] Hasman, E., M. Gvishi, and Y. Carmel. "Measurement of Shock Initiation Threshold of HNAB by Flyer Plate Impact," *Propellants, Explosives, Pyrotechnics.* Volume 11, Issue 5: 144-149 (October 1986).

[14] Nerheim, Eldon and Dave Hoff. "Integrated Silicon Secondary Explosive Detonator." US Patent 4862803. 5 September 1989.

[15] O'Brien, Dennis W., Robert L. Druce, Gary W. Johnson, George E. Vogtlin, Troy W. Barbee Jr., and Ronald S. Lee. "Method and System for Making Integrated Solid-State Fire-Sets and Detonators." US Patent 5731538. 24 March 1998.

[16] Kovacs, Gregory T. A. *Micromachined Transducers Sourcebook.* Boston: The McGraw Hill Company, 1998.

[17] MIL-STD-1316E. "*Safety Criteria For Fuze Design.*" Department of Defense Design Criteria Standard. 10 July 1998.

[18] Tong, Q. Y., and U. Gössele. *Semiconductor Wafer Bonding: Science and Technology.* New York: John Wiley and Sons, Inc., 1999.

4. Design Theory and Fabrication

While it is true that any microelectronic fabrication technique can be used to fabricate elaborate MEMS devices, typical designers are often constrained (usually by cost and time) to using a proven micromachining foundry process in order to systematically develop the first few iterations in their research effort. These established micromachining fabrication facilities often make available a variety of techniques to accommodate a reasonable amount of design possibilities; however, the fact is that some hard constraints must be incorporated into every fabrication process. These process constraints include such items as: the number of releasable layers; the layer thicknesses; the layer materials; and other inherent process variables that can affect both the electrical and mechanical properties of the final product. In this chapter, the specific fabrication process chosen for this research effort, along with its inherent constraints, will be described. Next, the approach chosen for providing the interruption of the flyer material in a slapper detonator will be presented, along with the theory behind the operation of its main component—the electrothermal actuator. This will be followed by a brief discussion into the operational theory of an electrothermal actuator, as well as the motive for selecting a particular actuator for the interrupter mechanism. Finally, the specific design parameters of the chosen actuator and interrupter mechanism will be presented.

4.1   PolyMUMPs Fabrication Process

The PolyMUMPs is one of three standard processes offered by the commercial program known as MUMPs® (Multi-User MEMS Processes). Specifically, the

PolyMUMPs fabrication process is a three-layer polysilicon surface-micromachining process that is intended to be used for fabricating "proof-of concept MEMS" designs and is not normally used to create production-type devices. The four materials it offers include: polysilicon for the structural layers; a phosphorus-doped oxide (phosphosilicate glass) for the sacrificial layers; silicon nitride for electrical isolation between the polysilicon and silicon substrate; and finally a gold layer used to provide low resistance wires, electrical contact pads, and reflective surfaces. All these layers, except metal, are deposited using a low pressure chemical vapor deposition (LPCVD) process [1]. The metal layer is deposited using electron-beam evaporation at an estimated maximum temperature of 110 ºC [2]. The two main advantages of this process are its low cost and reasonable turn-around times of approximately 2 months. This allows for several design iterations to be accomplished in a relatively short amount of time [3]. For example, four design runs were fabricated in this research effort, with the main interrupter design coming out of the third fabrication run.

4.1.1   Sequential Fabrication Procedures

A cross-sectional view of the layers available in the PolyMUMPs process, along with specific material layer names and nominal layer thicknesses are shown in Figure 4-1. The conformal step coverage of this fabrication process, which can be used to manipulate the topology of the upper layers, is clearly depicted in this figure.

The first material to be deposited is silicon nitride, which has a layer thickness of 0.6 μm and serves to insulate the above layers from the heavily doped silicon substrate. This nitride layer is typically not patterned, however it can be reached with a series of oxide etches that are performed using a reactive ion etch (RIE) process. Next, the first
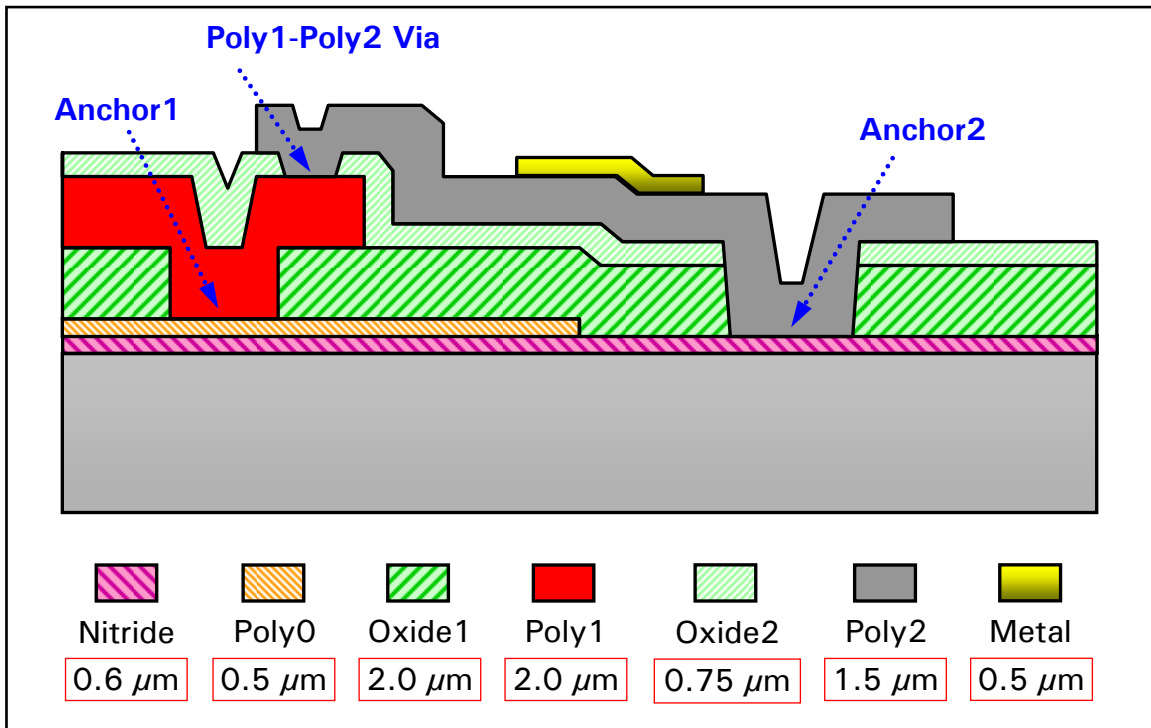
Figure 4-1. Cross-sectional illustration of the PolyMUMPs process (not to scale) [1]. The numbers below the layers represent nominal layer thicknesses and the blue text represents oxide layer etches performed during processing.

structural layer (Poly0) is deposited to a thickness of 0.5 μm. Poly0 is a non-releasable polysilicon layer often used for creating address electrodes and localized wiring. The patterning of the Poly0 layer is realized by using a standard photolithography process followed by a plasma etch. This patterning method is repeated for all of the polysilicon layers. The next step is the deposition of the first sacrificial oxide layer, Oxide1, to a thickness of 2.0 μm. If any contact dimples are necessary in the two releasable structural layers, they are defined by a 0.75-μm deep etch into this oxide layer. Next, the Oxide1 layer is patterned and etched by RIE. The primary purpose of this step is to provide a hole for the first polysilicon layer such that a support anchor can be created [1], [3].

These steps are followed by a 2.0-μm thick layer of polysilicon (Poly1), which is the first releasable layer used to create mechanical structures. A patterning and etch step

(similar to Poly0) is then performed to define the dimensions of the Poly1 structure. Next, a second sacrificial layer, Oxide2, is deposited to a thickness of 0.75 μm. This layer then undergoes two patterning and RIE steps. The first one enables a mechanical and electrical connection between the two upper polysilicon layers (Poly1 and Poly2). The second patterning and RIE step removes both Oxide1 and Oxide2 to permit access to either the Poly0 or Nitride layer, such that an anchor support can be formed from the final polysilicon deposition (Poly2). The Poly2 layer has a thickness of 1.5 μm and serves as a second releasable layer for creating mechanical structures. The patterning of this layer is performed using a process similar to the patterning of the other two polysilicon layers. Finally, a 0.5 μm gold layer is deposited, which provides a means for making reflective surfaces, as well as low-resistance wires and electrical contacts [1], [3].

In addition to the material deposition steps, a 1-hour anneal step at 1050°C follows each of the oxide layer depositions. This anneal step serves a dual purpose: 1) to diffuse the phosphorus in the surrounding oxide layers into the structural polysilicon layers to increase its conductivity; and 2) to reduce residual stress. It is important to note that this high temperature anneal makes the PolyMUMPs process incompatible with a simultaneous fabrication of integrated circuit (IC) devices, which generally require carefully timed diffusion steps for proper functioning. Consequently, if it is desirable to fabricate the IC control circuitry for a MEMS device on a single die, then an alternative fabrication process would have to be selected [1], [3].

The final step is to release the upper two polysilicon layers (Poly1 and Poly2) by selectively removing the two sacrificial oxide layers (Oxide1 and Oxide2). In general, release procedures consist of stripping the protective photoresist layer with acetone,

etching the sacrificial oxide layers in a hydrofluoric acid (HF) solution, and then finally drying the dies either by direct heating or by using a supercritical carbon dioxide (CO_2) dryer. The specific procedure for releasing the devices used in this research is described in Appendix A. Figure 4-2 shows the hypothetical structure depicted in Figure 4-1 after the release procedure has been performed.

4.1.2   Additional Process Constraints

Some additional constraints to consider in any micromachining process, other than the materials and layer thicknesses are tolerances of the fabrication process that determine specific feature sizes. The PolyMUMPs process offers conservative design rules and precautionary guidelines to assist designers in fabricating MEMS devices that have a high probability of successful operation [1]. However, the minimum feature tolerances can vary between each fabrication run, so a series of test structures are
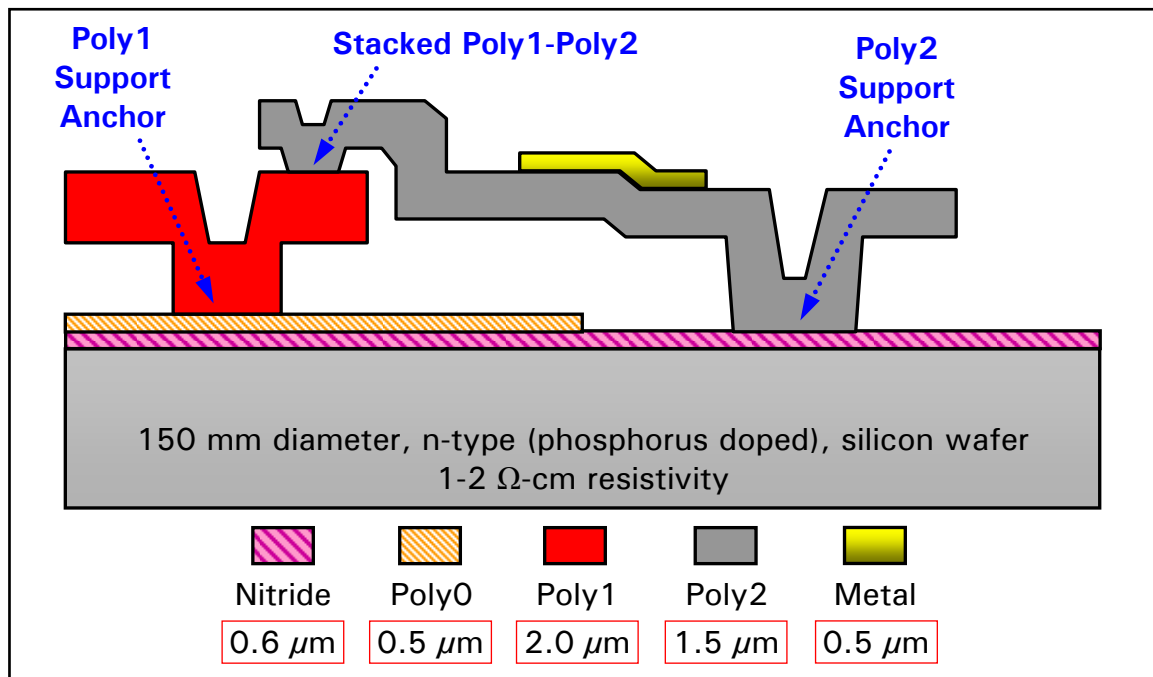
Figure 4-2. Illustration of the released PolyMUMPs structure [1] depicted in Figure 4-1. Note that the sacrificial oxide layers have been etched away by the 48% HF solution.

beneficial in determining the specific process limits for each run. The last two fabrication runs (#68 and #69) for this research effort consisted of test structures designed to observe/measure some of these limits. Specific parameters examined were minimum material widths and minimum spacing between similar materials, i.e., Poly0-to-Poly0, Poly1-to-Poly1, and Poly2-to-Poly2. Figure 4-3 and Figure 4-4 show the test structure design layouts used to determine the minimum fabrication width for all three polysilicon layers and the minimum spacing limits between similar material layers, respectively.

Additionally, the thickness, resistivity, and residual stress for each material layer may vary for each fabrication run. These material properties are measured at the MUMPs® foundry for each fabrication run and are made available to users. This
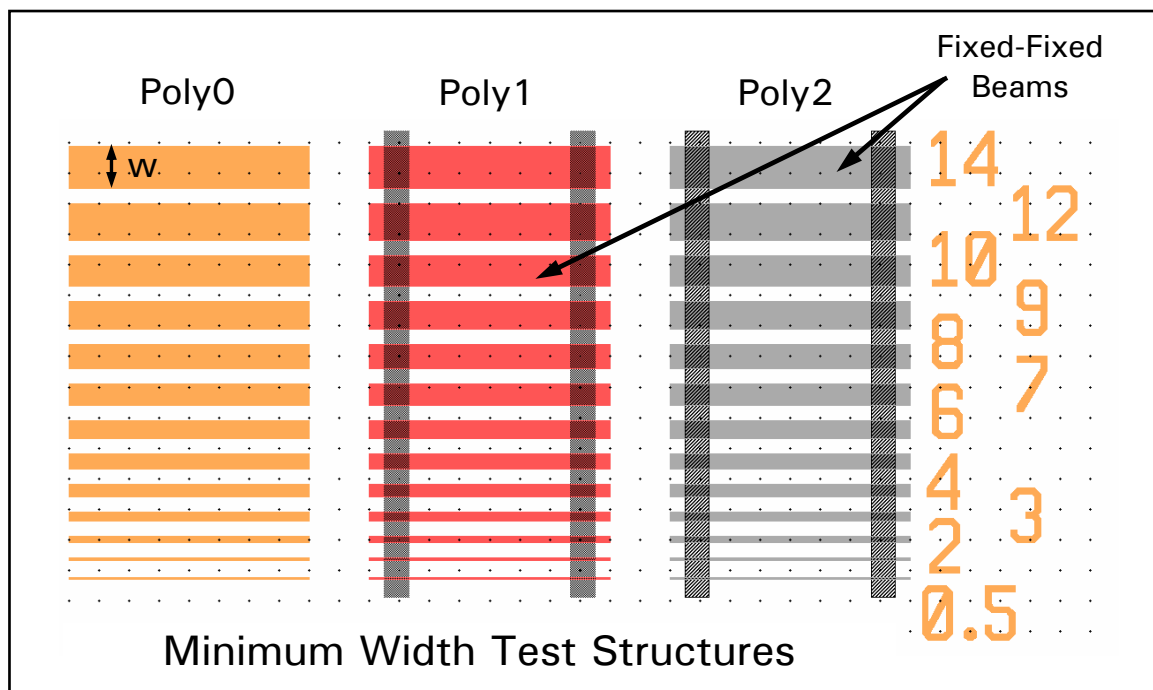
Figure 4-3. Design layout used to determine the minimum fabrication width, *w*, of all three polysilicon layers. The numbers to the right represent the designed width of each structure, in μm, with the last structure being 0.5 μm and the second to last structure being 1.0 μm. Note: the black dots represent a 10 μm reference grid used in the design layout tool, and the dark vertical bars on the Poly1 and Poly 2 are Anchor1 and Anchor2 etches, respectively.
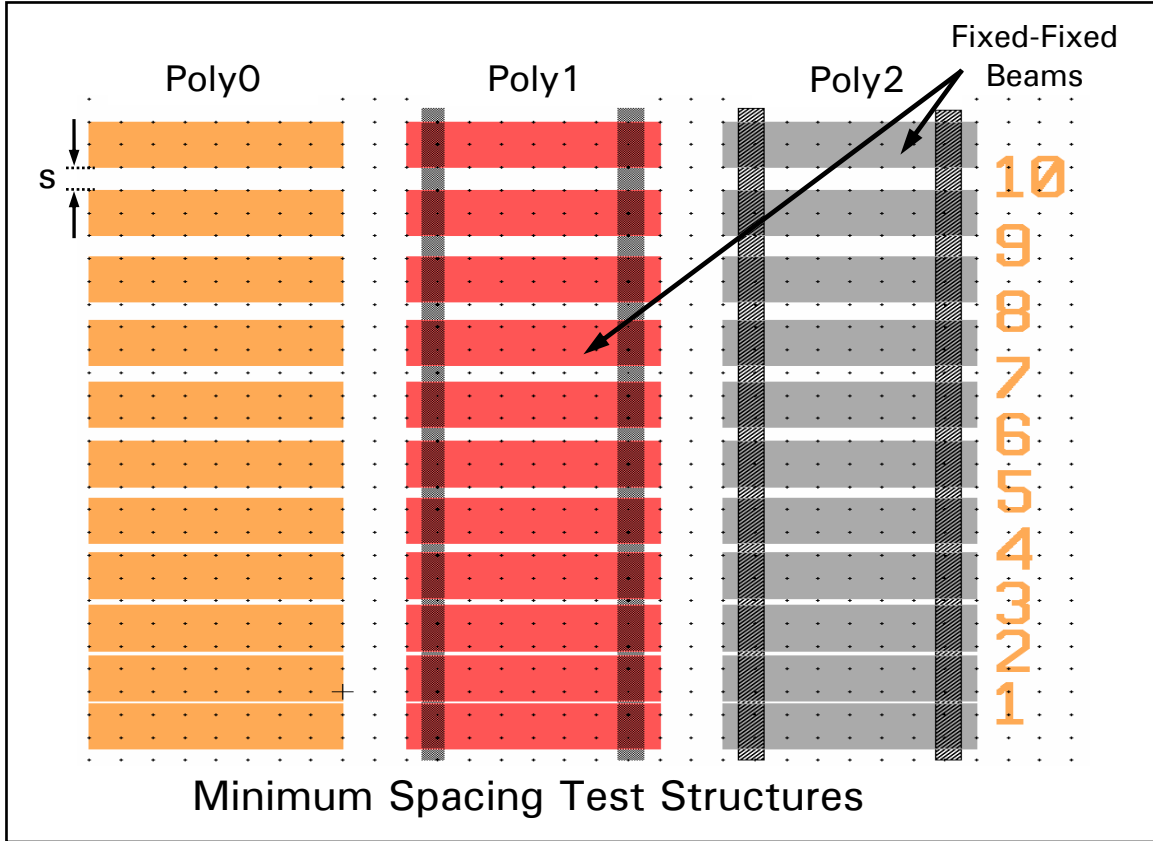
Figure 4-4. Design layout used to determine minimum spacing, *s*, between similar material layers. The numbers to the right represent the spacing between the two adjacent structures, in μm. Again, the black dots represent a 10 μm reference grid, and the dark vertical bars are Anchor1 (Poly1) and Anchor2 (Poly2) etches.

measured data for the four fabrication runs used in this research effort is provided in in Appendix B. However, to get precise thickness data for a specific structure, or to validate the MUMPs® data, a direct measurement of a structure can be acquired by using an optical profiler such as the Zygo Corporation's NewView 5000. This device can obtain vertical measurements, to a resolution greater than 0.1 nm, by using white light interferometry scans [4]. The optical profiler used in this research effort is shown in Figure 4-5.

Figure 4-5. Optical profiler used to obtain vertical measurements of fabricated MEMS structures.

4.2   Interruption Method for the MEMS S&A Interrupter

The specific purpose of the S&A interrupter device presented here is to prevent the flyer material in a solid-state slapper detonator from reaching the HE pellet in an explosive train. The interrupter mechanism design consists of four plates, which are each attached to the end of a MEMS electrothermal actuator. The four plates are arranged so that when no power is applied to the actuators, the plates are as close together as possible (ultimately determined by the fabrication process tolerances).   In this position, the interrupter prohibits passage of the flyer material, thus preventing the explosive train from detonating.   When power is applied to the actuators, the plates move linearly outward, creating an open area for the flyer material to pass through on its way to the HE pellet. Latches are designed for each actuator so that when the proper environmental conditions are satisfied, the mechanism can be permanently latched with the interrupter plates locked in the open (armed) position ensuring that the flyer material can pass through to the HE pellet. If an unlatching capability is desirable, such that the open interrupter plates can be closed (safe), an alternative latching mechanism will be required.

The design layout of the MEMS S&A interrupter device is shown in Figure 4-6, with an accompanying SEM image of the fabricated device shown in Figure 4-7.

While all of the key interrupter components (plates, actuators, and latches) are important to its proper functioning, the actuators have the most design parameters that need to be considered. By comparison, the plates are relatively simple structural components that are linked to the actuators by a fixed beam, and the latches are essentially fixed structures that enable locking by physically mating with an extension of the actuators. In the following section, some of the analysis that went into the design of the electrothermal actuator will be discussed.
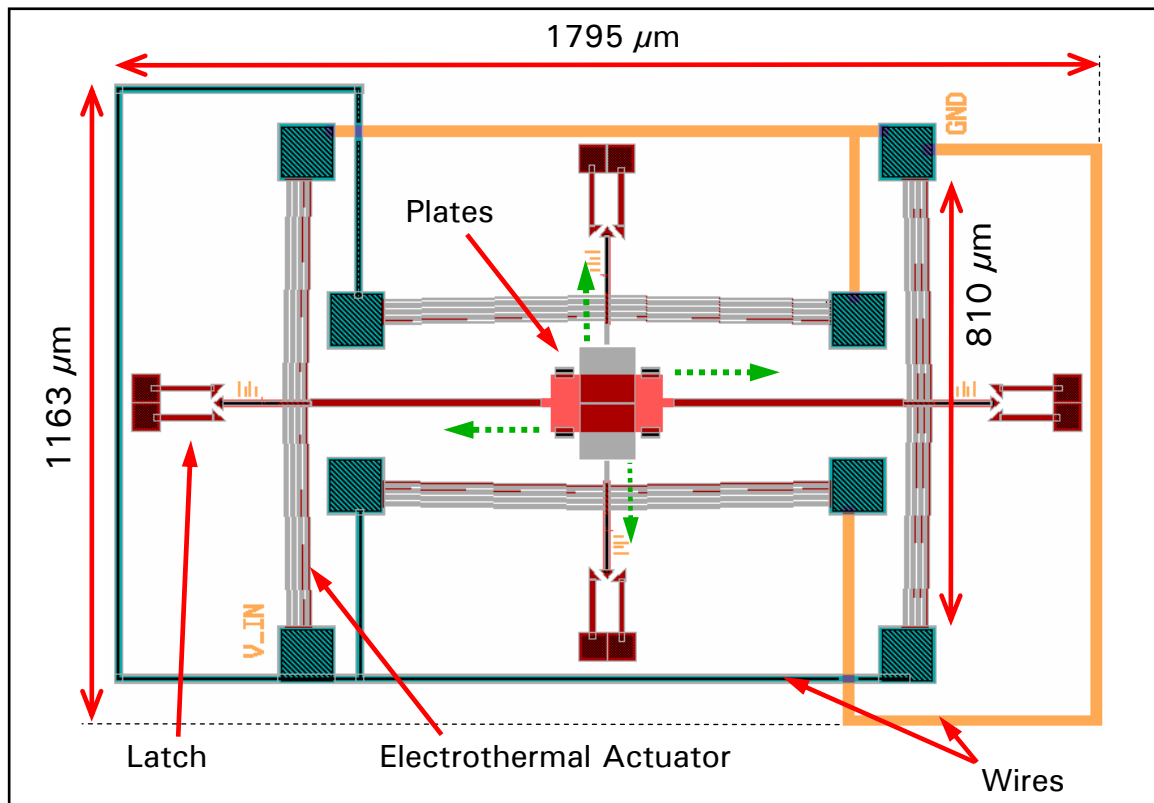
Figure 4-6. Design layout of the entire MEMS S&A interrupter device. The green arrows in the center represent the direction of motion upon actuation. The entire device covers an area less than 2.1 mm^2.
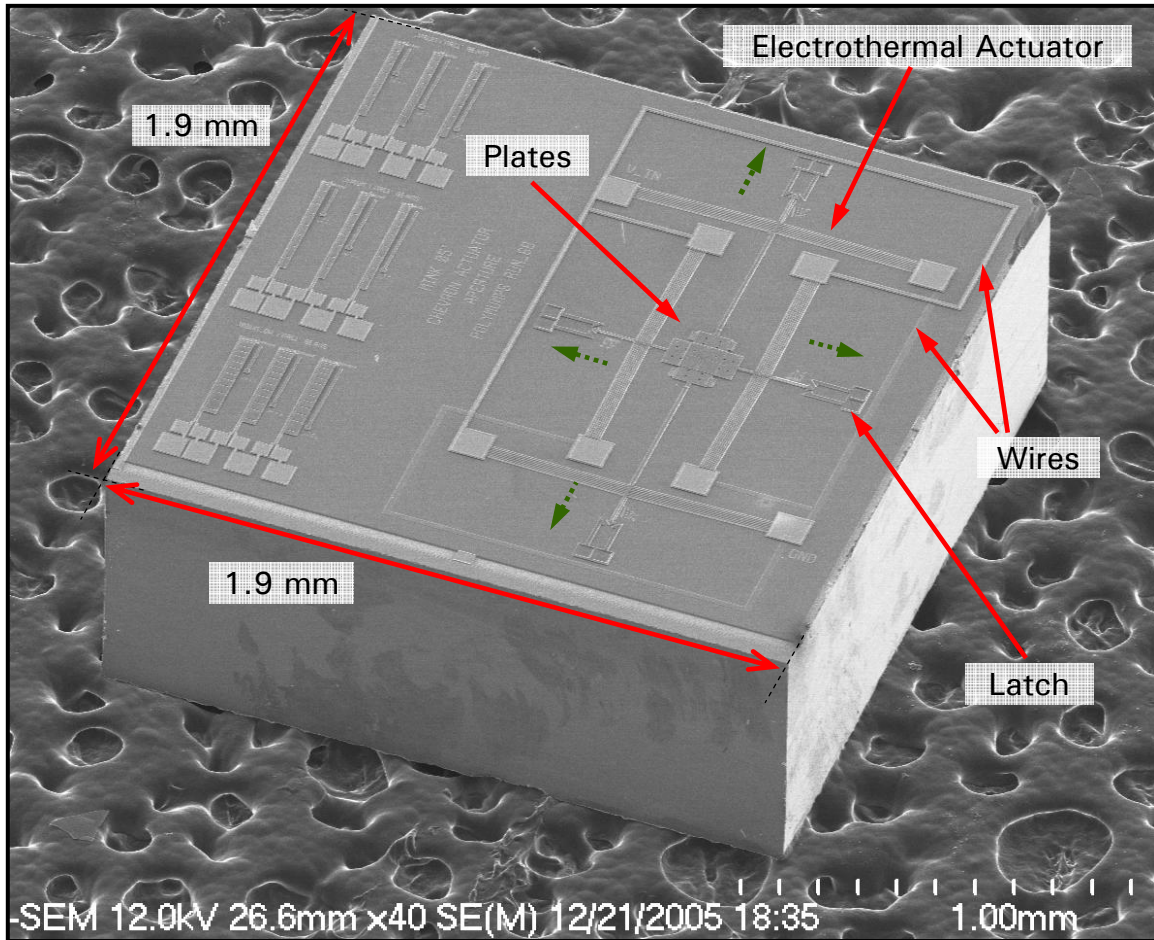
Figure 4-7. SEM image of the fabricated MEMS S&A interrupter device from the design layout shown in Figure 4-6. Again, the green arrows represent the direction of actuator motion when power is applied. Also, note that the entire device is smaller than the 3.8 mm^2 die.

4.3   Electrothermal Actuator Theory

All electrothermal actuators operate on the principles of Joule heating and thermal expansion. Joule heating is the increase in temperature that occurs due to a material's resistivity when a current flows through that material [5]. In general, the actuator is designed such that at least one arm (or length of material) has the proper dimensions to induce a large enough current density to cause the arm to expand as a result of the increase in temperature. As this arm expands, the entire device is forced to move in a specific direction, dependent on the arrangement of the structure and the location of its

anchored (fixed) ends. The two types of electrothermal actuators considered for the interrupter mechanism were the standard u-shaped actuator and the bent-beam actuator. The geometry of the u-shaped actuator causes it to deflect in an arcing motion, while the bent-beam actuator's geometry causes it to deflect in a linear direction. The motion of both actuators is in-plane with the substrate. Figure 4-8 shows a simple illustration of both electrothermal actuators. Note that the bent-beam actuator in Figure 4-8(b) is shown with four expanding arms (two on each side), and that the number of arms is considered a design parameter for optimizing the actuator.
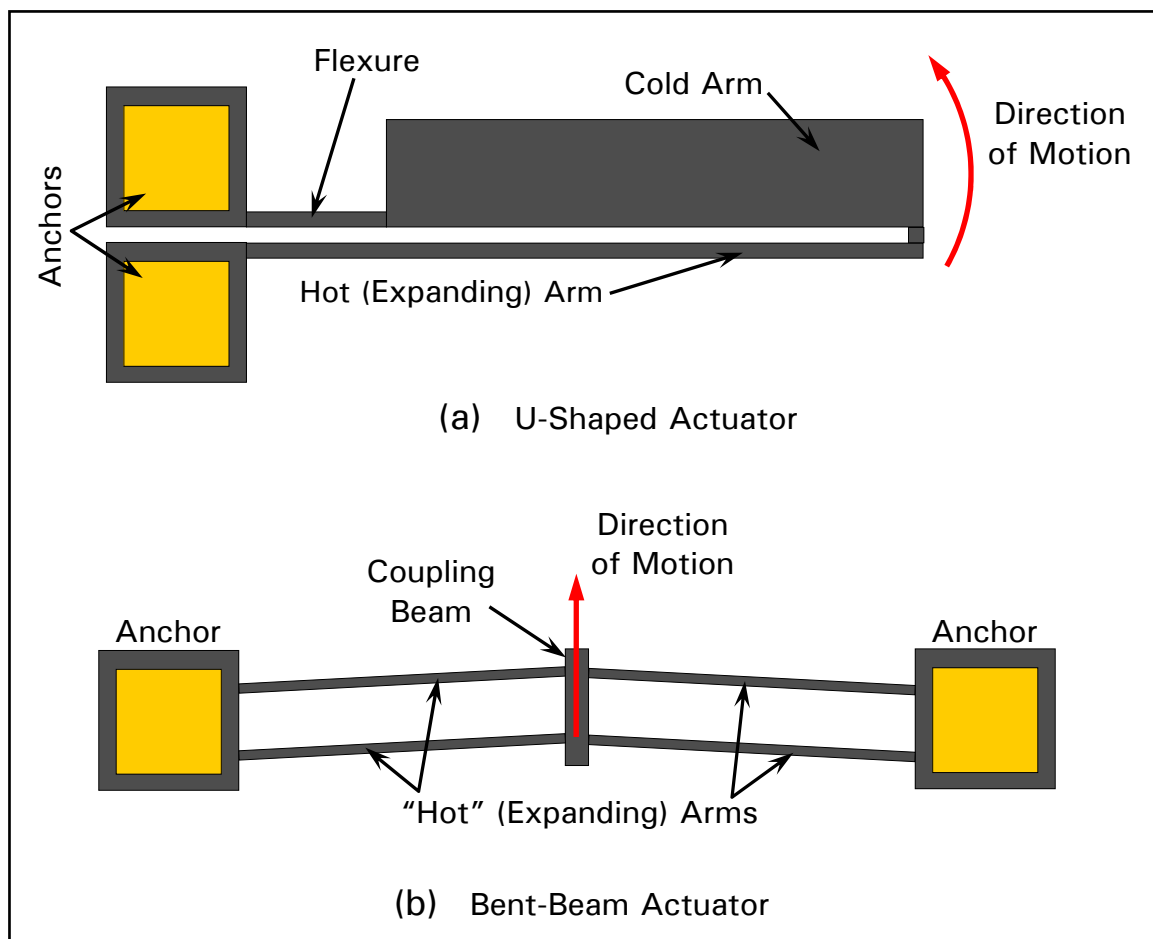
Figure 4-8. Simple schematics of two electrothermal actuators considered for use with the interrupter mechanism fabricated in this research effort. (a) U-shaped actuator showing in-plane arcing motion. (b) Bent-beam actuator showing linear in-plane motion.

4.3.1 Thermal Expansion Theory

To describe the expansion of a material due to Joule heating, look at the beam in Figure 4-9 [6]. The original beam length is L_0, the expansion as a result of Joule heating is ΔL, and the length of the beam after thermal expansion is L_{new}. Therefore:

$$L_{new} = L_0 + \Delta L \quad (\mu m) \qquad (4.1)$$

Furthermore, all materials have a coefficient of (linear) thermal expansion, α_L, that is used to quantify the relative linear change in an object as a result of a change in temperature, ΔT [7]. This relationship can be expressed as:

$$\alpha_L = \frac{\Delta L}{L} \frac{1}{\Delta T} \quad (K^{-1}) \qquad (4.2)$$

Consequently, the expansion due to Joule heating, ΔL, can be described by:

$$\Delta L = \alpha_L \cdot L \cdot \Delta T \quad (\mu m) \qquad (4.3)$$

In addition, if the final temperature of the beam is approximated as an average temperature, T_{ave}, and the initial temperature of the beam is T_0, then Equation (4.1) becomes:

$$L_{new} = L_0 + \alpha_L \cdot L \cdot (T_{ave} - T_0) \quad (\mu m) \qquad (4.4)$$
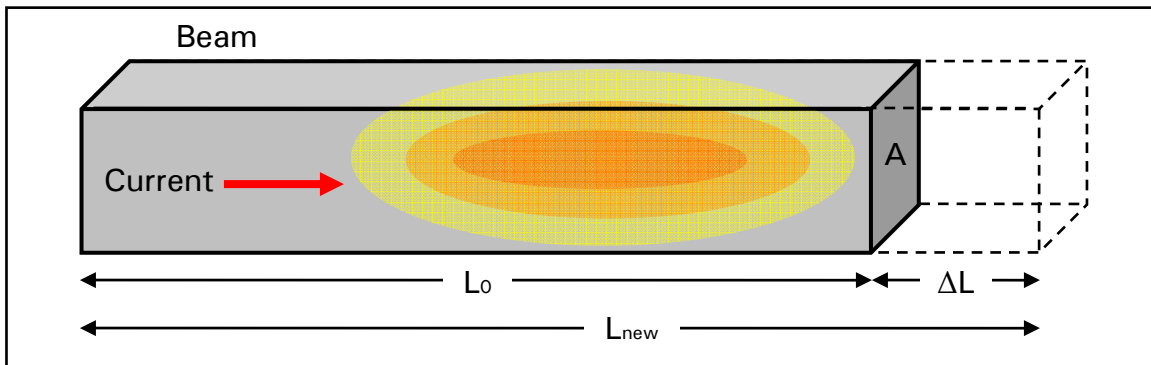
Figure 4-9. Thermal expansion of a beam due to Joule heating. The coefficient of thermal expansion associated with the specific beam material will be a key factor in determining the change in length. The other contributing factor is the current per cross-sectional area, A, that will produce a temperature change throughout the beam [6], [7].

The motion in electrothermal actuators is a result of the beam expansion that occurs when sufficient current density is present. Note that the expanding arms in the MEMS actuators shown in Figure 4-8, have a cross-sectional area, A, on the order of 10 μm^2. For reference, the coefficient of thermal expansion for polysilicon, which is the material used to fabricate the electrothermal actuators investigated in this thesis, has been reported to be 2.33×10^{-6} K^{-1} [7], [8].

4.3.2 Electrothermal Actuator Performance Considerations

One of the main benefits of electrothermal actuators is their low operating voltage, which makes them compatible with standard microelectronics circuitry – e.g., complementary metal-oxide-semiconductor (CMOS) devices. Clearly, a goal for any MEMS designer should be the integration of the electronics required for operation to be fabricated on the same die. Another benefit of electrothermal actuators is that their lateral motion is in the same plane as the substrate, and thus it is relatively simple to move other surface micromachined mechanisms by connecting them to these actuators [9]. Additionally, electrothermal actuators have been shown to reliably produce deflections and forces with magnitudes of approximately 15 μm and 10-100 μN, respectively [8], [10], [11]. In contrast to other types of MEMS actuators, for example, electrostatic actuators, which operate at high voltages, produce considerably smaller forces, and are usually limited to only a few micrometers of vertical deflection [12]. Nevertheless, a major drawback to electrothermal actuators is that they consume considerably more power than electrostatic actuators. However, this drawback is usually tolerated for the enhanced in-plane performance.

4.3.3   Electrothermal Actuator Comparisons

The following sections discuss the operation of the two electrothermal actuators –
u-shaped and bent-beam – considered for use with the interrupter mechanism.

U-Shaped Actuator

The basic operation of the u-shaped electrothermal actuator can be described by
referring to Figure 4-8(a). When a voltage is applied across the two anchors, a current
that is dependent on the resistance of the actuator is passed through the actuator. Since
the hot arm has a smaller cross-sectional area than the cold arm, it has a larger current
density. As a result, the hot arm heats up more than the cold arm, which produces a
proportionally larger thermal expansion of the hot arm. This difference in expansion
between the two arms causes the actuator tip to deflect in an arcing motion about the
anchored end of the cold arm [10], [13].

Furthermore, by maximizing the temperature difference between the hot and cold
arms the efficiency of the actuator can be increased. Several techniques available to
increase this temperature difference are: 1) increasing the thickness of the cold arm thus
reducing its current density, and 2) increasing the width of the cold arm such that more
surface area is available to dissipate heat [14]. In fact, any heat dissipated in the flexure
or cold arm is considered wasted power since it does not contribute to the actuator's
deflection [13]. Clearly, the dimensions for the various elements (hot arm, cold arm, and
flexure) of the u-shaped actuator are important design parameters that can be tailored to
maximize a particular desired performance, such as deflection, force, or power
consumption.

For example, increasing the actuator's overall length tends to increase the total deflection. However, the trade-off is an increase in power consumption since the voltage must increase to compensate for the increased resistance. In addition, the force of the actuator tends to decrease with increasing length. Alternatively, decreasing the width of the flexure will maximize deflection since the actuator is easier to bend as the hot arm expands. However, if the flexure is narrower than the hot arm, it may thermally fail before the hot arm generates any meaningful deflection. Also, increasing the length of the flexure tends to increase deflection; however, this increases power consumption in the flexure and expansion may result, thus counteracting any deflection due to the hot arm expanding. Another technique involves increasing the thickness of the actuator to generate more force, but the larger cross-sectional area of the hot arm will increase the power consumption of the device. The final technique is increasing the hot arm width to a value slightly greater than the thickness in order to maximize force, while again sacrificing a slight increase in power consumption   [11], [13], [14].   For illustrative purposes, Figure 4-10 shows a deflection versus input power curve for a typical u-shaped electrothermal actuator. The specific dimensions for this actuator are given in the figure.

Bent-Beam Actuator

The basic operation of the bent-beam electrothermal actuator can be described by referring to Figure 4-8(b). When a current is passed through the "hot" arms by an applied voltage across the two anchors, the arms tend to lengthen as a result of thermal expansion. The cross-sectional area of the arms is designed to be very small (on the order of 1 μm^2) in order to ensure a sufficient current density is obtained such that the arms thermally expand, as previously discussed. Furthermore, pairs of identical arms are
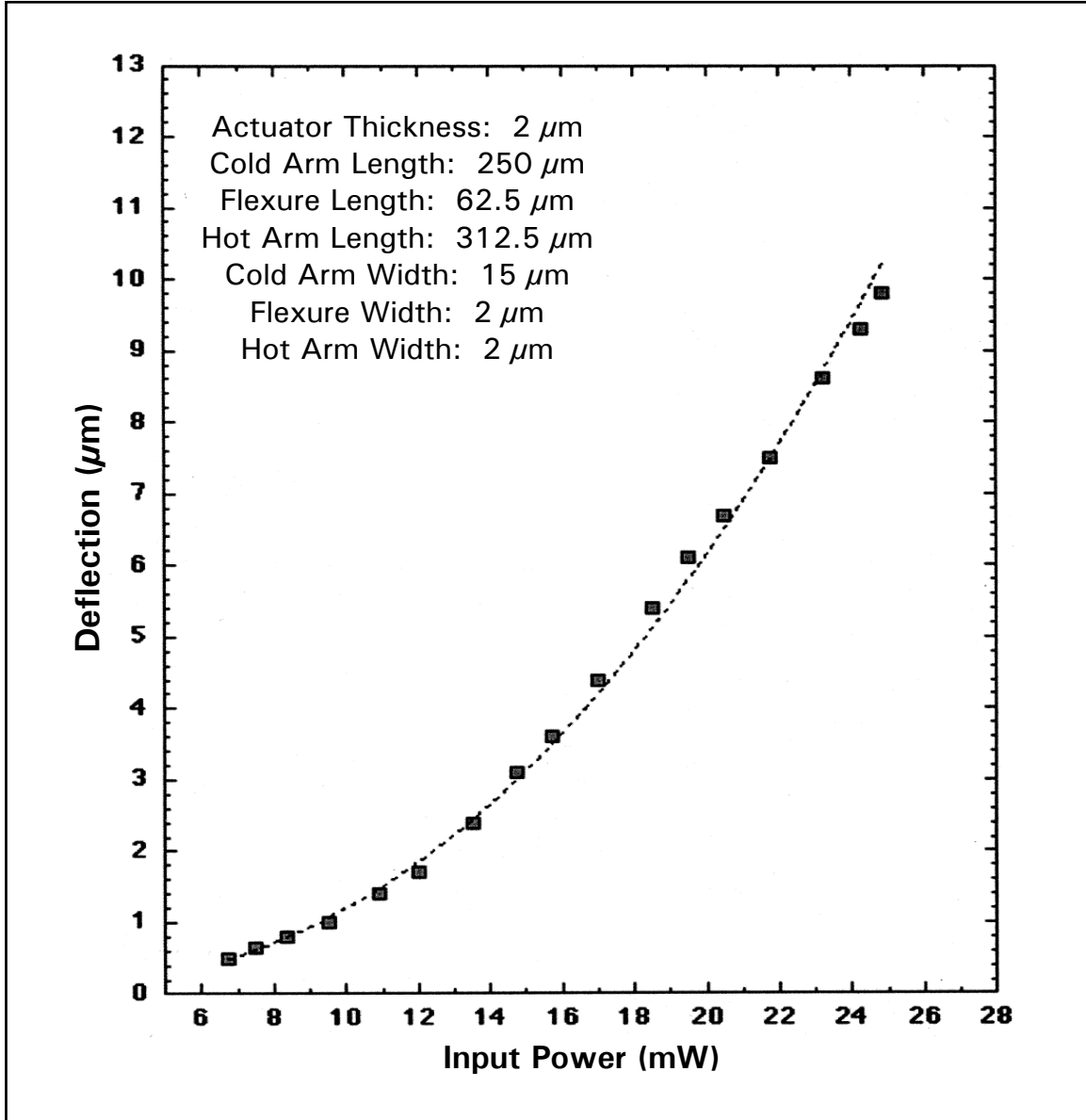
Figure 4-10. Measured deflection versus power input for an electrothermal u-shaped actuator fabricated in the PolyMUMPs process. Data points come from five identical actuators [13].

coupled by a beam placed in the center of the actuator. Since the arms are fixed by the anchors, the bent-beam actuator will move linearly as the arms expand. This linear movement due to the coupling beam provides a method to transmit the resulting linear force to another device, in addition to adding structural integrity to the actuator. To

ensure the expanding arms bend in the desired direction, the actuator is designed with a small pre-bend angle. The location of the pre-bend angle, θ, and the arm length, L, as used in this thesis are defined in Figure 4-11 [8].

The performance of the bent-beam actuator (e.g., deflection distance and force) can be optimized by varying the following design parameters: the number of arm pairs; the arm length; the pre-bend angle; and the actuator thickness. For example, the deflection of the actuator is dependent on the arm length and the pre-bend angle, but independent on the number of arm pairs and the actuator thickness. In addition, the deflection is directly related to the drive voltage, which, as expected, will result in an increase in current density. Obviously, there is a limit at which the current density will exceed the carrying capability of the arms and the device will catastrophically fail. As another example, the force of the actuator is directly proportional to the number of arm pairs and the actuator thickness, as well as the pre-bend angle [8]. Moreover, Que et al showed that a linear relationship exists between the actuator deflection and generated output force, such that the force of the bent-beam actuator decreases as the deflection increases [15].
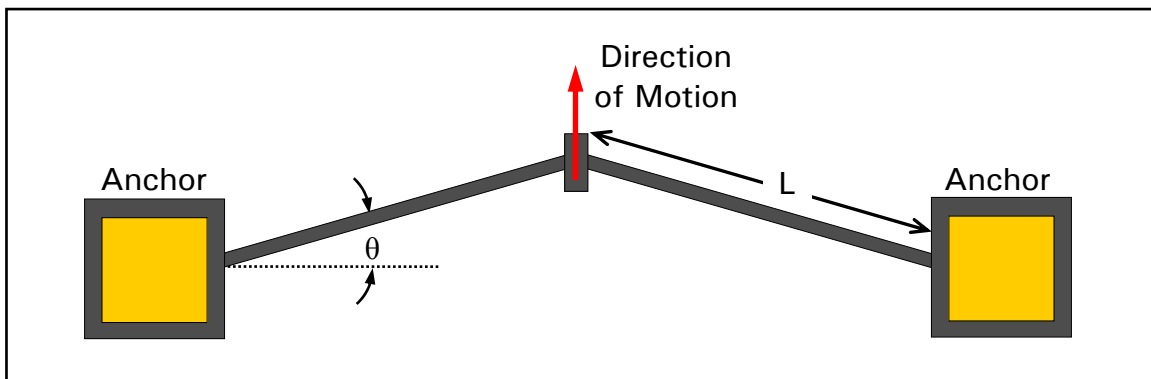
Figure 4-11. A simplified bent-beam actuator showing the basic design parameters of pre-bend angle, θ, and arm length, L. Note: that θ is exaggerated for illustrative purposes.

4.3.4 Electrothermal Actuator Designed for Interrupter Mechanism

Between the two electrothermal actuators discussed above, the bent-beam actuator was chosen to provide the actuation forces for the interrupter mechanism designed in this research effort. A number of factors contributed to this choice, but the desire to have the four interrupter plates separate themselves in a linear motion, was the most significant. The linear motion reduces the complexity of the interruption method and simplifies the implementation of the actuation, thereby increasing reliability. Implementation of the interrupter mechanism using the u-shaped actuator is more complex, because of its inherent arcing motion. While it is true that several u-shaped actuators can be designed with a common yoke, to provide a linear force, this type of linkage tends to significantly reduce the amount of force that can be delivered [8]. Clearly, this type of force reduction does not exist for the bent-beam actuator. It is worth noting that Comtois et al. investigated a creative rotary yoke design to be used with u-shaped actuators, however, this type of design requires a fabrication process with at least three releasable layers [16].

Another reason for selecting the bent-beam actuator was the larger output force available, which would be beneficial in rapidly separating the interrupter plates to create an opened path for the flyer material. The bent-beam actuator has a large force output because of the increased number of arms that can be added to its design [8]. However, it must be keep in mind that increasing the force by adding additional arms will also result in a decrease in deflection. This larger force may be advantageous if increasing the dimensions (and consequently the mass) of the interrupter plates is desirable. The next section will address specific design parameters selected for the bent-beam electrothermal actuator used in this research.

4.4   Bent-Beam Electrothermal Actuator

The primary objectives considered in selecting the design parameters for the bent-beam electrothermal actuators included: 1) ensure enough force was available to completely separate the four interrupter plates, and 2) provide the greatest amount of deflection to maximize the dimensions of the opened area. The force requirement was critical since the actuators must provide enough force to move the plates a reasonable distance. If this could not be accomplished, the entire interrupter mechanism would be ineffective. With the above goals in mind, the main design parameters of actuator thickness, the number of arm pairs, the length of the arm, and the pre-bend angle were chosen to optimize the actuator's performance. Additionally, various test structures were designed to characterize the true performance of the fabricated actuators.

4.4.1   Design Parameter Optimization

To ensure the force requirement was satisfied, the first parameter considered was the actuator thickness. PolyMUMPs offers three different thickness possibilities for its releasable layers: 1.5 μm (Poly2), 2.0 μm (Poly1), and 3.5 μm (Poly1 + Poly2). As described in section 4.3.3, an increase in actuator thickness will produce an increase in output force [8]. Therefore, the actuator was chosen to be the maximum thickness of 3.5 μm. Although the additional thickness is only required for the expanding arms, the entire actuator was designed to be 3.5-μm thick in order to maintain structural integrity. The only drawback from the increased thickness is an increase in power consumption due to the larger current density required to thermally expand the arms.

The second design parameter that can increase the output force is to increase the number of arm pairs. However, the maximum force occurs when the deflection is small,

and decreases linearly as the deflection continues to increase [15]. Therefore, since maximizing deflection is also desirable and deflection is dependent on arm length, a balance between arm length, and the number of arm pairs had to be considered. The selection for these design parameters was based on experimental data from a previously successful bent-beam actuator design. Szabo experimented with multiple bent-beam actuator designs that varied both the arm length and the number of arm pairs, while keeping the thickness of the arms constant at 3.5 μm [17]. A summary of the measured data he obtained is shown in Table 4-1. Observe that a maximum deflection of 19 μm was observed from the 350 μm × 8 arm (arm length × number of arm pairs) bent-beam actuator. However, it must be noted that this actuator required a relatively large input power when compared to the other actuator designs. A large power requirement was also necessary for the 350 μm × 16 arm and the 400 μm × 12 arm actuators. This could be expected due to the decreased parallel resistance provided by additional arm pairs that effectively reduces the current in each path for a given voltage. Clearly, a reasonable compromise between deflection and power is offered by the 400 μm × 8 arm actuator. Thus, the 400 μm × 8 arm actuator was chosen to provide the necessary actuation force for one of the three interrupter mechanisms designed in this thesis. For comparative purposes, a second interrupter mechanism with 400 μm × 12 arm actuators was designed.

In addition to arm length, the deflection of the bent-beam actuator is dependent on the pre-bend angle. Figure 4-12 shows the deflection versus pre-bend angle for a series of 2-μm thick polysilicon bent-beam actuators as presented by Sinclair [8]. The figure clearly shows that a pre-bend angle of 1.05° produced the most deflection. Furthermore, note that the deflection dramatically decreases as the pre-bend angle decreases from

1.05º. Sinclair also observed that for very small pre-bend angles the actuator bends in the

vertical direction, and no longer provides in-plane actuation [8]. The pre-bend angle for

the actuators tested by Szabo was approximately 1.0º [17], so it was for these reasons that

a pre-bend angle of 1.05º was chosen for this research effort.

Table 4-1. Summary of the bent-beam actuators tests described by Szabo [17].

Bent-Beam Actuator Design Parameters (Arm Length × No. of Arm Pairs)	Maximum Deflection (µm)	Input Power at Max. Deflection (mW)
250 µm × 8 arm	12.5	350
350 µm × 8 arm	19.0	775
350 µm × 16 arm	16.0	690
400 µm × 4 arm	16.0	320
400 µm × 8 arm	16.5	360
400 µm × 12 arm	16.5	880

Figure 4-12. Results of deflection versus pre-bend angle tests
performed on 2-µm thick polysilicon bent-beam electrothermal
actuators [8]. The maximum deflection was observed for a
pre-bend angle of 1.05º.

As a final attempt to maximize the performance of the bent-beam actuators, a third interrupter mechanism was designed with arms that were thicker in the middle than at the ends. This tapered design was investigated by Sinclair in an effort to increase the actuator's thermal power limits, and thus produce an improved mechanical output, in terms of increased deflection and force. For a straight design, the temperature profile is heavily dependent on the inherent heat sinks provided by the anchors at both ends of the actuator and the coupling beam that is geometrically centered between the arm pairs. By adding extra material at the center of the arm (where most of the heat is generated), the heat dissipation at that location is improved. As a result of the tapered design, the temperature over the length of the arm is more evenly distributed, thus reducing the probability of thermal failure [18]. Figure 4-13 shows the temperature distribution profile for two bent-beam actuators – one with straight arms and one with tapered arms. Notice that the maximum temperature for the tapered design (named P1-ST, for Poly1 – symmetric tapered) is distributed more evenly over the length of the arm. The arm length in both actuators is 220 μm, and the overall actuator length is approximately 460 μm.

To optimize both the force and deflection, it is desirable that these electrothermal actuators operate near their thermoelastic limit, which for polysilicon is around 1173 - 1273 K [18]. The thermoelastic limit is the maximum point at which polysilicon cools due to the thermoelastic effect, which occurs when a tensile load (or, in this case, arm expansion) is experienced. At temperatures above this limit, additional heating occurs due to its thermal expansion [19], and thermal failure of the actuator rapidly follows. For reference, note that the melting point of polysilicon is 1685 K. (This value is actually for bulk single-crystal silicon; but it does provide a reasonable approximation [20].)
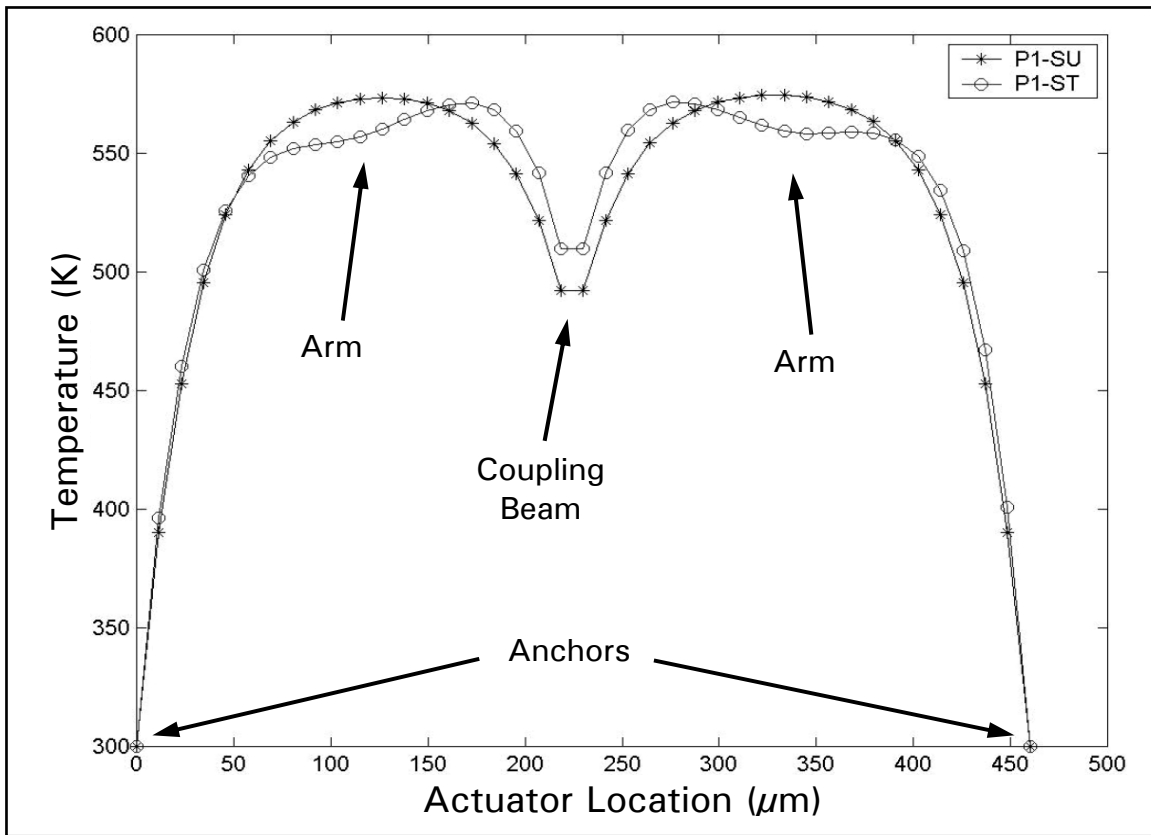
Figure 4-13. Modeled temperature distribution profile showing two bent-beam actuators – straight arms (P1-SU) and tapered arms (P1-ST) [18]. The more evenly distributed temperature over the length of the tapered arm is evident. Note, the length of the arms in both actuators is 220 μm, making the overall actuator length approximately 460 μm.

The naming convention used to define the tapered arm geometry is shown in Figure 4-14(a), along with a graphical representation of the deflection versus the C/D tapering ratio [18] in Figure 4-14(b). Using this data, a third interrupter mechanism was designed using the 400 μm × 8 arm bent-beam actuators with a C/D tapering ratio of 1.32 in order to maximum deflection. This will enable the observation of any performance improvements that result from this tapered design. A series of stand-alone bent-beam actuators were also designed so individual performance data could be obtained. Any performance relationships that exist between the individual actuators, and that of the entire interrupter mechanisms, will be examined and discussed in Chapter 5.
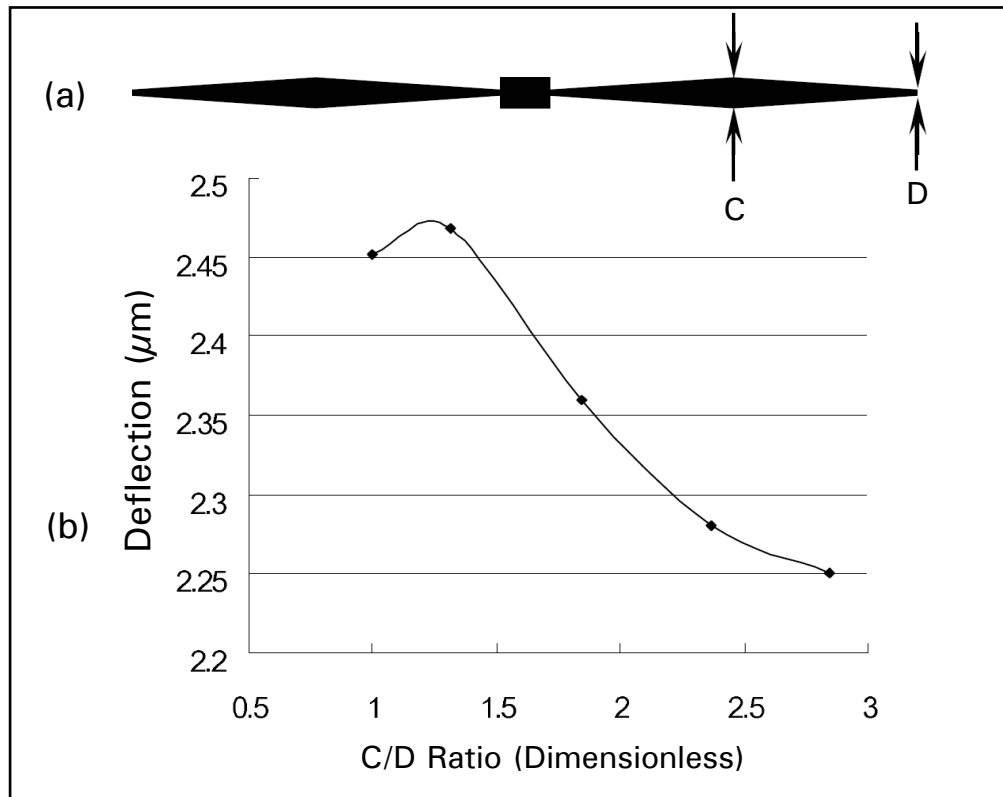
Figure 4-14. (a) Illustration of a hot arm pair that shows the naming convention used to define the tapering geometry. (b) Simulated deflection curve as a function of the C/D ratio. Note: maximum deflection is produced by a C/D ratio of 1.32 [18].

To summarize, three different sets of bent-beam electrothermal actuators were designed for use with each identical interrupter mechanism. The relevant design parameters chosen for each bent-beam actuator are shown in Table 4-2. Since the parameters were based on previously optimized bent-beam actuators, it is expected that the performance will be similar to what was shown in Table 4-1.

4.4.2   Force Measurement Technique

In addition, to designing a few stand-alone variations of the bent-beam electrothermal actuators for characterization testing, a few sets of actuators were designed with adjacent force measuring structures to determine the output force. The force

Table 4-2. Summary of the bent-beam actuator design parameters chosen for each of the interrupter mechanisms fabricated as part of this research effort.

Interrupter No.	Arm Length × No. of Arm Pairs	Actuator Thickness (μm)	Pre-Bend Angle (Degrees)	Arm Width (μm)	Tapered (Yes/No)
1	400 μm × 8 arm	3.5	1.05	3.0	No
2	400 μm × 12 arm	3.5	1.05	3.0	No
3	400 μm × 8 arm	3.5	1.05	3.0	Yes

measuring structures are essentially simple cantilever beams that are positioned perpendicular to the direction of the actuator's motion [13]. Figure 4-15 shows an illustration of this arrangement. By definition, a cantilever beam is rigidly fixed at one end and free to move at the other end when a load is applied somewhere along its length. For simplicity, the applied load was designed to be located at the end of the cantilever beam. To accomplish this, one end of the actuator's coupling beam was extended so that it could be placed adjacent to the beam's tip. This arrangement enabled the use of relatively simple formulas for an end-loaded cantilever beam. Figure 4-16 shows the specific cantilever beam arrangement used for this experiment.
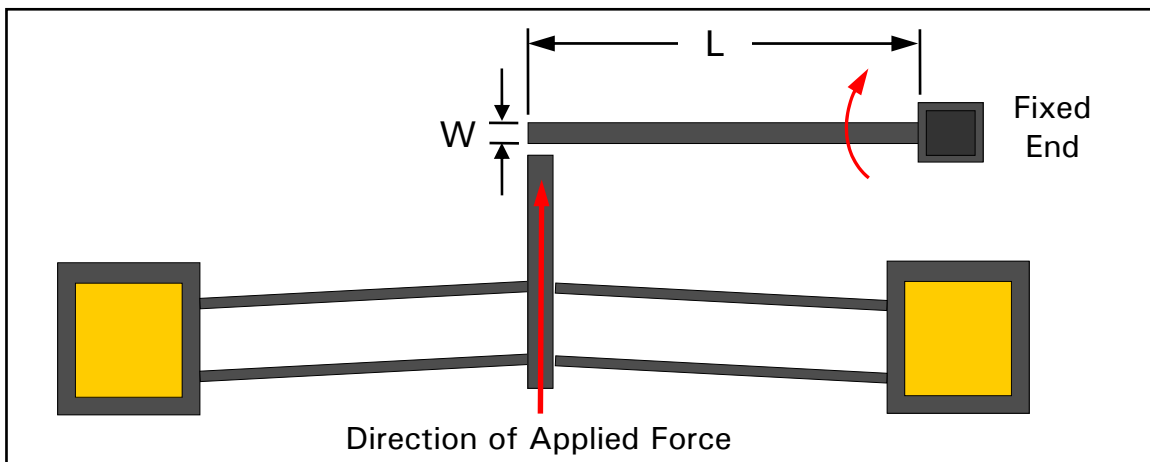
Figure 4-15. Illustration of actuator and cantilever beam arrangement for experimentally determining applied force. The length of the beam, L, and the width of the beam, w, are also shown.
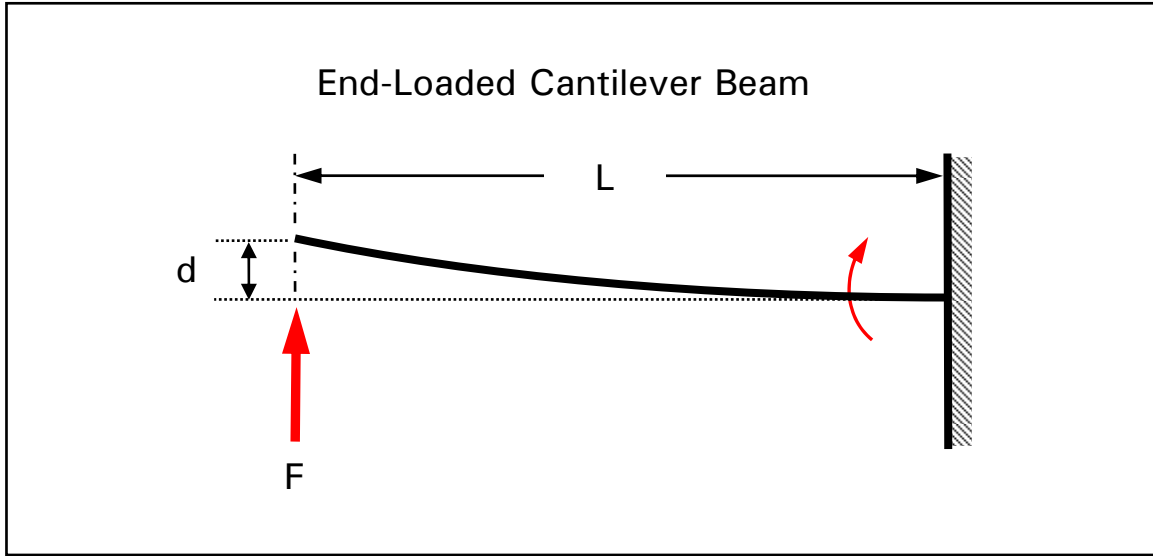
Figure 4-16. Schematic of an end-loaded cantilever beam arrangement used to determine the applied force from the bent-beam actuators [21]. The length of the beam, L, the applied force, F, and the deflected distance, d, are shown.

The equation that describes the maximum deflection of the cantilever beam, d_{max}, due to an applied force, F, at the tip of the beam is [21]:

$$d_{max} = \frac{F \cdot L^3}{3 \cdot E \cdot I} \quad (\mu m) \tag{4.5}$$

where

$$L = length\ of\ the\ beam \quad (\mu m)$$
$$E = Young's\ modulus \quad (GPa)$$
$$I = moment\ of\ inertia \quad (\mu m^4)$$

The polysilicon deposited by the PolyMUMPs process has a Young's modulus of 158 ± 7.9 GPa, as reported by Sharpe et al. This value varies widely throughout the literature; however, the extensive mechanical testing performed to obtain the above value provides the largest level of confidence available, other than directly measuring it for each fabrication run. In addition, Sharpe et al. showed that there was very little variance in Young's modulus for polysilicon samples provided by three separate fabrication processes [22].

Considering that the cantilever beam has a rectangular cross-sectional area, the moment of inertia is given by [21]:

$$I = \frac{t \cdot w^3}{12} \quad (\mu m^4)$$
(4.6)

where

$$t = thickness\ of\ the\ beam \quad (\mu m)$$
$$w = width\ of\ the\ beam \quad (\mu m)$$

Thus, by combining Equation (4.5) and Equation (4.6), the following relationship for the applied force, F, on the cantilever beam, when maximum deflection has occurred, is:

$$F = \frac{E \cdot t \cdot w^3 \cdot d_{max}}{4 \cdot L^3} \quad (\mu N)$$
(4.7)

Therefore, to experimentally determine the applied force, the actuator is powered thereby causing the coupling beam tip to move toward the free end of the cantilever beam. After contact is made, the load applied to the beam forces it to bend about its fixed end. When the beam has reached its maximum deflection, the deflection distance, d_{max}, is recorded and used in Equation (4.7) to determine the force applied by the actuator. Note that this force value does not represent the total force capacity of the actuator, but rather the force applied to the beam at the instance maximum *beam* deflection has occurred [8]. Moreover, using this method assumes that any effects due to friction are negligible [11].

The cantilever beams used for this experiment were fabricated in the same materials (Poly1 + Poly2) as the bent-beam actuators. Hence, both the actuators and the beams are designed to have a thickness of 3.5 μm. This theoretically implies that, upon release, both structures will likely be lined up at the same physical height, thus reducing any negative effects that might arise due to out-of-plane bending (e.g., the actuator

"jumping" over the cantilever beam as resistance is encountered). Furthermore, the initial separation between the actuator and the cantilever beam is designed to be approximately 2 μm, which is close enough to enable solid contact, but far enough away to ensure the two structures are indeed separated during fabrication. For example, if any mask misalignments occur, a spacing of less than 2 μm could cause the two structures to be fabricated as one structure, thus prohibiting performance of the force measuring experiment.

Additionally, the width of the cantilever beam had to be considered. It was reported in Sinclair that if the force measuring beams are not stiff enough to sufficiently resist the load applied by the actuator, maximum deflection will never occur and a valid force measurement value cannot be obtained [8]. Consequently, the widths of the cantilever beams were chosen to be 8 μm. Lastly, three different beam lengths (100 μm, 200 μm, and 300 μm) were designed for each variation of the bent-beam actuators. This was done to ensure maximum deflection data could be accurately obtained. For instance, as alluded above, the beam stiffness needs to be within a certain range to ensure that maximum deflection of the beam occurs before the actuator's deflection limit is reached. This limit is typically around 15 μm for the majority of u-shaped and bent-beam electrothermal actuators. If the beams are excessively short, they could be too stiff and the actuators may be unable to produce any measurable beam deflection. Alternatively, if the beams are excessively long, maximum deflection of the beam may never occur within the actuator's deflection range. Figure 4-17 shows a graphical representation of Equation (4.5), depicting the actuator force required to produce maximum deflection for a cantilever beam with three different lengths and the following parameters in common:

E = 158 GPa, t = 3.2 μm, and *w* = 8 μm. Notice that for the beam length of 100 μm, a

force of 200 μN is required to produce a maximum deflection of about 3 μm. In addition,

recognize that for a specific force output (dependent on the design parameters of a given

actuator), the optimal cantilever beam length should result in a maximum deflection of

less than 15 μm, which is the approximate limit of the bent-beam actuators. If the beam

is designed such that maximum deflection occurs above this limit, it will not be observed,

and the output force will be unmeasurable. However, the output force is usually not

known prior to testing, so the best approach is to design cantilever beams with multiple

lengths, such that the predicted maximum deflection falls within a reasonable and

measurable range.

Figure 4-17. Graphical representation of Equation (4.5), depicting the actuator force
required to produce maximum deflection for a cantilever beam with three different
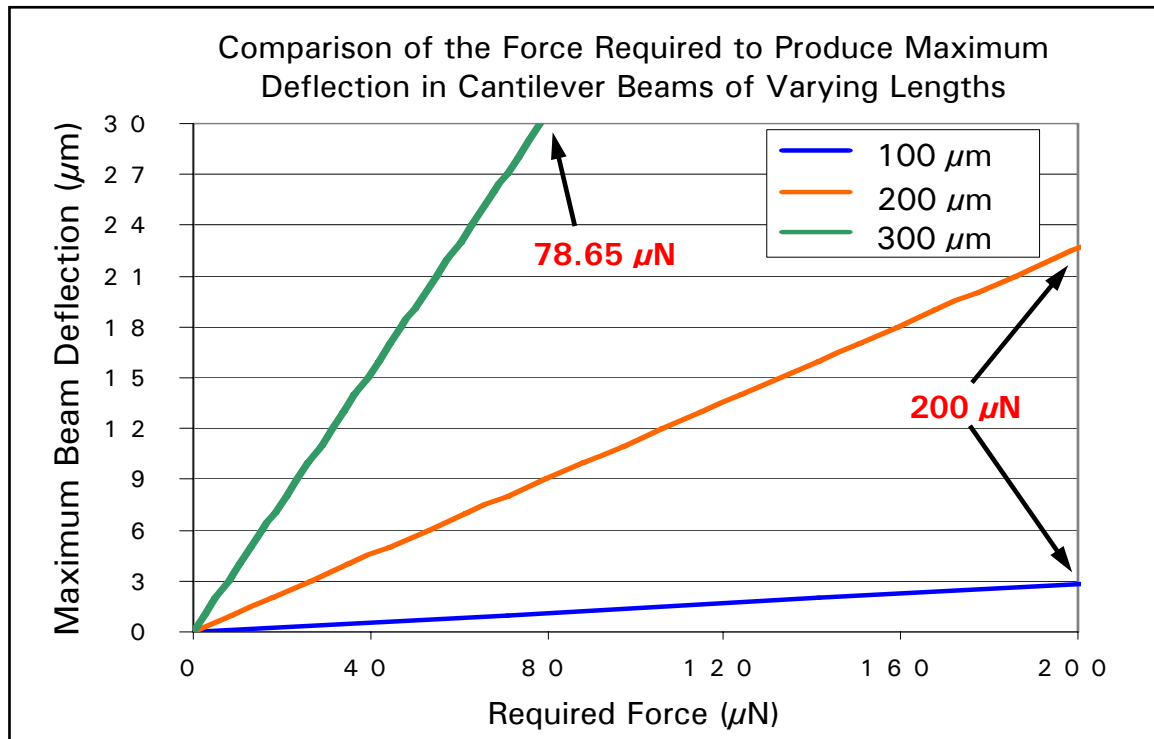
lengths and the following common parameters: *E* = 158 GPa, *t* = 3.2 μm, and *w* = 8 μm.

4.5   Interrupter Design Theory

The theoretical design of the interrupter mechanism presented in this thesis focuses on the means to interrupt the flyer, of a solid-state slapper detonator, so that it is prevented from initiating a HE pellet in the explosive train. Alternatively, it is just as important to allow the flyer to pass through the interrupter mechanism when a valid launch condition is present. The approach taken to perform the interrupting function was to arrange four moveable plates in an overlapping pattern in an effort to provide additional interruption strength than could otherwise be provide by only two plates. Figure 4-18 shows the arrangement of the four separate interrupter plates. Both Poly1 (bottom) and Poly2 (top) were used to create the overlapping pattern.

Additionally, each of the four interrupter plates is physically joined to its own bent-beam electrothermal actuator by a linkage beam that directly translates the actuator's motion to the plate. The operation of the bent-beam electrothermal actuators is described in section 4.4. The arrangement between the actuator and its interrupter plate is such that when the actuator moves linearly outward, the small initial aperture created between the four interrupter plates expands, providing an opening that the flyer material can pass through on its path to the HE pellet.

Finally, a latching structure was designed to provide a method for locking the opened aperture.   The latches function by the mating of two initially separated components. The first component is the triangular-tipped extension protruding from the deflection end of the actuator's coupling beam, and the second component is a fixed structure with two flexible locking beams that extends towards the first component. Upon activation of the actuator, the triangular-tipped extension of the actuator moves
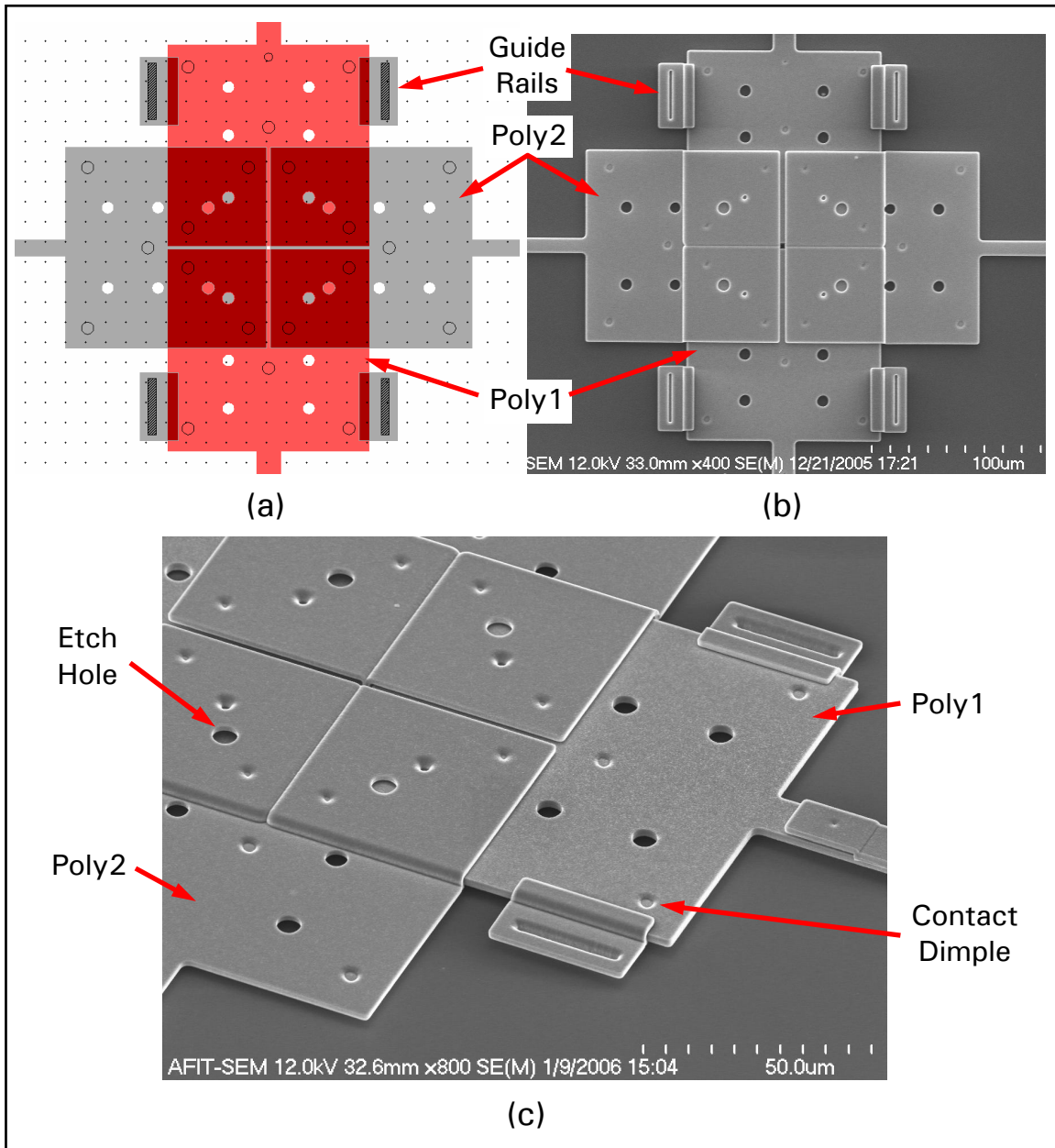
Figure 4-18. (a) Design layout of overlapping interrupter plates. (b) SEM image of fabricated overlapping interrupter plates. (c) SEM image of overlapping interrupter plates showing conformal topology.

toward the fixed component. When the two components come in contact with each other, the flexible beams will move perpendicular to the motion of the actuator (due to the applied force) and mating occurs when the triangular tip completely passes the tip of the flexible beam. Figure 4-19 shows two SEM images of the fabricated latching structure.
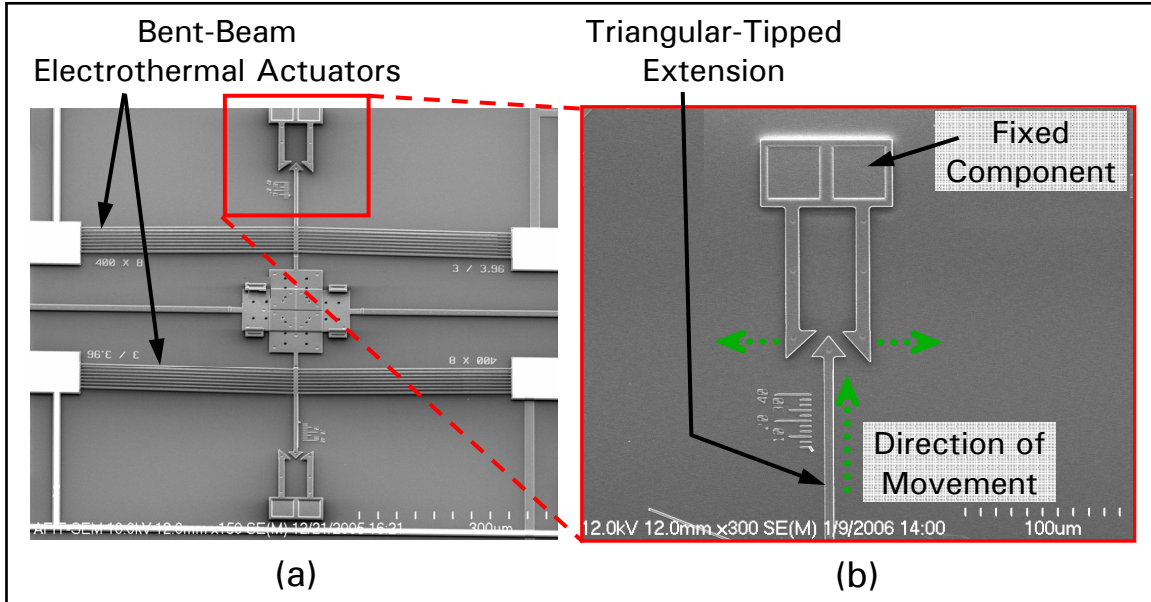
Figure 4-19. SEM images showing (a) the connections between the latching mechanism and the actuator, and (b) the two components which make up the latching mechanism.

It is important to note that using this latching method requires that the desired latching distance be pre-determined, since the distance between the two locking components is fixed after fabrication.

4.5.1   Analysis of Interrupter Aperture

The interrupter aperture is produced by the overlapping arrangement of the four fabricated square plates. Initially, the plates are designed to be in a closed, or safe, position in order to prevent the flyer material from initiating the HE pellet. However, because of the spacing constraints discussed in section 4.1.2, the two Poly1 plates and the two Poly2 plates are designed to have an initial separation of 2 μm. This prevents the possibility of having the two plates (Poly1-to-Poly1 and Poly2-to-Poly2) fused together due to any mask misalignments that could occur in the PolyMUMPs process. Consequently, in the initial "closed" position, there is a small 4 μm^2 opened area as shown in Figure 4-20.
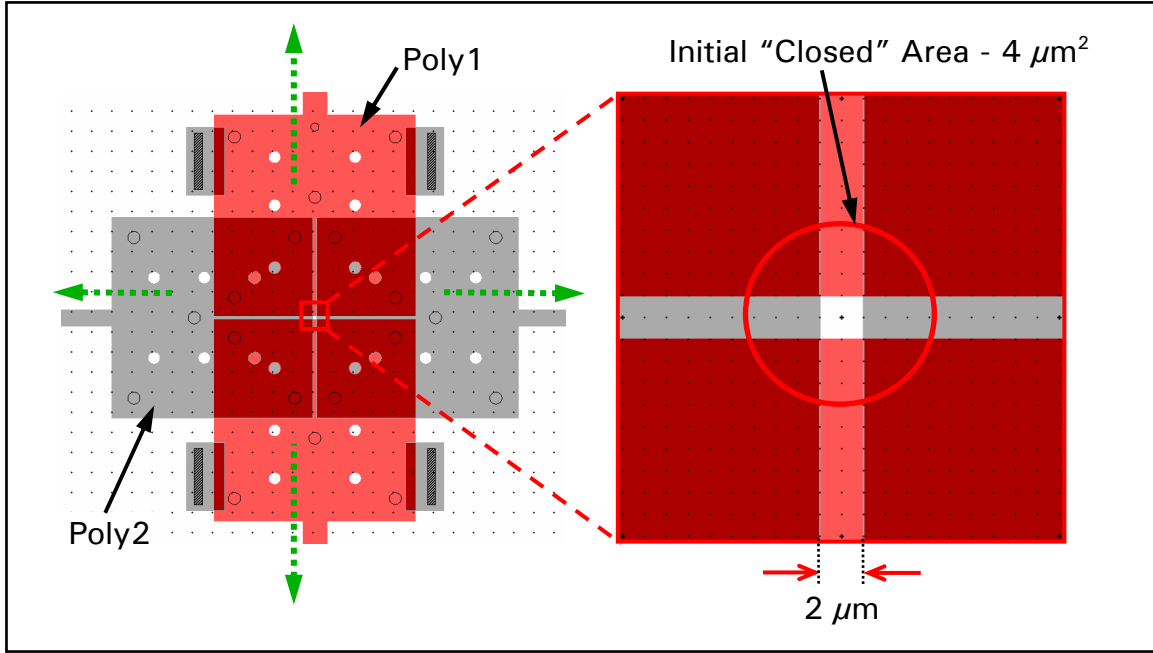
Figure 4-20. Design layout of the "closed" interrupter, depicting the 4-µm² area where no coverage exists.

When the actuators are powered, the interrupter plates will move outward, as shown by the green arrows in Figure 4-20. This causes the area of the aperture to rapidly expand, up to a limit resulting from the maximum deflection of the bent-beam actuators. Since each actuator is designed to the same exact design parameters (see Table 4-2), it is reasonable to assume they will all deflect exactly the same distance for a given applied power (i.e., when one actuator deflects 1 µm, all the other actuators also deflect 1 µm). This trend should continue until maximum deflection is reached, resulting in the aperture area being maximized. Consequently, the following relationship is used to describe the entire area of the aperture, A_a, as a function of a single actuator's deflection distance, d:

$$A_a = \left(2 \cdot d + 2\right)^2 \quad (\mu m^2) \tag{4.8}$$

Figure 4-21 shows an illustration of this change in aperture area as a result of actuator deflection. Notice that a small actuator deflection has a rather large affect on the aperture area in accordance with Equation (4.8). In addition, Figure 4-22 shows the graphical representation of Equation (4.8), which shows the quadratic increase in the aperture area as a function of actuator's deflection. From this graph, an aperture area of 1444 μm^2 is expected for the interrupter mechanism designed for this thesis, based on the anticipation of obtaining a reasonable actuator deflection of 18 μm. Accordingly, if this conceptual interrupter mechanism is integrated with a solid-state slapper detonator, the ejected flyer material must have a cross-sectional area of less than 1444 μm^2, so that it can pass through the aperture and initiate the HE pellet.
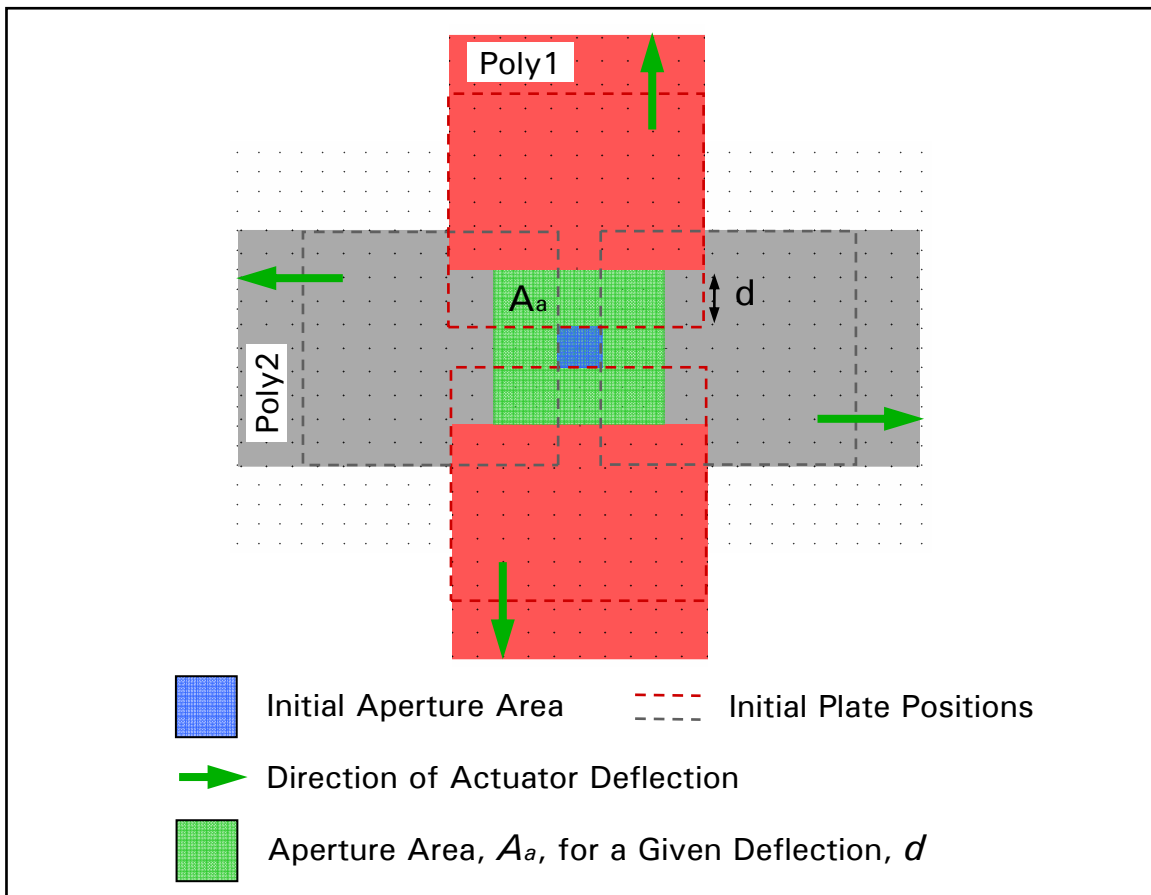
Figure 4-21. Illustration of the change in aperture area as a result of actuator deflection. Notice the difference between the initial aperture area and the resulting aperture area.

Potential Aperture Area as a Function of Actuator Deflection

$$A_a = (2 \cdot d + 2)^2$$
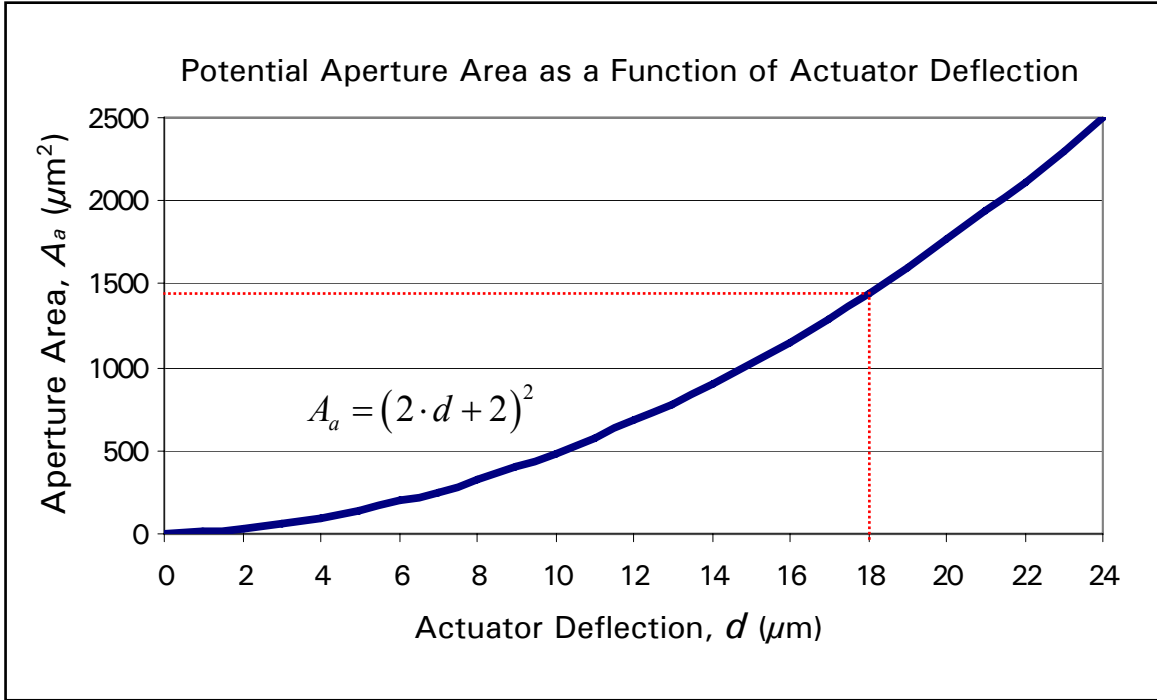
Figure 4-22. Graphical representation of the quadratic dependence of the actuator deflection on the aperture area in accordance with Equation (4.8). The red line indicates a realistic expectation for the aperture area based on the anticipated performance of the bent-beam actuators designed for the interrupter mechanism in this thesis.

4.5.2 Required Actuator Force Calculations

To determine the force required to move all the elements attached to the bent-beam actuators, a simple free-body diagram was constructed. Figure 4-23(a) shows one of the actuator elements that make up the complete interrupter mechanism. The element shown consists of a Poly2 interrupter plate, the Poly2 linkage, and the Poly1 + Poly2 latching beam component attached to the actuator. Even though this figure only shows one actuator element, this analysis can be easily repeated for the Poly1 interrupter plate, with slight modifications.

Figure 4-23(b) shows the free-body diagram corresponding to the element in Figure 4-23(a). The normal force, N, can be determined by:

$$N = m_T \cdot g = V_T \cdot \rho \cdot g \quad \text{(N)} \tag{4.9}$$

where

$$m_T = total\ mass\ of\ all\ components \quad (kg)$$
$$g = acceleration\ due\ to\ gravity \quad (m/s^2)$$
$$V_T = total\ volume\ of\ all\ components \quad (m^3)$$
$$\rho = density\ of\ polysilicon \quad (kg/m^3)$$

Once the normal force is known, the actuator force, F, can be calculated by referring to the free-body diagram and observing the relationship of:

$$F = f_s = \mu_s N \quad (N) \tag{4.10}$$

where

$$f_s = static\ friction\ force \quad (N)$$
$$\mu_s = coefficient\ of\ static\ friction \quad (dimensionless)$$
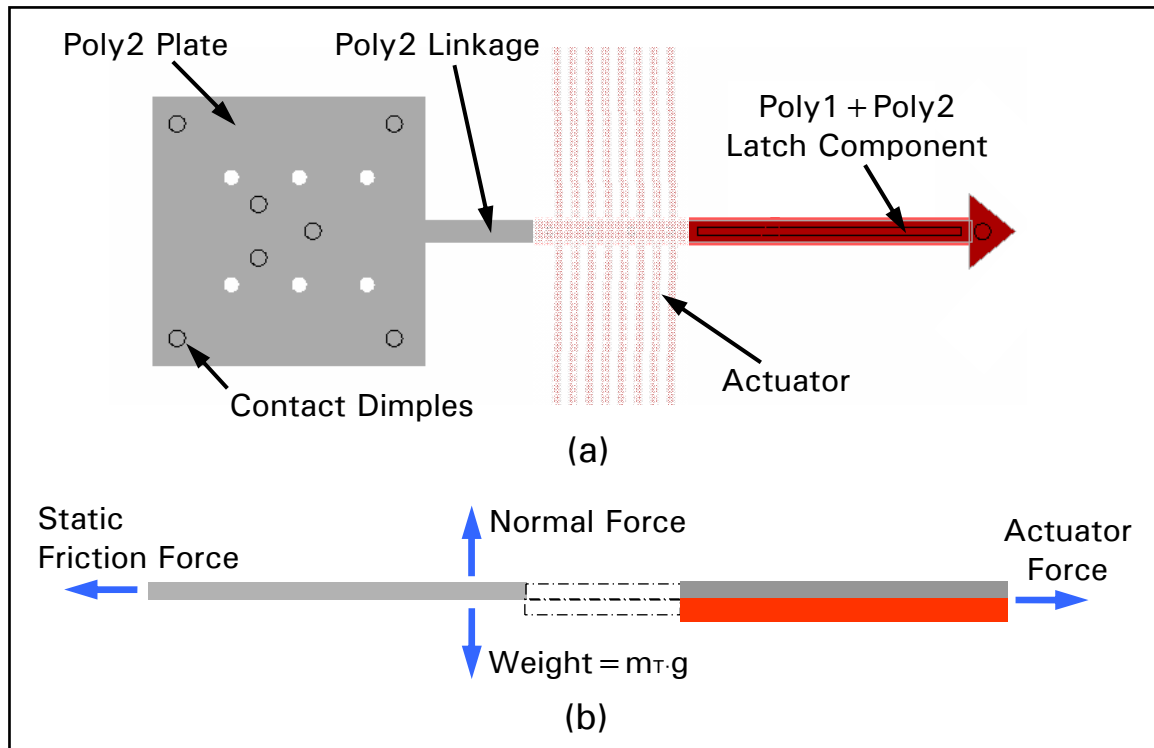
Figure 4-23. (a) One of the four actuator elements that make up the interrupter mechanism. The actuator is dimmed since it is not included in the free-body diagram. (b) Free-body diagram of the interrupter mechanism shown in (a). Only the (Poly1) plate, the linkage, and the latch component are considered in determining the required actuator force.

To simplify the calculation, several assumptions were made. First, the force required for the bent-beam actuator to move itself was assumed to be negligible and neglected from the free-body diagram. Second, the coefficient of static friction, μ_s, for polysilicon deposited by LPCVD, is assumed to be 0.11, as reported by Sundararajan et al [23]. This value for μ_s comes from the seven contact dimples (radius = 3 μm) on the interrupter plate, which results in a total contact area of 198 μm². For MEMS contact surfaces, μ_s is dependent on the contact area, as determined by Lumbantobing et al. This paper reports that for contact areas of 25 μm² and a 100 μm², the values for μ_s are 0.58 and 0.29, respectively [25]. Clearly, this shows a decreasing trend for increasing contact area, and therefore the value of 0.11 is reasonable. Finally, since the coefficient of kinetic friction, μ_k, is typically less that μ_s, its effect is assumed to be negligible [24]. However, this assumption is based on macro-scale material properties, and the research performed by Lumbantobing et al, suggests this may not be true for micro-scale devices.

Finally, the volume of each component is determined from the designed area of the structures and the layer thicknesses provided in Appendix B for run #68. Using the density of polysilicon to be 2.33 g/cm³ [7], the force required to move all the elements attached to a single actuator is calculated using Equations (4.9) and (4.10). The results are shown in Table 4-3. Since the actuator with the Poly1 interrupter plates have a much longer linkage, which is designed to be 3.5-μm thick (Poly1 + Poly2), the required force is over double that required for the actuator with the Poly2 interrupter plates. However, since both of these forces are much less than the micro-newton force usually produced by electrothermal actuators, it is anticipated that the actuators should be able to move the interrupter components with ease.

Table 4-3. Force required to move a single interrupter element
consisting of the plate, linkage, and latch component.

Actuator Element Plate Material	Required Actuator Force (nN)
Poly1	0.0965
Poly2	0.0474

4.5.3   Additional Considerations

The interrupter mechanism described in this thesis was designed as a proof of concept, and as such, it has some limitations that must be considered. For example, the interrupter mechanism does not have its own power supply, and therefore, it requires an external power supply for operation, which is a common requirement for munition fuze components. For instance, many munition items currently have on-board power supplies that derive their power from both electrochemical and electromechanical devices [26]. Additionally, this interrupter mechanism was not specifically designed to sense an environmental condition as a prerequisite to arming (i.e., opening the aperture), which is a fuze requirement under MIL-STD-1316E [27]. Therefore, a valid launch condition must be determined by some other means, before actuation of the interrupter mechanism is enabled.

Potential Power Sources

An example of an electrochemical power source is a thermal battery. Thermal batteries use electrically-initiated pyrotechnic chemicals to melt an initially solid electrolyte material. Other electrochemical power sources use the spin forces generated during launch to distribute an electrolyte into battery cells. These types of

electrochemical batteries are capable of providing a potential difference of approximately 30 V for a minimum discharge time of 30 minutes. An output voltage of this magnitude would be capable of operating the interrupter mechanism described in this research [26].

Two examples of electromechanical power sources are wind-driven generators and pulse-driven generators. Wind-driven generators develop their power as a result of ram air pressure and are capable of producing power outputs of 1-2 W at munition velocities greater than 200 ft/sec. The advantages of using a wind-driven power source are its low cost, essentially limitless shelf life, and simple operation that tends to increase reliability. On the other hand, one type of pulse-driven generator is a piezoelectric transducer that produces a sudden potential difference when the piezoelectric material is mechanically stressed. These devices are capable of instantaneously providing very large voltage outputs as a result of some type of environmental stimuli, such as launch acceleration or weapon impact [26].

Potential Environmental Sensing Capability

This interrupter mechanism, as currently designed, can only function through the operation of four bent-beam electrothermal actuators. As previously discussed, these electrothermal actuators provide linear motion due to the current density in the pre-bent arms causing them to thermally expand. As an alternative approach, it may be possible to induce thermal expansion of the arms through the use of a different energy source, and still produce the same actuation effect.

A unique environment that could provide this potential energy source for operating the actuators is the aerodynamic heating that results from the ballistic environment. Aerodynamic heating is produced as a result of the atmospheric drag

experienced by a munition as it travels through the air. As the munition approaches supersonic speeds, it can absorb a significant amount of heat from the compression of air flowing around the munition body. While the increased temperature tends to vary along the munition body, the maximum temperature increase is at the nose, where the air flow velocity is theoretically zero. Furthermore, the recovery temperature (defined as the temperature that can be recovered at the surface of the fuze, from the maximum temperature at the nose), can be related to the Mach number, M, of the air flow and the ambient temperature, T_a, by the following relationship [26]:

$$T_r = T_a \cdot \left(1 + 0.2 \cdot r_f \cdot M^2\right) \quad \text{(K)} \tag{4.11}$$

where

$$T_r = recovery\ temperature \quad \text{(K)}$$
$$r_f = correction\ factor \quad \text{(dimensionless)}$$

The correction factor accounts for the fact that the temperature at the fuze surface is reduced from the nose temperature. This correction factor is typically approximated to be 0.9, which accounts for a wide range of conditions [26]. If the bent-beam electrothermal actuators presented in this thesis could be linked, via a thermal conduction path, from the nose of the munition to the expanding arms, it may be possible to operate the S&A interrupter device using aerodynamic heating as the energy source. In addition, if this is possible, aerodynamic heating could potentially be used as one of the environmental stimuli that prevents unintentional arming required by MIL-STD-1316E.

Figure 4-24 shows a graphical representation of Equation (4.11), along with some recovery temperature comparisons between typical munition systems as a function of their Mach number. The Mach numbers for these systems come from Table 2-1 and the
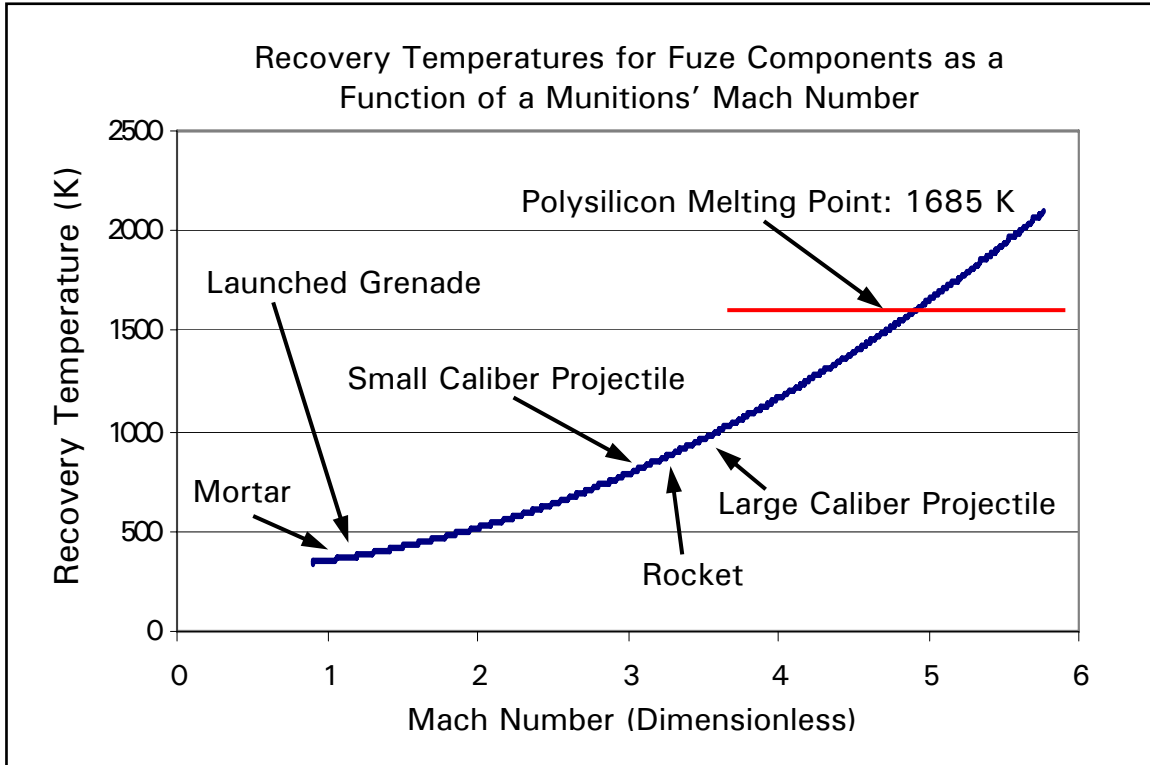
Figure 4-24. Graphical representation of Equation (4.11) along with some comparisons between typical munition systems using the Mach numbers as provided by Table 2-1. Note: all aerodynamic heating temperature for these munition systems are below the melting point of polysilicon.

ambient temperature, T_a, is assumed to be 300 K. As can be seen from the figure, all the recovery temperatures are below 1685 K, which implies the actuators would not suffer from thermal failure due to melting of the polysilicon arms. Furthermore, the small/large caliber projectiles and the rockets are just below the optimal operating temperature (1173 - 1273 K) of the bent-beam actuators as discussed in Section 4.4.1 [18]. Lastly, it should be noted that even though aerodynamic heating is a legitimate environment condition, as of 1994, it had not been used in any known fuze designs to initiate arming. However, it has been used to perform self-destruct functions in some small caliber projectiles [26].

4.6   Summary

This chapter has presented the theory on which the design of the MEMS interrupter mechanism was based. The specific fabrication process used for this research effort was presented along with a discussion of the inherent constraints (e.g., number of releasable layers and layer thicknesses) of this process. This was followed by a detailed discussion of the mechanism designed to interrupt the flyer material in a slapper detonator, as well as the bent-beam electrothermal actuator used to separate the interrupter plates, thereby enabling an unimpeded path for the flyer on it way to initiating the HE pellet. Finally, this chapter concluded with a brief discussion about some theoretical power sources that could be used to power the electrothermal actuators, as well as a potential environmental energy source that could enable a sensing function to be incorporated into this interrupter mechanism. The next chapter will discuss the results of testing that was performed on the actual fabricated devices.

Bibliography

[1] Koester, David and others. *PolyMUMPs Design Handbook (Revision 11.0)*. MEMSCAP, 2005. August 2005. <http://www.memsrus.com/documents/ PolyMUMPs.DR.v11.pdf>.

[2] *PolyMUMPs FAQ (Revision 2.0)*. MEMSCAP, 2004. August 2005. <http://www.memsrus.com/documents/PolyMUMPs.faq.v2.pdf>.

[3] Comtois, John H. and Victor M. Bright. "Design techniques for surface-micromachining MEMS processes," *Proceedings of SPIE – The International Society for Optical Engineering.* Volume 2639: 211-222 (September 1995).

[4] *Zygo Corporation's NewView 5000™, Precise, Rapid, Noncontact 3D Surface Profiling*. Middlefield: Zygo Corporation, 2001.

[5] Seely, J. H. and R. C. Chu. *Heat Transfer in Microelectronic Equipment – A Practical Guide*. New York: Marcel Dekker, Inc. 1972.

[6] Kladitis, Paul. Class handout, EENG 636, Microelectromechanical Systems. Graduate School of Engineering and Management, Air Force Institute of Technology, Wright-Patterson AFB OH, January 2005.

[7] Kovacs, Gregory T. A. *Micromachined Transducers Sourcebook.* Boston: The McGraw Hill Company, 1998.

[8] Sinclair, Michael J. "A High Force Low Area MEMS Thermal Actuator," *The Seventh Intersociety Conference on Thermal and Thermomechanical Phenomena in Electronic Systems*. Volume 1, 127-132. IEEE Press, 2000.

[9] Comtois, John Henry. *Structures and Techniques for Implementing and Packaging Complex, Large Scale Microelectromechanical Systems Using Foundry Fabrication Processes.* Air Force Institute of Technology (AU), Wright-Patterson AFB OH, May 1996 (ADA310747).

[10] Reid, James R. *Microelectromechanical Isolation of Acoustic Wave Resonators*. Air Force Institute of Technology (AU), Wright-Patterson AFB OH, November 1996 (ADA321364).

[11] Reid, James R. "Force Measurements of Polysilicon Thermal Micro-Actuators," *Proceedings of the SPIE - The International Society for Optical Engineering*. Volume 2882: 296-306 (October 1996).

[12] Park, J. S., L. L. Chu, E. Siwapornsathain, A. D. Oliver, and Y. B. Gianchandani. "Long Throw and Rotary Output Electro-Thermal Actuators Based on Bent-Beam Suspensions," *Proceedings of the Thirteenth Annual International Conference on Micro Electro Mechanical Systems*. 680 – 685. IEEE Press, 2000.

[13] Kolesar, Edward S. and others. "In-Plane Tip Deflection and Force Achieved With Asymmetrical Polysilicon Electrothermal Microactuators," *Thin Solid Films*. Volume 377-378, 719-726 (December 2000).

[14] Comtois, John H., Victor M. Bright, and Mark W. Phipps. "Thermal Microactuators for Surface-Micromachining Processes," *Proceedings of SPIE - The International Society for Optical Engineering*. Volume 2642: 10-21 (October 1995).

[15] Que, L., J.-S. Park, and Y. B. Gianchandani. "Bent-Beam Electro-Thermal Actuators for High Force Applications," *Proceedings of the IEEE Micro Electro Mechanical Systems (MEMS)*. 31-36. IEEE Press, 1999.

[16] Comtois, John H., M. Adrian Michalicek, and Carole Craig Barron. "Characterization of Electrothermal Actuators and Arrays Fabricated in a Four-Level, Planarized Surface-Micromachined Polycrystalline Silicon Process." *Proceedings of the 1997 International Conference on Solid-State Sensors and Actuators*. Volume 2, 769 – 772. IEEE Press, 1997.

[17] Szabo, Francis R. *Demonstrating Optothermal Actuators for an Autonomous MEMS Microrobot*. MS Thesis, AFIT/GE/ENG/04-23. School of Engineering and Management, Air Force Institute of Technology (AU), Wright-Patterson AFB OH, March 2004 (ADA426469).

[18] Sinclair, Michael J. and Kerwin Wang. "Thermal Actuator Improvements: Tapering and Folding," *Proceedings of the SPIE - The International Society for Optical Engineering*. Volume 5116: 237-251 (April 2003).

[19] Srikar, V. T. and Stephen D. Senturia. "Thermoelastic Damping in Fine-Grained Polysilicon Flexural Beam Resonators," *Journal of Microelectromechanical Systems*. Volume 11, No. 5, 499-504. IEEE Press, 2002.

[20] National Aeronautics and Space Administration. *MEMS Reliability Assurance Guidelines for Space Applications*. Ed. Brian Stark. JPL Publication 99-1. Pasadena: Jet Propulsion Laboratory, January 1999.

[21] Simon, Andrew L. and David A. Ross. *Principles of Statics and Strength of Materials*. Dubuque: Wm. C. Brown Company Publishers, 1983.

[22] Sharpe Jr., W. N., K. Jackson, G. Coles, and D. A. LaVan. "Young's Modulus and Fracture Strength of Three Polysilicons," *Proceedings of Materials Science of Microelectromechanical Systems (MEMS) Devices III*. Volume 657: 551-556. Materials Research Society, 2001.

[23] Sundararajan, Sriram and Bharat Bhushana. "Static Friction and Surface Roughness Studies of Surface Micromachined Electrostatic Micromotors Using an Atomic Force Friction/Force Microscope," *Journal of Vacuum Science and Technology*. Volume 19(4), 1777-1785 (July-August 2001).

[24] Sternheim, Morton M. and Joseph W. Kane. *General Physics* (2nd Edition). New York: John Wiley and Sons, 1991.

[25] Lumbantobing, Ari and Kyriakos Komvopoulos. "Static Friction in Polysilicon Surface Micromachines," *Journal of Microelectromechanical Systems*. Volume 14, Issue 4, 651-663 (August 2005).

[26] MIL-HDBK-757(AR). "*Fuzes*." Military Handbook. 15 April 1994.

[27] MIL-STD-1316E. "*Safety Criteria For Fuze Design.*" Department of Defense Design Criteria Standard. 10 July 1998.

5. Experimental Procedure and Results

In an effort to determine the overall effectiveness of the conceptual MEMS interrupter mechanism designed for this research effort, several individual aspects of the complete device were examined in an attempt to quantify their performance characteristics. These test results will provide valuable insight into the feasibility of using this device as an interrupter in a solid-state slapper detonator. The devices used in most of these tests were fabricated in PolyMUMPs run #68, with the only exception being some of the process test structures, which were designed in both run #68 and run #69. (Appendix C shows all the design layouts produced as part of this research.)

To begin, the structures used to determine the limits of the PolyMUMPs fabrication process will be examined, along with the impact of those results on the design of the interrupter mechanism. Next, the experiments performed on the stand-alone bent-beam electrothermal actuators will be discussed and some measured performance data will be presented. Finally, the complete interrupter mechanism will be investigated to determine if it is capable of operating as intended. In addition, some measured data from these tests will be presented in order to quantify its performance.

5.1 PolyMUMPs Fabrication Process Test Structures

Since the limits of the fabrication process can vary slightly between each run, several test structures were designed with the goal of determining the minimum tolerances for device width and device spacing. These features are relevant to the design of the interrupter mechanism and knowing these specific limits can help determine if any

design flexibility exists. For example, the minimum line width for both Poly1 and Poly2 is listed by the PolyMUMPs design rules to be 3 μm [1]. If it can be determined that narrower line widths are possible, it may enable more effective actuators to be designed, since it is desirable for the width of the expanding arms, in a bent-beam actuator, to be as small as possible in order to maximize bending near the anchors [2]. Figure 5-1 shows the fabricated width test structures, for both Poly1 and Poly2. It can be readily observed that the 1-μm wide beam is the minimum beam width that could be fabricated in this run. Nevertheless, notice that a larger width would most likely be required for any practical device, since the 1-μm wide beams do not appear to be very structurally sound. In addition, notice that the 0.5-μm wide beam could not be fabricated at all in this fabrication run, as evident by the material left behind in the anchor etch holes. The specific structures in Figure 5-1 are from run #69, and the test structures in run #68 produced similar results, however, this does not guarantee that every fabrication run will produce the same results.
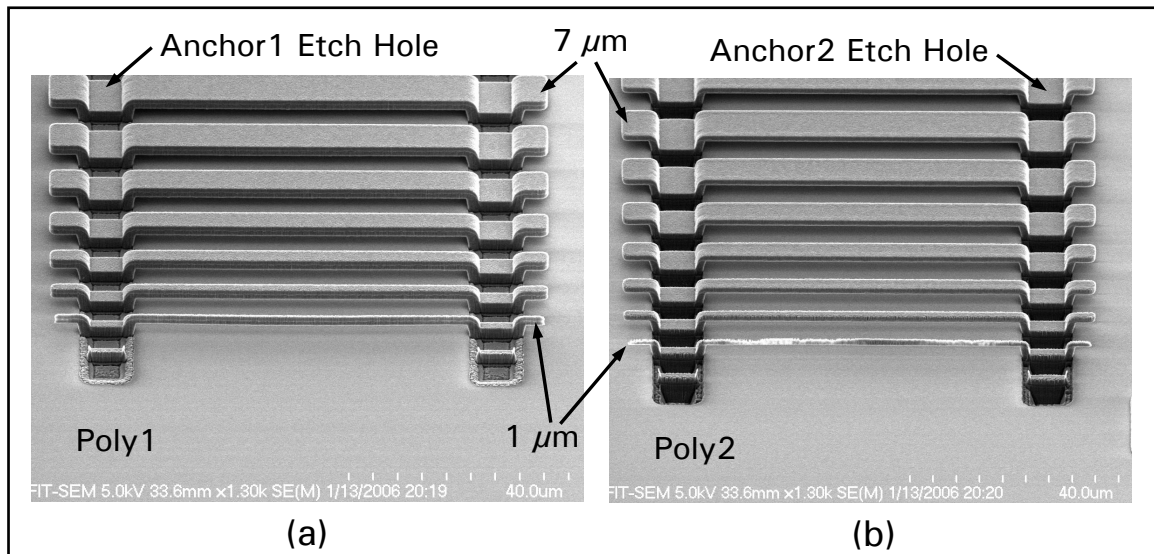
Figure 5-1. SEM images of width test structures showing that a minimum beam width of 1 μm survived the fabrication process for both (a) the Poly1 beam, and (b) the Poly2 beam. However, the Poly2 beam does not look to have very much structural rigidity.

Another process feature that is relevant to the design of the interrupter mechanism is the minimum spacing between similar layers. The minimum spacing is important because it ultimately determines the initial "closed" area of the interrupter aperture. For instance, the 2 μm separation selected for the interrupter plates designed in this thesis is what causes the 4-μm^2 open area when the interrupter aperture is closed, as discussed in section 4.5.1. If the minimum spacing could be reduced to 1 μm, the resulting "closed" area would decrease significantly to 1 μm^2. However, if the reduced spacing exceeded the capability of the fabrication process, the two interrupter plates could become permanently connected and would inhibit separation upon actuation. Figure 5-2 and Figure 5-3 shows the spacing test structures from both PolyMUMPs fabrication run #68 and #69, respectively. Clearly, the 2 μm spacing gap is successfully fabricated in both process runs. In addition, the 1 μm spacing gap, shown in Figure 5-3, should obviously be avoided.

A final fabrication process test that was performed as part of this research was the validation of the layer thickness data provided by MUMPs$^{®}$. Since this thickness is known to vary for each fabrication, several measurements were taken of various structures fabricated in run #68 to see how they compare with the data provided by the MUMPs$^{®}$ foundry (see Appendix B). Furthermore, since the results of the actuator force tests are dependent on the actual thickness of the force measuring beams, precise layer thickness data is critical to producing accurate results. Additionally, the output force of the bent-beam actuator depends on the expanding thicknesses.
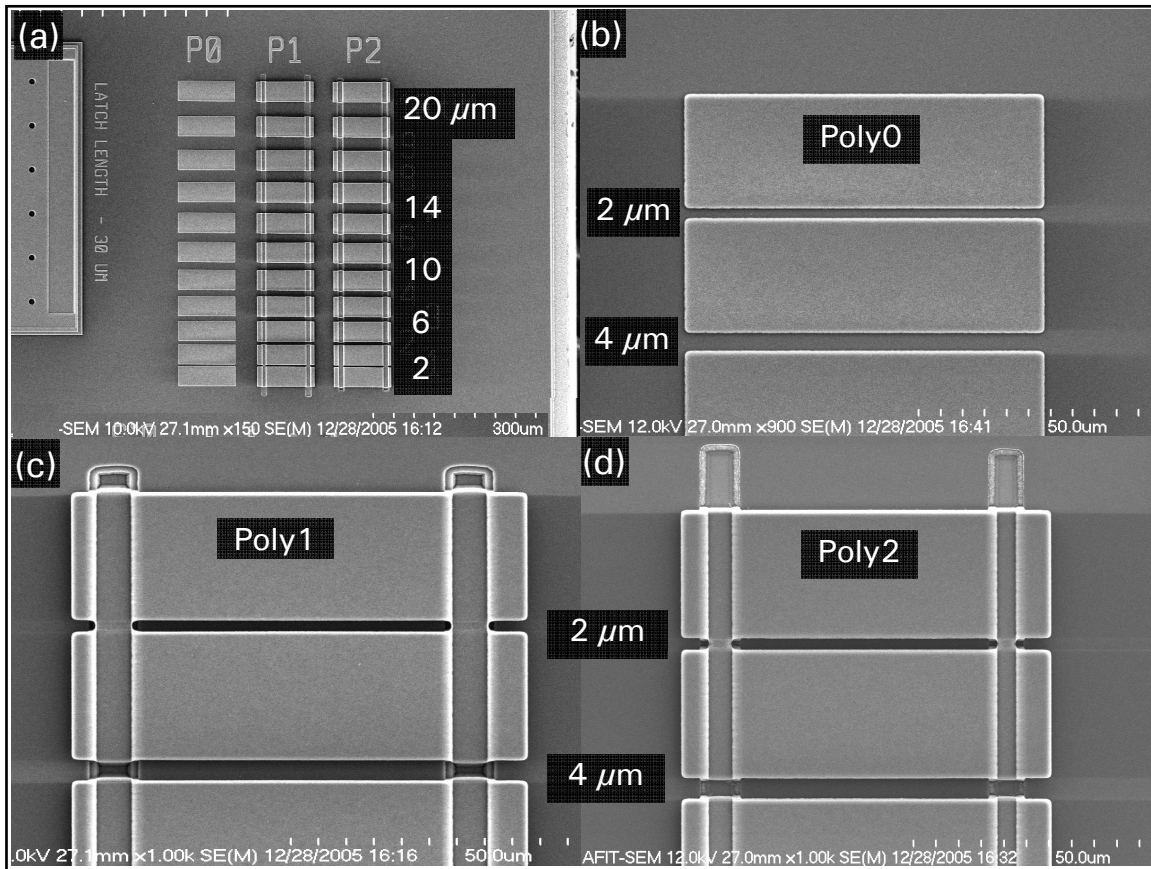
Figure 5-2. SEM images of the spacing test results for fabrication run #68: (a) Image of all three polysilicon layers with associated gap measurements, (b) Image of the Poly0 layer, (c) Image of the Poly1 layer, and (d) Image of the Poly2 layer. Note: the minimum spacing of 2 μm could clearly be fabricated in this process run.

The optical profiler shown in Figure 4-5 was used to measure the vertical dimensions of the width test structures, the force measuring beams, and the expanding arms of the bent-beam actuator. To determine the thicknesses for each structure, approximately five to ten measurements were taken, then averaged to produce the measured thickness values shown in Table 5-1. An example of a measurement being taken with the optical profiler is shown in Figure 5-4. This example shows the spacing test structures being used to obtain a *single* measurement of the Poly0 thickness. All the other thickness measurements were taken in a similar manner.
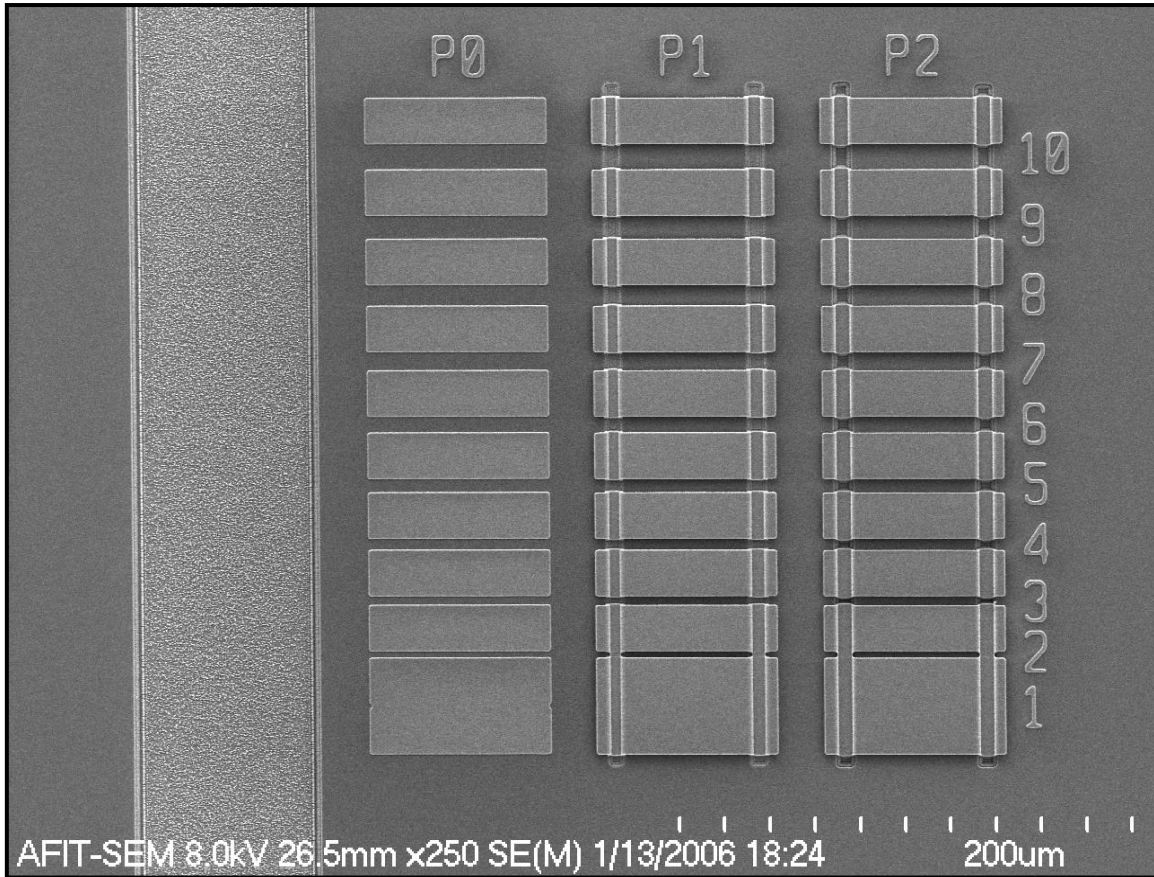
Figure 5-3. SEM image of the spacing test results for run #69 that includes the polysilicon layers – Poly0 (P0), Poly1 (P1), and Poly2 (P2). The numbers to the right represent the spacing between the two adjacent structures, in µm. Again, the 2 µm spacing is the minimum spacing gap that could be fabricated in this run. Clearly, the 1 µm spacing could not be fabricated in this process.

Table 5-1. Comparison between the average thicknesses measured for several fabricated structures and the thickness data provided by MUMPs® for run #68 [3].

	Poly0 (µm)	Poly1 Beam (Ox1 + P1)* (µm)	Poly2 Beam (Ox1 + Ox2 + P2)* (µm)	Force Beam (Ox1 + P1 + P2)* (µm)	Actuator Arm (Ox1 + P1 + P2)* (µm)
Measured Thickness	0.5446	3.8275	3.7108	5.1124	5.1538
Std. Dev.	0.0021	0.0239	0.0162	0.033	0.0116
Run Data	0.4999	3.9732	4.1997	5.4337	5.4337
Percent Difference	8.55	3.73	12.36	6.09	5.29

* Ox1 – Oxide1; Ox2 – Oxide2; P1 – Poly1; P2 – Poly2

5-5

Figure 5-4. Optical profiler measurement to determine the thickness of the deposited polysilicon layer (Poly0). Note: the value shown is for only one measurement, and the reported values in Table 5-1 shows the average thickness values based on multiple measurements.

For the Poly1 and Poly2 fixed-fixed beams, measurements were taken at both the center and outer ends of the beams and the thickness values shown in Table 5-1 come from an average of both of these measurements. Differences between the vertical measurements taken from these two beam locations averaged 34 nm and 23 nm for both the Poly1 and Poly2, respectively. This is most likely due to the beam centers being slightly bowed up as a result of the compressive residual stress in both materials. In addition, since every structure, except Poly0, is a releasable structure, the thickness of the sacrificial oxide layer was accounted for in the run data values. The layer names that make up each releasable structure are also noted in Table 5-1.

The comparison between the measured thickness values and the values from the MUMPs® run data shows percent differences typically less than 10%. (The Poly2 beam was the only exception.) In addition, the measured values for the releasable layers are all slightly lower than the MUMPs® values. A possible cause for the lower measured values is that these structures are fabricated through a series of deposition and etch steps, which define the structure's final dimensions. Hence, the underlying materials tend to experience more etches than the higher layers, which causes them to be unexpectedly thinned [1]. This may also explain the relatively larger error in the Poly2 beam since it uses the most sacrificial layers (Oxide1 and Oxide2) in its fabrication. Because these measurements did not directly measure the individual Poly1 and Poly2 thicknesses, some uncertainty exists in the measured results. As a result, the thickness from the MUMPs® run data is used in Equation (4.7) to calculate the force of the bent-beam actuators.

5.2   Bent-Beam Electrothermal Actuator Experiments

In order to better understand the performance characteristics of the complete interrupter mechanism, a series of stand-alone bent-beam actuators were fabricated .and tested to determine how they would perform on an individual basis. (The design layouts, for the specific actuators tested, are shown in Appendix C as Die #12 and Die #13.) The data gathered from these stand-alone tests should allow for a more complete analysis of the interrupter mechanism. For example, examining the input power required for each actuator to produce a given deflection can help determine which actuator is the most efficient. In addition, the output force of each actuator can be measured and compared with the power-deflection measurements to identify if one particular design is preferred over another. Recall, three different sets of bent-beam actuators were fabricated for the

interrupter mechanisms, and the design parameters chosen for each are summarized in Table 4-2.

5.2.1   Electrothermal Actuator Deflection Experiment

After performing the release procedures outlined in Appendix A, the individual bent-beam electrothermal actuators were tested on a Micromanipulator probe station. A specific set of actuators were designed to quantify the deflection characteristics of each type of actuator listed in Table 4-2. Moreover, a 400 μm × 12 *tapered* arm actuator configuration was also fabricated and tested, along with those listed in Table 4-2, in order to provide completeness. This additional actuator had the same design parameters as the Interrupter #2 actuator, except for the tapered arms. The electrical connection to the actuators was accomplished by placing two microprobes (tip radius of 0.5 μm) on the gold probe pads incorporated into the anchors. Figure 5-5 shows one side of two 400 μm × 8 arm (straight and tapered) actuators prior to testing. This figure points out various elements that make up each actuator, such as the gold probe pads, the fabricated Poly0 scale used to measure deflection, and the tapered versus straight arm designs. The 400 μm × 12 arm actuators (not shown) are the same in every way except they have 12 arms instead of the eight shown in Figure 5-5.

To obtain the individual deflection characteristics for each actuator listed in Table 4-2, at least six identical actuators (from three different die) were tested. The only exception was for the 400 μm × 8 tapered arm actuator, where a total of nine identical actuators were tested. Hence, a total of 27 bent-beam electrothermal actuators were used to measure the deflection characteristics.
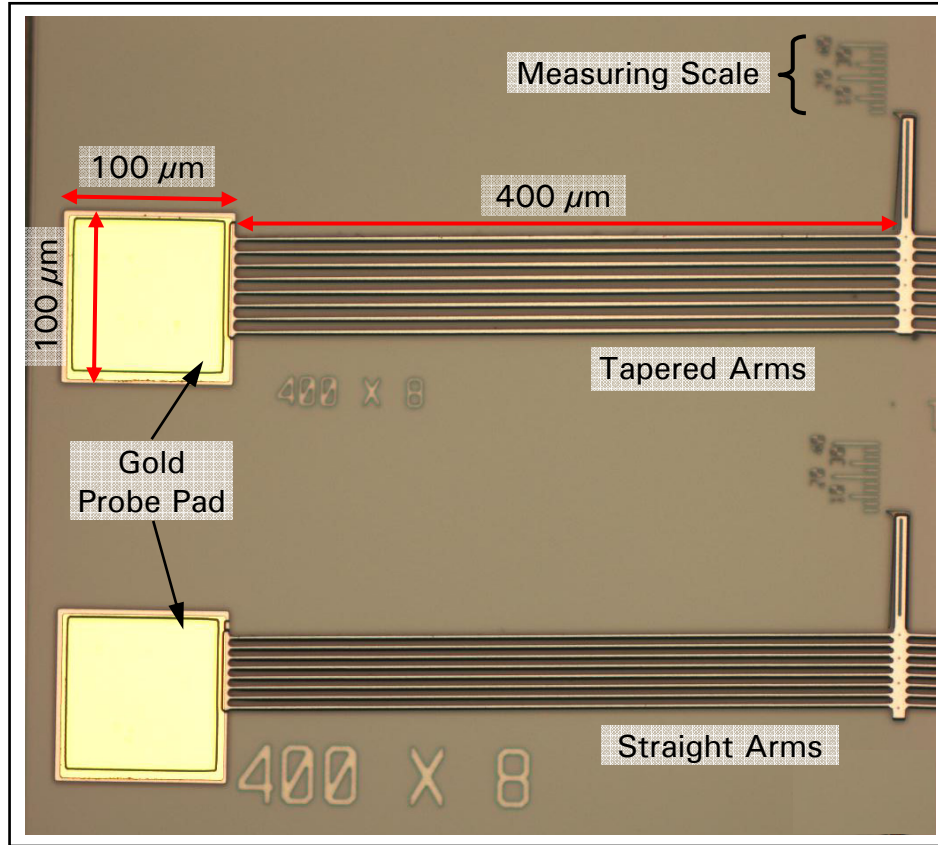
Figure 5-5. 20X magnification image of 400 µm × 8 arm (straight and tapered) electrothermal actuators. Note: the tapered arms are visibly thicker in the center of the arms than the straight arms.

To get a better understanding of the power requirements for the different actuators, the resistance of each actuator was measured and analyzed using an Agilent 34401A digital multimeter. Figure 5-6 shows the averaged resistance obtained from these measurements, with the error bars indicating one standard deviation. As shown, the actuators with 12 arms have a lower resistance than those with 8 arms.

To quantify this relationship, recognize that each expanding arm has a resistance given by [4]:

$$R = \frac{\rho \cdot l}{t \cdot w} \quad (\Omega) \tag{5.1}$$

where

$$\rho = resistivity \ of \ polysilicon \quad (\Omega\text{-}\mu m)$$
$$l = total \ length \ of \ the \ arms \quad (\mu m)$$
$$t = thickness \ of \ the \ arms \quad (\mu m)$$
$$w = width \ of \ the \ arms \quad (\mu m)$$

Since each arm is designed to be the same length, thickness and width, they will all have the same resistance, R, as described by Equation (5.1).

Next, the entire actuator (neglecting the coupling beam) was modeled as a circuit consisting of parallel and series resistors that depend on the number of arm pairs, N, designed for the bent-beam actuator. The N-armed bent-beam actuator is shown in Figure 5-7(a). Subsequently, the actuator model can be reduced to a single resistive circuit with an equivalent resistance, R_a, as shown in Figure 5-7(b) and described by:

$$R_a = \frac{2 \cdot R}{N} \quad (\Omega) \tag{5.2}$$

where

$$N = number \ of \ arm \ pairs \quad (Dimensionless)$$
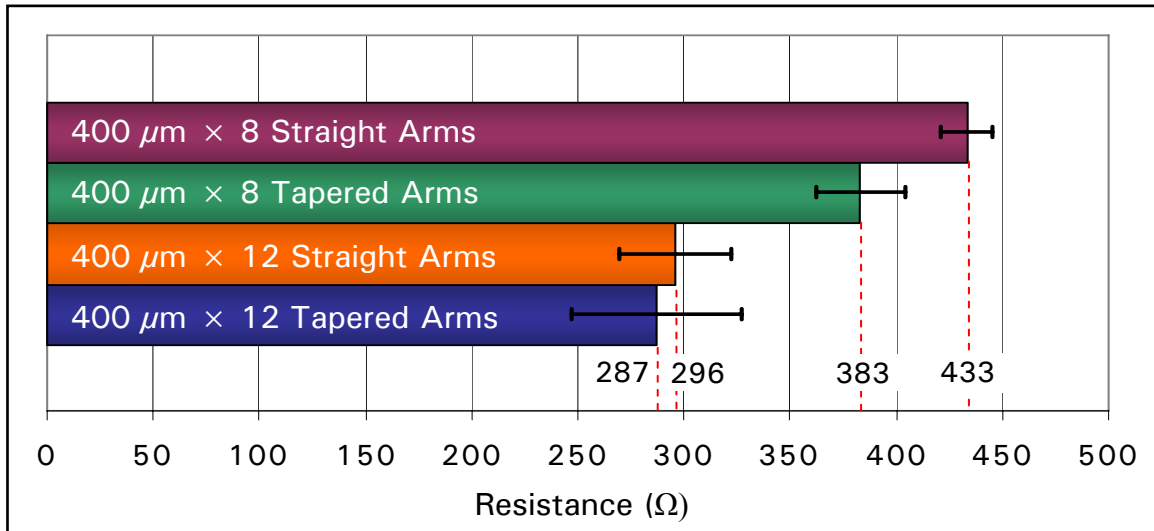
Figure 5-6. Measured resistance of the bent-beam electrothermal actuators. The error bars indicate one standard deviation from the mean.
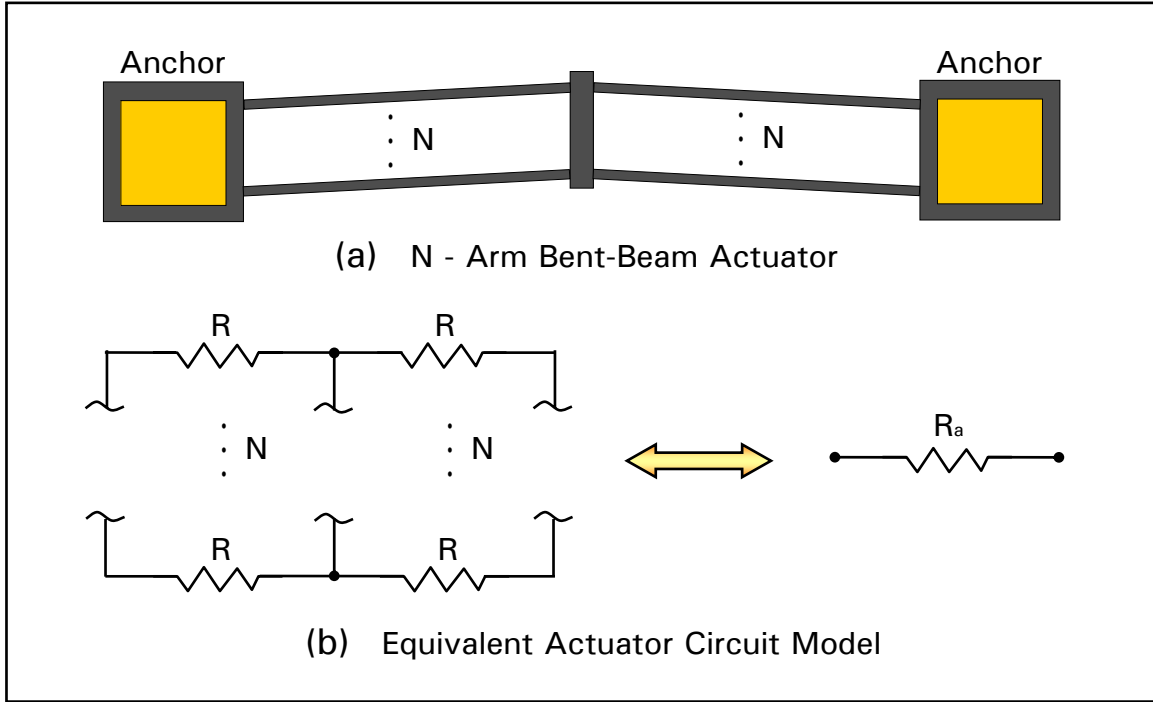
Figure 5-7. (a) Bent-beam electrothermal actuator with N arms. (b) Equivalent circuit model of the N-arm actuator showing its reduction into a single resistive element with an equivalent resistance, R_a, as described by Equation (5.2).

As a result of the relationship shown in Equation (5.2), an increase in the number of arms, N, will have the anticipated result of decreasing the resistance of the entire actuator, as was observed in Figure 5-6. Furthermore, it is expected that a decrease in resistance will cause a given deflection to require a larger input power, since more current will be needed to induce the same thermal expansion in the arms.

Figure 5-6 also shows that the actuators with tapered arms have a smaller resistance when compared to their counterparts with the same number of arm pairs. From Equation (5.2) this is also an expected result, since the resistance is inversely proportional to width. Without going into the details of width as a function of arm length, it can be intuitively appreciated that the width in the center of the tapered beams will be greater

than the width in the center of the straight beams, thus the resistance will decrease accordingly as shown in Figure 5-6.

To measure the deflection of the actuators as a function of input power, an Agilent 3631A DC power supply was used to step the input voltage from 0 V to 25 V (in one volt increments) and measure the current at each voltage step. Still images were captured for each voltage step using an Optronics DEI-750 microscope camera and ATI video capturing software. To determine the deflection of the actuator, the location of the actuator tip versus the fabricated Poly0 measuring scale was recorded (to an uncertainty of ± 0.5 μm) for each voltage step by observing the captured still images. This process was repeated for each of the 27 actuators and the data was tabulated and analyzed to produce the results shown in Figure 5-8 and Figure 5-9.

Figure 5-8 shows the measured deflection as a function of input power for the 400 μm × 8 tapered arm electrothermal actuator. The error bars indicate one standard deviation away from the average deflection at each particular voltage step. These results are based on measurements from nine different actuators that were fabricated on three different die. The intention of this figure is to show that repeatable results were obtained from this testing method. Thus, this testing method was repeated for each of the other 18 actuators, with similar precision being obtained.

Figure 5-9 shows the average deflection as a function of input power for all four bent-beam electrothermal actuators tested as part of this thesis. It can be seen that for a given input power, the 400 μm × 8 straight arm actuator produced the largest deflection. This is consistent with the tests performed by Szabo, which were summarized in Table 4-1. Moreover, the actuators with 8 arms also produced a greater deflection for a given
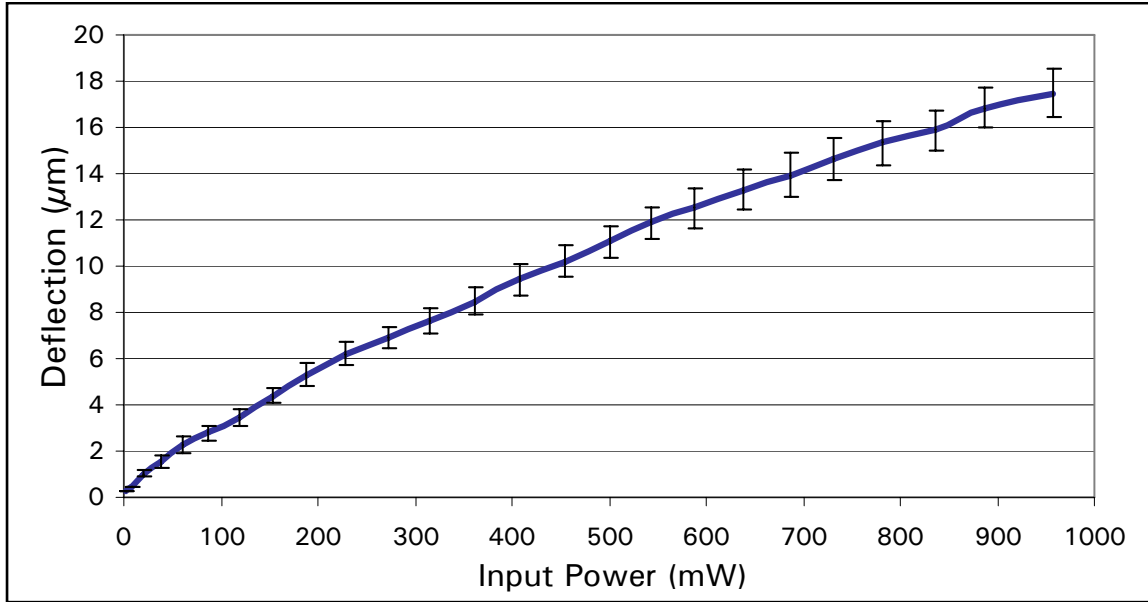
Figure 5-8. Average deflection as a function of input power for nine 400 μm × 8 tapered arm electrothermal actuators. The error bars indicate one standard deviation from the average deflection for each voltage step measured.

input power over those with 12 arms. Finally, when comparing the actuators with the same number of arms and input power, the actuators with tapered arms produced less deflection than those with straight arms. Therefore, it is easy to conclude that to produce the largest deflection with the smallest input power, a 400 μm × 8 straight arm actuator, would be preferred over a 400 μm × 8 tapered arm actuator, or a 400 μm × 12 arm actuator (either straight or tapered). Furthermore, a performance-to-energy analysis can be performed by comparing the deflection-to-power ratio at each voltage step for all four actuators. Figure 5-10 shows this comparison, and it is clear that the 400 μm × 8 straight arm actuator does indeed have advantages over the other actuators, if low power performance is required. In conclusion, the bent-beam actuators designed for the interrupter mechanism should be able to produce an aperture area of approximately 1300 μm², based on Equation (4.8) and an actuator deflection of 17 μm, as shown in Figure 5-9.
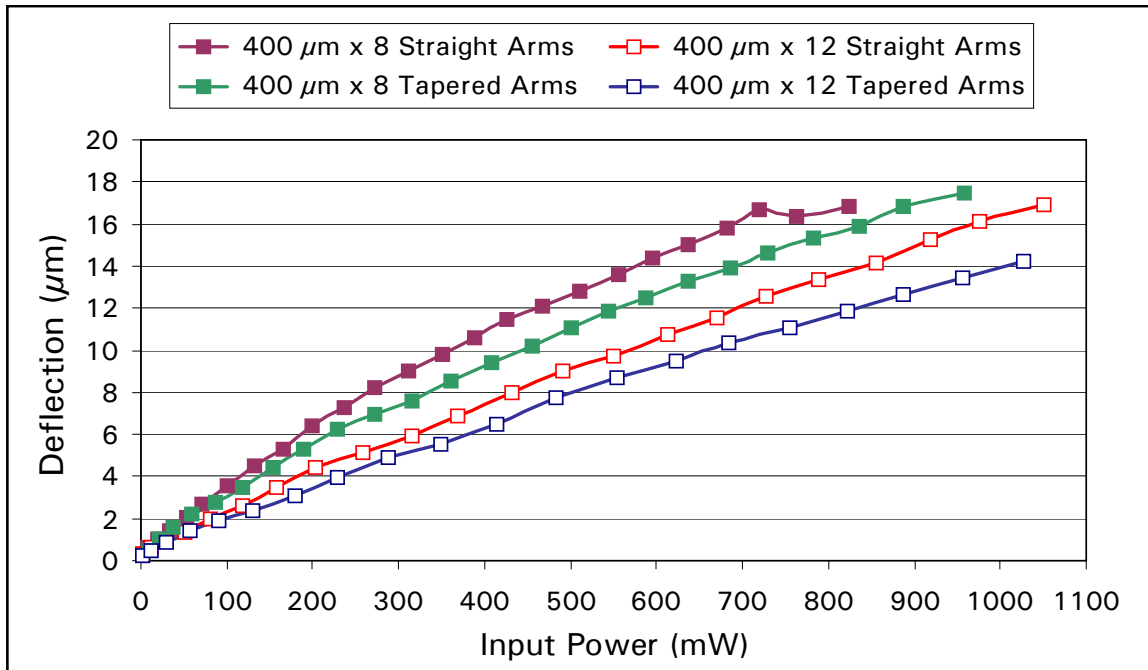
Figure 5-9. Average deflection as a function of input power for all four different bent-beam electrothermal actuators. For a given input power, the 400 μm × 8 straight arm actuator produced the largest deflection. Moreover, the actuators with 8 arms also produced a greater deflection for a given input power over those with 12 arms. Lastly, the tapered actuators produced less deflection than their straight armed counterparts.
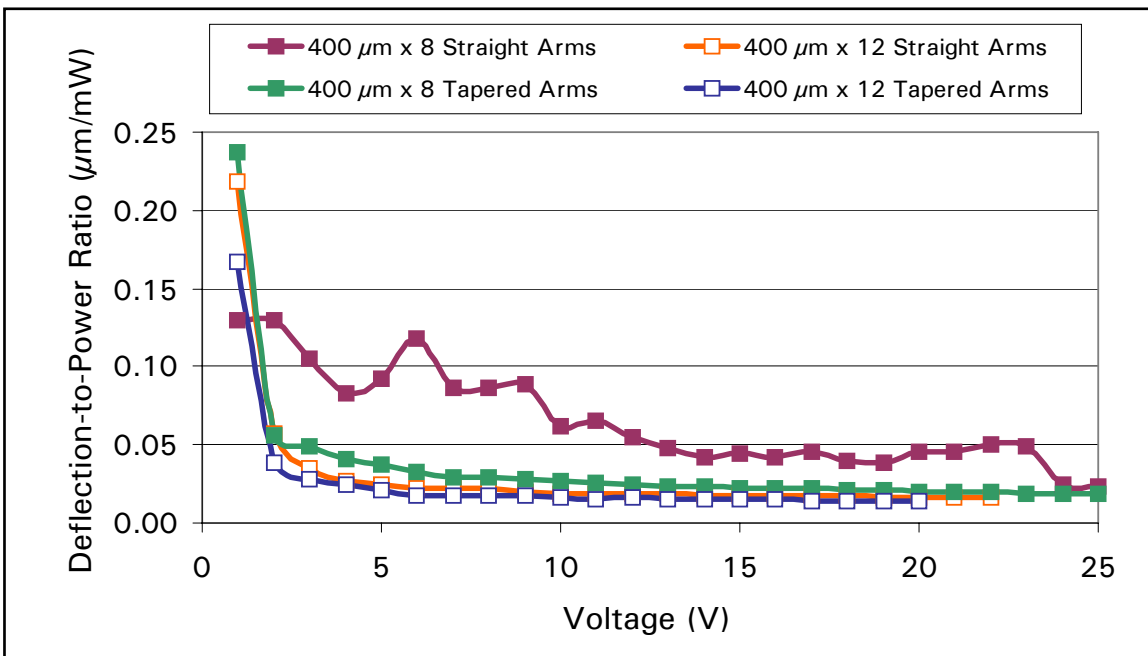
Figure 5-10. Performance-to-energy comparison between all four bent-beam electrothermal actuators. The deflection-to-power ratio at each voltage step is compared to show that the 400 μm × 8 straight arm actuator does indeed have advantages, over the other actuators, if low power performance is desired.

5-14

5.2.2 Electrothermal Actuator Force Experiment

In order to determine the output force for each type of bent-beam actuator, a set of three actuators (for each type) were fabricated adjacent to force measuring cantilever beams, as described in section 4.4.2. The cantilever beams for each set of actuators were designed for three different lengths: 100 µm, 200 µm, and 300 µm. Figure 5-11 shows one set of actuators (400 µm × 8 straight arms) with the three fabricated force measuring cantilever beams. In addition, for each cantilever beam length, three individual actuators of the same type (albeit from different die) were tested resulting in a total of nine actuators being tested for each type of actuator. Hence, a total of 36 bent-beam electrothermal actuators were tested to produce the force characteristics presented below.
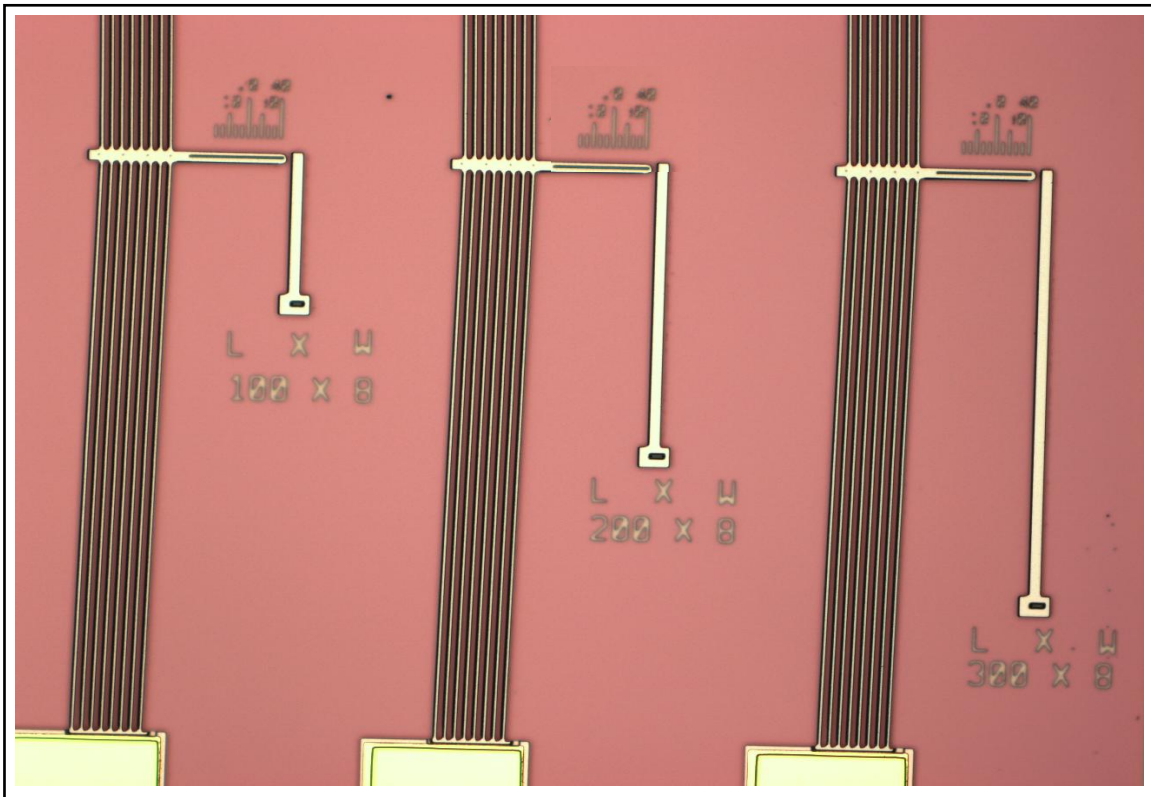
Figure 5-11. One set of bent-beam electrothermal actuators (400 µm × 8 straight arms) designed adjacent to the force measuring cantilever beams of three different lengths: 100 µm, 200 µm, and 300 µm.

To measure the force as a function of input power, each actuator was placed on the Micromanipulator probe station and connected to the Agilent 3631A DC power supply in the same manner described in section 5.2.1. The actuator was driven by stepping an applied voltage from 0 V to 25 V, in one volt increments, while simultaneously measuring the current for each voltage step. In a similar manner to that described for the deflection measurements, still images of each voltage step were captured with the microscope's video equipment. Next, the maximum deflection was determined (to an uncertainty of ± 0.5 μm) by examining the still images and observing how far the cantilever beam moved before the actuator was no longer able to bend the beam. Figure 5-12 shows an example of the still images used to measure the maximum deflection data. This deflection value was recorded three times for each actuator type, and each cantilever beam length, until the entire batch of 36 force measuring actuators were tested.
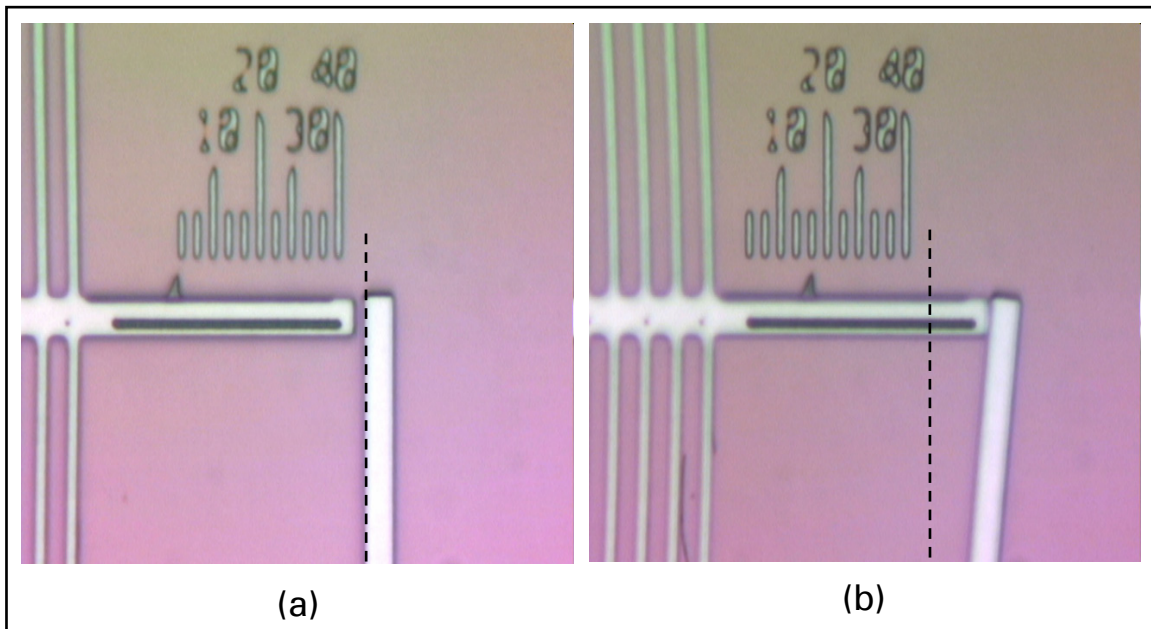
Figure 5-12. (a) Image of the 400 μm × 8 tapered arm actuator at 0 V. (b) Image of the same actuator at 23 V and a maximum cantilever beam deflection of 11 μm. Note: the dashed lines represent the initial beam location.

It is important to note that the maximum deflection of the cantilever beam is not the maximum deflection of the actuator, because the actuator and cantilever beam are initially separated by a 2.5 µm gap. This gap is intended to satisfy the design rules to ensure the two separate structures are not inadvertently fabricated as one structure. Figure 5-13 shows an SEM image of a 400 µm × 8 straight arm actuator with a 100 µm cantilever beam. The inset shows a magnified view of the 2.5 µm gap.

Equation (4.7) is used to calculate the output force, yet a few other cantilever beam parameters (thickness, width, and length) must be known. The thickness of the
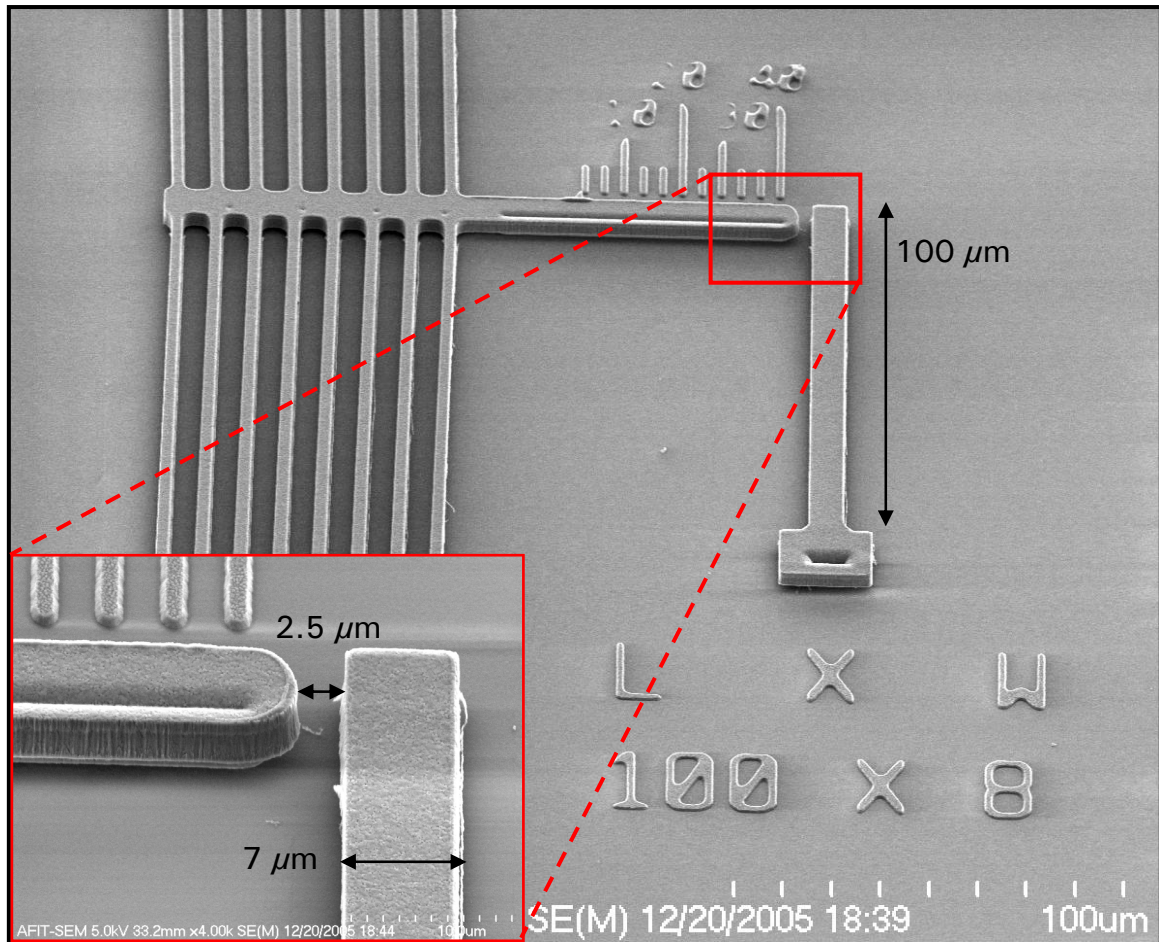
Figure 5-13. SEM image of a 400 µm × 8 straight arm actuator with a 100 µm force measuring cantilever beam. The inset shows the 2.5 µm gap that must be accounted for in determining the maximum deflection of the cantilever beam, along with the measured width of the beam.

beam is taken from the PolyMUMPs run data provided in Appendix B, which is 3.4527 μm for the stacked (Poly1 + Poly2) beam. The width of the beam was designed to be 8 μm; however measurements taken in the SEM indicated that the fabricated width is 7 μm ± 0.25 μm. The lengths of the beams were designed to be either 100 μm, 200 μm, or 300 μm, and since multiple measurements of these lengths produced very little deviation from the exact designed lengths, no adjustments were made to the designed values. Finally, a Young's modulus of 158 GPa [5] was used for the polysilicon cantilever beam.

The maximum beam deflection, d_{max}, used in calculating the output force, comes from the average (measured) maximum deflection produced by each actuator type, for each cantilever beam length. Consequently, three different measurements are used to evaluate the value for the average maximum beam deflection. Table 5-2 summarizes the results of the force measuring tests, to include, the average maximum deflection used to calculate the output force in Equation (4.7), the standard deviation produced by these three measured values, and finally, the calculated output force for each actuator type.

For every actuator type (except the 400 μm × 8 straight arm actuator) the calculated output force is reasonably consistent whenever either the 100 μm or 200 μm cantilever beams are used to determine the maximum deflection values. In contrast, the 300 μm beam consistently results in a significantly lower output force for all actuator types (by approximately 50%) when compared to the other two cantilever beam lengths. The most likely cause for this is that the maximum deflection of the 300 μm beam exceeds the maximum deflection capability of the actuator. By examining the graph of Equation (4.7) shown in Figure 4-17, and assuming the other calculated output forces are correct, it can be seen that the maximum deflection for the 300 μm beam occurs at

approximately 19 μm for the 8 armed actuators and approximately 24 μm for those with 12 arms. Clearly, none of the actuator types were capable of deflecting 24 μm, and 19 μm was just above the deflection limit for the unloaded actuators, as shown in Figure 5-9. As a result, the force produced by the 300 μm beam was considered to be invalid, and only the results from the 100 μm and 200 μm cantilever beams were considered valid.

Table 5-2. Summary of the data collected from the bent-beam actuator force measurement tests to include, the average maximum beam deflection (based on three actuators of each type), the standard deviation, and the calculated output force. Note: the calculated force for the 300 μm beam is considered invalid because the required maximum beam deflection exceeds the maximum deflection capability of the actuator.

Actuator Type		Cantilever Beam Length (μm)		
		100	200	300
400 μm × 8 Arm [Straight]	Ave. Max. Beam Deflection (μm) (Std Dev)	0.67 (0.14)	11.00 (2.65)	13.17 (1.15)
	Calculated Force (μN)	**31.19**	**64.32**	**22.81**
400 μm × 8 Arm [Tapered]	Ave. Max. Beam Deflection (μm) (Std Dev)	1.00 (0.00)	8.33 (2.31)	15.0 (1.73)
	Calculated Force (μN)	**46.78**	**48.73**	**25.99**
400 μm × 12 Arm [Straight]	Ave. Max. Beam Deflection (μm) (Std Dev)	1.25 (0.25)	10.75 (1.06)	12.50 (0.50)
	Calculated Force (μN)	**58.47**	**62.86**	**21.66**
400 μm × 12 Arm [Tapered]	Ave. Max. Beam Deflection (μm) (Std Dev)	1.42 (0.14)	10.33 (4.16)	15.83 (0.29)
	Calculated Force (μN)	**66.27**	**60.42**	**27.43**

Figure 5-14 graphically shows the average output force for each type of bent-beam electrothermal actuator, along with one standard deviation from the calculated average. These averages are based on the two force data points (for the 100 µm and 200 µm cantilever beams only) provided in Table 5-2. The standard deviations provide some confidence that the force tests produced valid results for each type of actuator, except the 400 µm × 8 straight arm actuator. This actuator has an extremely large standard deviation due to the large difference between the two maximum beam deflections (100 µm and 200 µm beams only). This suggests the existence of a random error in one, or both, of these measurements. To determine the true output force for this actuator would require additional testing.

Another possible error source is the cantilever beam width used for calculating the output force. The value of 7 µm for the beam width was determined from measurements taken in the SEM, however this method produced an uncertainty of ± 0.25 µm. Thus, the width variable in Equation (4.7) can range from 6.75 µm to 7.25 µm. Since the calculated force is dependent on the cube of the width, any small variations in this
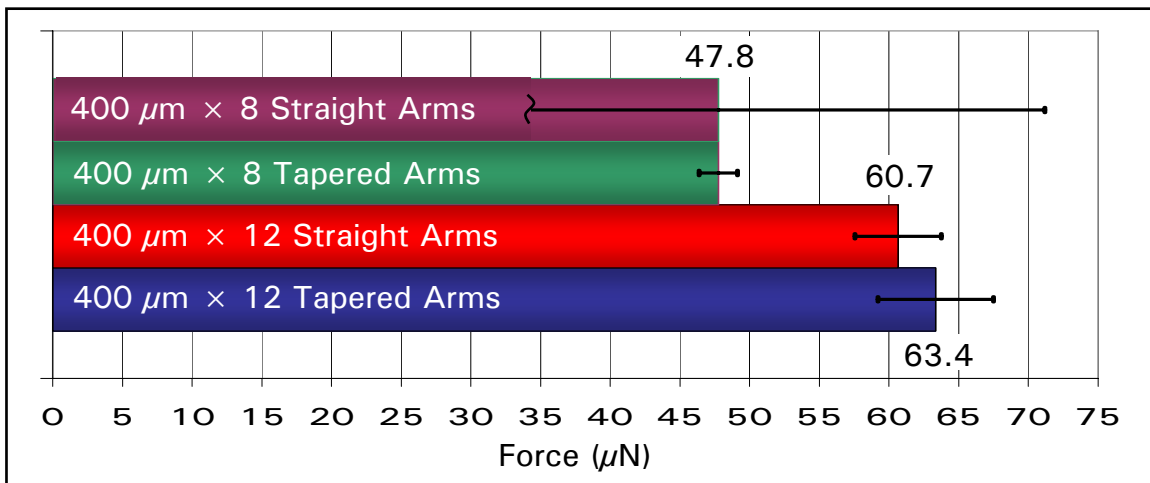
Figure 5-14. Average output force for each type of bent-beam electrothermal actuator, along with one standard deviation from the calculated averages based on the two force data points (for the 100 µm and 200 µm cantilever beams) provided in Table 5-2.

measurement may produce a significant error. For example, the widths of 6.75 μm and 7.25 μm correspond to force measurements of 43.7 μN and 54.1 μN, respectively, when using the data for the 400 μm × 8 tapered arm actuator. In addition, note the uncertainty in the beam lengths is not as significant, since even an uncertainty of ± 2 μm does not have a large effect on the calculated forces. For example, considering a 200 μm ± 2 μm range in beam lengths, the corresponding change in calculated force would be 50.2 μN and 47.3 μN, respectively.

Nevertheless, Figure 5-14 does clearly show a higher output force being produced by the 12 armed actuators than the 8 armed actuators, as suggested by the bent-beam actuator theory discussed in Section 4.3.3. Moreover, the micro-newton forces produced by the bent-beam actuators are significantly higher than the required nano-newton forces shown in Table 4-3. To conclude, the bent-beam actuators designed for the interrupter mechanism should have plenty of force to separate the interrupter plates and provide an aperture for the flyer material to pass through.

5.3   Interrupter Mechanism Tests

The final test in this research effort was to determine the operating characteristics of the fabricated MEMS S&A interrupter device, which was first presented in Section 4.2 and shown in Figure 4-6. Recall that this device has two main functions: 1) to impede the path of the flyer material in a solid-state slapper, thus preventing inadvertent initiation of an explosive train, and 2) to create an unimpeded path for flyer material so it can impact the HE pellet and initiate an explosive train. Assuming the first function is satisfied by the initial "closed" position of the four interrupter plates (shown in Figure 4-18); only the second function needs to be demonstrated. Since the interrupter plates are attached to the

end of the bent-beam electrothermal actuators, an experiment was designed to simultaneously power the individual actuators, which will cause the interrupter plates to move linearly outward, thus creating an open area for the flyer material to pass through.

The design layouts for the specific interrupter mechanisms tested are shown in Appendix C as Die #11 (Interrupter #1), Die #14 (Interrupter #2), and Die #15 (Interrupter #3). In addition, Table 4-2 shows the type of bent-beam actuators incorporated into each of these three interrupter mechanisms. Prior to testing each fabricated die, the release procedures, outlined in Appendix A, were accomplished. In addition, the same equipment described previously for the stand-alone actuator tests was again used to perform the following experiments and capture the results. Specifically, this equipment was the Micromanipulator probe station, the Agilent DC power supply and digital multimeter, the Optronics microscope camera, and the ATI video capturing software.

In order to supply power to all the actuators at the same time, five microprobes were used to facilitate the electrical connections. The initial intention was to power the device using only two microprobes and the fabricated Metal and Poly0 wires shown in Figure 4-6. However, upon initial testing it was determined that the much higher resistance (by two orders of magnitude) of the Poly0 wires, as compared to the Metal wires, made this approach impossible to implement. Therefore, it was concluded that the best alternative approach was to connect five microprobes to the actuators of the interrupter mechanism as shown in Figure 5-15. Figure 5-15(a) shows a simplified circuit model for the interrupter mechanism and Figure 5-15(b) shows an actual image of an interrupter mechanism with five microprobes connected to the four 400 μm × 12

straight arm actuators. Since the Metal wires offered a resistance of approximately 2 - 10 Ω, they worked well for supplying the input voltage to each actuator.

Furthermore, the four parallel resisters shown in Figure 5-15(a) can be reduced into a single resistive value for the complete interrupter mechanism. Figure 5-16 shows

(a)

(b)
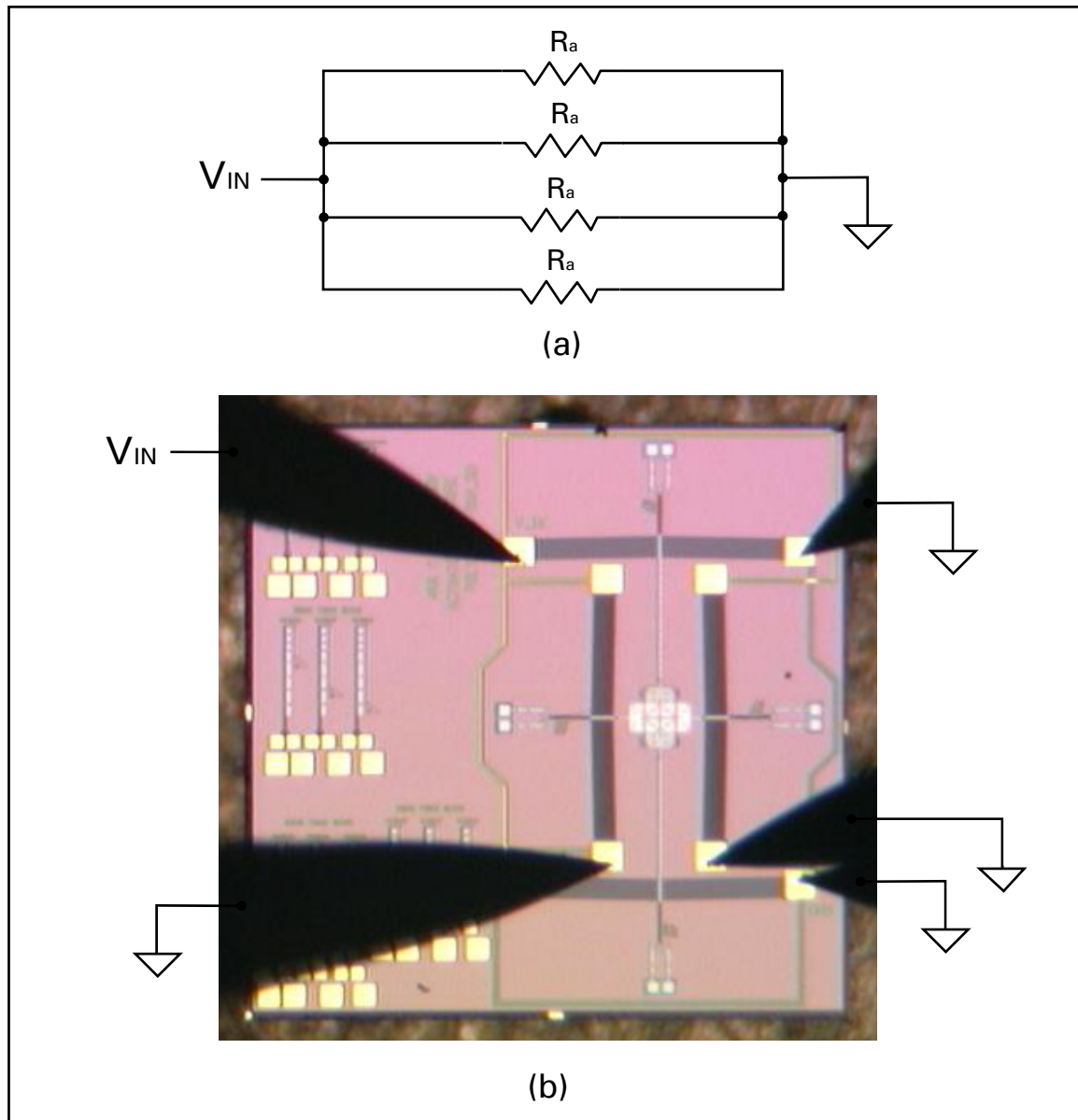
Figure 5-15. (a) Equivalent circuit model for the interrupter mechanism, where R_a is given by the actuators' resistance values shown in Figure 4-6. (b) Image of actual interrupter mechanism (just prior to activation) showing how the electrical circuit was connected. Note: this image is from Die #14, which uses four 400 μm $\times$ 12 straight arm actuators.

the resistance values for all three of the fabricated interrupter mechanisms, along with the standard deviation based on measurements of at least three separate devices. These results are similar to those observed with the individual actuators. For instance, the interrupter mechanisms with 12 arm actuators have a lower resistance than those with 8 arms, and the interrupters with tapered arm actuators produce a lower resistance over the ones with straight arms.

Based on these resistance results, it is expected that the interrupter mechanisms fabricated with the 400 μm × 8 straight arm actuators will have the lowest operating power. Figure 5-17 shows the measured power requirements for each interrupter mechanism. As can be observed, the interrupter with the 400 μm × 8 straight arm actuators does indeed have a lower operating power for a given applied voltage. In
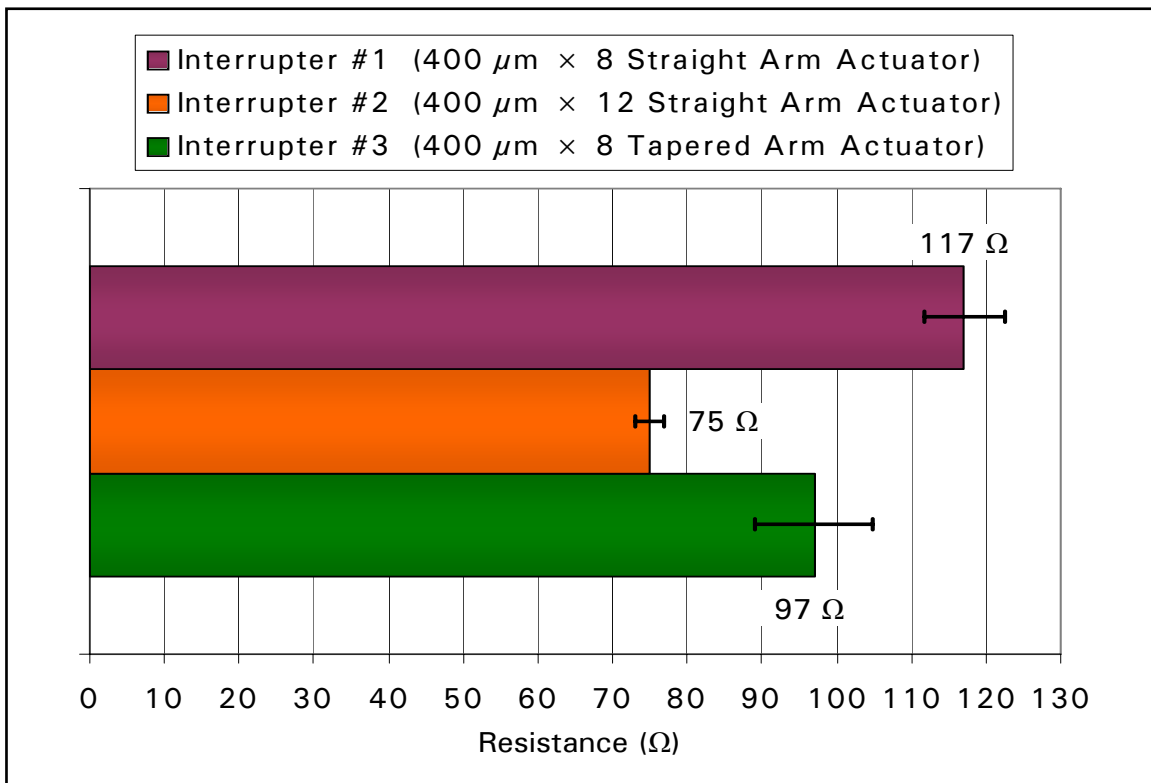
Figure 5-16. Measure resistance values for the complete interrupter mechanism, along with the standard deviation based on measurements of at least three separate devices.
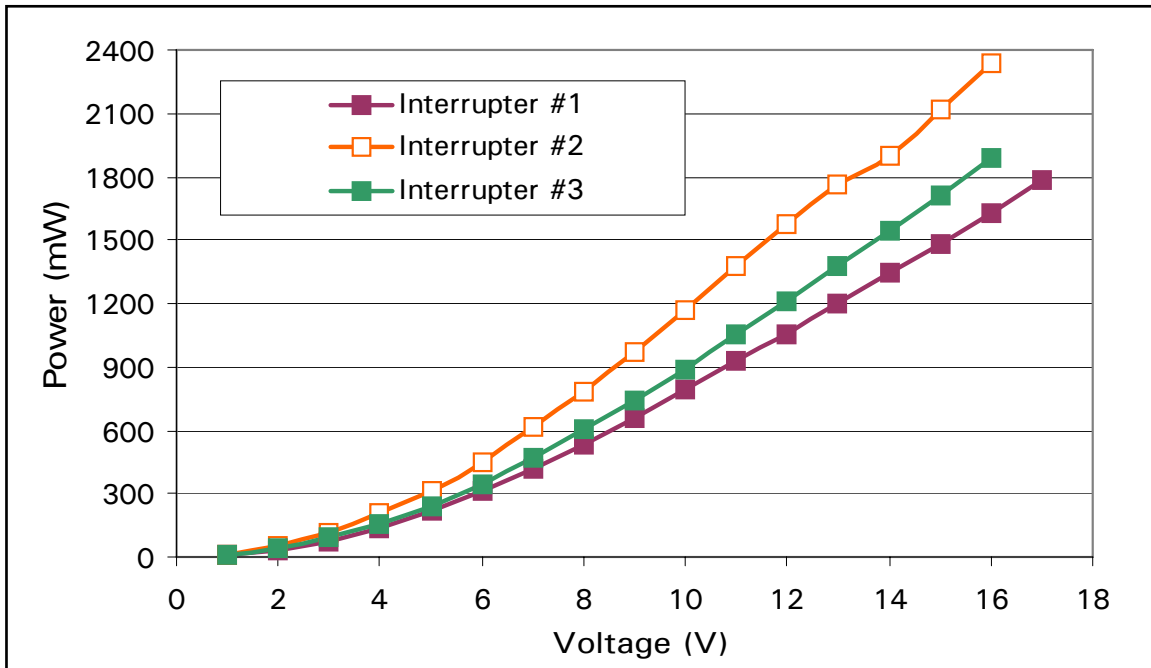
Figure 5-17. Input power as a function of the applied voltage for each interrupter mechanism. Consistent with the results seen in Section 5.2.1, the interrupter mechanism with the 400 μm × 8 straight armed actuators has the lowest power requirements.

addition, Figure 5-17 shows that the maximum operating voltage of these interrupter mechanisms is approximately 16-17 V. Higher applied voltages tended to result in at least one of the actuators suffering a catastrophic thermal failure.

Finally, to show functionality of the interrupter mechanism, the DC power supply was used to step the input voltage from 0 V to 15 V. This maximum voltage was selected to prevent thermal failure of any actuator and to ensure that repeatable device operation could be shown. Still images were captured for each voltage step using the video capturing equipment and the area of the aperture was estimated by comparing the distance between dimples and etch holes fabricated on the interrupter plates. In addition, deflection was measured using the Poly0 measuring scales fabricated alongside the latching arm extension, and these measurements were used to confirm the opened area estimations made by observing features on the interrupter plates.

The objective for these interrupter mechanism experiments was to demonstrate simultaneous actuation of the four independent interrupter plates, thus creating an opened area in the otherwise closed interrupter mechanism. Figure 5-18 shows an example of this objective being met for Interrupter #3 at four different voltages ranging from 0 V to 15 V. Clearly, the still images of this MEMS interrupter mechanism successfully demonstrates the four interrupter plates independently moving linearly outward to produce an aperture. By comparing the distances between features on the interrupter plates, the dimensions of the maximum opened area can be estimated to be approximately 32 μm × 32 μm. This implies that the maximum deflection attained by the four parallel bent-beam actuators is only 15 μm, which is about 88% of the maximum deflection (17 μm) observed in Figure 5-9. Therefore, an aperture area of approximately 1024 μm^2 was produced, as opposed to the 1300 μm^2 that would have resulted for a 17 μm actuator deflection, as suggested in Section 5.2.1.

This same experiment was performed repeatedly with Interrupters #1, #2, and #3, with similar results being observed for all three interrupter mechanisms, i.e., no perceivable differences in performance were discerned. Therefore, the only comparisons that could be made between the three interrupter mechanisms are based on the individual actuator performance discussed above.

Figure 5-19 and Figure 5-20 show the operation of Interrupter #1 (20X magnification) and Interrupter #2 (10X magnification), respectively. Both images show the interrupter mechanism at 0 V and at 15 V. Observe the expansion of the bent-beam actuator arms, which causes deflection and separation of the interrupter plates, in Figure 5-19(b) and Figure 5-20(b), respectively.
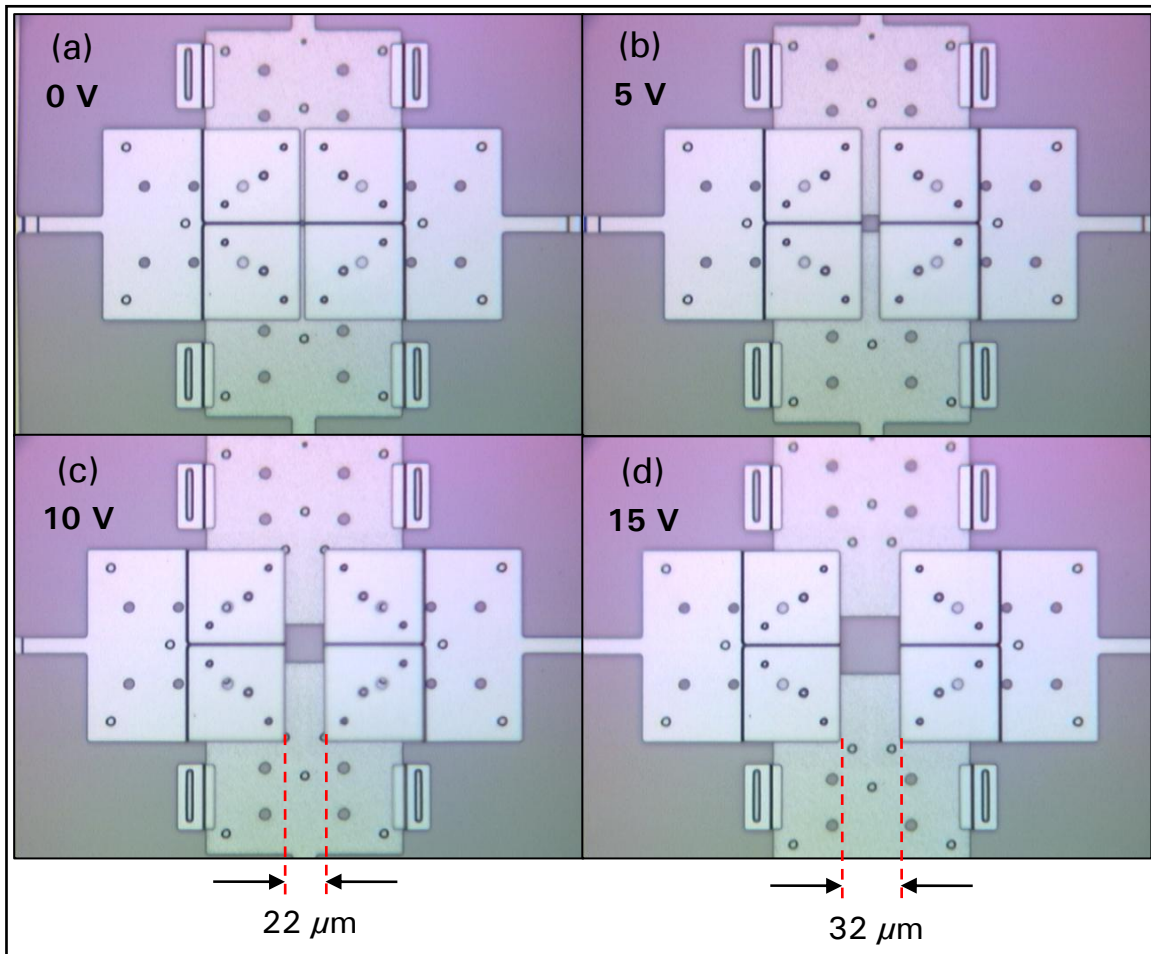
Figure 5-18. Operation of a MEMS interrupter mechanism at 50X magnification. This sequence of images shows Interrupter #3 at: (a) 0 V, (b) 5 V, (c) 10 V, and (b) 15 V.
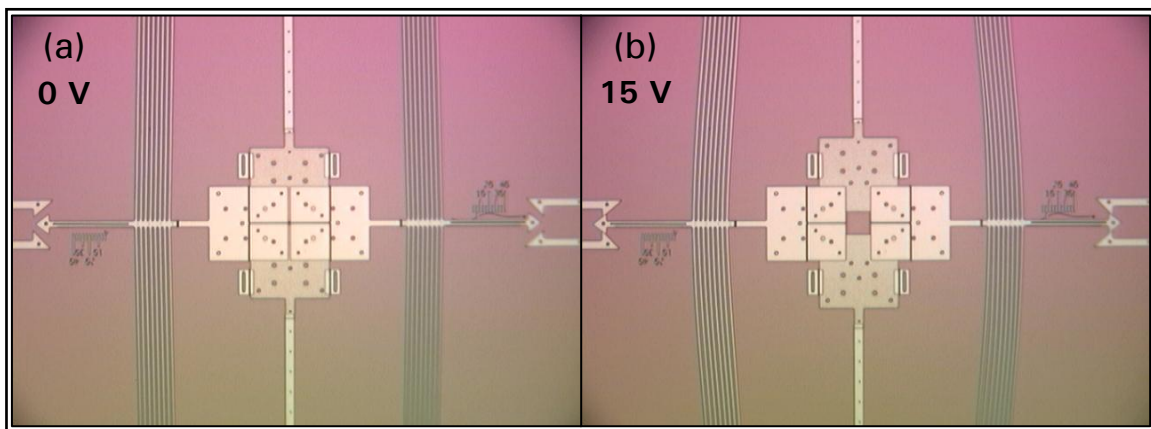
Figure 5-19. Operation of Interrupter #1 at: (a) 0 V, and (b) 15 V. These images show center of interrupter mechanism at 20X magnification. Note: the expansion of the bent-beam actuator arms is visible in (b).
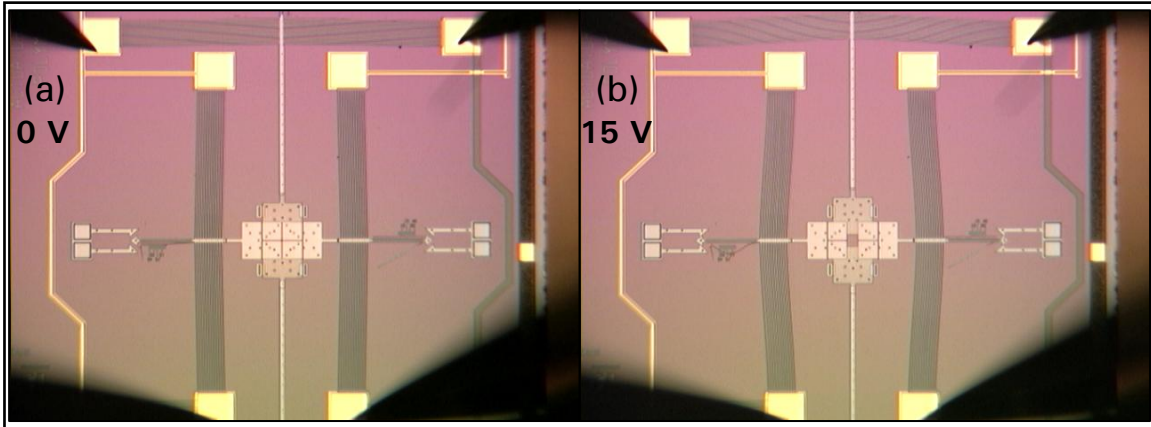
Figure 5-20. Operation of Interrupter #2 at: (a) 0 V, and (b) 15 V. These images show center of interrupter mechanism at 10X magnification. Again, note the expansion of the bent-beam actuator arms in (b).

An examination of the latching arm extension of the interrupter mechanism, and the Poly0 measuring scale, revealed that the actuators were limited to 15 μm deflection by the inability of the actuators to force open the fixed component of the latching mechanism. Figure 5-21 shows an actuator at this maximum deflection point. Notice the measuring scale indicates a deflection of approximately 15 μm, which confirms the estimated deflection that was based on the features of the opened interrupter plates.

A quick analysis of the fixed latching component, using Equation (4.7), shows that approximately 900 μN of force would be required to move one of the 11-μm wide by 100-μm long beams the 5 μm distance necessary to enable latching. This required force is one order of magnitude greater than the lateral output force produced by the bent-beam actuators, as shown in Table 5-2. Therefore, in order to produce the necessary 5 μm deflection of the fixed latching components, the beam widths need to be decreased to approximately 3 - 4 μm, which would result in a required actuator force of approximately 18 - 43 μN, respectively. Clearly, this range of required output forces is within the

capabilities of the actuators tested in this research effort. The design layout shown in Figure 5-22 indicates the designed dimensions for the latching mechanism.
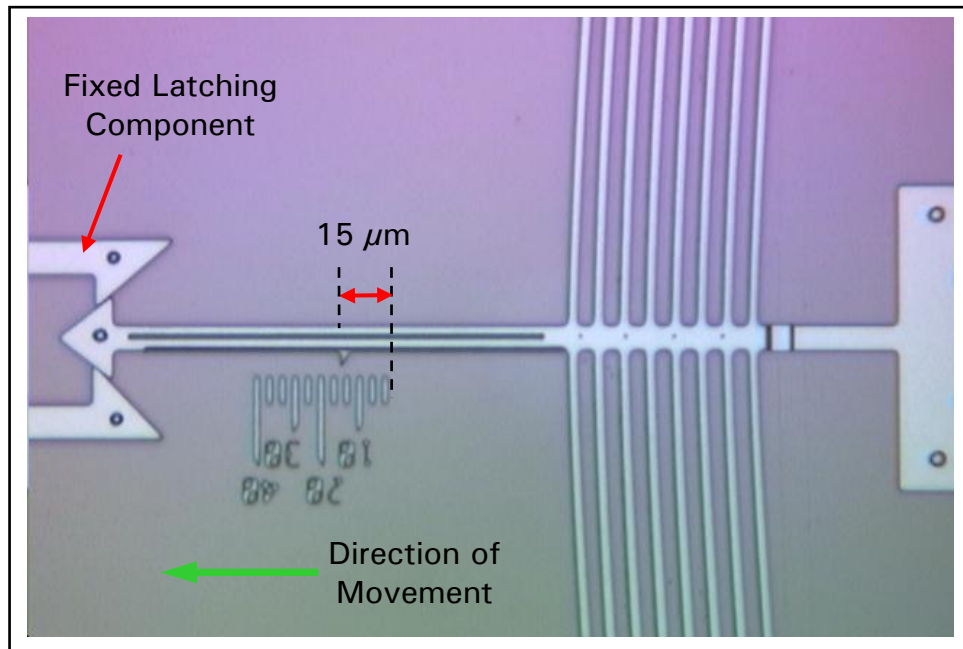
Figure 5-21. Maximum actuator deflection shown at 50X magnification. The inability of the actuator to move the fixed latching components limits the maximum deflection of each actuator to approximately 15 μm.
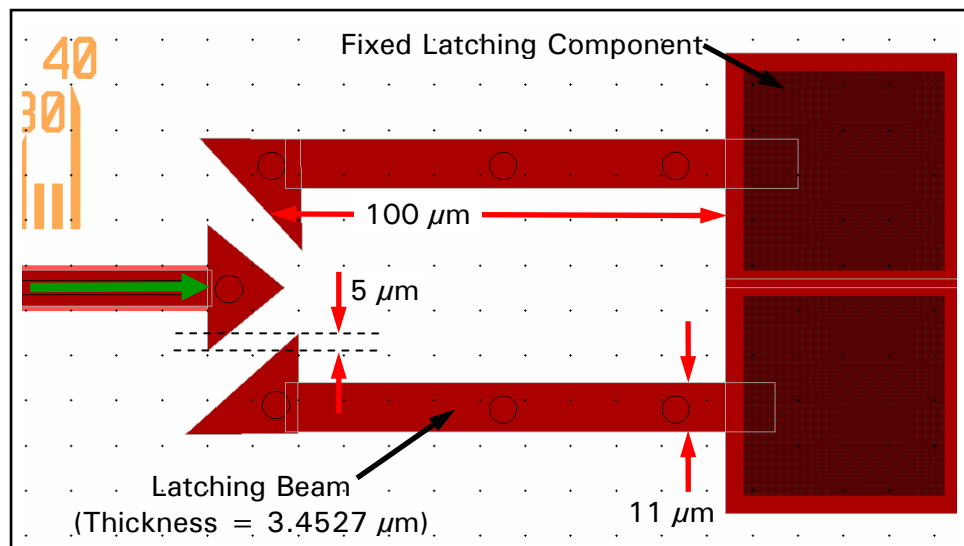
Figure 5-22. Design layout of latching components for interrupter mechanism. The latching beams require a force of approximately 900 μN to produce the 5 μm deflection required for latching to occur. This force value is based on the length and width of the designed beam. Note: the latching beam thickness is a result of the stacked Poly1 + Poly design.

5.4   Summary

This chapter presented the test results performed on the fabricated interrupter mechanism and its individual components, in an effort to determine the overall effectiveness of the conceptual MEMS interrupter design. The tests on the PolyMUMPs fabrication process determined that the minimum separation distance between the two interrupter plates should be no closer than 2 µm, thus ensuring that they are not fabricated as one structure. In addition, the performance characteristics of the four individual bent-beam actuators showed that the 400 µm × 8 straight arm actuator performed the best, in terms of its relatively large deflection and low operating power. Even though this actuator produced 20% less force than the 12 armed actuators, the lower operating power makes the 400 µm × 8 straight arm actuator a better choice over the other tested actuators. Finally, the operation of the complete interrupter mechanism demonstrated the feasibility of using this device to create an aperture for the flyer material, in a solid-state slapper detonator, to pass through on its way to initiating a HE pellet.

Bibliography

[1]   Koester, David and others. *PolyMUMPs Design Handbook (Revision 11.0)*.
      MEMSCAP, 2005. August 2005. <http://www.memsrus.com/documents/
      PolyMUMPs.DR.v11.pdf>.

[2]   Sinclair, Michael J. and Kerwin Wang. "Thermal Actuator Improvements: Tapering
      and Folding," *Proceedings of the SPIE - The International Society for Optical
      Engineering*. Volume 5116: 237-251 (April 2003).

[3]   "PolyMUMPs.rundata.xls." *PolyMUMPs Run Data*. <http://www.memsrus.com/
      nc-pmumps.refs.html>.

[4]   Jaeger, Richard C. *Introduction to Microelectronic Fabrication* (2nd Edition). New
      Jersey: Prentice Hall, 2002.

[5]   Sharpe Jr., W. N., K. Jackson, G. Coles, and D. A. LaVan. "Young's Modulus and
      Fracture Strength of Three Polysilicons," *Proceedings of Materials Science of
      Microelectromechanical Systems (MEMS) Devices III*. Volume 657: 551-556.
      Materials Research Society, 2001.

6. Conclusions and Recommendations

The objective of this research effort was to investigate a MEMS-based solution to a problem that has been facing the munitions community in recent years – the aging stockpile of weapon system components (e.g., fuzes and S&A devices). The aging problem is compounded by the decreasing number of weapon component manufacturers over the last 15 years [1]–[3]. Therefore, a practical replenishment program, that considers both old and new weapon systems, is desirable. Since MEMS devices have inherent benefits over their macro-scale counterparts (e.g., significantly lower costs per unit due to their large fabrication volumes), they offer an obvious area to explore for potential exploitation.

The approach taken in this research was to design, fabricate, and test a conceptual interrupter mechanism to determine the feasibility of operating a MEMS device for this purpose. For instance, the designed S&A interrupter device had to have a normally closed configuration (safe), and be capable of forming an opened area (armed) upon activation. This type of device was successfully demonstrated, as described in Chapter 5, and conclusions based on the observed results will be briefly discussed in this chapter. In addition, recommendations for future work will also be discussed.

6.1 Conclusions and Recommendations Based on Experimental Work

Several different aspects of the interrupter mechanism were tested in an effort to better characterize the operation of the complete device. The fabrication process was investigated to understand its limits and determine if any design parameters could be

optimized. The stand-alone actuators were tested to provide a baseline for their performance in order to better characterize the performance of the fabricated interrupter mechanism. Finally, the complete interrupter mechanism was tested to ensure device operation, in addition to collecting performance data.

6.1.1 Fabrication Process

The interrupter mechanisms designed in this research effort were fabricated exclusively in the PolyMUMPs fabrication process. To investigate the limitations of this process, several test structures were fabricated to get an understanding of the process constraints that will effect any future modifications of the existing interrupter mechanism.

First, width test structures (shown in Figure 5-1) were used to investigate the minimum design width for the bent-beam actuator arms, to determine if a narrower arm could be fabricated that could possibly increase deflection for future actuator designs. If more deflection could be produced, then a larger aperture could be created. The results of these tests showed that beams fabricated in the individual polysilicon layers (Poly1 and Poly2) could be fabricated to a 2 μm width, however, these test structures did not consider a 3.5-μm thick (Poly1 + Poly2) beam, which the PolyMUMPs design rules suggest should have a minimum line width of 3.5 μm [4]. Nevertheless, the width of the actuators' arms fabricated in this thesis was 3 μm, and satisfactory performance was observed, however, this does not imply anything about the performance of these actuators over time, nor does it imply that the fabrication process would yield the same results over many runs. A recommendation for future work would be to determine the performance characteristics of bent-beam actuators with arms that are narrower than 3 μm. Figure 6-1 shows an image of a bent-beam electrothermal actuator, with 2.5-μm wide × 3.5-μm
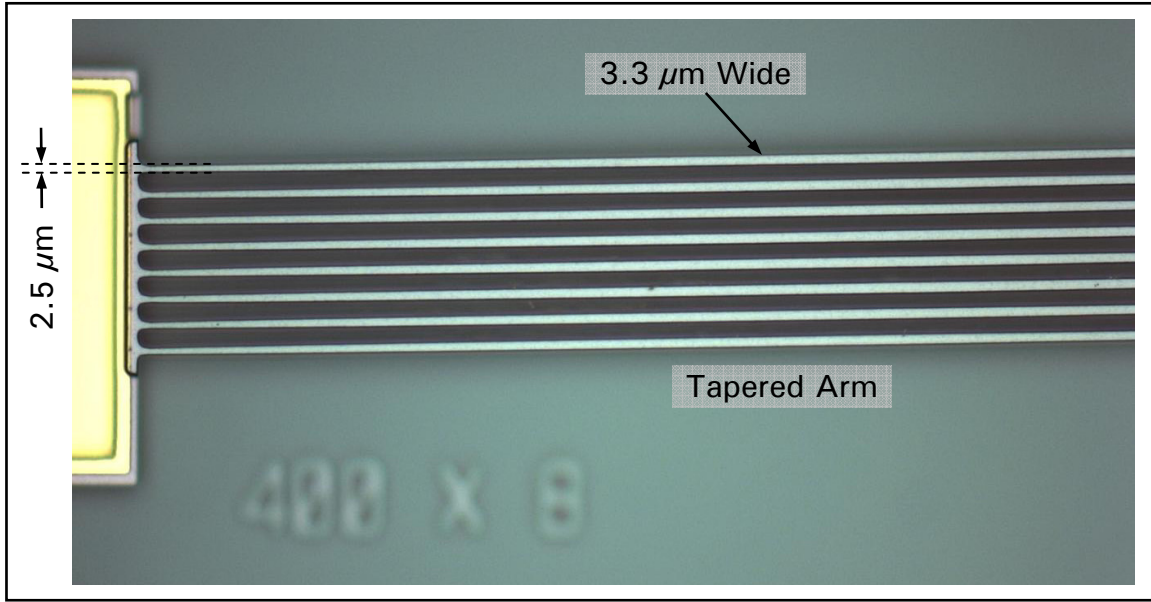
Figure 6-1. Image of a 400 μm × 8 tapered arm electrothermal actuator, fabricated in run #69, shown at 100X magnification. This figure shows that 2.5-μm wide × 3.5-μm thick arms could be fabricated in the PolyMUMPs process.

thick arms at the anchor points, that was fabricated in run #69. These arms appear to be satisfactorily fabricated; however, its operating performance was never examined due to time constraints.

Next, spacing test structures (shown in Figure 5-2 and Figure 5-3) were used to investigate the minimum spacing between two structures of the same material layer. This spacing defines the minimal opened area of the "closed" interrupter, which could be reduced if the spacing could be minimized. The results of the spacing test structures confirm that the designed 2 μm minimum spacing between the similar materials was a suitable choice for the interrupter mechanism fabricated for this research, and that a spacing of 1 μm should be avoided. Therefore, it appears that the minimum *designed* aperture area is 4 μm². However, Figure 6-2 shows an image of the center of a fabricated interrupter mechanism, which indicates that the fabricated spacing is a little larger (by 0.5 μm) than the designed spacing. This resulted in a minimum *fabricated* aperture area of
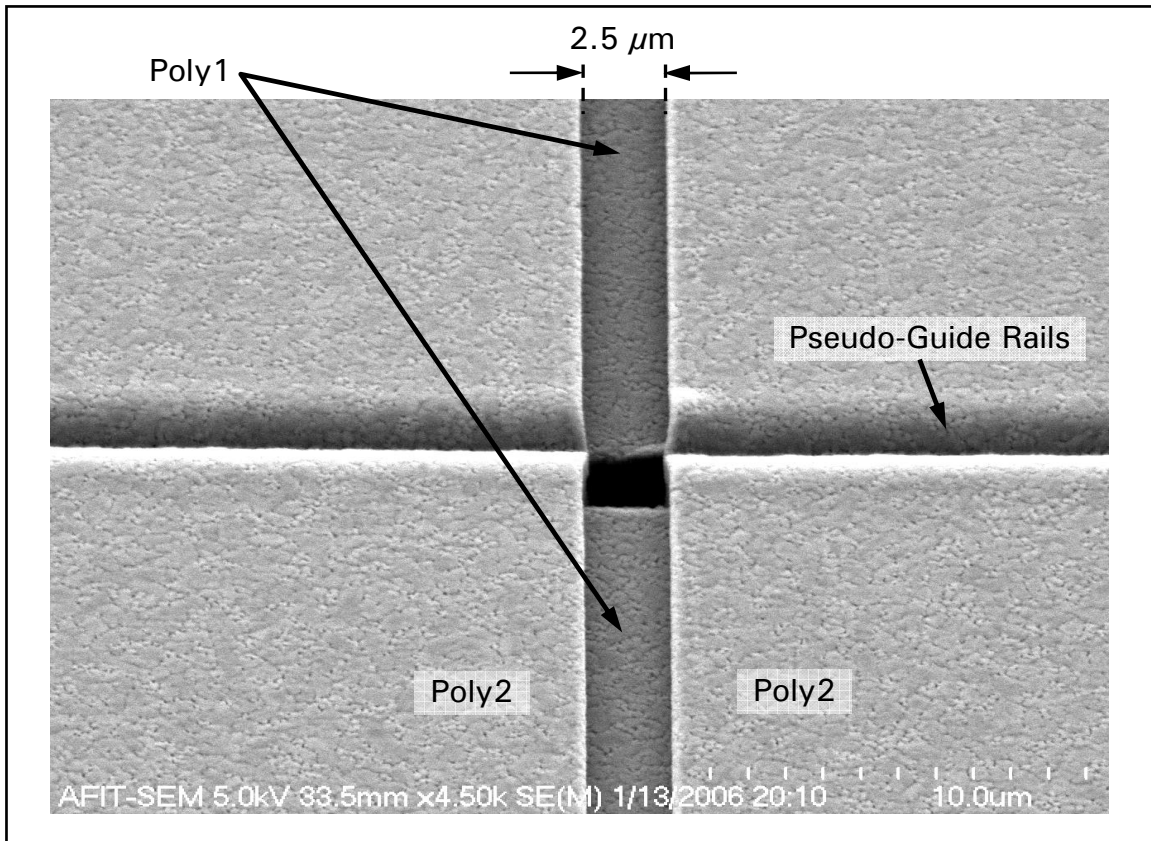
Figure 6-2. SEM image showing interrupter mechanism. The fabricated spacing between the two structures of the same material layer was measured to 2.5 μm (Designed spacing was 2 μm.) This produced a "closed" aperture area of 6.25 μm^2 (Designed to be 4 μm^2.) Note: the pseudo-guide rails that were formed on the Poly2 layer as a result of the spacing between the two Poly1 layers and the conformality of the fabrication process.

6.25 μm^2. Also, note from Figure 6-2, that pseudo-guide rails are formed on the Poly2 layer as a result of the spacing between the two Poly1 layers and the conformality of the fabrication process. It was concluded that these rails may actually help to ensure smooth operation of the interrupter mechanism as power is applied. A recommendation for future work would be to determine if the spacing could be reduced further by designing spacing test structures that have gaps between 1 - 2 μm (e.g., 1.75 μm, 1.5 μm, or 1.25 μm). This could potentially decrease the initial designed aperture area from 4 μm^2 (at 2 μm spacing) to 3.06 μm^2, 2.25 μm^2, or 1.56 μm^2, respectively.

The last process consideration that should be discussed is how significant a factor the thickness of the interrupter plates (Poly1 - 2 µm and Poly2 - 1.5 µm), play in preventing the energy of the flyer material from passing through the closed interrupter. The approach taken here was to increase the blocking strength of the interrupter by arranging the four interrupter plates in an overlapping pattern. However, the effectiveness of this approach was never examined. Therefore, future work in this area could include determining if the overlapping interrupter plates could absorb the energy imparted on the flyer material by the slapper detonator. As a further recommendation, if it is determined that the two overlapping polysilicon interrupter plates are inadequate, an alternative fabrication process, such as MetalMUMPs™, could be selected. MetalMUMPs is another process offered by the MUMPs® foundry that uses a 20-µm thick, electroplated nickel layer as the primary structural material [5]. In addition to being a much thicker layer than polysilicon, nickel has a larger density (9.04 g/cm^3) and a higher Young's modulus (210 GPa) than polysilicon (2.33 g/cm^3 and 158 GPa, respectively) [6], [7]; and thus would provide for a stronger interruption barrier.

6.1.2 Stand-Alone Actuators

Four types of stand-alone bent-beam electrothermal actuators (the three listed in Table 4-2 plus the 400 µm × 12 *tapered* arm actuator used to provide completeness) were designed to assist in characterizing the complete interrupter mechanism. The only varied parameters were the number of arm pairs (8 or 12) and whether the arms were straight or tapered. Tests were performed to determine the actuator deflection as a function of input power, as well as the output force generated by each actuator type.

First, data was collected from 27 stand-alone bent-beam electrothermal actuators in order to characterize the deflection and power relationship for each of the four types of actuators. The results showed that the best performance, in terms of greatest deflection for the least amount of input power, was from the 400 μm × 8 straight arm actuator. These results were consistent with what was expected based on the measured resistance of each actuator, which showed that the 400 μm × 8 straight arm actuator had the largest resistance of all the other actuators. In this case, the larger resistance caused a reduced power requirement for a given deflection, since the higher resistance resulted in less current being needed to thermally expand the arms and cause deflection.

Next, data was collected from 36 stand-alone bent-beam actuators that were fabricated adjacent to cantilever beams of varying lengths to determine the output force being generated by each actuator type. By measuring the maximum beam deflection produced by the actuators, the output force could be calculated using Equation (4.7). Theoretically, for a given actuator, three different maximum beam deflections should be observed, with the output force calculations producing the same results. However, an anomaly existed for the results produced by the 300 μm cantilever beam. It was determined that since the theoretical maximum deflection for the 300 μm beam was beyond the deflection capability of the actuator, the results obtained from this beam were invalid. In contrast, the results from the 100 μm and 200 μm cantilever beam measurements, agreed to within less than 10%, for three out of four of the actuator types tested. As expected from the bent-beam actuator theory discussed in Section 4.3.3, the greatest force was produced by the actuator with the greater number of arm pairs (i.e., the actuators with 12 arms produced greater output force than those with 8 arms).

Recommendations for future work would be to determine the deflection and force characteristics of the bent-beam electrothermal actuators fabricated in run #69. These actuators are similar to the ones fabricated for this thesis, except that the straight arms have a 2.5 μm width, and the tapered arms have been adjusted accordingly to maintain the 1.32 C/D ratios, as discussed in Section 4.4.1.

6.1.3   Interrupter Mechanism

The final test was to demonstrate the operation of the complete MEMS interrupter mechanism, to determine if the device was capable of being actuated from the normally closed configuration to an opened configuration. For each of the three interrupter mechanisms tested, successful lateral motion of the interrupter plates created an aperture that was repeatedly observed. In addition, it is clear from Figure 5-18, Figure 5-19, and Figure 5-20, that simultaneous operation of all four actuators in each interrupter mechanism was achieved. The opened area created by the interrupter plates was determined from the captured still images to be a little less than expected (1024 μm^2 as opposed to 1300 μm^2) since the actuators were limited to only 15 μm of deflection by the latching mechanism. After examining the stand-alone deflection data, it was noticed that the power increase needed to produce a deflection greater than 17 μm, usually resulted in thermal failure of at least one arm of the actuator. Therefore, it is reasonable to conclude that the actual operation of the interrupter mechanism should not attempt to obtain the maximum deflection of the individual actuator, but should be operated at a reduced power to ensure an adequate margin exists to account for uncertainties in the complete system.
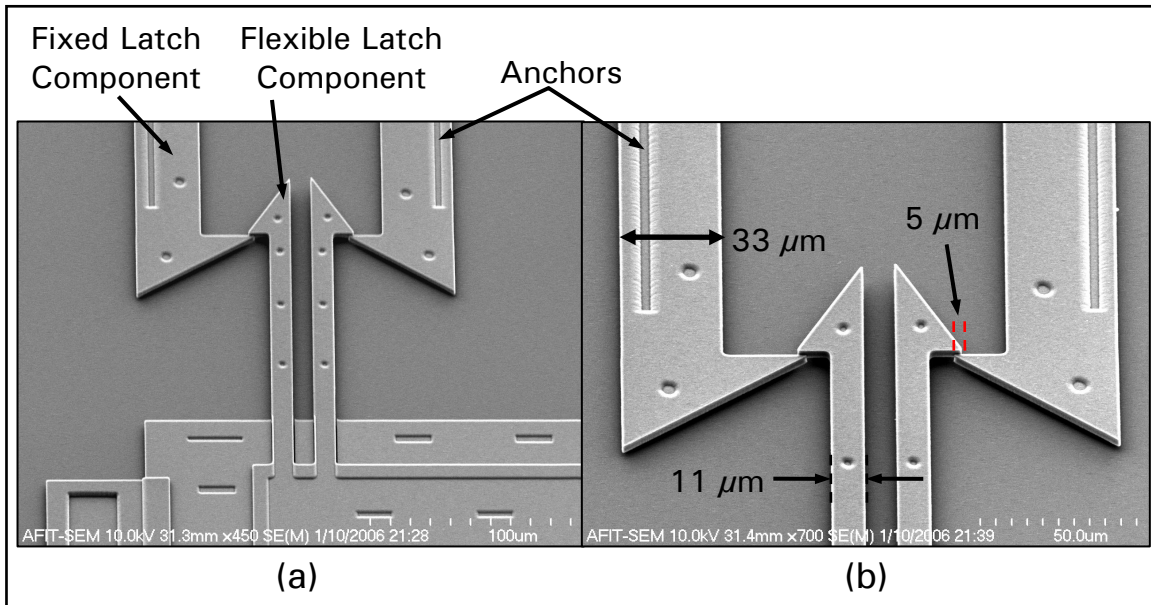
Figure 6-3. (a) Alternative latching mechanism that was fabricated in PolyMUMPs run #68 using both Poly and Poly2. This latch was demonstrated by using a microprobe to push the structure until latching occurred. (b) Magnified view of (a) showing the two latching components are "latched" at only a 5 μm portion of the locking mechanism. However, the validity of the latching mechanism was clearly demonstrated, and better results could be obtained by optimizing this design.

A recommendation for future work is to design a latching mechanism that is capable of locking the interrupter plates in the opened position. An alternative latching mechanism that was fabricated in PolyMUMPs run #68 is shown in Figure 6-3. Based on preliminary testing that was performed, it was concluded that this mechanism was more successful than the latches used in the interrupter mechanisms. However, it can be observed in Figure 6-3(b) that the "latching" occurs for only a very small portion (5 μm) of the locking mechanism, and thus further modifications and testing would be necessary to obtain better results. Also, note that the latching seen here was the result of a microprobe being used to push the structure into its latched position.

Finally, there were no issues that prevented the actuators from separating the interrupter plates repeatedly for each interrupter mechanism tested. On the other hand,

there was some initial binding on the interrupter plates due to an inadvertent design error. For each interrupter tested, the initial binding was eliminated after a one-time voltage (6-7 V) was applied to the device. Figure 6-4(a) shows several fabricated features (each designed to a diameter of 6 µm) on the surface of the interrupter plates that could have contributed to the binding. However, it was concluded based on these images that the most likely cause for the binding was the result of the Poly2 material over a Poly1 etch hole, as shown in Figure 6-4(b). A recommendation to eliminate this from occurring is to either, line up the Poly1 and Poly2 etch holes, or completely avoid fabricating Poly1 etch holes where it is desirable for Poly2 to cover Poly1.
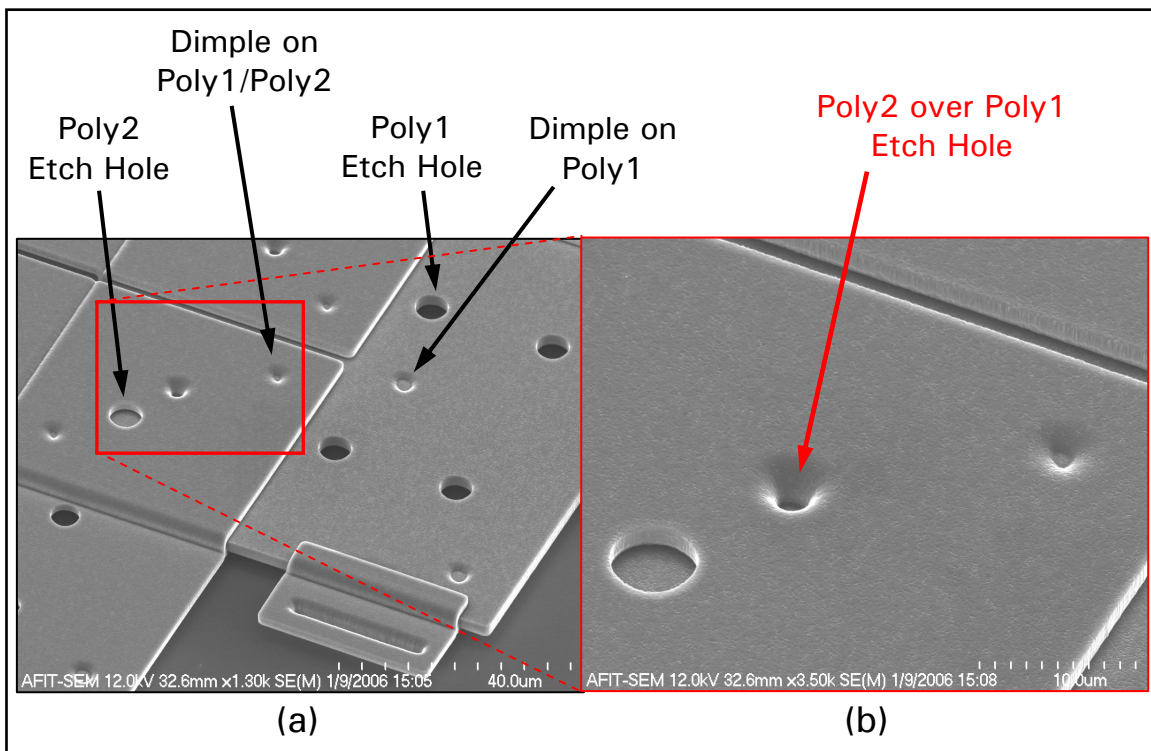

Figure 6-4. (a) SEM images showing fabricated features on the surface of the interrupter plates. All of the following features were designed to a diameter of 6 µm: dimples shown on both Poly1 and Poly2, Poly1 etch holes, Poly2 etch holes, and an inadvertent error – Poly1 etch hole under a Poly2 layer.

6.2   Recommendations for Future Work

Since the interrupter mechanism designed in this research effort is a conceptual device, many opportunities exist for this device to be optimized. In addition, there are other MEMS methods that can be explored to provide a similar interruption method for the flyer material in a solid-state slapper detonator. The following list offers some recommendations for future work in developing a MEMS-based interrupter mechanism for state-of-the-art safe and arm devices.

- Optimize deflection by using an alternative actuation method. For example, a ratcheting mechanism could be created with the bent-beam, or u-shaped, electrothermal actuators that could dramatically increase the distance over which the interrupter plates could move. This increased movement would result in a far greater aperture area.

- Design a gear system operated by scratch drives that is capable of moving a single interrupter plate in-line to pass the flyer material, and out-of-line to prevent the flyer material from initiating the HE pellet. Multiple scratch drives could be implemented so that the interrupter plate can move in both directions.

- Investigate using bent-beam actuators with less than 8 arms to further reduce power consumption. Note the resulting reduction in force should not be an issue based on the required force calculations performed as part of this thesis.

- Implement an operational latching mechanism, possibly based on the $3 - 4$ μm width suggested in Chapter 5. This latching mechanism could include an unlatching capability that would enable the S&A interrupter device to return to the safe mode after having received an arming signal.

- Redesign the current interrupter mechanism to optimize the components for a more efficient use of chip area. Sinclair et al. offers some suggestions using a *folded* bent-beam electrothermal actuator design [8].

- Etch through a MUMPs[®] die, under the interrupter plates, to determine if an adequate hole could be created in the substrate that would allow for the flyer material to pass through when the interrupter plates are in the open (armed) position.

- Investigate wafer bonding of the die containing the interrupter mechanism to another die that functions as the barrel in a solid-state slapper detonator.

- Design and fabricate an alternative interrupter scheme where an out-of-line barrel plate functions as the interrupter for the flyer material, and is physically moved in-line when armed [9].

- Design and fabricate an alternative MEMS safe and arm mechanism that keeps a micro-scale HE pellet normally out-of-line (safe), then physically moves the HE pellet in-line when armed [10].

- Fabricate a solid-state slapper detonator, or components thereof, i.e., fabricating a solid-state capacitor capable of being charged to multi-kilovolt potentials and delivering large current pulses [10].

Bibliography

[1] Skibbie, Lawrence F. "Fuze Industrial Base Problems Should No Longer Be Ignored," *National Defense Magazine*, (June 2001). March 2005. <http://www.nationaldefensemagazine.org/issues/2001/Jun/Fuze_Industrial.htm>.

[2] Erwin, Sandra I. "Army Not Producing Enough Ammunition," *National Defense Magazine*, (May 2003). June 2005. <http://www.nationaldefensemagazine.org/issues/2001/Dec/Munitions_Sector.htm>.

[3] Erwin, Sandra I. "Munitions Sector 'In Trouble,' Despite New Funds," *National Defense Magazine*, (December 2001). June 2005. <http://www.nationaldefense magazine.org/issues/2001/Dec/Munitions_Sector.htm>.

[4] Koester, David and others. *PolyMUMPs Design Handbook (Revision 11.0)*. MEMSCAP, 2005. August 2005. <http://www.memsrus.com/documents/PolyMUMPs.DR.v11.pdf>.

[5] Cowan, Allen and others. *MetalMUMPs Design Handbook (Revision 1.0)*. MEMSCAP, 2002. January 2005. <http://www.memsrus.com/documents/MetalMUMPs.dr.v1.pdf>.

[6] Kovacs, Gregory T. A. *Micromachined Transducers Sourcebook*. Boston: The McGraw Hill Company, 1998.

[7] Sharpe Jr., W. N., K. Jackson, G. Coles, and D. A. LaVan. "Young's Modulus and Fracture Strength of Three Polysilicons," *Proceedings of Materials Science of Microelectromechanical Systems (MEMS) Devices III*. Volume 657: 551-556. Materials Research Society, 2001.

[8] Sinclair, Michael J. and Kerwin Wang. "Thermal Actuator Improvements: Tapering and Folding," *Proceedings of the SPIE - The International Society for Optical Engineering*. Volume 5116: 237-251 (April 2003).

[9] Garvick, Donald R., Lawrence C. Fan, Bruce R. Kuester, and Gregory R. Birk. "MEMS Energetic Actuator with Integrated Safety and Arming System for a Slapper/EFI Detonator." US Patent 6173650. 16 January 2001.

[10] O'Brien, Dennis W., Robert L. Druce, Gary W. Johnson, George E. Vogtlin, Troy W. Barbee Jr., and Ronald S. Lee. "Method and System for Making Integrated Solid-State Fire-Sets and Detonators." US Patent 5731538. 24 March 1998.

Appendix A.Release Procedures for Microelectromechanical Systems

The specific release procedures used for the devices produced for this research effort are described in the following paragraphs. The chemicals used were acetone, methanol, deionized water (DIW), and a 48% hydrofluoric acid (HF) solution. Several variations of these release procedures were attempted in the beginning of this effort and the following method was finally adopted because it consistently produced the best results. The criteria used to determine the best results were completely released structures (i.e., no oxide remained beneath the structures) and cleanliness of the entire die. In some early variations of the release procedures, particulates were observed on the surface of the dies that could potentially prevent successful device operation. It was hypothesized that these particulates most likely came from remnants of silicon dust that comes from dicing and the protective photoresist removed by the acetone. Therefore, the immersion in a single acetone bath was split into two separate acetone baths.

Another modification to the early release procedures was the die immersion time in the HF solution. The general release instructions provided by the MUMPs$^{®}$ website states that a 2 − 2.5 min. immersion in an HF bath should completely free the structures from the sacrificial oxide layers [1]. However, it must be noted that for devices with dimensions greater than 50 μm, etch holes should be fabricated in the structural material to allow the HF to access the oxide [2]. Therefore, with these recommendations in mind, etch holes were fabricated on the two releasable polysilicon layers and an HF immersion time of 4.0 min. was used to ensure a successful release. The complete procedures are listed in Appendix A, along with the main purpose for including that step in the process.

Table A-1. Release procedures used for MEMS dies fabricated in this research effort.

Step	Chemical	Time	Main Purpose
1	Acetone	10 min	Removes the protective photoresist layer.
2	Acetone	10 min	Clears the particulates removed from the previous step and continues to remove the protective photoresist.
3	Methanol	5 min	Rinses the acetone from the die and clears any particulates remaining from the previous step.
4	DIW	2 min	Rinses the methanol from the previous step. (This time is flexible)
5	48% HF	4 min	Etches the sacrificial oxide layer from between the two structural polysilicon layers.
6	DIW	10 sec	Stops the HF etching process.
7	Methanol	2 min	Rinses the DIW from the previous step and prepares the dies for the supercritical CO_2 drying process.

The supercritical drying method was used exclusively for removing the methanol from the dies. The main purpose of the supercritical CO_2 drying procedure is to completely avoid the surface tension effects that often lead to stiction in MEMS structures. Stiction is a leading cause of low yield in MEMS fabrication, and reducing its occurrences can increase manufacturing efficiencies. Surface tension arises in the drying process when liquid CO_2 transitions to CO_2 vapor. This interface point can be circumvented by cycling through a specific sequence of pressure and temperature changes that result in the liquid CO_2 transitioning directly to vapor form [3]. Figure depicts the cycle required for supercritical drying on a CO_2 phase diagram and a summary of the process is described in the following paragraph.
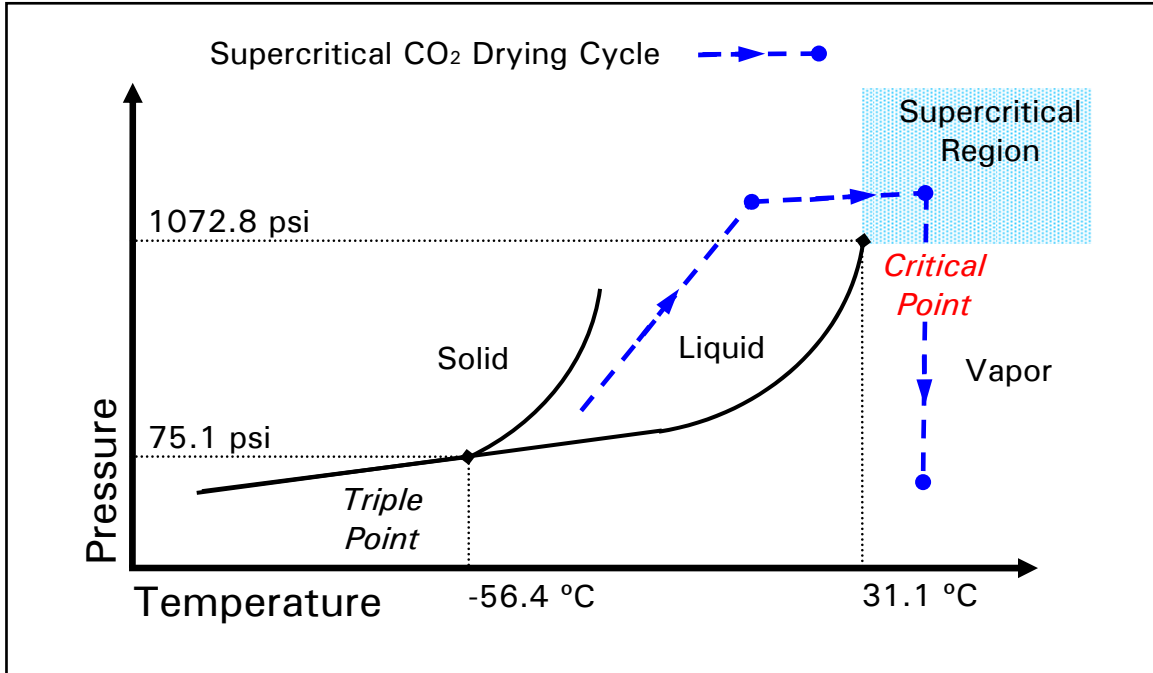
Figure A-1. Carbon dioxide phase diagram showing the supercritical CO_2 drying cycle.

The specific equipment used for this process was an Autosamdri®-815, Series B Automatic Supercritical Point Dryer as shown in Figure A-2. The MEMS dies are placed into the methanol-filled chamber of the supercritical CO_2 dryer at room temperature. Next, the chamber is cooled and purged with liquid CO_2 to replace the methanol. The pressure of the chamber is then raised to above 1072.8 psi (the model used here stabilized at approximately 1350 psi), while the temperature is increased to just above 31.1 ℃. At this point, the pressure and temperature is above the critical point for CO_2 and the liquid transitions directly into the vapor phase through the supercritical region. Finally, the CO_2 gas is vented from the chamber at a constant temperature [3], [4]. This procedure proved very effective for drying MEMS devices without inducing stiction damage.

Figure A-2. Automatic supercritical CO_2 dryer used to prevent stiction in the MEMS dies used in this research effort.

[1]   "PolyMUMPs[TM] General Release Instructions." *PolyMUMPs Reference Library*. Durham: MEMSCAP. January 2006. <http://www.memsrus.com/documents/ PolyMUMPs.Release.Instructions.pdf>.

[2]   *PolyMUMPs FAQ (Revision 2.0)*. MEMSCAP, 2004. August 2005. <http://www.memsrus.com/documents/PolyMUMPs.faq.v2.pdf>.

[3]   Jafri, Ijaz, Heinz Busta, and Steven Walsh. "Critical Point Drying and Cleaning for MEMS Technology," Proceedings *of SPIE – The International Society for Optical Engineering.* Volume 3880: 51-58 (September 1999).

[4]   *Autosamdri®-815, Series B User Manual*. Serial Number 2112. Rockville: Tousimis, 2003.

Appendix B. PolyMUMPs Run Data

The material properties of every PolyMUMPs™ fabrication run are measured and made available to users so that deviations from the nominal values can be accounted for during device testing. The following tables show the measured data for each fabrication run as provided by the MUMPs® foundry [1]. The "T" and "C" in the Residual Stress column represents tensile or compressive stress, respectively.

Table B-1. PolyMUMPs Run #66 measured fabrication data [1].

	Thickness (μm)	Standard Deviation (μm)	Sheet Resistance (Ω/□)	Resistivity (Ω-cm)	Residual Stress (MPa)
Nitride	0.6136	0.0115			78.5 T
Poly0	0.5010	0.0026	31.4	1.57×10^{-3}	33 C
Oxide1	2.0497	0.0477			
Poly1	1.9782	0.0141	24.3	4.81×10^{-3}	6.3 C
Oxide2	0.7521	0.0129			
Poly2	1.4960	0.0094	12.3	1.84×10^{-3}	7.3 C
Metal	0.5421		0.049	2.66×10^{-6}	25.7 T

Table B-2. PolyMUMPs Run #67 measured fabrication data [1].

	Thickness (μm)	Standard Deviation (μm)	Sheet Resistance (Ω/□)	Resistivity (Ω-cm)	Residual Stress (MPa)
Nitride	0.5805	0.0192			88 T
Poly0	0.5014	0.0033	29.8	1.49×10^{-3}	9 C
Oxide1	2.0191	0.0324			
Poly1	2.0044	0.0256	11.6	2.33×10^{-3}	8.5 C
Oxide2	0.7442	0.0100			
Poly2	1.4888	0.0104	21.8	3.25×10^{-3}	7.6 C
Metal	0.4971		0.058	2.88×10^{-6}	20.1 T

Table B-3. PolyMUMPs Run #68 measured fabrication data [1].

	Thickness (μm)	Standard Deviation (μm)	Sheet Resistance (Ω/□)	Resistivity (Ω-cm)	Residual Stress (MPa)
Nitride	0.6008	0.0292			95 T
Poly0	0.4999	0.0051	35.6	1.78×10^{-3}	16.33 C
Oxide1	1.9810	0.0316			
Poly1	1.9922	0.0220	13.9	2.77×10^{-3}	6.33 C
Oxide2	0.7582	0.0072			
Poly2	1.4605	0.0240	28	4.09×10^{-3}	6.00 C
Metal	0.5245		0.048	2.52×10^{-6}	17.13 T

Table B-4. PolyMUMPs Run #69 measured fabrication data [1].

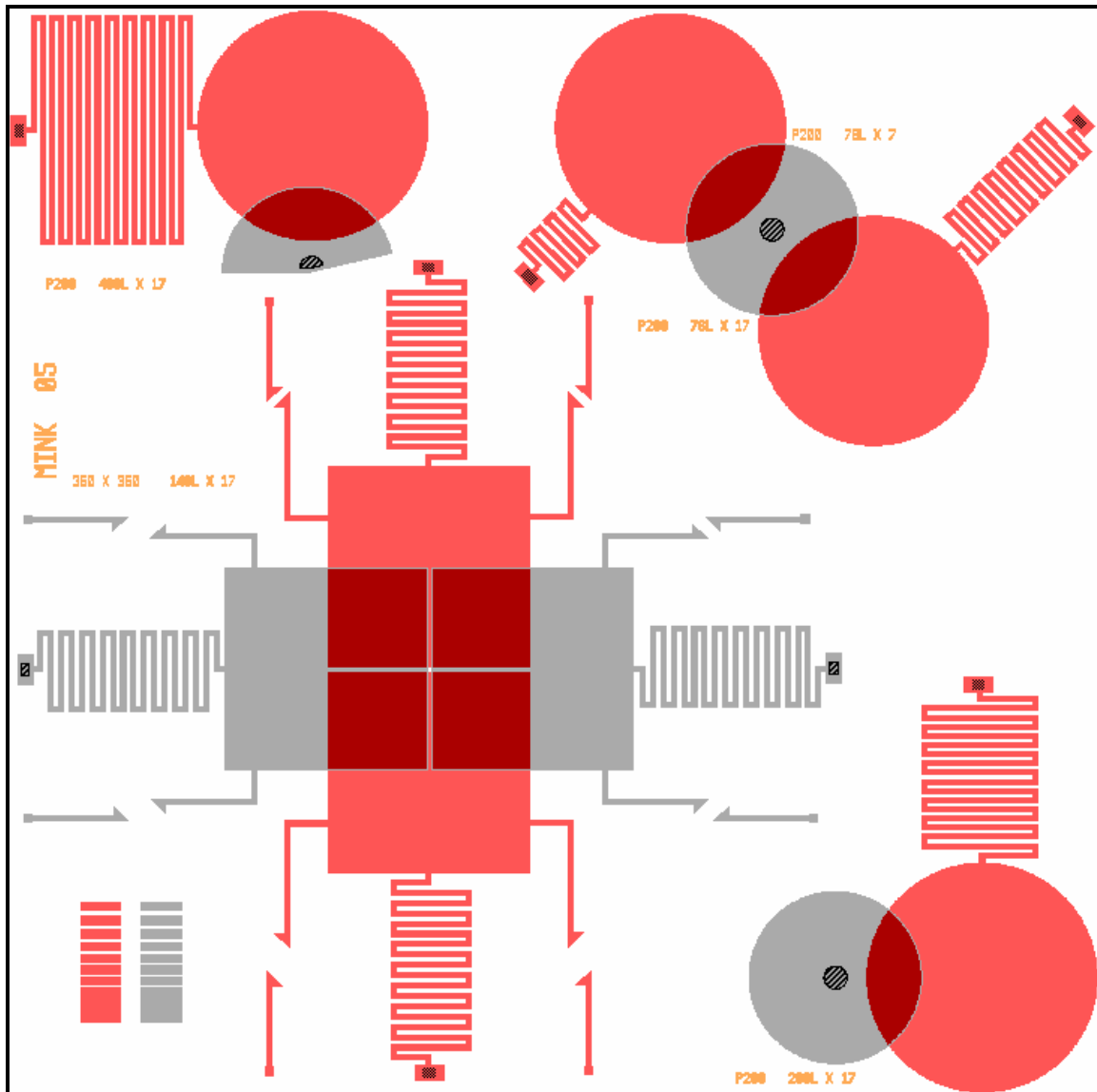|	Thickness (μm)	Standard Deviation (μm)	Sheet Resistance (Ω/□)	Resistivity (Ω-cm)	Residual Stress (MPa)
Nitride	0.5968	0.0506			95 T
Poly0	0.5011	0.0077	28.1	1.41×10^{-3}	24.3 C
Oxide1	1.8884	0.0405			
Poly1	2.0132	0.0116	10.5	2.11×10^{-3}	8.00 C
Oxide2	0.6915	0.0026			
Poly2	1.4966	0.0087	20.9	3.13×10^{-3}	7.66 C
Metal	0.5117		0.055	2.81×10^{-6}	15.76 T

[1]   "PolyMUMPs.rundata.xls." *PolyMUMPs Run Data.* <http://www.memsrus.com/ nc-pmumps.refs.html>.

Appendix C. Fabricated Design Layouts

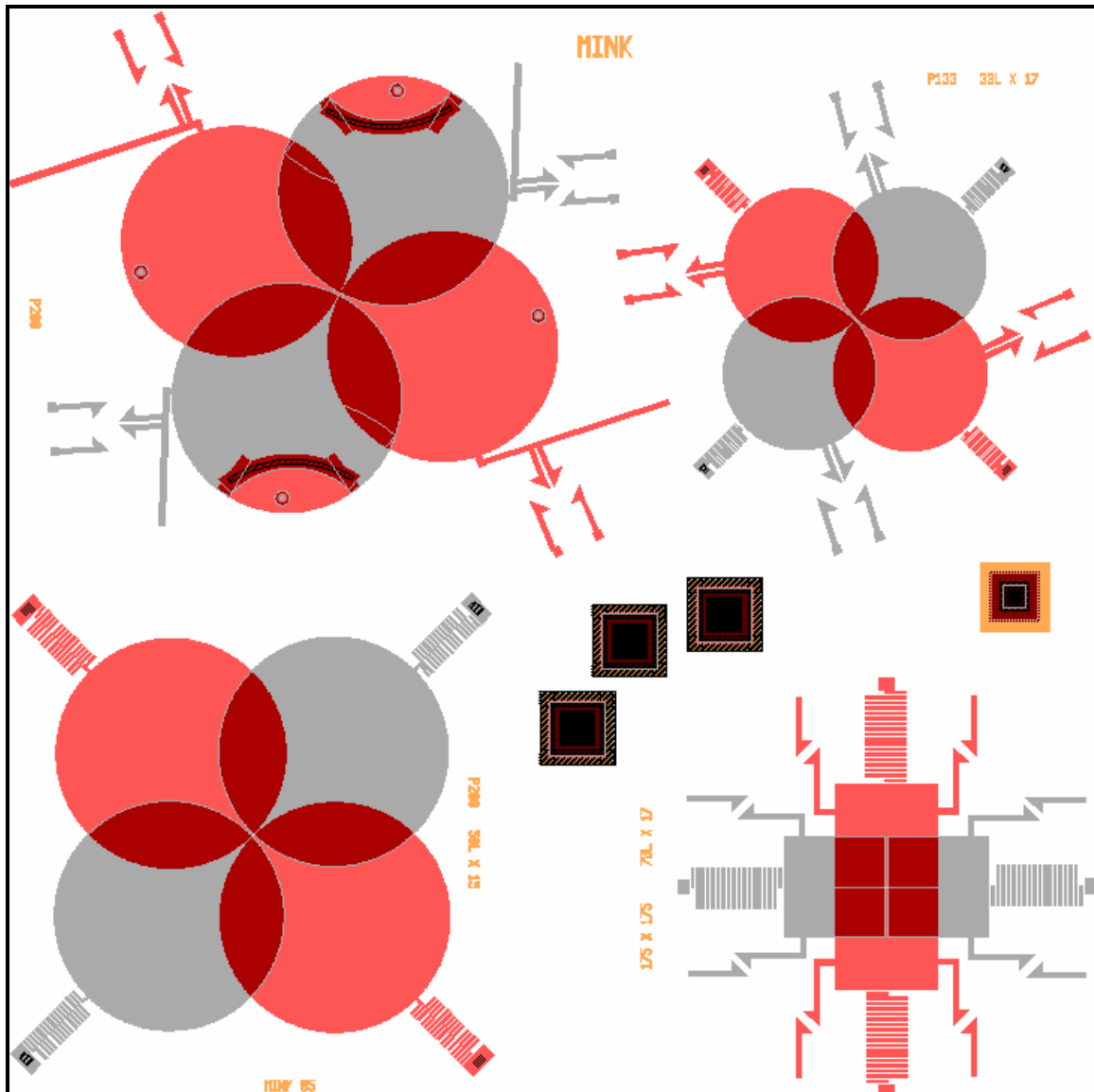Each layout on the following pages is designed to a 1.9 mm × 1.9 mm die.

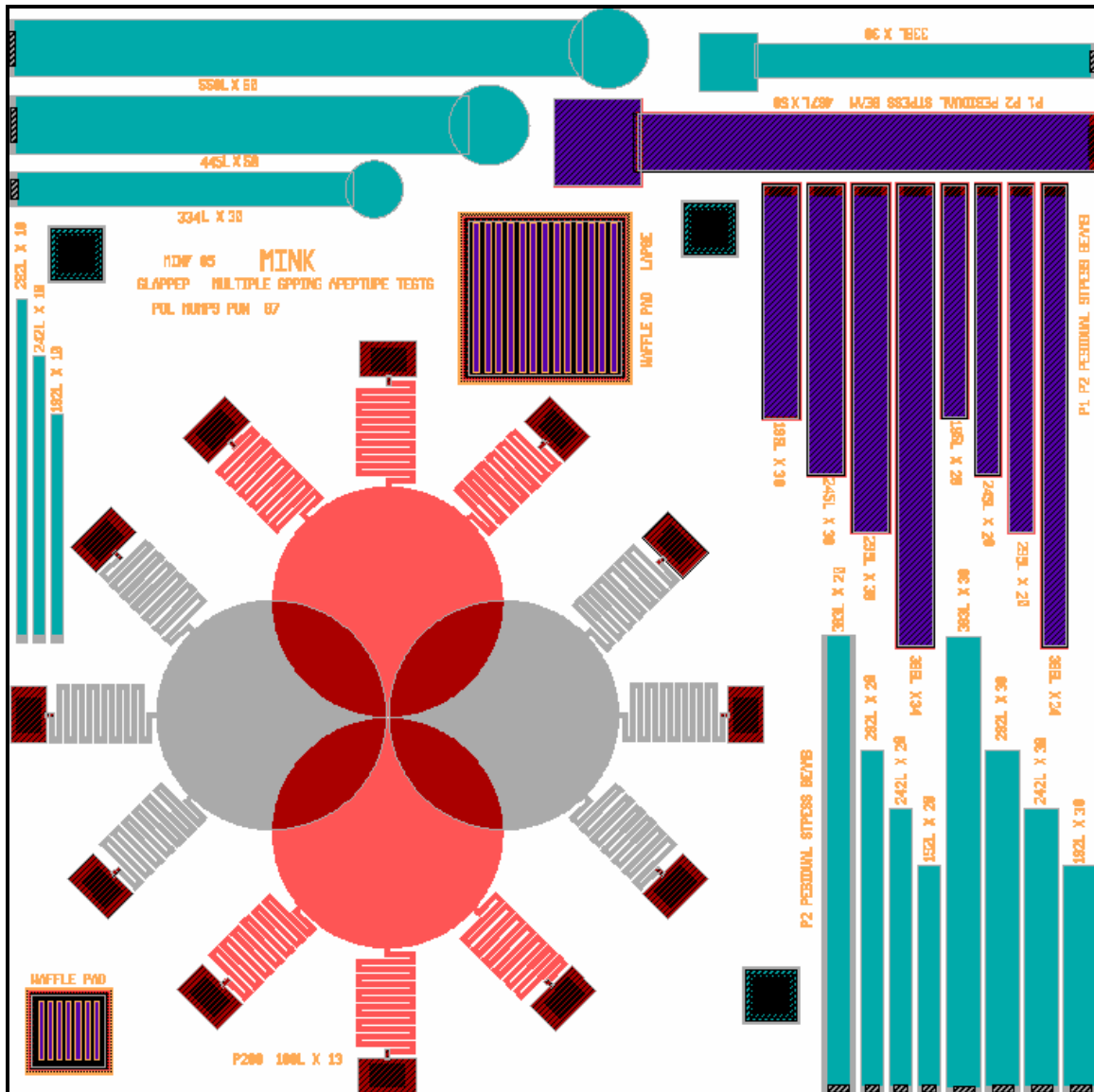| PolyMUMPs™ Run No.:	66
Working Nomenclature	Die#1
Fabricated Devices:	Poly1/Poly2 Electrothermal Actuators Electrostatic Actuators/Micromirrors Poly2/Metal Residual Stress Beams/Structures Hinge Structures (Rotating/Non-Rotating) Fabrication Process Test Structures
Main Uses:	Test/Compare Various Actuators Observe/Measure Residual Stress Investigate Fabricated Mechanical Structures

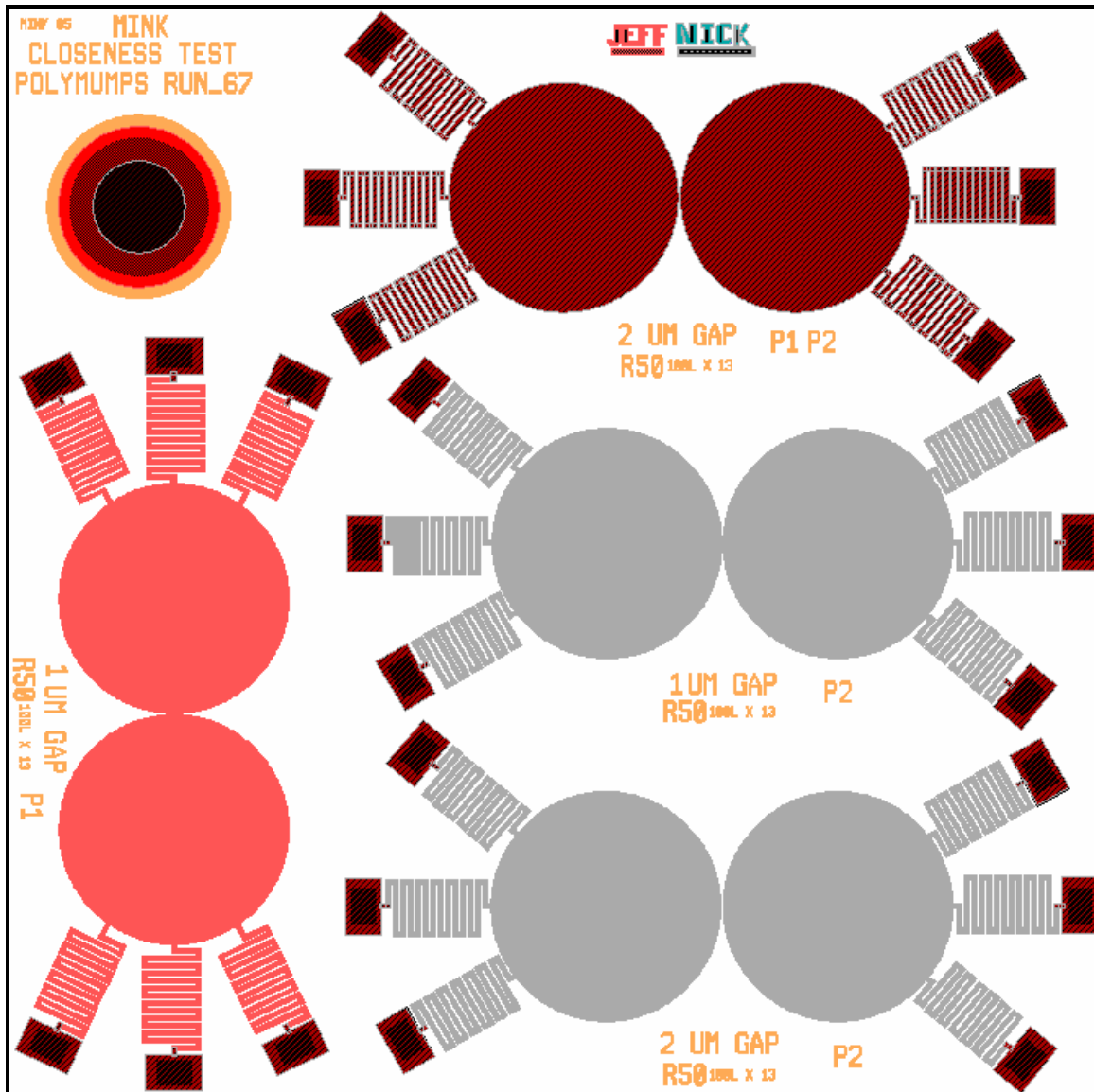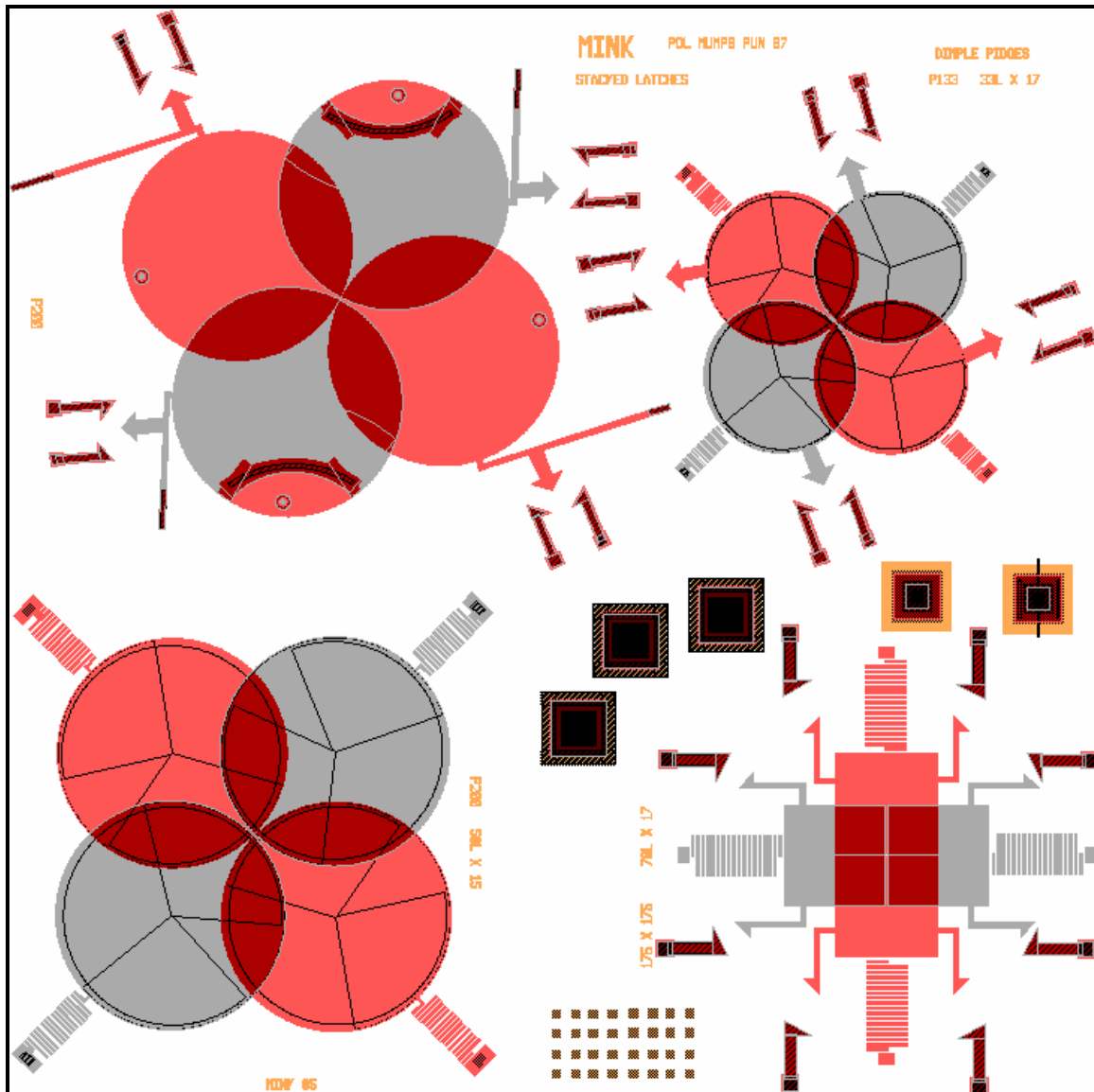| PolyMUMPs Run No.:	66
Working Nomenclature	Die#2
Fabricated Devices:	350 μm x 350 μm Square Plates, Rotating Aperture 200 μm Radius, Spring-Based, Poly1 Disk with Anchored Poly2 – Test Structures Poly1/Poly2 Minimum Spacing Test Structures
Main Uses:	Test Feasibility of Spring-Based Rotating Design Test/Observe Various Springs Designs Test/Observe, Single Layer, Fabricated Latches Test/Observe Conformal Deposition Observe/Measure Poly1/Poly2 Minimum Spacing Limitations in Fabrication Process

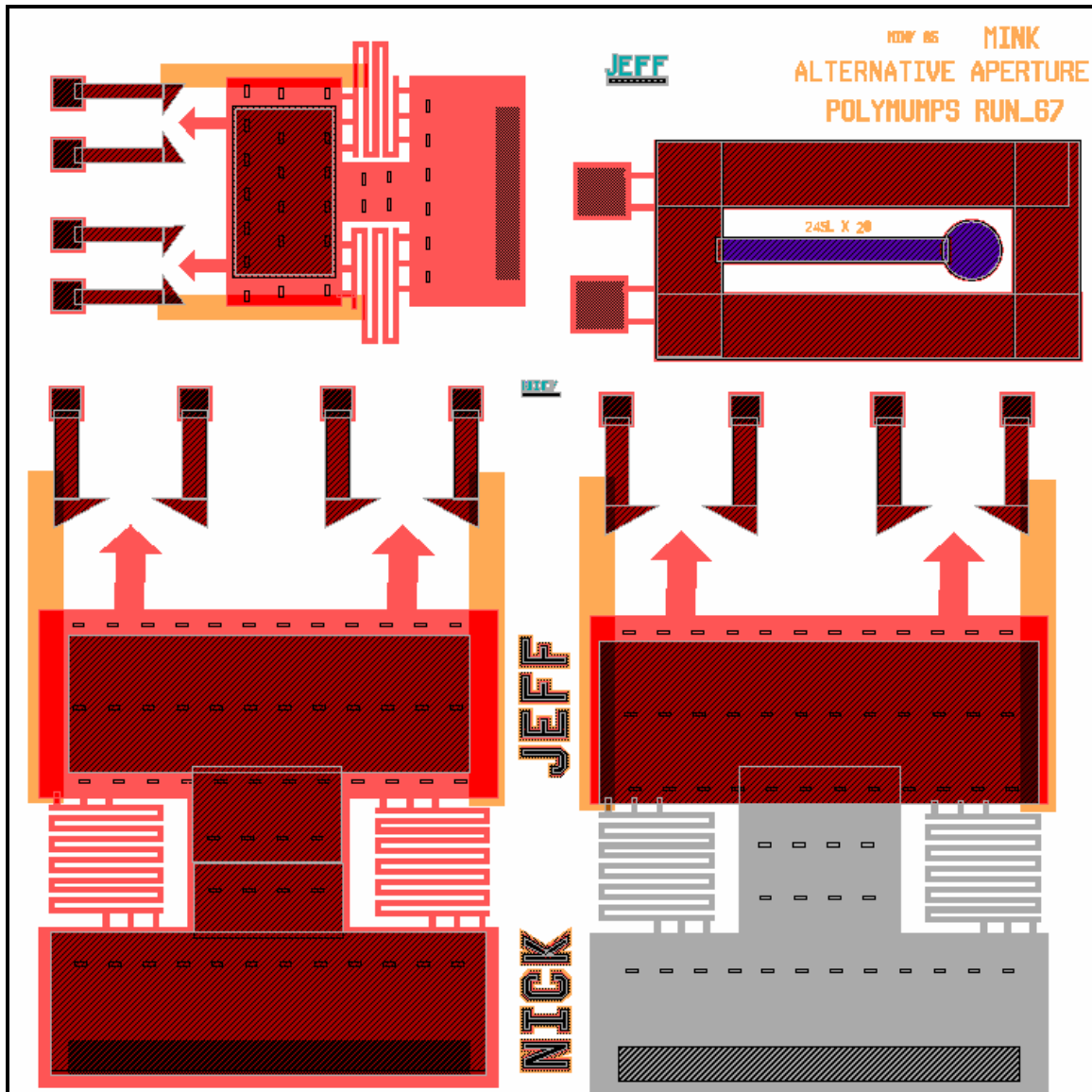| PolyMUMPs Run No.:	66
Working Nomenclature	Die #3
Fabricated Devices:	200 μm Radius, Hinge-Based Rotating Aperture 200 μm Radius, Spring-Based Rotating Aperture 135 μm Radius, Spring-Based Rotating Aperture 175 μm x 175 μm Square Plates, Rotating Aperture Layer Deposition Test Structures
Main Uses:	Test Feasibility of Hinge-Based Rotating Design Test Feasibility of Spring-Based Rotating Design Test/Observe, Single Layer, Fabricated Latches Observe/Measure Fabricated Layer Thicknesses and Etch Depths

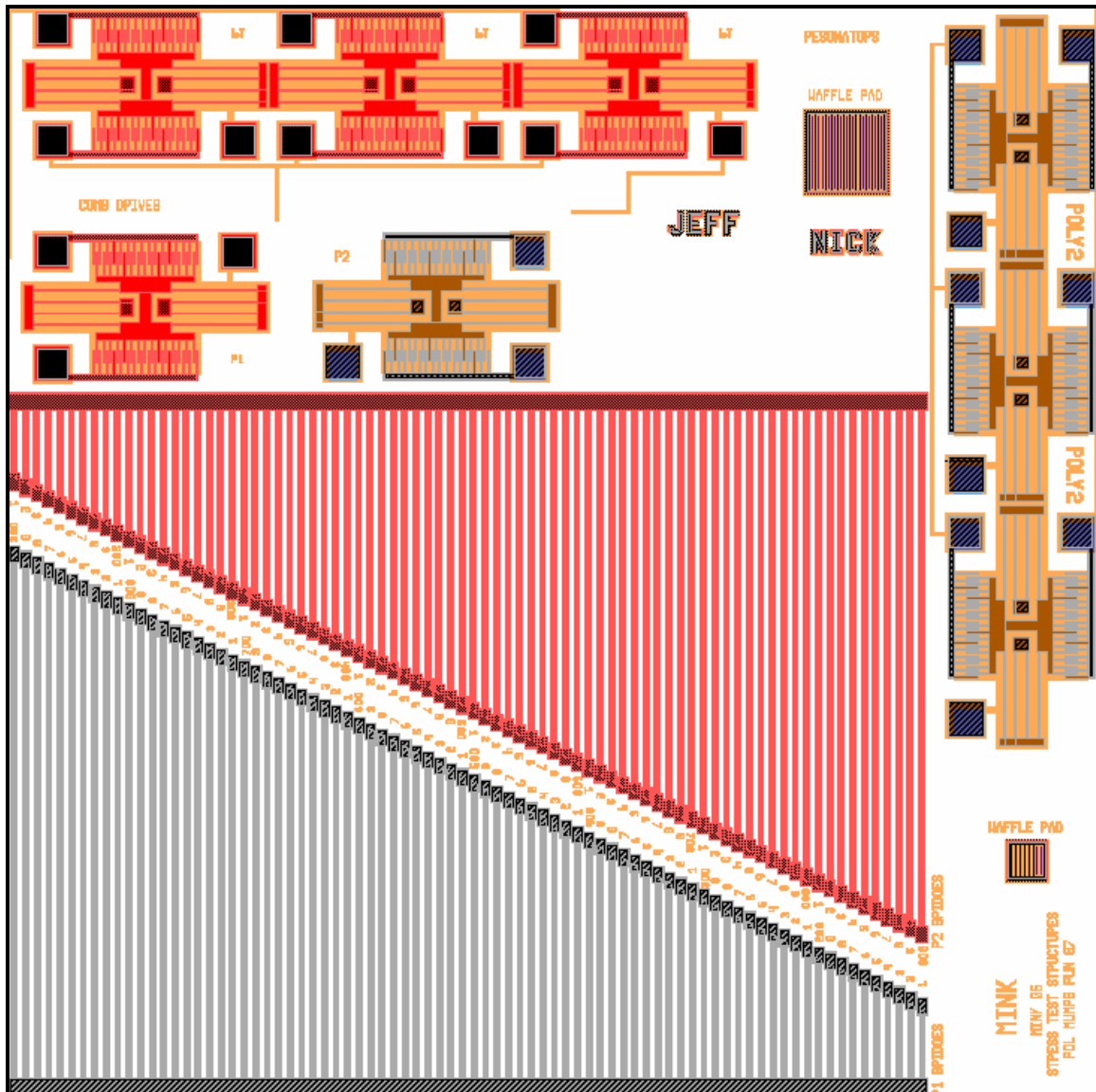| PolyMUMPs Run No.:	67
Working Nomenclature	Die #4
Fabricated Devices:	200 μm Radius, Multiple Spring, Rotating Aperture Poly2/Metal Residual Stress Beams Poly1/Poly2/Metal Residual Stress Beams Layer Deposition Test Structures Electrical Contact Pad to Substrate – Test Structures

Main Uses:	Test Feasibility of Multiple Spring Rotating Design
	Observe/Measure Residual Stress Beams of Varying
	   Thicknesses
	Observe/Measure Fabricated Layer Thicknesses and
	   Etch Depths

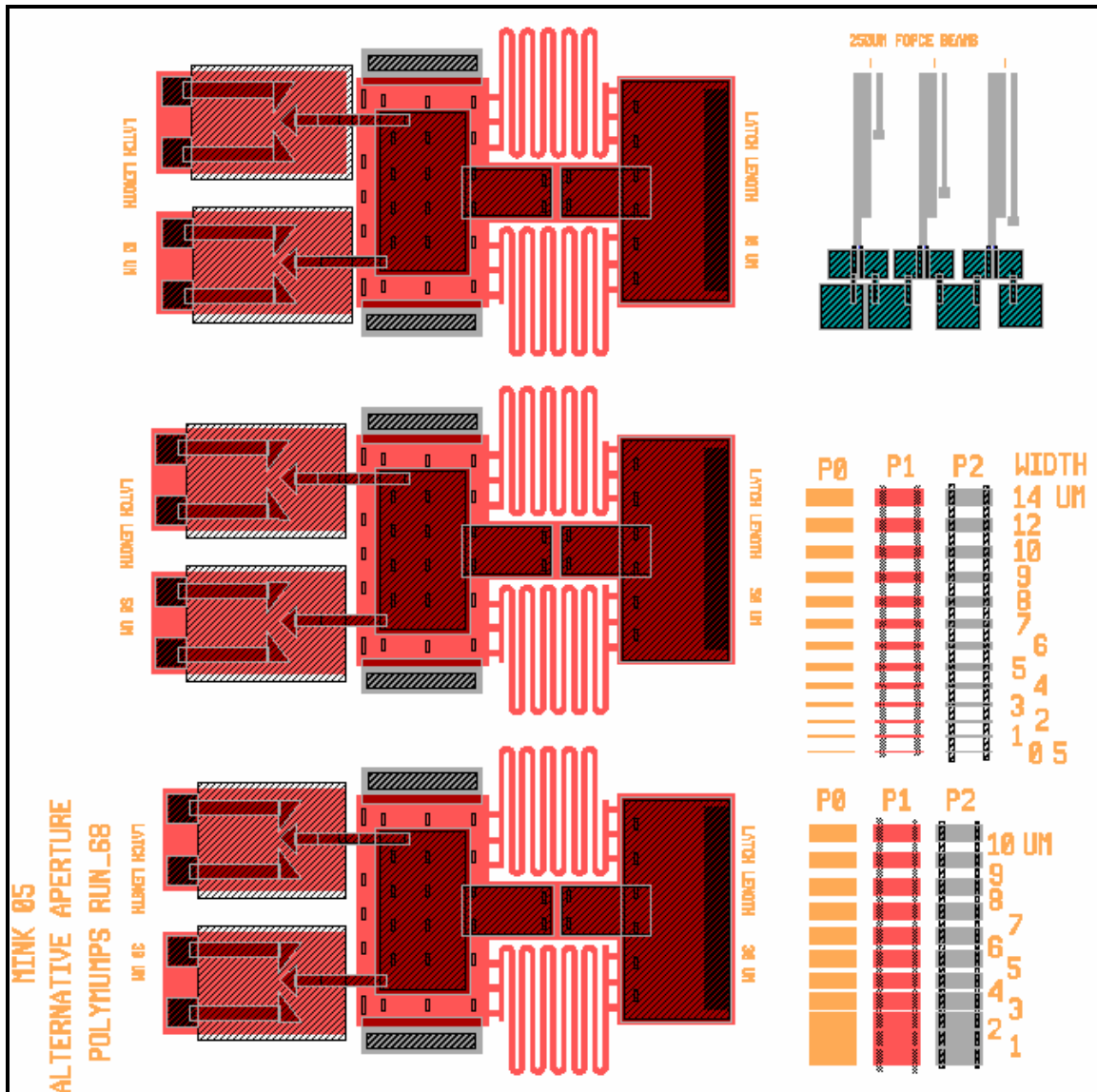| PolyMUMPs Run No.:	67
Working Nomenclature	Die #5
Fabricated Devices:	200 μm Radius, Poly1 Multiple Spring Aperture, 200 μm Radius, Poly2 Multiple Spring Aperture, 200 μm Radius, Poly1/Poly2 Multiple Spring Aperture Layer Deposition Test Structure
Main Uses:	Test Separation Distance Between Aperture Designs Observe Variations in Apertures due to Fabricated Layer Thicknesses Observe/Measure Stacked Layer Thicknesses and Etch Depths

PolyMUMPs Run No.:	67
Working Nomenclature	Die #6 (Modified Die #3)
Fabricated Devices:	200 μm Radius, Hinge-Based Rotating Aperture 200 μm Radius, Spring-Based Rotating Aperture 135 μm Radius, Spring-Based Rotating Aperture 175 μm x 175 μm Square Plates, Rotating Aperture, Layer Deposition Test Structures

Main Uses:	Test/Observe, Double Layer (3.5 μm) Latches on the
	    Hinge-Based and Spring-Based Rotating Designs
	Observe/Measure Fabricated Layer Thicknesses and
	    Etch Depths

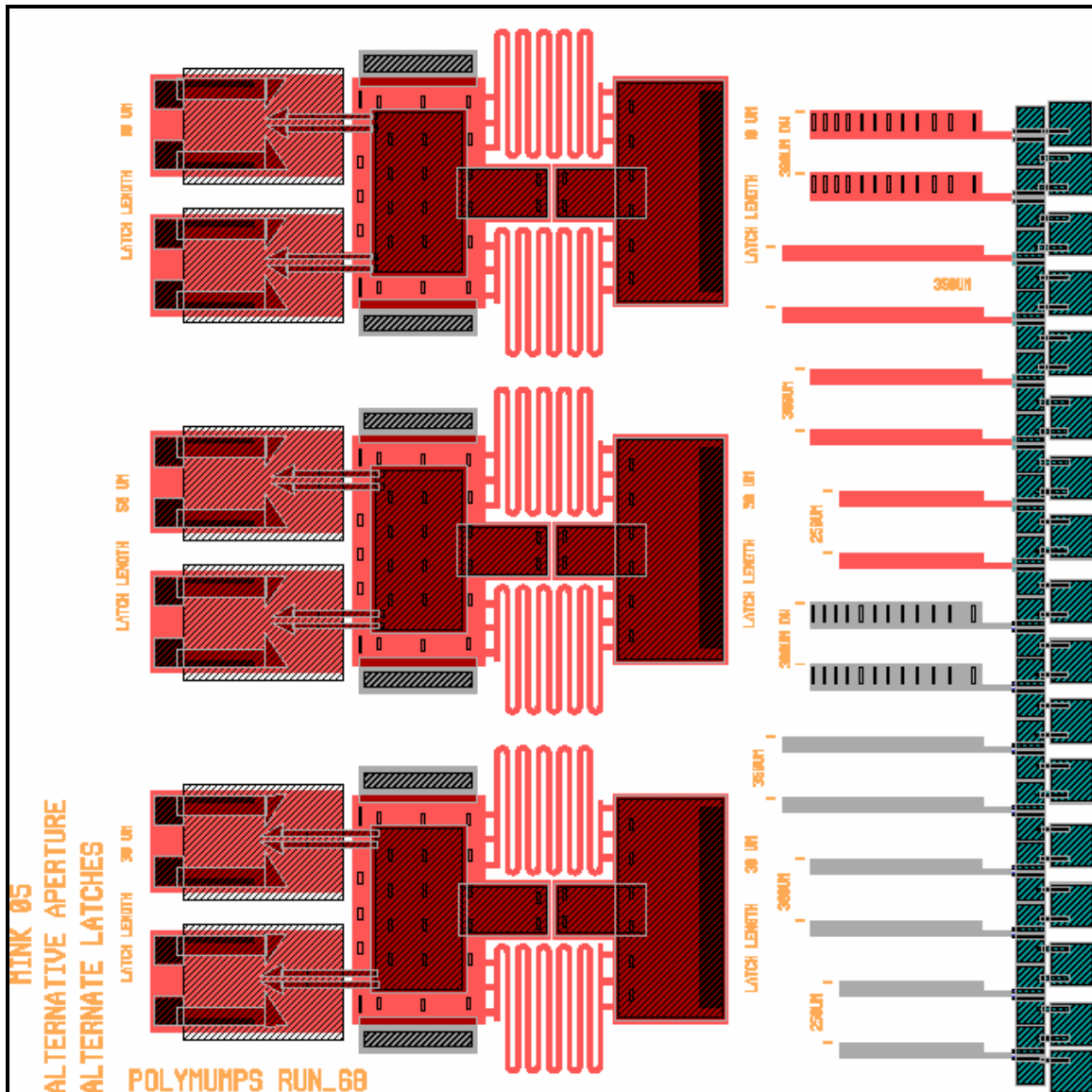| PolyMUMPs Run No.:	67
Working Nomenclature	Die #7

Fabricated Devices:	Rotating Apertures:
	    140 μm Poly1/Poly2 Single-Sided Sliding Plate
	    140 μm Poly2 Single-Sided Sliding Plate
	    50 μm Poly1 Single-Sided Sliding Plate
	 240 μm Poly1/Poly2/Metal Releasable Residual Stress
	    Beam

Main Uses:	Test Alternative Rotating Aperture Designs Observe Variations Based on Different Sliding Masses Observe Effects of Poly0 Runners for Sliding Plate Observe/Measure Effects of Residual Stress on a Long Releasable Structure

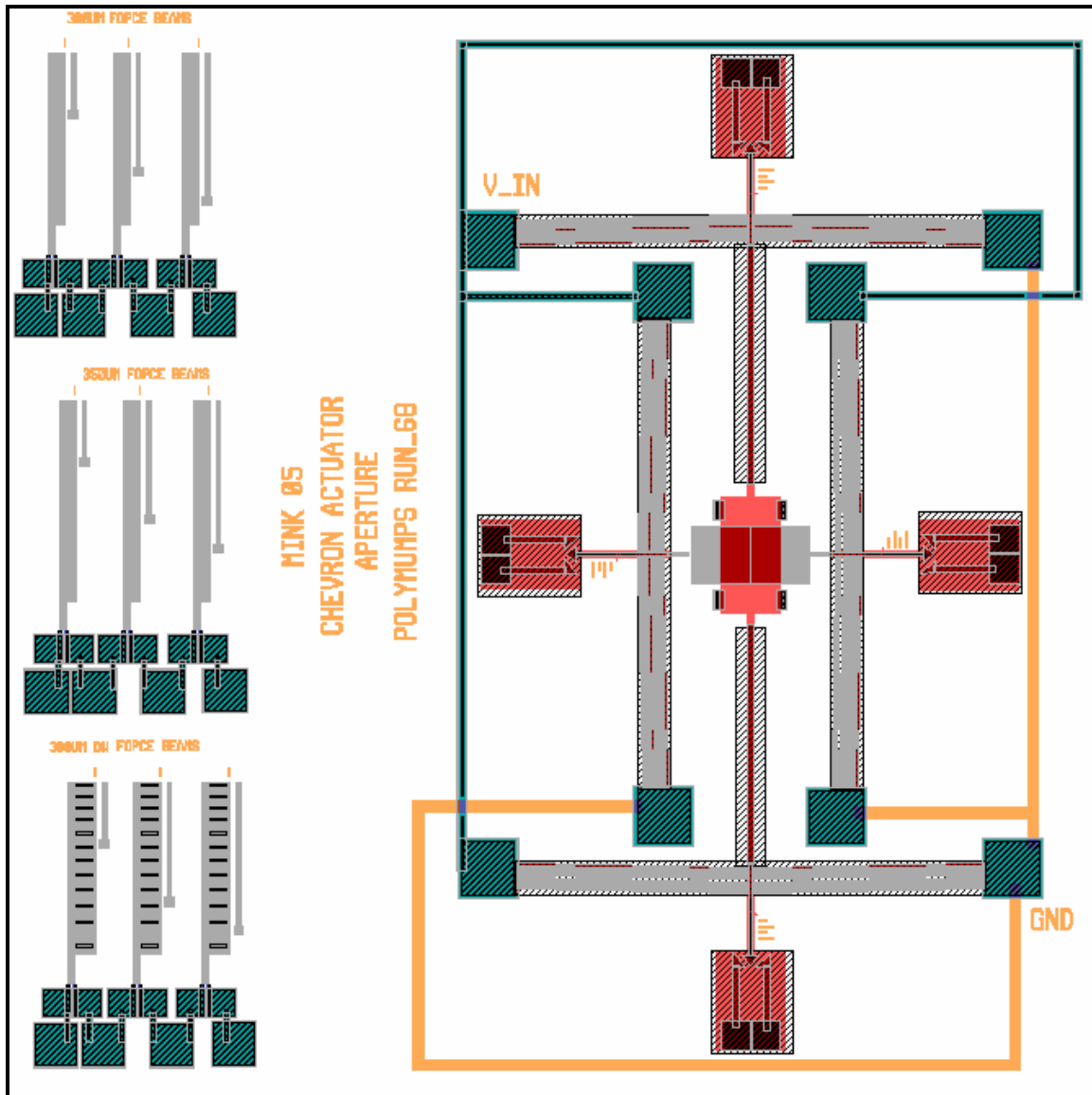| PolyMUMPs Run No.:	67
Working Nomenclature	Die #8
Fabricated Devices:	Poly1 Fixed-Fixed Beams – 110 μm to 900 μm Poly2 Fixed-Fixed Beams – 110 μm to 900 μm Poly1 Comb Drive Resonators Poly2 Comb Drive Resonators Fabrication Process Test Structures

Main Uses:	Measure Beam Deflection to Determine Residual Stress
	Measure Resonating Frequency in Comb Drives to
	    Determine Young's Modulus
	Observe Fabrication Process Versus Design Layout
	Observe/Measure Fabricated Layer Thicknesses and
	    Etch Depths

PolyMUMPs Run No.:	68
Working Nomenclature	Die #9
Fabricated Devices:	100 μm Poly1/Poly2 Single-Sided Sliding Plate Rotating Apertures, with Latch Distances of: 30 μm, 40 μm, and 50 μm. 250 μm Poly2 Electrothermal Actuators with 8 μm-Wide Force Measuring Beams Width and Spacing Test Structures
Main Uses:	Test Alternative Rotating Aperture Designs with Varying Latching Distances Observe Effects of Guide Rails on Sliding Plate Measure Deflection of Electrothermal Actuator to Determine Force Observe/Measure Limits of Fabrication Process

PolyMUMPs Run No.:	68
Working Nomenclature	Die #10 (Modified Die #9)
Fabricated Devices:	100 µm Poly1/Poly2 Single-Sided Sliding Plate Rotating Apertures, with Modified Latches Latch Distances:30 µm, 40 µm, and 50 µm. Poly1 Electrothermal Actuators of Various Dimensions Poly2 Electrothermal Actuators of Various Dimensions

Main Uses:	Test Alternative Rotating Aperture Designs with
	    Modified Latches
	Observe Effects of Guide Rails on Sliding Plate
	Test/Measure Performance Characteristics of
	    Electrothermal Actuators

PolyMUMPs Run No.:	68
Working Nomenclature	Die #11 (Interrupter Mechanism #1)
Fabricated Devices:	S&A Interrupter Device: Four Chevron Actuators with Latches, 8 × (400 μm × 3 μm) Arms, Poly1 and Poly2 Overlapping Interrupter Plates 350 μm, 300 μm, and 300 μm (Double Width) Poly2 Electrothermal Actuators (ETA) with 8 μm-Wide Force Measuring Beams
Main Uses:	Test Operation of S&A Interrupter Device Measure Opened Aperture Area, Actuator Deflection, System Resistance, and Drive Power Limit Observe/Measure Latch Capability Test Operation of Device with Dissimilar Wires Measure Deflection of ETAs to Determine Force

MINK 05
400 X 8 TEST ACTUATORS
POLYMUMPS RUN_68
END WIDTH 3UM

PolyMUMPs Run No.:	68
Working Nomenclature	Die #12
Fabricated Devices:	Chevron Electrothermal Actuators Test Die: - 8 × (400 µm x 3 µm) Arms - Stand-Alone Actuators - Actuators with 8 µm-Wide Force Measuring Beams (Straight and Tapered Armed Actuators Included)

Main Uses:	Test Operation of Chevron Electrothermal Actuators
	Measure Actuator Deflection, Drive Voltage, and
	    Resistance
	Measure Deflection on Force Beams to Determine
	    Actuator Force

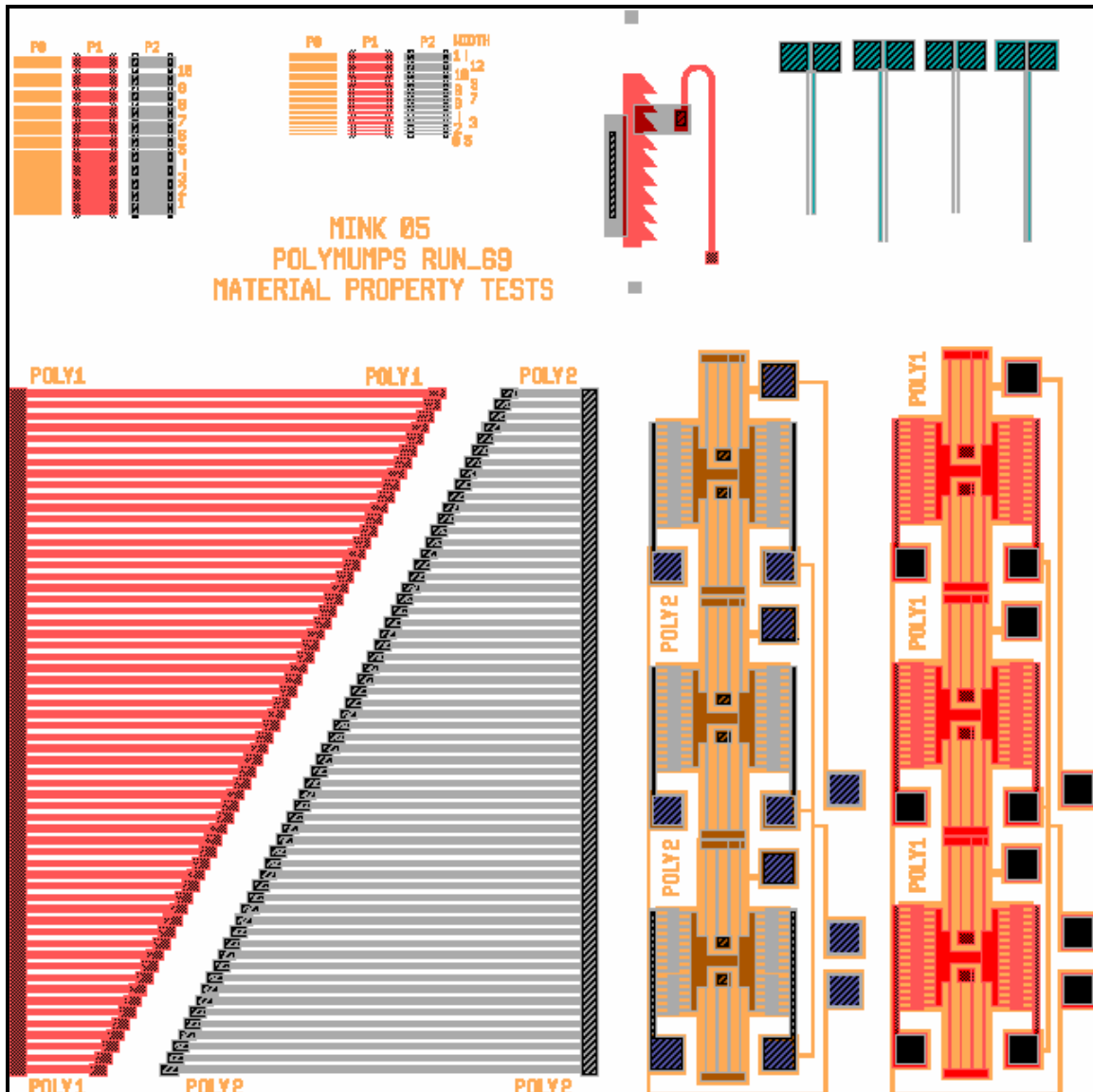| PolyMUMPs Run No.:	68
Working Nomenclature	Die #13

Fabricated Devices:	Chevron Electrothermal Actuators Test Die:
	  - 12 × (400 μm x 3 μm) Arms
	  - Stand-Alone Actuators
	  - Actuators with 8 μm-Wide Force Measuring Beams
	  (Straight and Tapered Armed Actuators Included)

Main Uses:	Test Operation of Chevron Electrothermal Actuators
	Measure Actuator Deflection, Drive Voltage, and
	    Resistance
	Measure Deflection on Force Beams to Determine
	    Actuator Force

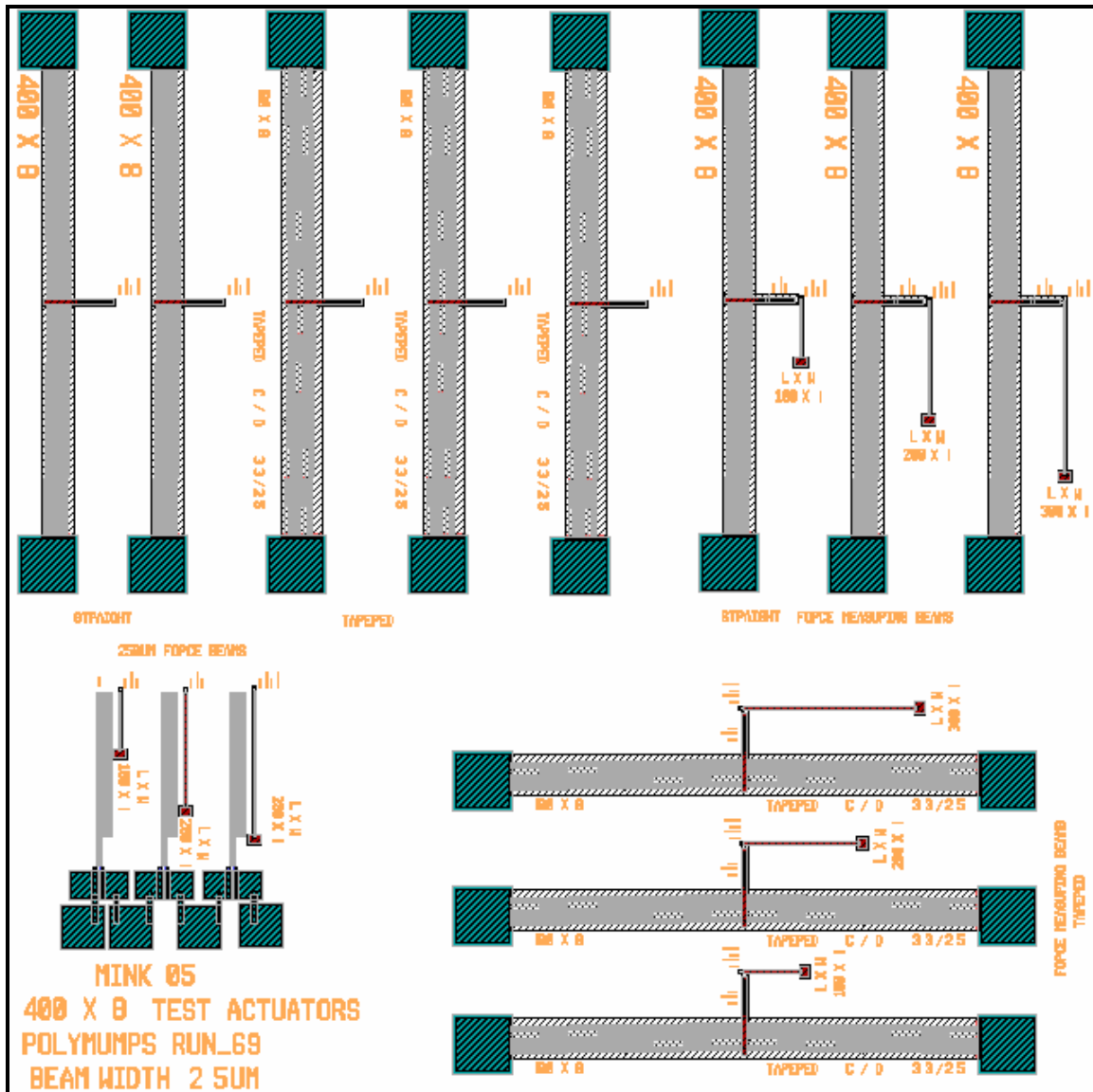| PolyMUMPs Run No.:	68
Working Nomenclature	Die #14 (Interrupter Mechanism #2)
Fabricated Devices:	S&A Interrupter Device: Four Chevron Actuators with Latches, 12 × (400 μm × 3 μm) Arms, Poly1 and Poly2 Overlapping Interrupter Plates 350 μm, 300 μm, 300 μm (Double Width), and 250 μm Poly1 Electrothermal Actuators (ETA) with 8 μm-Wide Force Measuring Beams
Main Uses:	Test Operation of S&A Interrupter Device Measure Opened Aperture Area, Actuator Deflection, System Resistance, and Drive Power Limit Observe/Measure Latch Capability Test Operation of Device with Dissimilar Wires Measure Deflection of ETAs to Determine Force

PolyMUMPs Run No.:	68
Working Nomenclature	Die #15 (Interrupter Mechanism #3)

Fabricated Devices:	S&A Interrupter Device:
	    Four Chevron Actuators with Latches,
	    $8 \times (400\ \mu m \times 3\ \mu m)$ Tapered Arms,
	    Poly1 and Poly2 Overlapping Interrupter Plates

Main Uses:	Test Operation of S&A Interrupter Device Measure Opened Aperture Area, Actuator Deflection, System Resistance, and Drive Power Limit Observe/Measure Latch Capability Test Operation of Device with Dissimilar Wires

PolyMUMPs Run No.:	69
Working Nomenclature	Die #16
Fabricated Devices:	Poly1 and Poly2 Fixed-Fixed Beams – up to 700 μm Poly1 and Poly2 Comb Drive Resonators Width and Spacing Test Structures Ratcheting Latch Test Structure Residual Stress Beams with Electrical Contacts

Main Uses:	Measure Beam Deflection to Determine Residual Stress
	Measure Resonating Frequency in Comb Drives to
	      Determine Young's Modulus
	Observe/Measure Limits of Fabrication Process
	Test/Observe Feasibility of Ratcheting Structure
	Test/Measure Joule Heating Effects on Residual Stress
	      Beams

PolyMUMPs Run No.:	69
Working Nomenclature	Die #17
Fabricated Devices:	Chevron Electrothermal Actuators Test Die: - 8 × (400 μm x 2.5 μm) Arms; Straight & Tapered - Stand-Alone Actuators - Actuators with 4 μm-Wide Force Measuring Beams 250 μm Poly2 Electrothermal Actuators with 4 μm- Wide Force Measuring Beams
Main Uses:	Test Operation of Chevron Electrothermal Actuators Measure Actuator Deflection, Drive Voltage, and Resistance Measure Deflection on Force Beams to Determine Actuator Force

PolyMUMPs Run No.:	69
Working Nomenclature	Die #18
Fabricated Devices:	Chevron Electrothermal Actuators Test Die: - 12 × (400 μm x 2.5 μm) Arms; Straight & Tapered - Stand-Alone Actuators - Actuators with 4 μm-Wide Force Measuring Beams 300 μm Poly2 Electrothermal Actuators with 4 μm- Wide Force Measuring Beams
Main Uses:	Test Operation of Chevron Electrothermal Actuators Measure Actuator Deflection, Drive Voltage, and Resistance Measure Deflection on Force Beams to Determine Actuator Force

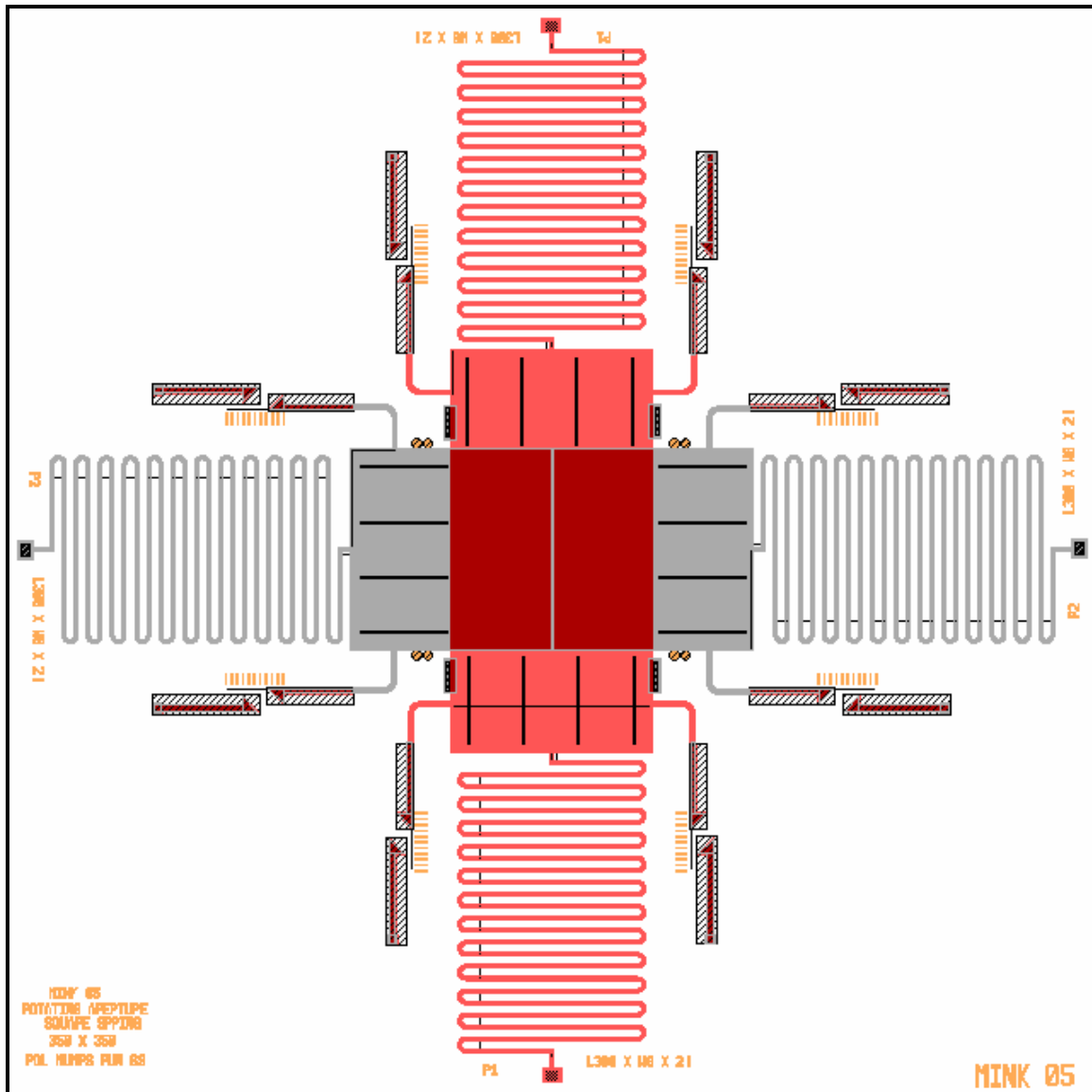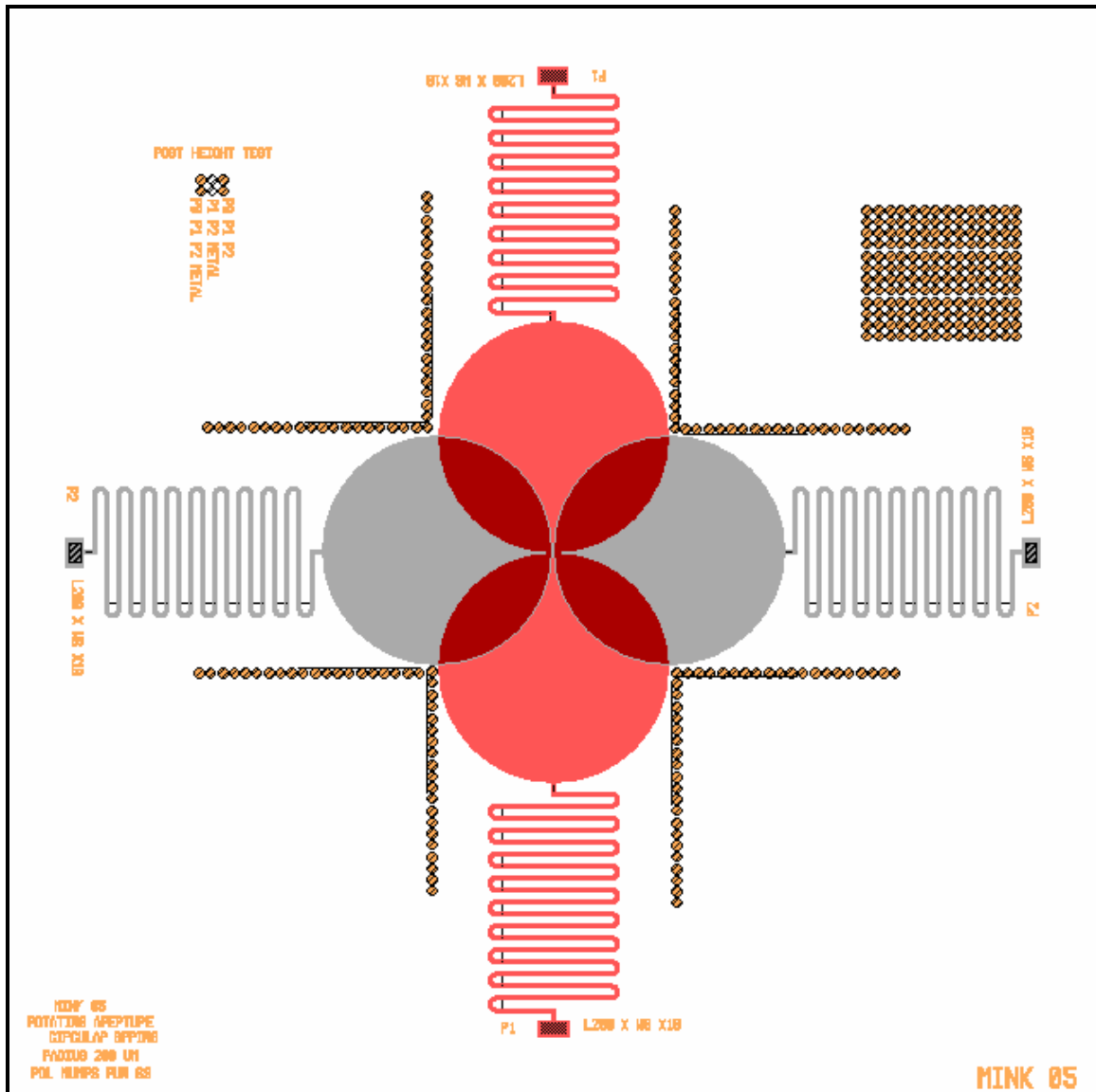| PolyMUMPs Run No.:	69
Working Nomenclature	Die #19

Fabricated Devices:	Chevron Electrothermal Actuators Test Die:
	   - 16 × (400 µm x 2.5 µm) Arms; Straight & Tapered
	   - Stand-Alone Actuators
	   - Actuators with 4 µm-Wide Force Measuring Beams
	250 µm Poly1 Electrothermal Actuators with 4 µm-Wide Force Measuring Beams

Main Uses:	Test Operation of Chevron Electrothermal Actuators
	Measure Actuator Deflection, Drive Voltage, and
	   Resistance
	Measure Deflection on Force Beams to Determine
	   Actuator Force

PolyMUMPs Run No.:	69
Working Nomenclature	Die #20
Fabricated Devices:	Rotating S&A Interrupter Device (with Latches): - 350 μm x 350 μm Square Plates - Poly1/Poly2 Stacked Latches - Guide Rails on Poly1 Plates - Guide Posts for Poly2 Plates - Dimpled Springs
Main Uses:	Test Operation of Rotating S&A Interrupter Device Measure Spin Rate Required to Latch Observe Effects of Guide Rails on Poly1 Sliding Plate Observe Effects of Guide Posts on Poly2 Sliding Plate Observe/Measure Latching Capability

PolyMUMPs Run No.:	69
Working Nomenclature	Die #21

Fabricated Devices:	Rotating S&A Interrupter Device :
	   - 200 μm Radius Plates
	    - Guide Posts for Both Poly1 and Poly2 Plates
	    - Dimpled Springs
	Fabrication Process Test Structures

Main Uses:	Test Operation of Rotating S&A Interrupter Device Determine Spin Rate Required to Observe Motion Observe Effects of Guide Posts on Sliding Plate Measure Heights of Fabricated Test Posts

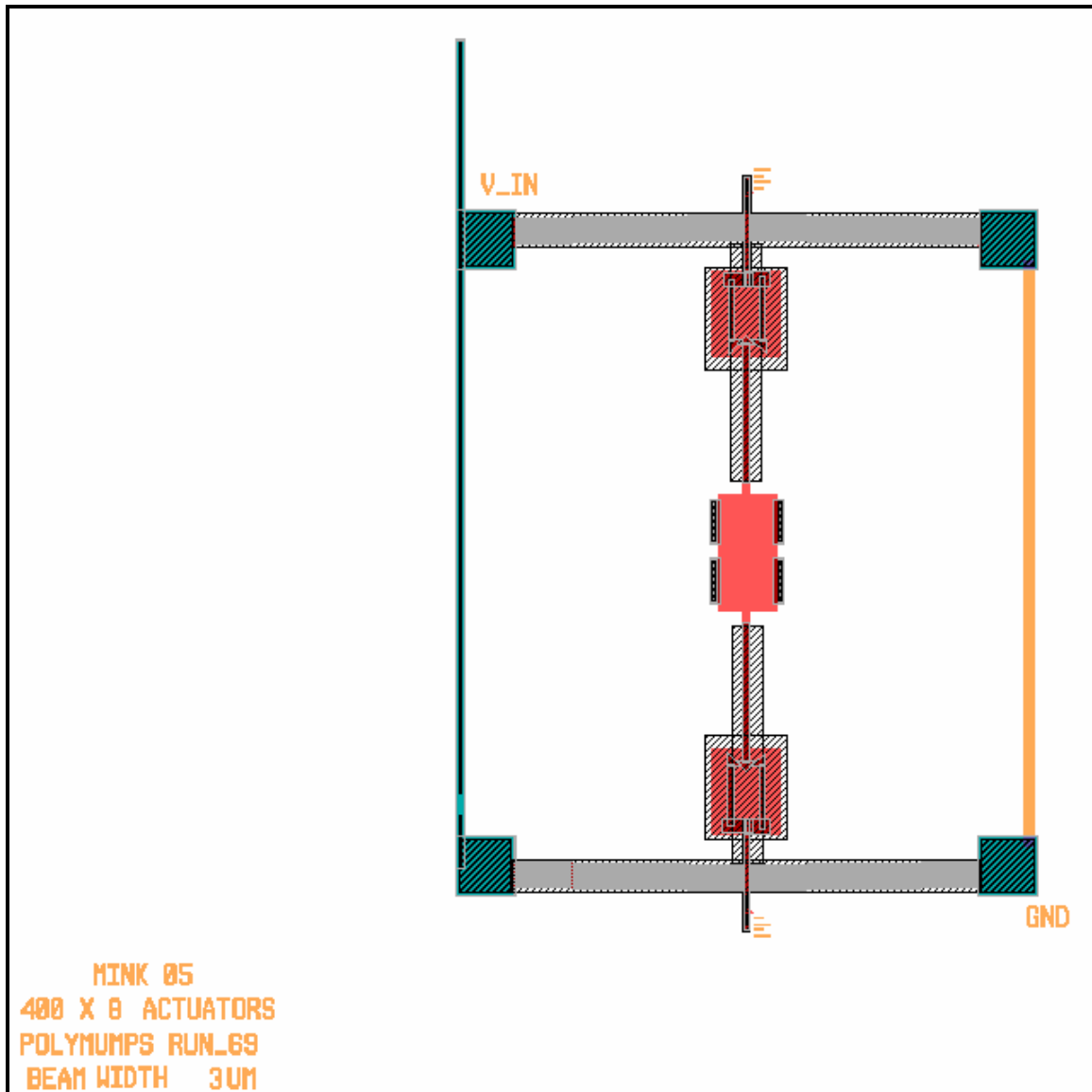| PolyMUMPs Run No.:	69
Working Nomenclature	Die #22

Fabricated Devices:	Layer Etch Process Test Structures:
	   - Poly0
	   - Anchor1 and Poly1
	   - Anchor2 and Poly2
	   - Poly0, Anchor1, Poly1, Via, and Poly2
	   - Poly0, Anchor1, and Poly1
	   - Poly0, Anchor2, and Poly2
	   - Poly0, Anchor1, Poly1, Via, Poly2, and Metal
	   - Other Combination

Main Uses:	Observe/Measure Post-Process Etched Depths and Layer Thickness

PolyMUMPs Run No.:	69
Working Nomenclature	Die #23

Fabricated Devices:	Rotating S&A Interrupter Device :
	   - 200 μm Radius Plates
	   - Guide Posts for Both Poly2 Plates
	   - Multiple Dimpled Springs on Poly1 Plates
	Fabrication Process Test Structures

Main Uses:	Test Operation of Rotating S&A Interrupter Device Determine Spin Rate Required to Observe Motion Observe Effects of Guide Posts on Poly2 Sliding Plate Observe Effects of Multiple Springs on Poly1 Plates Measure Heights of Fabricated Test Posts

PolyMUMPs Run No.:	69
Working Nomenclature	Die #24

Fabricated Devices:	Modified S&A Interrupter Device:
	    Two Chevron Actuators
	    8 × (400 μm × 3 μm) Arms,
	    Poly1 Interrupter Plates
	    Latch Mechanism Connects Chevron to Plate

Main Uses:	Test Operation of Modified S&A Interrupter Device Observe Feasibility of Modified Latch Capability Measure Actuator Deflection, System Resistance, and Drive Power Limit

Vita

      Captain Steven S. Mink enlisted in the U. S States Air Force in 1987. He was accepted into the Airman Education and Commissioning Program in 1997, and attended the University of California, Irvine. In 2001, he graduated Cum Laude with a Bachelor of Science degree in Electrical Engineering and a specialization in Electro-Optics and Solid-State Devices. After earning his commission in Officer Training School, Captain Mink was assigned as a Test Engineer to the tri-agency Integrated Program Office that manages the National Polar-orbiting Operational Environmental Satellite System. In 2004, he was assigned to the Air Force Institute of Technology to pursue a Master of Science degree in Electrical Engineering with a focus on Microelectronics and Laser/Electro-Optical Systems. Upon graduation, Capt Mink will be assigned to the Electro-Optical Sensor Technology Division at the Air Force Research Laboratory, Sensors Directorate.

REPORT DOCUMENTATION PAGE

1. REPORT DATE *(DD-MM-YYYY)*	2. REPORT TYPE	3. DATES COVERED *(From – To)*
23-03-2006	**Master's Thesis**	Sep 2004 – Mar 2006

4. TITLE AND SUBTITLE	5a. CONTRACT NUMBER
Microelectromechanical Systems (MEMS) Interrupter for Safe and Arm Devices	5b. GRANT NUMBER
	5c. PROGRAM ELEMENT NUMBER

6. AUTHOR(S)	5d. PROJECT NUMBER
Mink, Steven, S., Captain, USAF	5e. TASK NUMBER
	5f. WORK UNIT NUMBER

7. PERFORMING ORGANIZATION NAMES(S) AND ADDRESS(S)	8. PERFORMING ORGANIZATION REPORT NUMBER
Air Force Institute of Technology Graduate School of Engineering and Management (AFIT/EN) 2950 Hobson Way WPAFB OH 45433-7765	AFIT/GE/ENG/06-43

9. SPONSORING/MONITORING AGENCY NAME(S) AND ADDRESS(ES)	10. SPONSOR/MONITOR'S ACRONYM(S)
AFRL/MNMF Attn: Capt Kenneth Bradley 306 W. Eglin Blvd., Bldg 432 Eglin AFB, FL 32542 DSN: 875-0039 Comm: (850) 883-0039 E-mail: kenneth.bradley@eglin.af.mil	
	11. SPONSOR/MONITOR'S REPORT NUMBER(S)

12. DISTRIBUTION/AVAILABILITY STATEMENT
    APPROVED FOR PUBLIC RELEASE; DISTRIBUTION UNLIMITED.

13. SUPPLEMENTARY NOTES

14. ABSTRACT

    This thesis addresses the development of a new micro-scale interrupter mechanism for a safe and arm device used in modern weapon systems. The interrupter mechanism often consists of a physical barrier that prevents an initial source of energy, in an explosive train, from being transferred to subsequent charges. In general, when the physical barrier is removed, the weapon is considered armed, and the charge is allowed to propagate. Several issues facing current safe and arm devices systems are the shrinking industrial base for manufacturing these devices and the desire for modern safe and arm devices to be compatible with next generation weapon systems that are generally decreasing in size and increasing in complexity. The solution proposed here is to design, fabricate, and test a conceptual interrupter mechanism using Microelectromechanical Systems (MEMS) components. These components have inherent benefits over current devices, such as smaller feature sizes and lower part counts, which have the capability to improve performance and reliability. After an extensive review of existing micro-scale safe and arm devices currently being developed, a preliminary design was fabricated in a polysilicon surface micromachining process. The operating principle of this conceptual interrupter mechanism is to have MEMS actuators slide four overlapping plates away from each other to create an aperture, thus providing an unimpeded path for an initiating energy source to propagate. Operation of the fabricated MEMS interrupter mechanism was successfully demonstrated with an approximate aperture area of $1024 \ \mu m^2$ being created.

15. SUBJECT TERMS
    Safe & Arm Device, Fuze Arming Units, Microelectromechanical Systems, MEMS, Explosives Initiators, Exploding Foil Initiator, Munitions

16. SECURITY CLASSIFICATION OF:			17. LIMITATION OF ABSTRACT	18. NUMBER OF PAGES	19a. NAME OF RESPONSIBLE PERSON LaVern A. Starman, Maj, USAF (ENG)
REPORT	**ABSTRACT**	**c. THIS PAGE**			19b. TELEPHONE NUMBER *(Include area code)*
U	U	U	UU	196	(937) 255-3636 x 4618; e-mail: lavern.starman@afit.edu